DISSERTATION

PHYSICAL AND CHEMICAL CHARACTERISTICS BEHIND MEMBRANE INTERACTIONS OF SMALL MOLECULES

AND ELECTRON TRANSPORTERS

Submitted by

Benjamin J. Peters

Department of Chemistry

In partial fulfillment of the requirements

For the Degree of Doctor of Philosophy

Colorado State University

Fort Collins, Colorado

Fall 2018

Doctoral Committee:

      Advisor: Debbie C. Crans

      Dean C. Crick
      Melissa M. Reynolds
      Eric D. Ross

ABSTRACT

PHYSICAL AND CHEMICAL CHARACTERISTICS BEHIND MEMBRANE INTERACTIONS OF SMALL MOLECULES

AND ELECTRON TRANSPORTERS

There are many types of molecules that interact with and within membranes whereas many factors can dictate how they interact with membranes. Often, the interactions with the membrane interface can affect the mechanism of action of these molecules. Here, the interactions of small molecules and an electron transporter with model membranes under varying conditions are described. In the first chapter, the pH dependence of membrane association of a commonly used food preservative, benzoic acid was discussed and compared to the mechanism of action of general weak acid preservatives. Next the interactions of many structurally very similar compounds with model membranes were compared. These studies outline the importance of both the environment and that by just altering the molecules slightly, the interactions of the molecules can be changed. Chapter 4 outlines the importance of lipid density on the interactions of the electron transporter used within the electron transport system of *Mycobacterium tuberculosis* (menaquinone-9) to show that menaquinone is capable of membrane transport of protons and electrons. Together, these studies show how interactions and diffusion across membranes are not straight forward and more research is necessary to fully understand the interactions of molecules with cell membranes.

ACKNOWLEDGEMENTS

DEDICATION

I would like to dedicate this work to Jedd N. Conwell.

TABLE OF CONTENTS

Chapter 1: Probing Interactions with Membranes

1.1   Cellular Membranes

1.1.1   A Brief History of the Cell Membrane

In the mid to late 1800's, the existence of an osmotic barrier between the protoplasm of plants and their environment was established.[1] Around this time, the osmotic barrier was also described as being selectively permeable.[1] In 1899, Overton originally proposed the idea that these membranes consisted of a lipid/oil (lipid membrane theory).[2-3] The idea that a cell is surrounded by a lipid/oil layer was then replaced by the mosaic theory (1904, Nathansohn).[2, 4] The mosaic theory was simply a mixture of lipid/oil and semipermeable protoplasmic-like parts spread across the cell surface which would allow for permeation of ions and water.[2, 4] Later in 1925, Gortor and Grendel first observed the amount of lipid that could be extracted from erythrocytes was sufficient to cover twice the surface area of the cell using Langmuir monolayers suggesting a lipid bilayer surrounded cells (see section 1.2.1.2).[2, 5] Then in 1939, a model of the lipid bilayer membrane surrounded by protein coating on each side of the bilayer was proposed by Danielli and Davson.[2, 6] Following a series of studies that include studying of ion movement across the bilayer, lipid lateral movement within the bilayer, and protein interactions with the bilayer, came the current theory for membranes which was presented by Singer and Nicolson as the fluid mosaic model.[2, 7] The fluid mosaic model outlines all the characteristics discovered with membranes at the time as can be seen in Figure 1.1 and the author would like to recommend a review by Lombard for a more detailed historical account.[2] Briefly, this model outlines a fluid like bilayer membrane composed primarily of lipids. Within this bilayer are varying types of proteins that can interact peripherally or integrally with the bilayer. Lipids may even be glycosylated, thus adding to the complexity of the membrane.[8] Details

behind the fluid mosaic model have been further explored and added to the model, still the fluid mosaic

model is currently used to teach students about membrane structure.[8]
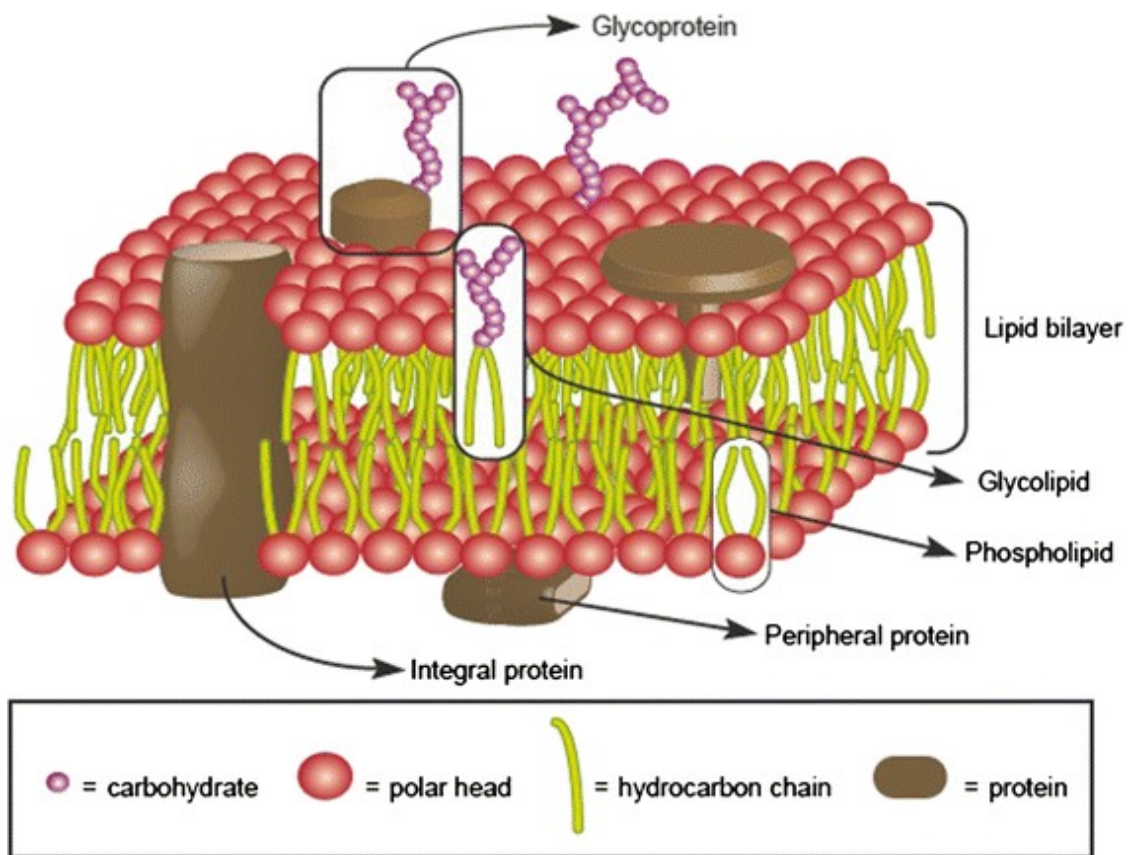
Figure 1.1. Schematic of the fluid mosaic model of a cell membrane. This figure was originally from
Lombard.[2]

1.1.2   Brief Introduction of Structural Components of Cellular Membranes

Since the introduction of the fluid mosaic model, the complexity of the membrane has been

extensively studied.[8] The 3-5 nm thick bilayer consists of numerous types of lipids that can have varying

functions or even affect the bilayer physical characteristics.[8-10] The lipid composition, protein composition,

and glycosylation of the proteins and lipids can have dramatic effects on the membrane curvature and

elasticity.[8, 11] Along with all of these characteristics, lipids can form rafts that can affect the local

environments.[8, 12] Considering the cell membrane consists of about 40 lipids to every protein (varying by

species), this discussion will focus only on the specific single or interlipid interactions.[8, 10, 13]

Cell membrane lipids are composed of having a hydrophilic headgroup and a hydrophobic alkyl tail. Depending on the headgroup and tail composition, characteristics such as lipid shape can be affected. Lipid shape is defined as the inherent shape of a specific lipid.[14] Examples of lipids with specific shapes include dipalmitoylphosphatidylethanolamine (DPPE, cone, Figure 1.2A), dipalmitoylphosphatidylcholine (DPPC, cylinder, Figure 1.2B), or lysophosphatidylcholine (LPC, inverted cone, Figure 1.2C).[14] The specific shape of the lipids can cause local alterations of the membrane curvature and therefore certain lipids with a given shape can be found more commonly within particular regions of the cellular membrane.[14] One structural region of the lipids that can affect the lipid shape is the headgroup.[14-15] Larger headgroups as compared to their tail size can cause the lipids to have inverted cone shape (LPC). [14] Another characteristic that can affect the shape of the lipid is the interlipid interactions.[14-15] As shown in Figure 1.2, the only structural difference between DPPC and DPPE is the choline ($RN(CH_3)^+$) and the ethanolamine (RNH_3^+). Due to the hydrogen bond donating capability of the ethanolamine, DPPE headgroups can interact closely with another DPPE molecule headgroup allowing tight packing of the headgroups allowing for the tails to spread.[14-15] This then causes DPPE to have a conical shape.[14-15] This is not the case with DPPC (cylinder) which is known to spread across water interfaces and is utilized within the alveolar membrane of the lungs for this purpose to allow for easier gaseous diffusion across the alveolar membranes.[16-17] Therefore, headgroup differences can have drastic effects on the lipid shape, how the lipids behave, and therefore affect the overall membrane structure.

Another alteration of the chemical structure of lipids that can affect the shape of lipids and the cell membrane, is the hydrophobic tail double bond content (unsaturation). Most of the unsaturations found within the lipid tails are found to be in the cis conformation.[8, 11, 14, 18] The cis conformation, as opposed to the trans conformation, is more commonly found in biological systems due to that the trans conformation overall structure does not deviate much from the fully saturated conformation.[8, 11, 14, 18] With the cis

conformation, the tails are forced into angles (affecting the shape of the lipid) that prevent easy stacking of the lipids, causing an overall spreading of the lipids within the cell membrane (Figure 1.2D).[8, 11, 14, 18]

Cells can also vary the length of the hydrophobic tail depending on the needs of the cell (Figure 1.2). The tail length of the fatty acids that make up the hydrophobic tails of the lipids vary in length depending on temperature.[14, 19] Cells can also vary the structure of the fatty acid tails by instead of having a straight carbon chain, hydrophobic region of the lipids can consist of isoprene units, cyclopropanes, other alterations or mixtures.[20] Through these alterations, the membrane can become more permeable or less permeable caused by differences in stacking ability of the lipid tails.[14, 18-19] If the lipids can stack easier, then the membrane is less permeable due to a more rigid cell membrane.[14, 18-19]

In summary, many structural characteristics of lipids can be adjusted to fit the cell's needs.[21-22] By controlling the shape of the lipids, the membrane shape can be altered, the amount of unsaturations within the tail can expand the lipids within the membrane, and the tail length can allow for easier/more difficult diffusion of metabolites into the cell.[8, 11, 14, 18]
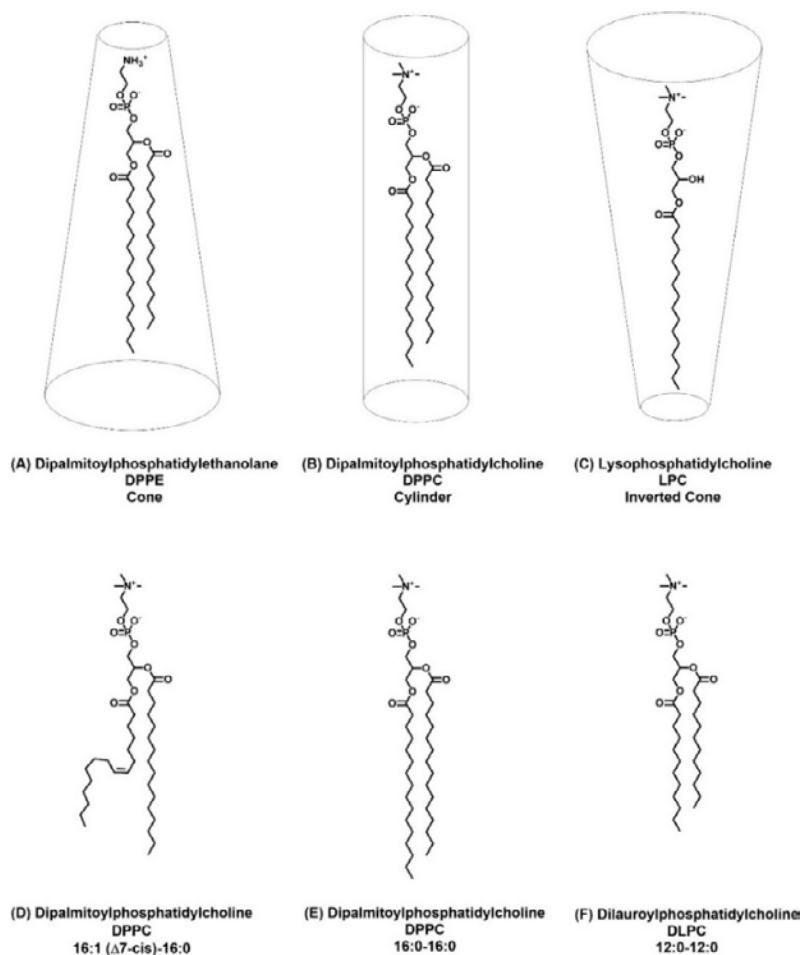
Figure 1.2. Chemical structures and shapes of dipalmitoylphosphatidylcholine (DPPC, A and E), Dipalmitoylphosphatidylethanolamine (DPPE, B), Lysophosphatidylcholine (LPC, C). Chemical structures of DPPC with one unsaturation beginning on carbon 7 within a palmitate tail (D) and dilauroylphosphatidylcholine (DLPC, F).

1.2   Molecular interactions with Membranes

There have been many studies describing the cellular membranes themselves, but studying the specific interactions of molecules with the cell membrane lipids has proven to be much more difficult.[23-25] Considering that many drug therapeutics currently in use diffuse across membranes, it is important to understand the details behind the interactions that allow for this diffusion.[10, 13] The limited information is largely due to the complexity of the cell membrane and therefore, it is difficult to study the specific interactions of small molecules with the membrane interface along with specific chemical and physical characteristics that lead to these interactions. In efforts to study the membrane interactions of small

5

molecules with cell membrane lipids, models of the cell membrane have been utilized to simplify the cell membrane to more manageable systems.

1.2.1 Studying Molecular Interactions with Model Membranes

To study and understand small molecule interactions with cell membranes, there have been many models developed. A few of the common models used include Black Lipid Membranes (BLM), liposomes, micelles, reverse micelles (RM), and Langmuir monolayers (Figure 1.3).[2, 26] BLMs (also known as painted lipid bilayers) are bilayers that are formed by utilizing a paintbrush and painting an lipid solution in organic solvent over a small hole.[26] When the solvent evaporates, the less volatile lipids are left behind forming a bilayer spanning the hole.[26] BLMs have been used successfully to determine rates of diffusion across bilayers, but limited information about specific details behind molecular interactions with membranes can be obtained.[26] Liposomes are characterized as being of at least a bilayer of lipids with water on the inside and outside of the vesicle.[18, 27-29] Liposomes are arguably the most relevant model membrane to cell membranes as they are bilayer vesicles. The use of liposomes have been useful for determining molecular information behind the interactions of small molecules with the lipids composing the liposome.[23, 25] These studies are normally very cumbersome and many techniques are necessary to determine these specific interactions.[23, 25] The micelles are monolayers formed from surfactant/lipid and are highly controllable. Micelles have been used very successfully in determining the interactions of surfactants/lipids with small molecules.[18, 30-32] Similarly, RMs (inverted micelles) have been used to determine the interactions of surfactants with small molecules, but are easier to control and form.[30, 33-36] Specifically, the characteristics of the sodium aerosol-OT (AOT) RM has been characterized very well.[37-39] Langmuir monolayers are water insoluble monolayers consisting of lipid or surfactant at an air-water interface.[18] Langmuir monolayers have also been characterized very well and can be utilized to obtain information about how molecules affect lipid interfaces allowing for information about how the small molecules affect cell membranes.[40-42] By altering the area per molecule of lipid on a given surface, Langmuir monolayers can provide information

on how lipid density alters affects small molecules have on the monolayer.[40-42] Considering the models

presented here (Figure 1.3), the following studies to determine a few of the physical characteristics behind

molecular interactions with membrane-like interfaces was conducted utilizing AOT RMs and Langmuir

monolayers. AOT RMs and Langmuir monolayers were chosen because they are well characterized and

can give both molecular information and information about how small molecules affect the cell

membrane interface.
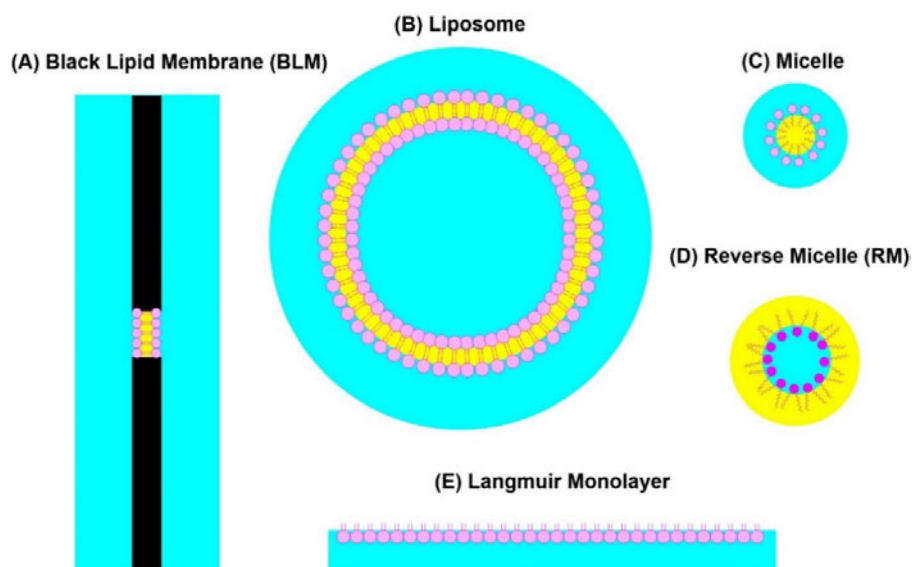
Figure 1.3. Schematics of a Black Lipid Membrane (BLM, A), a liposome (B), a micelle (C), a reverse micelle (D), and a Langmuir monolayer (E). The blue represents water, yellow represents hydrophobic solvent/region, and lipids/surfactants are given in pink.

1.2.1.1 AOT Reverse Micelles

Reverse micelles (RMs) are inverted micelles described as containing a nano-sized water pool

surrounded by surfactant and dissolved in organic solvent (Figure 1.4).[37, 43] To form this ternary

microemulsion, water, organic solvent and a surfactant are mixed together and upon agitation, the RMs

spontaneously form.[37-39, 43] Once formed, RMs, on average, are spheres consisting of a bulk water core, a

more solid Stern layer of the water near the headgroups of the surfactant, the surfactant tail region, and

the organic solvent.[37-39, 43] Shown in Figure 1.4 is an RM formed from one of the more commonly utilized

ternary systems which consists of water, the sodium salt of AOT, and 2,2,4 trimethylpentane as the organic solvent (isooctane).[37-39, 43-45]
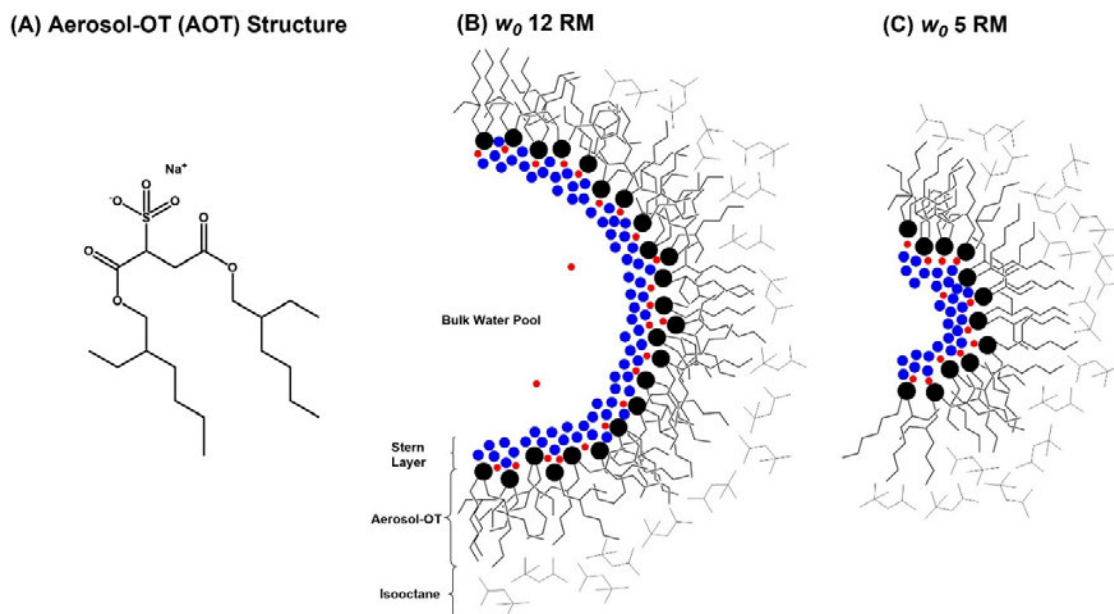
Figure 1.4. Chemical Structure of Sodium AOT (A), illustration of a w_0 12 RM (B), and an illustration of a w_0 5 RM (C). The location of the Na$^+$ ions within the Stern layer are given by red circles (B and C), and water within the Stern layer is given by blue circles. The number of Na$^+$ within the Stern layer relates to 80-90% of the Na$^+$ as is consistent with computational studies.[46] This figure was adapted from Crans *et al*.[44]

RMs have been characterized by numerous methods including spectroscopies such as ultraviolet-visible (UV-Vis), dynamic light scattering (DLS),[45, 47] infrared (IR), and nuclear magnetic resonance (NMR).[38] Utilizing these methodologies, RM characteristics have been found to be dependent on a number of factors, but primarily RMs are altered by changing the water to surfactant ratio (w_0 =[H$_2$O]/[Surfactant]).[36-39, 43, 45, 47-48] Just by altering the RM w_0 value, desired characteristics of the RMs can be acquired easily. As shown in Table 1.1, many characteristics of the RM can be calculated from known values in literature allowing for a highly controllable system including the volume of the RM (V_h), volume of the water pool (V_w), surface area of the RM (SA_h), surface area of the water pool (SA_w), AOT per RM surface area (AOT/SA_h), and AOT per water pool surface area (AOT/SA_w).[38, 45] Then by taking the ratio of the AOT per surface area of the RM to AOT per surface area of the water pool, it is clear that within the larger RM (w_0 20) the overall shape of the AOT is shape altered slightly to have more of a conical shape (increasing tail

area per headgroup area). By comparing the varying characteristics of varying w_0 values of RMs, the

interactions of molecules within the RM interface have been very successfully characterized.[33-36, 44-45, 48-52]

The author would recommend a review by De *et al.* for a more detailed description of RMs.[37] Therefore,

the RM interface has been used as a general model for a cellular membrane to study the molecule

interactions of molecules with a surfactant interface.[33, 44, 49]

Table 1.1. Size description of RMs within Isooctane.[a] [a]The table outlines the reverse micelles (RM) hydrodynamic radius (R_h), water pool radii (R_w), aggregation number (average AOT molecule per RM, η_{agg}), volume of RM (V_h), and volume of water pool (V_w), surface area of the RM (SA_h), and surface area of the water pool (SA_w) ; [b]Literature value of R_h, R_w, and η_{agg} are from Maitra and Day *et al.*;[38, 45] Values of V_h, V_w, SA_h, SA_w and the number of water molecules were calculated here from values given by Maitra and Day *et al.*.[38, 45]

w_0	R_h (nm)	R_w (nm)	η_{agg} (nm)	V_h (nm³)	V_w (nm³)	SA_h (nm²)	SA_w (nm²)	SA_h per AOT (nm²/AOT)	SA_w per AOT (nm²/AOT)	(SA_h per AOT) /(SA_w per AOT)
8	3.2	1.6	72	140	17	130	32	1.8	0.43	4.2
12	3.7	2.2	129	210	45	170	61	1.3	0.47	2.8
16	4.2	2.9	215	310	100	220	110	1.0	0.51	2.0
20	4.4	3.5	302	360	180	240	150	0.77	0.50	1.5

1.2.1.2 Langmuir Monolayers

Originally developed by Agnes Pockels, but later named after Irving Langmuir's version of the

monolayer, Langmuir monolayers are described as single molecule thick films residing on an aqueous

subphase as depicted in Figure 1.5.[2, 53-54] Langmuir monolayers are formed by the addition of a volatile

organic phospholipid solution to an aqueous subphase in a dropwise manner.[42, 53-55] Once added to the

subphase, the volatile organic solvent evaporates and an insoluble monolayer of lipids forms at the air-

water interface with the headgroups of the lipids in the water.[42, 55] Langmuir monolayers can be formed

using many types of lipids or even lipid extracts from cells to allow for as close to a cellular membrane

mixture as possible if preferred.[56-57] The presence of the lipid monolayer then reduces the surface tension

of water (72.8 mN/m) which can then be measured by a wire probe connected to a balance (Wilhemy

plate method).[58] The surface pressure (π) of the monolayer can be calculated by subtracting the surface

tension of water in the presence of lipid (γ) from the initial surface tension of water (γ_0, 72.8 mN/m) as

shown in equation 1.1.[42, 55] By measuring the area the monolayer covers at specific surface pressures, expansion or contraction effects on the lipid monolayer by other molecules can be determined. [42, 55]

$$\pi = \gamma_0 - \gamma \qquad (1.1)$$

The most common experiment used to determine the area of the Langmuir monolayer is the compression isotherm. As the name implies, a compression isotherm is an experiment where the Langmuir monolayer is compressed at a specific temperature and at a given rate (usually 10 mm min^{-1} or less). During this experiment, phase transitions of the lipids can be observed as shown in Figure 1.5. These phase transitions especially apparent with DPPC since it spreads across the aqueous interface and will exhibit all of the phase transitions.[16-17] Other lipids may not exhibit these phase transitions due to a limited amount of spreading across the water interface.[16-17] The resulting graphs from the compression isotherms are read from right to left as the area per molecule is decreased (monolayer is compressed). During this compression, the surface pressure is recorded at specific areas which can give information about the phase transitions of the lipids.[40-42] For example, at about 5 mN/m a phase transition of DPPC from gas phase to liquid phase can be observed and a collapse of the monolayer occurs at higher pressures.[41] During a compression, the lipids present transition from being in a gas-like state to a liquid-like state, and finally to a solid-like state with the pressures of 30-35 mN/m being accepted as near biologically related lipid densities.[42, 55] The author would recommend the review by Kaganer *et al.* for a more detailed description of Langmuir monolayers.[55] As Langmuir monolayers are currently the only method to determine how lipid density can affect interactions with small molecules and they are composed of any lipid of choice (as long as they are insoluble in the aqueous subphase), the following studies use Langmuir monolayers as another model membrane of choice.
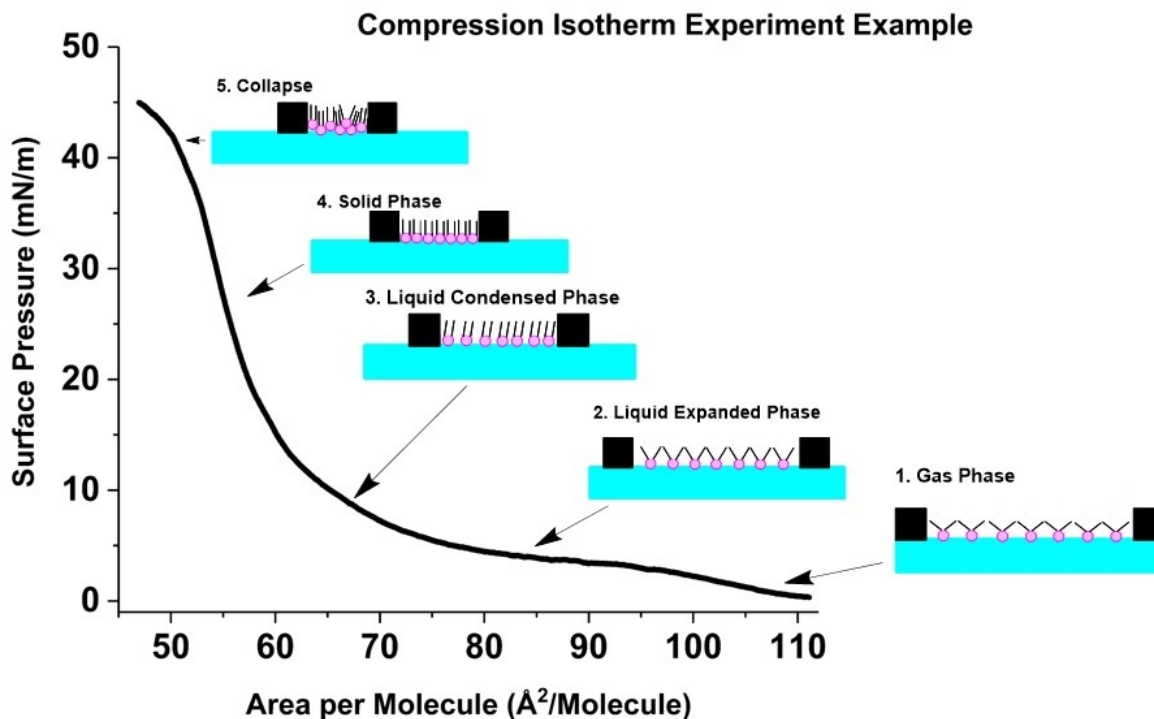
Figure 1.5. Example compression isotherm of a DPPC Langmuir monolayer. The compression isotherm graph reads from right to left and has an illustration of the lipids at each phase of the compression isotherm curve.

1.4   Studies of the Subsequent Chapters

Within these studies, physical and chemical characteristics behind membrane interactions of small molecules are explored. Chapter one explores the membrane interactions of a common food preservative as a function of pH.[34] Chapter three shows that even small structural differences can affect the specific interactions with interfaces using small aromatic amides and hydrazides. Then in chapter four, the interactions of an electron transporter with phospholipids is explored as a function of phospholipid density. Finally, Chapter five discusses future studies and the direction the author believes these studies should resume.

In chapter one, the pH dependence of the membrane interactions of small molecules is discussed in terms of the weak acid preservative, benzoic acid. The interactions of benzoic acid and benzoate with model membrane systems was characterized to understand the molecular interactions of the two forms of a simple aromatic acid with the components of the membrane. The RM microemulsion system based

on AOT allowed determination of the molecular positioning using ^{1}H 1D NMR and ^{1}H-^{1}H 2D NMR spectroscopic methods. Benzoic acid and benzoate were both found to penetrate the membrane/water interfaces; however, the benzoic acid was able to penetrate much deeper into the hydrophobic tail region of the AOT RM microemulsion. This data would suggest that benzoic acid is much more readily able to traverse a cellular membrane. The Langmuir monolayer model system, using DPPC, was used as a generic membrane lipid for a cell. Compression isotherms of monolayers demonstrated a pH dependent interaction with a lipid monolayer and confirmed the pH dependent observations shown in the reverse micellar model system. These studies provide an explanation for the antimicrobial activity of benzoic acid while benzoate is inactive against microorganisms.[34]

Pyridine based small molecule drugs, vitamins, and cofactors are vital for many cellular processes, but little is known about their interactions with membrane interfaces and is discussed in chapter two. This study explores how minor differences in small molecules (isoniazid, benzhydrazide, isonicotinamide, nicotinamide, picolinamide, and benzamide) affect their interactions with model membranes. Langmuir monolayer studies of DPPC or DPPE, in the presence of the molecules listed, show that isoniazid and isonicotinamide affect the DPPE monolayer at lower concentrations than the DPPC monolayer, demonstrating a preference for one phospholipid over the other. The Langmuir monolayer studies also suggest that nitrogen content and stereochemistry of the small molecule can affect the phospholipid monolayers differently. To obtain determine the molecular interactions of the simple N-containing aromatic pyridines with a membrane-like interface, ^{1}H 1D NMR and ^{1}H-^{1}H 2D NMR techniques were utilized to obtain information about position and orientation of the molecules of interest within AOT RMs. These studies show that all six of the molecules reside near the AOT sulfonate headgroups and ester linkages in similar positions, but nicotinamide and picolinamide tilt at the water-AOT interface to varying degrees. Combined, these studies demonstrate that small structural changes of small molecules can affect their specific interactions with membrane-like interfaces, and specificity toward specific cells.[59]

Chapter four discusses how lipid density and varying lipid types can affect the interactions with the *Mycobacterium tuberculosis* electron transporter, Menaquinone-9 (MK-9). Despite quinones from different organisms having varying structures, they are all thought to move within their respective electron transport systems similarly. All quinones within the electron transport chain are commonly illustrated as moving through the bilayer in a circular motion. This is even true with the electron transporter, MK-9, even though little information about the interactions of MK-9 with phospholipids is known. In this study, the interactions of MK-9 with common phospholipids, DPPC and DPPE, were determined using Langmuir monolayer techniques. Through the compression isotherm mixed monolayer studies, ideal area calculations, normalization to phospholipid content, and compression modulus calculations, these studies show that MK-9 does get partially compressed out of the monolayers, but not to the extent as has previously been reported. Brewster Angle Microscopy (BAM) studies were able to confirm most of the observations make through the surface pressure measurements. These studies specifically show that MK-9 does become partially compressed out of the Langmuir monolayers in a manner that would be consistent with the interactions of other quinones with lipids.

The summary, implications, and direction the author believes to be the next steps in these studies are presented in chapter five. Through the previous studies in chapters two through four, a few of the physical and chemical characterisitcs behind molecular interactions with membrane interfaces were explored. Though chapter one, the effects of pH on the membrane interactions of were determined, small structural differences affecting membrane interactions were explored in chapter three, and lipid density affects were determined for an electron transporter in chapter four. These studies have implications far and wide in the food industry, drug industry, and the mechanism behind electron transport within the bilayer of cells. There are many avenues for future studies from the studies presented here, but some of the most interesting would be to measure the pK_a of a few weak acids within the membrane interface using Langmuir monolayers, use insertion profiles of Langmuir monolayers at varying pH values to show that

the membrane interface affinity of molecules change as a function of pH, and computational studies of

quinone interactions with membranes.

References

(1)	Loeb, J., *The Dynamics of Living Matter*. Columbia University Press: **1906**.

(2)	Lombard, J. Once Upon a Time the Cell Membranes: 175 years of Cell Boundary Research. *Biol. Direct.* **2014,** *9*, 1-35.

(3)	Overton, E., *Ueber Die Allgemeinen Osmotischen Eigenschaften Der Zelle, Ihre Vermutlichen Ursachen Und Ihre Bedeutung FüR Die Physiologie*. S.L., **1899**.

(4)	A, N. Ueber Die Regulation Der Aufnahme Anorganischer Salzedurch Die Knollen Von Dahlia. *Jahrb f wiss Bot.* **1904,** *39*, 607-644.

(5)	Gorter, E.; Grendel, F. On Bimolecular Layers of Lipoids on the Chromocytes of the Blood. *J. Exp. Med.* **1925,** *41* (4), 439-443.

(6)	Danielli, J. F.; Davson, H. A Contribution to the Theory of Permeability of Thin Films. *J. Cell. Comp. Physiol.* **1935,** *5* (4), 495-508.

(7)	Singer, S. J.; Nicolson, G. L. The Fluid Mosaic Model of the Structure of Cell Membranes. *Science.* **1972,** *175* (4023), 720-731.

(8)	Stillwell, W.; Stillwell, W., *An Introduction to Biological Membranes Composition, Structure and Function Second Edition Preface*. **2016**; p IX-X.

(9)	Tulenko, T. N.; Chen, M.; Mason, P. E.; Mason, R. P. Physical Effects of Cholesterol on Arterial Smooth Muscle Membranes: Evidence of Immiscible Cholesterol Domains and Alterations in Bilayer Width During Atherogenesis. *J. Lipid Res.* **1998,** *39* (5), 947-956.

(10)	Yang, N. J.; Hinner, M. J. Getting across the Cell Membrane: An Overview for Small Molecules, Peptides, and Proteins. *Methods Mol. Biol.* **2015,** *1266*, 29-53.

(11)	Cantor, R. S. Lipid Composition and the Lateral Pressure Profile in Bilayers. *Biophys. J.* **1999,** *76* (5), 2625-2639.

(12)	Lingwood, D.; Simons, K. Lipid Rafts as a Membrane-Organizing Principle. *Science.* **2010,** *327* (5961), 46-50.

(13)	Di, L.; Artursson, P.; Avdeef, A.; Ecker, G. F.; Faller, B.; Fischer, H.; Houston, J. B.; Kansy, M.; Kerns, E. H.; Kramer, S. D.; Lennernas, H.; Sugano, K. Evidence-Based Approach to Assess Passive Diffusion and Carrier-Mediated Drug Transport. *Drug Discov. Today.* **2012,** *17* (15-16), 905-912.

(14)	Mouritsen, O. G., *Life - as a Matter of Fat : Lipids in a Membrance Biophysics Perspective*. Second edition. ed.; Cham : Springer: **2016**.

(15)	Leekumjorn, S.; Sum, A. K. Molecular Simulation Study of Structural and Dynamic Properties of Mixed DPPC/DPPE Bilayers. *Biophys. J.* **2006,** *90* (11), 3951-3965.

(16)	Veldhuizen, E. J. A.; Haagsman, H. P. Role of Pulmonary Surfactant Components in Surface Film Formation and Dynamics. *Biochim. Biophys. Acta, Biomembr.* **2000,** *1467* (2), 255-270.

(17)	Veldhuizen, R.; Nag, K.; Orgeig, S.; Possmayer, F. The Role of Lipids in Pulmonary Surfactant. *Biochim. Biophys. Acta, Mol. Basis Dis.* **1998,** *1408* (2-3), 90-108.

(18)	Jones, M. N., *Micelles, Monolayers, and Biomembranes*. New York : Wiley-Liss: New York, **1995**.

(19)	Dordas, C.; Brown, P. H. Permeability of Boric Acid across Lipid Bilayers and Factors Affecting It. *J. Membr. Biol.* **2000,** *175* (2), 95-105.

(20)	Suutari, M.; Laakso, S. Microbial Fatty-Acids and Thermal Adaptation. *Crit. Rev. Microbiol.* **1994,** *20* (4), 285-328.

(21)	Cebecauer, M., Introduction: Membrane Properties (Good) for Life. In *Methods in Membrane Lipids, Second Edition*, Owen, D. M., Ed. 2015; Vol. 1232, pp 7-17.

(22)   van Meer, G.; Voelker, D. R.; Feigenson, G. W. Membrane Lipids: Where They Are and How They Behave. *Nat. Rev. Mol. Cell Biol.* **2008,** *9* (2), 112-124.

(23)   Marques, A. V.; Trindade, P. M.; Marques, S.; Brum, T.; Harte, E.; Rodrigues, M. O.; D'Oca, M. G. M.; da Silva, P. A.; Pohlmann, A. R.; Alves, I. D.; de Lima, V. R. Isoniazid Interaction with Phosphatidylcholine-Based Membranes. *J. Mol. Struct.* **2013,** *1051*, 237-243.

(24)   Martini, M. F.; Disalvo, E. A.; Pickholz, M. Nicotinamide and Picolinamide in Phospholipid Monolayers. *Int. J. Quantum Chem.* **2012,** *112* (20), 3289-3295.

(25)   Rodrigues, C.; Gameiro, P.; Prieto, M.; de Castro, B. Interaction of Rifampicin and Isoniazid with Large Unilamellar Liposomes: Spectroscopic Location Studies. *Biochim. Biophys. Acta, Gen. Subj.* **2003,** *1620* (1-3), 151-159.

(26)   Winterhalter, M. Black Lipid Membranes. *Curr. Opin. Colloid Interface Sci.* **2000,** *5* (3-4), 250-255.

(27)   Colley, C. M.; Ryman, B. E. Liposome - from Membrane Model to Therapeutic Agent. *Trends Biochem. Sci.* **1976,** *1* (9), 203-205.

(28)   Maghraby, G. M.; Barry, B. W.; Williams, A. C. Liposomes and Skin: From Drug Delivery to Model Membranes. *Eur. J. Pharm. Sci.* **2008,** *34* (4-5), 203-222.

(29)   Contreras, F. X.; Sanchez-Magraner, L.; Alonso, A.; Goni, F. M. Transbilayer (Flip-Flop) Lipid Motion and Lipid Scrambling in Membranes. *Febs Letters.* **2010,** *584* (9), 1779-1786.

(30)   Gaidamauskas, E.; Cleaver, D. P.; Chatterjee, P. B.; Crans, D. C. Effect of Micellar and Reverse Micellar Interface on Solute Location: 2,6-Pyridinedicarboxylate in CTAB Micelles and CTAB and AOT Reverse Micelles. *Langmuir.* **2010,** *26* (16), 13153-13161.

(31)   Kreke, P. J.; Magid, L. J.; Gee, J. C. H-1 and C-13 Nmr Studies of Mixed Counterion, Cetyltrimethylammonium Bromide Cetyltrimethylammonium Dichlorobenzoate, Surfactant Solutions: The Intercalation of Aromatic Counterions. *Langmuir.* **1996,** *12* (3), 699-705.

(32)   Vermathen, M.; Stiles, P.; Bachofer, S. J.; Simonis, U. Investigations of Monofluoro-Substituted Benzoates at the Tetradecyltrimethylammonium Micellar Interface. *Langmuir.* **2002,** *18* (4), 1030-1042.

(33)   Crans, D. C.; Trujillo, A. M.; Bonetti, S.; Rithner, C. D.; Baruah, B.; Levinger, N. E. Penetration of Negatively Charged Lipid Interfaces by the Doubly Deprotonated Dipicolinate. *J. Org. Chem.* **2008,** *73* (24), 9633-9640.

(34)   Peters, B. J.; Groninger, A. S.; Fontes, F. L.; Crick, D. C.; Crans, D. C. Differences in Interactions of Benzoic Acid and Benzoate with Interfaces. *Langmuir.* **2016,** *32* (37), 9451-9459.

(35)   Samart, N.; Beuning, C. N.; Haller, K. J.; Rithner, C. D.; Crans, D. C. Interaction of a Biguanide Compound with Membrane Model Interface Systems: Probing the Properties of Antimalaria and Antidiabetic Compounds. *Langmuir.* **2014,** *30* (29), 8697-8706.

(36)   Silva, O. F.; Fernandez, M. A.; Silber, J. J.; de Rossi, R. H.; Correa, N. M. Inhibited Phenol Ionization in Reverse Micelles: Confinement Effect at the Nanometer Scale. *Chemphyschem.* **2012,** *13* (1), 124-130.

(37)   De, T. K.; Maitra, A. Solution Behavior of Aerosol OT in Nonpolar-Solvents. *Adv. Colloid Interface Sci.* **1995,** *59*, 95-193.

(38)   Maitra, A. Determination of Size Parameters of Water Aerosol OT Oil Reverse Micelles from Their Nuclear Magnetic-Resonance Data. *J. Phys. Chem.* **1984,** *88* (21), 5122-5125.

(39)   Zulauf, M.; Eicke, H. F. Inverted Micelles and Microemulsions in the Ternary-System H_2O-Aerosol-OT-Isooctane as Studied by Photon Correlation Spectroscopy. *J. Phys. Chem.* **1979,** *83* (4), 480-486.

(40)   McConnell, H. M. Structures and Transitions in Lipid Monolayers at the Air-Water-Interface. *Annu. Rev. Phys. Chem.* **1991,** *42*, 171-195.

(41)   Knobler, C. M.; Desai, R. C. Phase-Transitions in Monolayers. *Annu. Rev. Phys. Chem.* **1992,** *43*, 207-236.

(42) Ulman, A. Formation and Structure of Self-Assembled Monolayers. *Chem. Rev.* **1996,** *96* (4), 1533-1554.

(43) Eicke, H. F.; Rehak, J. Formation of Water-Oil-Microemulsions. *Helv. Chim. Acta.* **1976,** *59* (8), 2883-2891.

(44) Crans, D. C.; Peters, B. J.; Wu, X.; McLauchlan, C. C. Does Anion-Cation Organization in Na^+-Containing X-Ray Crystal Structures Relate to Solution Interactions in Inhomogeneous Nanoscale Environments: Sodium-Decavanadate in Solid State Materials, Minerals, and Microemulsions. *Coord. Chem. Rev.* **2017,** *344*, 115-130.

(45) Day, R. A.; Robinson, B. H.; Clarke, J. H. R.; Doherty, J. V. Characterization of Water-Containing Reversed Micelles by Viscosity and Dynamic Light-Scattering Methods. *J. Chem. Soc., Faraday Trans.* **1979,** *75*, 132-139.

(46) Faeder, J.; Albert, M. V.; Ladanyi, B. M. Molecular Dynamics Simulations of the Interior of Aqueous Reverse Micelles: A Comparison between Sodium and Potassium Counterions. *Langmuir.* **2003,** *19* (6), 2514-2520.

(47) Bohidar, H. B.; Behboudnia, M. Characterization of Reverse Micelles by Dynamic Light Scattering. *Colloids Surf., A.* **2001,** *178* (1-3), 313-323.

(48) Riter, R. E.; Willard, D. M.; Levinger, N. E. Water Immobilization at Surfactant Interfaces in Reverse Micelles. *J. Phys. Chem. B.* **1998,** *102* (15), 2705-2714.

(49) Crans, D. C.; Trujillo, A. M.; Pharazyn, P. S.; Cohen, M. D. How Environment Affects Drug Activity: Localization, Compartmentalization and Reactions of a Vanadium Insulin-Enhancing Compound, Dipicolinatooxovanadium(V). *Coord. Chem. Rev.* **2011,** *255* (19-20), 2178-2192.

(50) Koehn, J. T.; Magallanes, E. S.; Peters, B. J.; Beuning, C. N.; Haase, A. A.; Zhu, M. J.; Rithner, C. D.; Crick, D. C.; Crans, D. C. A Synthetic Isoprenoid Lipoquinone, Menaquinone-2, Adopts a Folded Conformation in Solution and at a Model Membrane Interface. *J. Org. Chem.* **2018,** *83* (1), 275-288.

(51) Sripradite, J.; Miller, S.; Tongraar, A.; Johnson, M.; Crans, D. Probing the Effects of Environments on pK_a Values: Interaction of Aniline with Reverse Micelles as Monitored Using by ^{1}H NMR Spectroscopy. *Abstr. Pap. Am. Chem. Soc.* **2015,** *249*.

(52) Sripradite, J.; Samart, N.; Tongraar, A.; Crans, D. 1h-and 19f-Nmr Spectroscopic Studies of 4-Fluorophenylbiguanide with the Interface of Reverse Micelles. *Abstr. Pap. Am. Chem. Soc.* **2015,** *249*.

(53) Pockels, A. On the Spreading of Oil Upon Water. *Nature.* **1894,** *50*, 223-224.

(54) Langmuir, I. The Constitution and Fundamental Properties of Solids and Liquids. Ii. Liquids. *J. Am. Chem. Soc.* **1917,** *39*, 1848-1906.

(55) Kaganer, V. M.; Mohwald, H.; Dutta, P. Structure and Phase Transitions in Langmuir Monolayers. *Rev. Mod. Phys.* **1999,** *71* (3), 779-819.

(56) Alonso, C.; Alig, T.; Yoon, J.; Bringezu, F.; Warriner, H.; Zasadzinski, J. A. More Than a Monolayer: Relating Lung Surfactant Structure and Mechanics to Composition. *Biophys. J.* **2004,** *87* (6), 4188-4202.

(57) Aroti, A.; Leontidis, E.; Maltseva, E.; Brezesinski, G. Effects of Hofmeister Anions on DPPC Langmuir Monolayers at the Air-Water Interface. *J. Phys. Chem. B.* **2004,** *108* (39), 15238-15245.

(58) Welzel, P. B.; Weis, I.; Schwarz, G. Sources of Error in Langmuir Trough Measurements Wilhelmy Plate Effects and Surface Curvature. *Colloids Surf., A.* **1998,** *144* (1-3), 229-234.

(59) Peters, B. J.; Van Cleave, C.; Haase, A. A.; Hough, J. P. B.; Giffen-Kent, K. A.; Cardiff, G. M.; Sostarecz, A. G.; Crick, D. C.; Crans, D. C. Structure Dependence of Pyridine and Benzene Derivatives on Interactions with Model Membranes. *Langmuir.* **2018**.

Chapter 2: pH Dependence for Cellular Uptake: Weak Acid Food Preservatives

2.1   Weak Acid Food Preservatives as Antimicrobials

There are many methods used for food preservation that are in use today.[1-2] Of them, the weak acid preservatives are some of the most widely utilized in food and beverages to prevent the growth of microorganisms.[2-4] The weak acid preservative class (E200-E299) includes weak acids such as acetic acid, formic acid, and benzoic acid (HB). Weak acid preservatives only have antimicrobial activity when in an acidic environment (below their pK_a).[1-2] This has been shown through numerous experiments where consistently the weak acids become more able to diffuse across cell and organelle membranes as the pH of the media is decreased.[2, 5-8] This is likely due to the differences in the interactions of the charged conjugate base and uncharged acid with the membrane interface.[2-4, 9]

To combat weak acid preservatives, the adaptation of *Saccharomyces cerevisiae (S. cerevisiae)* has been well characterized in relation to larger weak acids such as benzoic acid (HB).[2-4, 7-11] Considering that the acid is uncharged and the conjugate base is negatively charged, it's thought that the neutral acid can diffuse across the cellular membrane. Once across the membrane, the HB dissociates into the conjugate base (benzoate, B$^-$) and a proton within the higher pH cytosol.[6, 8] After this dissociation, the intercellular environment pH decreases and an accumulation of toxic B$^-$, and an upregulation of the transcription factor *Pdr12* occurs.[12-17] *Pdr12* codes for an ABC transporter (Pdr12) that exports carboxylic acids.[12-17] Simultaneously, an ATPase that exports protons is upregulated (Pma1) to restore the homeostatic pH of the cytosol.[9, 18] After Pdr12 exports B$^-$ into the cytosol with a low pH, B$^-$ reprotonates and HB forms. This event then leads to the final step of what has been described as a futile cycle and has been described in detail using HB and B$^-$ as the weak acid preservative by Piper *et al.* shown in Figure 2.1.[3, 9, 19] Although the

details behind how HB affects microorganisms such as *S. cerevisiae* have been studied in detail, little

information is available about the differences between the interactions of HB and B$^-$ with the cell

membrane.

    Therefore, this chapter aims to determine if there are differences in interactions with membrane

interfaces between HB and B$^-$. Using HB and B$^-$ as models for the weak acid food preservative class, we

hypothesize that HB and B$^-$ interact with membranes differently with interfaces which allows for the

preferential entry of HB into the cell. Specifically, HB can penetrate deeper into a membrane interface

than B$^-$, which will prefer to stay within water. To test this hypothesis, we used reverse micelles in

conjunction with ^{1}H NMR techniques and surface pressure compression isotherms of Langmuir

monolayers comprised of dipalmitoylphosphatidylcholine (DPPC) as discussed in greater detail in the

previous chapter or within the published manuscript.[20]
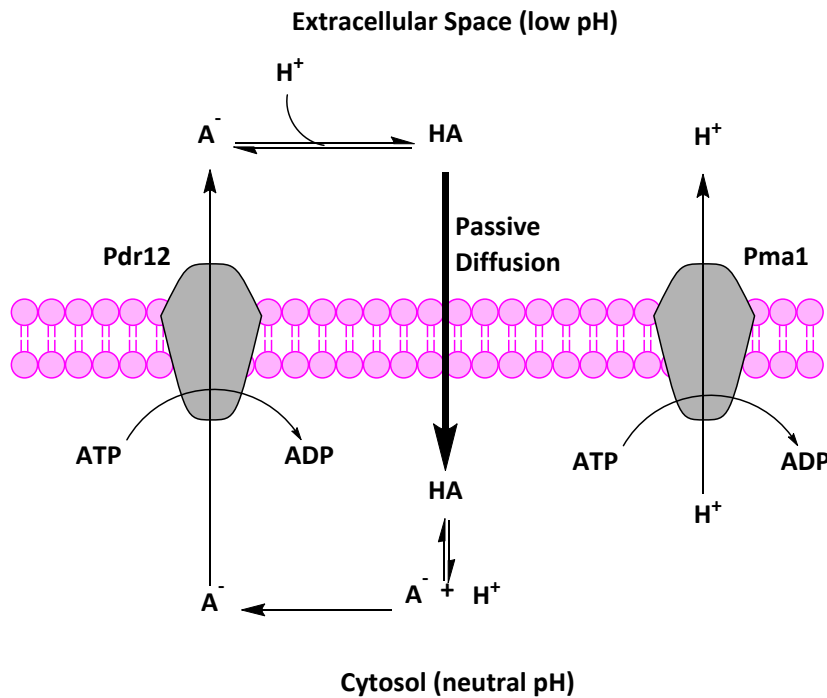
Figure 2.1. Diagram representing the "futile" cycle described by Piper *et al.* for *S. cerevisiae* with more solid arrow outlining the importance of passive diffusion for weak acid uptake into the cell[3, 9, 19] A$^-$, H$^+$, HA, ATP, and ADP represent, the conjugate base of the acid, proton, weak acid, adenosine triphosphate, and adenosine diphosphate respectively.

2.2 Materials and Methods

2.2.1 Materials

Most reagents were used without further purification including HB (Sigma-Aldrich, ≥99.5%), 2,2,4-trimethylpentane (isooctane, Sigma-Aldrich, ≥99.0%), deuterium oxide (D_2O, Cambridge Isotope Laboratories, 99.9%), 1,2-dipalmitoyl-sn-glycero-3- phosphocholine (DPPC, Avanti Polar Lipids Inc., >99%), d6-dimethyl sulfoxide containing tetramethyl silane (d_6-DMSO, Cambridge Isotope Laboratories, 99.9% + 0.05% TMS), activated charcoal (Sigma-Aldrich, 8–20 mesh), methanol (Omnisolve, 99.9%), 3-(trimethylsilyl)- propane-1-sulfonic acid (DSS, Wilmad), hexane (Fisher Scientific, 99.9%), and isopropanol (EMD, 99.8%). Bis(2-ethylhexyl)- sulfosuccinate sodium salt (AOT, Aldrich, 99.8%) was purified using activated charcoal and methanol to remove acidic impurities as described previously.[21] Briefly, 50.0 g AOT was dissolved into 150 mL of methanol. Then 15 g activated charcoal was added to the mixture. This suspension was stirred for 2 weeks. After mixing, the suspension was filtered to remove the activated charcoal. The filtrate was then dried under rotary evaporation at 50 °C until the water content was below 0.2 molecules of water per AOT as determined by ^{1}H NMR spectroscopy. All pH measurements were conducted using a Thermo Orion 2 Star pH meter equipped with a VWR semimicro pH probe. When conducting the NMR experiments, deuterium oxide was used in the presence of aqueous solutions and the pH was adjusted to consider the presence of deuterium (pD = 0.4 + pH).[21] The pD is customarily referred to as pH and therefore we refer to pD as pH.[21-23] NaOD and DCl solutions were prepared by dissolving NaOH or HCl into D_2O.

2.2.2 Preparation of Aqueous Solutions of HB and B⁻ for ^{1}H 1D NMR Experiments

The aqueous stock solution was prepared by dissolving HB (0.031 g, 0.25 mmol) in D_2O (25.0 mL). This 10 mM solution was then separated into 2 mL aliquots. The pH of each of the aliquots was adjusted using NaOD or DCl (1.0 and 0.1 M) to prepare a range of pH values.

2.2.3 Preparation of AOT-Isooctane Stock Solutions and Reverse Micelle Microemulsions of HB and B[-] for ^{1}H 1D NMR Experiments

The 750 mM AOT-isooctane stock solution was prepared by dissolving sodium AOT (8.34 g, 18.8 mmol) in isooctane (25 mL). Specific volumes of the AOT stock solution was added to specific volumes of the aqueous stock solutions of HB or B[-] and vortexed until clear to form reverse micelles of w_0 values of 20, 16, 12, and 8 (w_0 = [H$_2$O]/[AOT]).

2.2.4 ^{1}H 1D NMR Experiments with Reverse Micelle Microemulsion and D$_2$O Samples

^{1}H NMR experiments were performed using a 400 MHz Varian NMR spectrometer using a 45° pulse at 25°C. The aqueous samples were referenced to an external DSS sample at the same pH. The pH of the reverse micelles was assumed to be the same as the aqueous solutions. Reverse micelle samples were referenced to the isooctane methyl peak (0.904 ppm) as previously reported.[21] ^{1}H 1D NMR spectral data were analyzed using MestReNova NMR processing software version 10.0.1. Chemical shifts of proton H$_a$ for HB and B[-] were then transferred to OriginPro version 9.61 where the chemical shifts were graphed as a function of pH. A best fit sigmoidal curve was fit to the data points and the pH corresponding to the maximum of the derivative of the best fit curve allowed for the determination of the pK$_a$ of HB in both the aqueous and reverse micelle solutions.

2.2.5 Preparation of B[-] Containing Reverse Micelles for ^{1}H-^{1}H 2D NOESY NMR Experiments

To prepare the 200 mM B[-] aqueous stock solution, HB (0.0050 g, 0.040 mmol) was dissolved into 2 mL of doubly deionized (DDI) H$_2$O as the pH was adjusted to 7.8 using HCl and NaOH (1.0 and 0.1 M). The 750 mM AOT stock solution was prepared by dissolving sodium AOT (0.333 g, 0.750 mmol) into 1 mL of 95% isooctane/5% d_{12}-cyclohexane (v/v). The w_0 16 reverse micelles were then prepared by dissolving 215 μL of B[-] aqueous stock solution into 785 μL AOT stock solution for a final concentration for 43 mM B[-] in the overall reverse micellar microemulsion.

2.2.6 Preparation of HB Containing Reverse Micelles for ^{1}H-^{1}H 2D NOESY NMR Experiments

To prepare the 200 mM HB sample, HB (0.0053 g, 0.043 mmol) was added to 215 μL of D_2O. To this suspension, 785 μL of 750 mM AOT stock solution in isooctane was added to the suspension. The AOT stock solution was prepared as previously described in section 2.2.5. The mixture was then vortexed until all HB was dissolved, and the mixture turned clear.

2.2.7 ^{1}H-^{1}H 2D NOESY NMR Experiments of B$^-$ or HB Containing RMs

The ^{1}H-^{1}H 2D NOESY NMR spectra were obtained using a 500 MHz Varian NMR at 25 °C. The experiments were conducted using a standard pulse sequence with 32 scans per transient, 200 transient pairs in the f1 dimension, 200 ms mixing time, and the NMR was locked onto d_{12} -cyclohexane. The spectrum was referenced to the isooctane methyl peak at 0.904 ppm as previously reported and the data was processed using MestReNova NMR processing software. The ^{1}H-^{1}H 2D NOESY spectrum was worked up by first mildly phasing the spectrum in both the f1 and f2 dimensions then subjecting the spectrum a 90º sine^2 weighting function. Then a 3rd order Bernstein polynomial baseline. After baselining, the spectrum was then subjected to a cozy-like symmetrization function.

2.2.8 Reverse Micelle Sample Preparation for Dynamic Light Scattering

HB (0.012 g, 0.10mmol) was dissolved into 10 mL of DDI H_2O to prepare a 10.0 mM stock solution. The pH of the of aliquots (5 mL) of HB was adjusted to 3.0 and 7.0 with HCl and NaOH (1.0 and 0.1 M). The 100 mM AOT stock solution was prepared by dissolving sodium AOT (8.89 g, 20.0 mM) into 200 mL isooctane. The reverse micelles were prepared then by adding specific volumes of DDI H_2O or HB solution at specific pH values to specific volumes of AOT stock solution and vortexed until clear to prepare reverse micelles sizes of w_0 20, 16, 12, and 8.

To prepare the 200 mM samples of HB, 0.0035 g (0.029 mmol) of HB was dissolved into 5 mL of w_0 16 reverse micelle solution by vortexing until the solution was clear. To prepare the 200 mM B$^-$ solution, 0.049 g (0.40 mmol) of HB was dissolved in 2 mL of DDI H2O while the pH was adjusted to 9.0 using HCl

and NaOH (1.0 and 0.1 M). Then 5 mL of w_0 16 reverse micelle solution was prepared by mixing the 200

mM B⁻ solution with 100 mM AOT solution.

The 1 cm × 1 cm glass cuvettes used for the dynamic light scattering (DLS) measurement were cleaned

by first rinsing 3 times with isooctane followed by rinsing three times with the sample solution to be

measured. The cuvettes were then filled with 1 mL of a reverse micelle sample and capped with a Teflon

cap. Identical results were obtained whether samples were filtered or not as has previously been done.

Each sample was made in triplicate and measured according to section 2.2.9.

2.2.9   DLS Measurements of Reverse Micelle Solutions

DLS measurements were conducted using a Zetasizer nano-ZS. Each measurement consisted of a 700

s equilibration time at 25 °C followed by 10 acquisitions consisting of 15 scans for each acquisition. The

data was analyzed using Zetasizer software and the values reported are the average of triplicate samples.

2.2.10   Langmuir Monolayer Studies

Langmuir monolayers of dipalmitoylphosphatidylcholine (DPPC) were prepared using a Kibron

µTroughXS (59 mm wide and 232 mm long) The subphase consisted of 25 mL of DDI H_2O or 1.0 mM HB

(0.0031 g, 25 µmol) at pH 7.0 or 3.0. The pH was adjusted using HCl or NaOH (1.0 and 0.1 M). The

phospholipid 2.7 mM stock solution of DPPC consisted of 2.7 µmol DPPC dissolved in 1 mL of *n*-

hexane/isopropanol (3:2, v/v). DPPC stock solution was applied to the surface of the subphase (7 µL, 19

nmol) in a dropwise manner. This was then allowed to equilibrate 10 minutes. The trough barriers were

then compressed at a constant rate of 35 mm min⁻¹. Surface Pressure was monitored throughout

compression via the Wilhemy plate method where a wire probe was used in place of a plate. The surface

pressure is calculated using equation 1 where π is the surface pressure, γ_o is the surface tension of water

without lipid present (72.8 mN/m), and γ is the surface tension in the presence of lipid.[24] [25]

$$\pi = \gamma_o - \gamma \tag{1}$$

The results of each measurement are reported as an average of three trials. The compression modulus of each average was calculated as previously reported using equation 2 where $C_s{}^{-1}$ is the compression modulus, A is the area per molecule, and π is the surface pressure.[24] [25-26]

$$C_s^{-1} = -A\left(\frac{d\pi}{dA}\right)$$

(2)

2.3   Results and Discussion

2.3.1 ^{1}H NMR Spectra of Aqueous HB and B$^-$
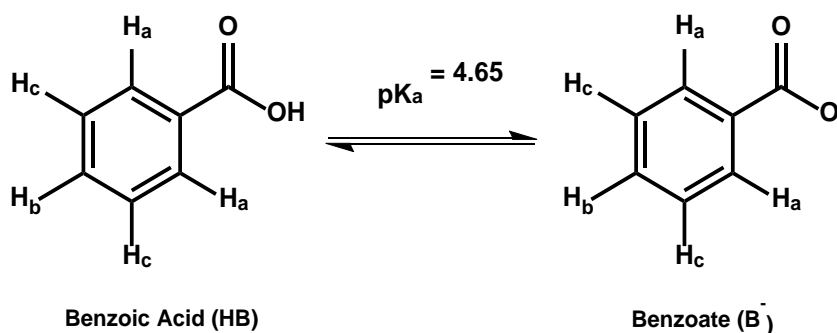
Figure 2.2. Chemical Structures of HB and B$^-$ with labeled protons for ^{1}H NMR interpretation. The pK$_a$ of HB is from Wehry *et al.* and is the pK$_a$ in D$_2$O.[27]

With the only structural difference between HB and B$^-$ being the protonation state (Figure 2.2), a titration of HB/B$^-$ was conducted in D$_2$O to determine if it was possible to see chemical shift differences using ^{1}H NMR (Figure 2.3). Below pH 3.6, the chemical shifts of the aromatic protons of HB/B$^-$ do not shift. Between pH 3.6 to 6.0 the three HB/B$^-$ aromatic proton peaks shift (H$_a$ (-0.17 ppm), H$_b$ (-0.14), and H$_c$ (-0.07 ppm)). Above pH 6.0, the chemical shifts of the aromatic protons of HB/B$^-$ do not change. The chemical shifting pattern is interpreted as HB being the only species present below pH 3.6, B$^-$ being the only species above pH 6.0, and varying mole fractions of HB and B$^-$ between pH 3.6 and 6.0. As the pH increases from 3.6 to 6.0 the ratio of HB to B$^-$ decreases. Using this curve, it was possible to determine that the pK$_a$ value in D$_2$O was 4.7 which is in agreement with the reported literature value of 4.65. [27-28]
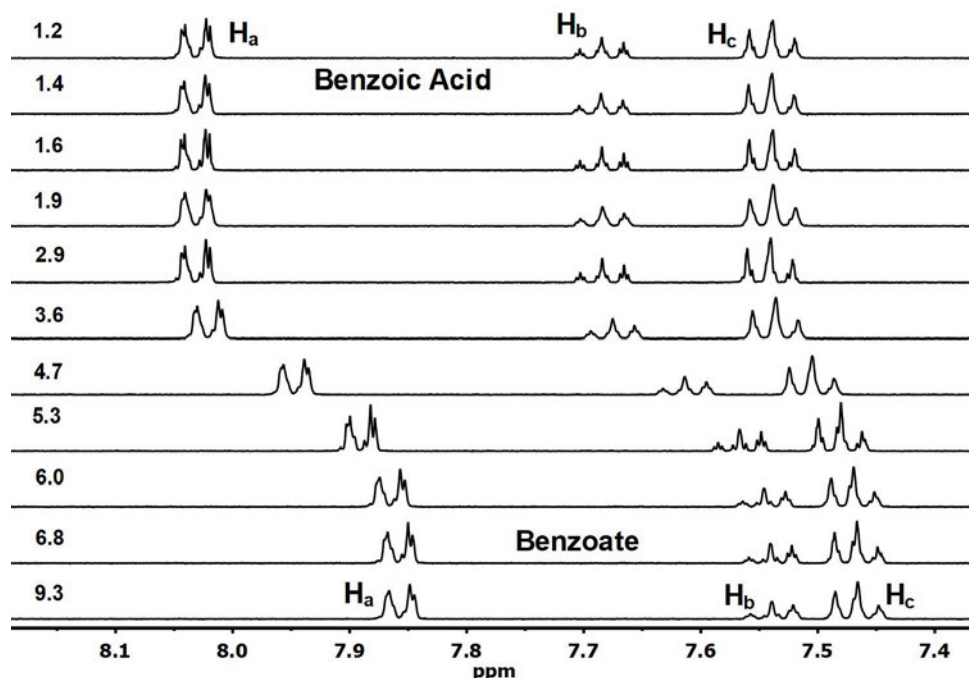
Figure 2.3. Titration from pH 1.2 to 9.3 of 10 mM HB/B⁻ in D₂O. ¹H NMR peaks are labeled with according the HB/B⁻ structures in Figure 2.2.

2.3.2   ¹H NMR of HB and B⁻ in Reverse Micelles

Considering there is a difference between the HB and B⁻ aromatic proton chemical shifts, it is then possible to independently study HB and B⁻ with the reverse micelle model membrane. For an initial study to place HB and B⁻ within a model membrane, HB or B⁻ were added to varying sizes of reverse micelles to determine how the varying environment of the differently sized reverse micelles (w_0 20, 16, 12, and 8) affect the chemical shifts of the aromatic protons of HB or B⁻.

The HB aromatic proton peaks all have different chemical shifts than what was found in the varying RM samples as shown in Figure 2.4. From the D₂O sample to the RM sample with the least amount of D₂O (w_0 8) the peak corresponding to H_a shifted downfield (+0.6 ppm) and the peaks corresponding to H_c and H_b shifted upfield (-0.3 ppm and -0.2 ppm respectively). The upfield shifting of H_b and H_c proton peaks is consistent with a reduction in solvent polarity.[29] The downfield shifting of the H_a proton peak is likely caused by a difference in hydrogen bonding of the carboxylic acid with D₂O and the AOT interface. When

25

considering the peak broadness, the HB aromatic proton peaks are sharpest when HB is in the D_2O sample, and the peaks become sharper as the RMs are smaller. This is consistent with HB residing within the AOT aliphatic chains, otherwise the peak sharpness would be similar to that of D_2O.[24] Although the reverse micelle microemulsion is a heterogeneous environment, it is conceivable that HB forms dimers under these conditions causing the shifting that is observed.[30-31] The samples contain few HB molecules (1.1 molecules or fewer on average) requiring a high affinity to form dimers within the RM microemulsion (see Table 2.1).[23, 32]
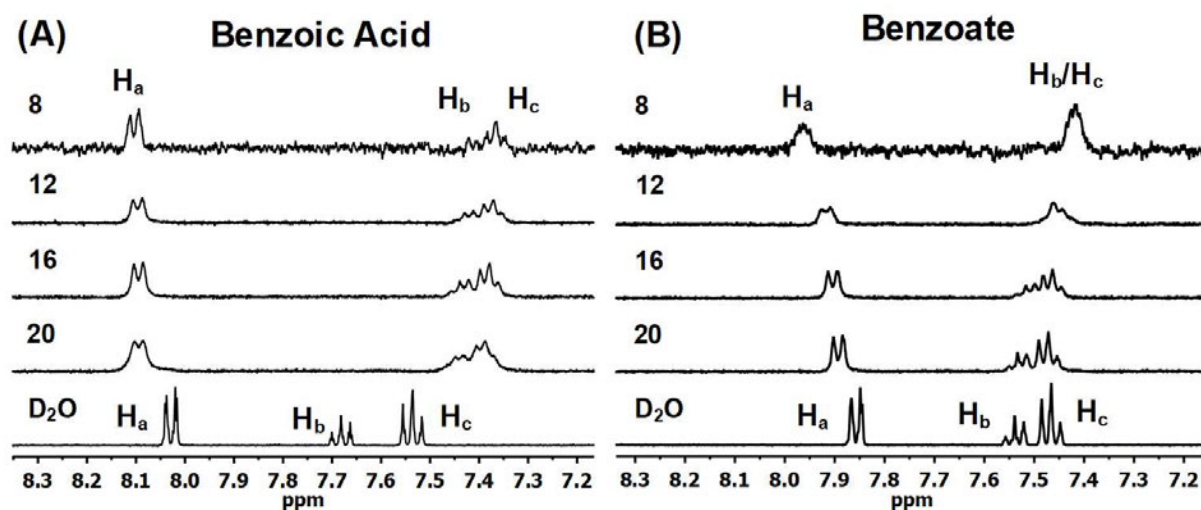
Figure 2.4. ^1H 1D NMR spectra of 10 mM HB (pH 1.2, A) and B$^-$ (pH 9.3, B) aromatic protons inside RMs of varying w_o values (left of spectra) and D_2O. ^1H NMR peaks are labeled with according the HB/B$^-$ structures in Figure 2.2.

The B$^-$ aromatic proton peaks have a very different shifting pattern than that found with HB, as Shown in Figure 2.4. The shifting of all the aromatic B$^-$ proton peaks were more gradual from the D_2O sample to the RM with the least amount of D_2O (w_0 8) where H_a shifts downfield (+0.1 ppm), and H_b and H_c shift upfield (-0.1 ppm and -0.1 ppm respectively). Within the larger of the RMs (w_0 20), the B$^-$ chemical shifts are similar to that found in D_2O, but then shift as the RM size is reduced suggesting placement of B$^-$ near the Stern layer of the RM. The peak broadness is of the B$^-$ aromatic proton peaks is also similar to that found in D_2O for the w_0 20 RM sample supporting the finding that B$^-$ resides within the water.

2.3.3 ^{1}H NMR Titrations of HB Within Reverse Micelles

In order to explore the pH dependence of HB with the RM model membrane further, titrations within RMs of varying sizes were conducted. Figure 2.5 depicts the titration of HB within w_0 16 RMs and compared to HB and B$^-$ in aqueous solution. As the pH decreased within the RM samples, the peak corresponding to H$_a$ shifts gradually downfield (+0.2 ppm) in a similar manner as with the D$_2$O samples. This similarity is consistent with B$^-$ becoming protonated at lowering pH values. The slight downfield shift of the H$_a$ peak also suggests a placement near the Stern Layer.
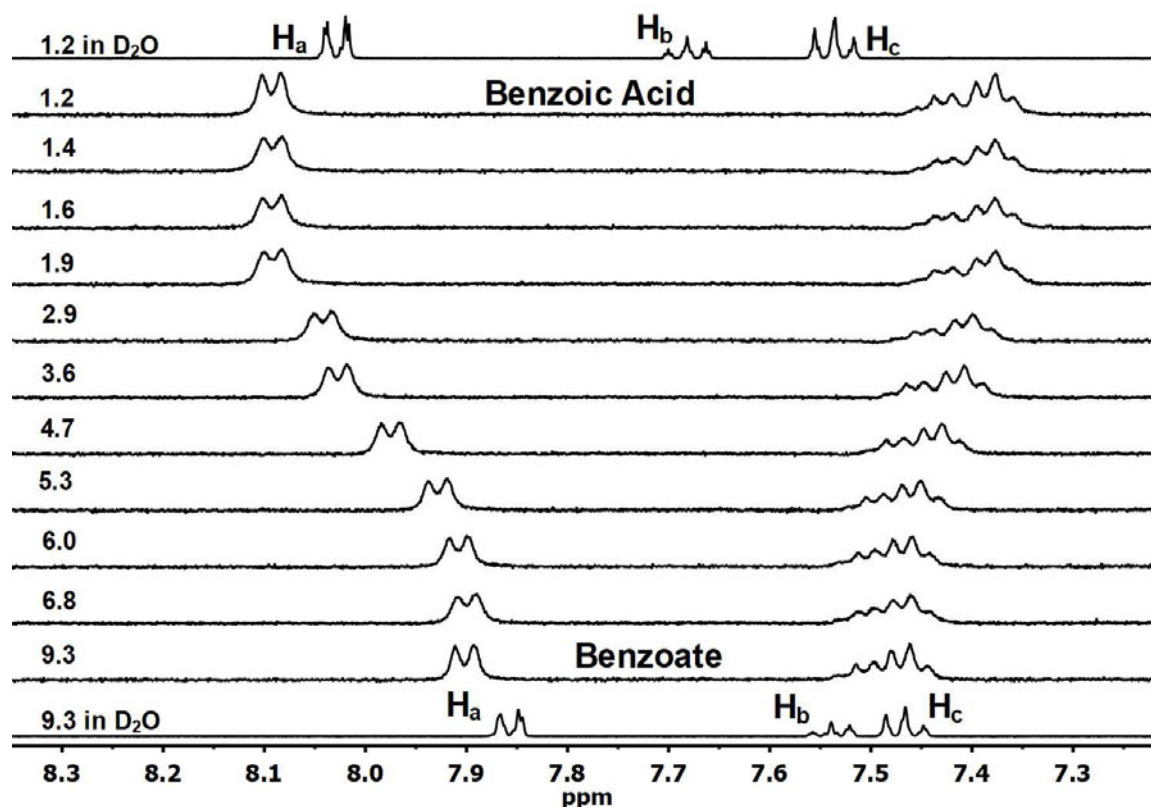
Figure 2.5. Titration from pH 1.2 to 9.3 of 10 mM HB/B$^-$ in w_0 16 reverse micelles with 10 mM HB/B$^-$ D$_2$O spectra at pH 1.2 and 9.3 for comparison. ^{1}H NMR peaks are labeled with according the HB/B$^-$ structures in Figure 2.2.

In contrast, The H$_c$ and H$_b$ peaks at high pH values (*ex.* 9.3) have similar chemical shifts as the D$_2$O sample, but shift upfield (-0.10 ppm, instead of downfield in D$_2$O) as the pH is lowered. Considering a protonation of B$^-$ causes a downfield shifting as shown in the D$_2$O titration, this upfield shifting pattern is

most likely due to a difference in placement of B⁻ and HB within the RM interface (Stern Layer vs AOT aliphatic tails respectively). This shifting pattern is consistent within many sizes of RM as shown in Figure 2.6. In summary HB/B⁻ are positioned in a pH dependent manner, where B⁻ would prefer the Stern layer and HB is closer to the RM aliphatic tails.
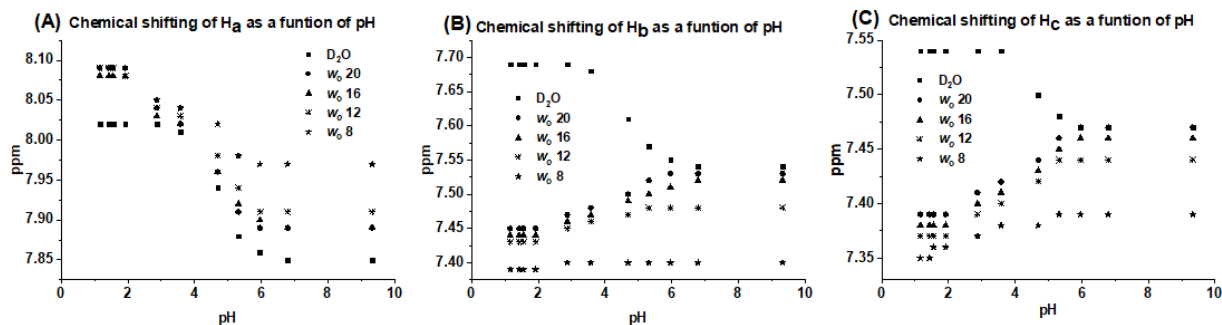
Figure 2.6. Chemical shifting of HB/B⁻ aromatic protons peaks as a function of pH for H_a (A), H_b (B), and H_c (C) in RMs of w_o values of 8, 12, 16, and 20. The chemical shifting of HB/B⁻ aromatic protons in the D₂O spectra were added for comparison. ¹H NMR peaks are labeled with according the HB/B⁻ structures in Figure 2.2.

The titrations also allowed for the determination of the pK_a of HB within the RM interface. Considering that the chemical shift of the H_a peak is most affected by the protonation state of HB/B⁻ and consistently shifts in a similar manner in RM and aqueous samples, the H_a chemical shift was used to calculate pK_a. The pKa values determined to be 4.0 (w_0 20), 4.1 (w_0 20, 16), and 3.7 (w_0 8). The pK_a values decrease from the D₂O sample to RM samples (-0.6 to -0.9) which is most likely due to an interaction with the AOT interface or characteristic of the reverse micellar interface, supporting an interaction of HB/B⁻ with the RM interface.

2.3.4   ¹H-¹H 2D NOESY NMR of HB and B⁻ Within Reverse Micelles

To confirm the ¹H 1D NMR study findings, more information was sought using ¹H-¹H 2D NOESY NMR for direct information about placement of HB and B⁻ within the AOT RM interface. For both HB and B⁻, the concentration was raised to 200 mM within the RM water pool (43 mM overall) to compensate for the

lowered sensitivity of the experiments as compared to the ^{1}H 1D NMR experiments. Partial ^{1}H-^{1}H 2D

NOESY NMR spectra are shown in Figure 2.8 to focus on the region of interest.
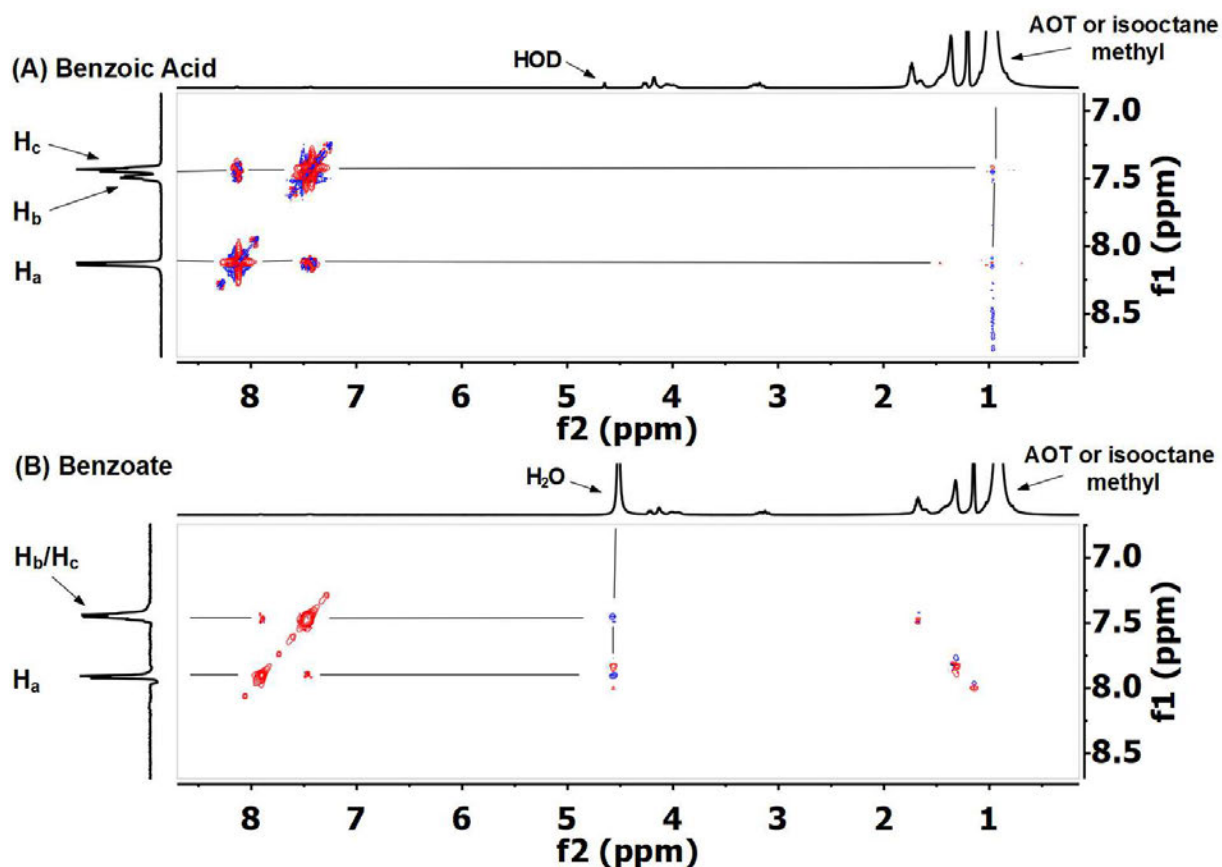
Figure 2.8. ^{1}H-^{1}H 2D NOESY NMR spectra of 200 mM HB (A) and B$^-$ (B) in w_o 16 RMs. Both Spectra were run using the standard ^{1}H-^{1}H NOESY NMR pulse sequence and spectra were processed as described in section 2.2.7. Correlations between off-diagonal peaks and diagonal peaks are indicated by lines. ^{1}H NMR peaks in the f1 dimension are labeled with according the HB/B$^-$ structures in Figure 2.2.

In Figure 2.8, off-diagonal cross peaks between H_a and H_b/H_c for both HB and B$^-$ can be observed and

is expected considering the corresponding protons are within the same aromatic ring. When just

considering HB (Figure 2.8A), very small off-diagonal cross peaks between H_a and H_b/H_c with the peak

corresponding to the AOT/isooctane methyl can be observed at 0.9 ppm in the f2 dimension. This finding

would be consistent with a placement of HB within the aliphatic regions of the RM microemulsion. Moving

to B$^-$ (Figure 2.8B), small off-diagonal cross peaks between the aromatic proton peaks of B$^-$ and H_2O can

be observed at 4.6 ppm in the f2 dimension. This is consistent with placement of B$^-$ within the water pool.

It is important to note that the spectra were extensively worked up to be able to obtain the observed peaks through the noise level. This most likely introduced some artifacts like the one observed at about 1.2 ppm and 1.4 ppm in the f2 dimension in Figure 2.8B. Although the spectra had to be extensively worked up, the data does support the findings of the ^{1}H 1D NMR experiments where B$^-$ resides within the water, and HB resides within the aliphatic region.

2.3.5   DLS of RMs Containing HB or B$^-$

For further characterization of the RM microemulsion system, DLS was used to determine if RMs were forming and of appropriate size in the presence of the concentrations of B$^-$ and HB used for the NMR studies. As shown in **Table 2.1**, the hydrodynamic radius, radius of the water pool, the polydispersity, the aggregation number, and the average molecules per RM are given. Overall, it seems that there may be a slight decrease in hydrodynamic radius when 200 mM B$^-$ is present within w_0 16 RMs (12.4 molecules per RM) but more information should be acquired before making any conclusions. Otherwise, the size of the RMs were consistent in the presence of HB/B$^-$ and was consistent with literature values.[33] This would suggest that any kind of alteration to the RM structure caused by the presence of HB/B$^-$ is minor and is not observed within this study.

Table 2.1. Comparing Sizes of RMs of Different w_0 Values with and without HB/B[-a] [a]The table outlines the contents of the reverse micelles (RM), their relative observed hydrodynamic radii (R_h), water pool radii (R_w), polydispersity index (PDI), aggregation number (η_{agg}), and molecules per reverse micelle as calculated using the aggregation number (# AOT/RMs); [b]Literature value is from Maitra.[33]

w_0	RM content	R_h (nm)	R_w (nm)	PDI	R_h reported (nm)[b]	η_{agg}	HB/B[-] per RM
20	Water	4.7 +/- 0.2	3.6 +/- 0.2	0.3 +/- 0.1	4.4	302	0
	10 mM B[-]	4.4 +/- 0.3	3.3 +/- 0.3	0.6 +/- 0.1			1.1
	10 mM HB	4.5 +/- 0.4	3.4 +/- 0.4	0.4 +/- 0.1			1.1
16	Water	4.1 +/- 0.1	3.0 +/- 0.1	0.3 +/- 0.1	4.2	215	0
	10 mM B[-]	4.4 +/- 0.8	3.3 +/- 0.8	0.4 +/- 0.1			0.6
	10 mM HB	4.0 +/- 0.3	2.9 +/- 0.3	0.4 +/- 0.1			0.6
	200 mM B[-]	3.8 +/- 0.1	2.7 +/- 0.1	0.3 +/- 0.1			12.4
	200 mM HB	4.4 +/- 0.7	3.3 +/- 0.7	0.4 +/- 0.1			12.4
12	Water	3.9 +/- 0.4	2.8 +/- 0.4	0.3 +/- 0.1	3.7	129	0
	10 mM B[-]	3.7 +/- 0.2	2.6 +/- 0.2	0.3 +/- 0.1			0.3
	10 mM HB	3.5 +/- 0.3	2.4 +/- 0.3	0.4 +/- 0.2			0.3
8	Water	3.7 +/- 0.9	2.6 +/- 0.9	0.9 +/- 0.1	3.2	72	0
	10 mM B[-]	3.6 +/- 0.8	2.5 +/- 0.8	0.2 +/- 0.1			0.1
	10 mM HB	6.6 +/- 1.0	2.5 +/- 1.0	0.2 +/- 0.1			0.1

2.3.6 Langmuir Monolayers of the Phospholipid DPPC in the Presence of HB/B[-]

To determine the interactions of HB/B[-] with a phospholipid interface, DPPC, compression isotherms of Langmuir monolayers were used. In order to differentiate between the interactions of HB from B[-] with DPPC, the aqueous subphase was prepared at pH 2.9 when studying HB and pH 7.0 when studying B[-].[27-28] In the presence of B[-] (Figure 2.9A), the DPPC monolayer decreases the area per molecule between the surface pressures of 5 mN/m and 25 mN/m. Conversely, the presence of HB increases the area per molecule between the same surface pressures. This data suggests that B[-] had a condensing effect on the DPPC monolayer when the DPPC monolayer was in liquid phase, while HB did the opposite, showing a protonation state dependence on the interactions with the phospholipids.
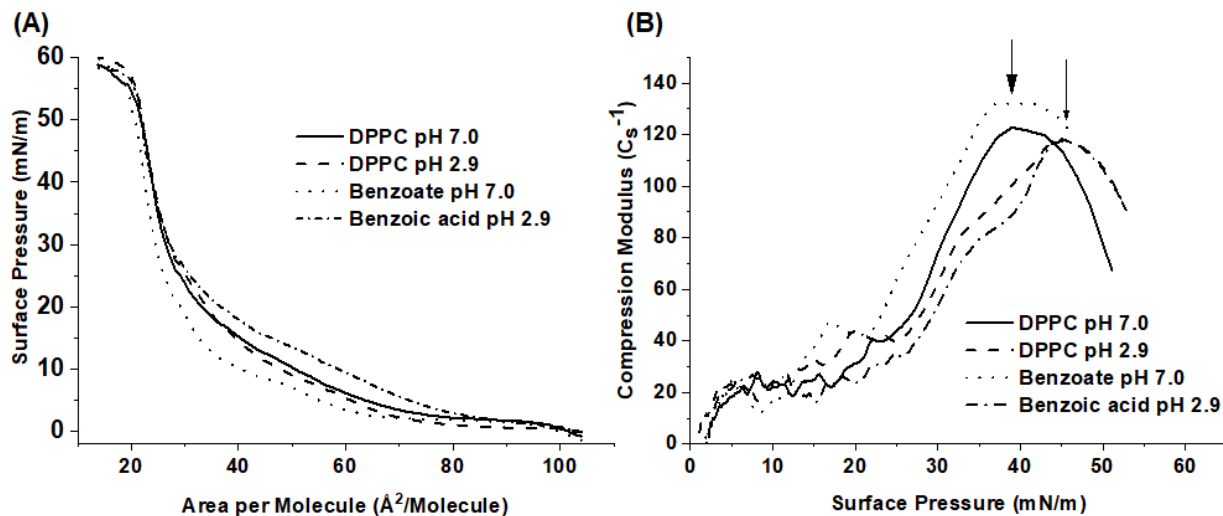
Figure 2.9. Compression isotherm surface pressure measurements of DPPC monolayers as a function of area per molecule (A) with the subphase consisting of either DDI H_2O or 1 mM HB/B⁻ at pH 7.0 or 2.9. The compression moduli (B) were calculated from the compression isotherm data using equation 2 with the maximum compression modulus indicated by the arrows.

To determine how the presence of HB or B⁻ can affect the compressibility of the phospholipid, the compression modulus of each average compression isotherm was calculated and shown in Figure 2.9B. The maximum compression modulus (C_s^{-1}) was increased in the presence of B⁻, but HB had no effect on the maximum compression modulus. Generally, an increase in compression modulus is consistent with a decrease in compressibility (more difficult to compress).[25-26] Therefore, the presence of B⁻ causes the DPPC monolayer to become more difficult to compress in the solid phase (above 25 mN/m) presumably through charge repulsion with the phosphates of the DPPC and B⁻. This data suggests that despite the charge on B⁻, it still interacts with the DPPC interface even at physiological phospholipid densities (30-35 mN/m)[34] and there is a pH dependence on the interactions of HB/B⁻ with a phospholipid interface.

2.3.7 Comparing Interactions of HB and B⁻ with RMs and Langmuir Monolayers

The interactions of HB and B⁻ with model membranes were characterized using different methods to evaluate the effect that the protonation state has on the interactions of HB/B⁻ with model membrane interfaces. The ¹H 1D NMR and ¹H-¹H 2D NOESY NMR studies with RMs repeatedly show a pH dependent placement within the RM system where B⁻ can be positioned near the Stern layer of water and HB can be

positioned within the AOT aliphatic tails. The DLS experiments were able to show that the placement of B[-] and HB did not affect, or minimal effect on the RM structure. A pH dependent interaction of HB/B[-] was also shown using DPPC Langmuir monolayers further confirming that the protonation state of HB/B[-] is a deciding factor in its membrane interface interactions.

2.3.8 Comparing HB/B[-] Membrane Interactions to Previous Studies

It is known that weak aromatic carboxylic acids interact with interfaces in both the anionic and neutral protonation states.[35] Even the doubly deprotonated dipicolinate was found to reside within the AOT interface instead of the RM water pool.[23] This study shows that B[-] did not reside as deeply in the RM interface as anionic dipicolinate species which is likely due to differences in specific interactions with the AOT sulfonate headgroups.[23, 36] The HB natural species was found to reside at least as deep into the AOT aliphatic region as the dianionic dipicolinate species and similar to benzyl alcohol.[23, 36-37] Previously, HB and B[-] had been shown to interact with the interfaces of anionic and cationic micelles but the specific molecular detail and the difference in the preferred placement within the interface were not explored.[35]

Phenols have been shown to exhibit a time dependent protonation caused by hydrogen bonding with the AOT.[38] Similar observations were not observed with HB/B[-]. We hypothesize this difference originates in the structural difference of phenol and benzoic acid molecules. A possible result of this difference could be that phenolates are residing deeper into the AOT interface than benzoate. Deep penetration into the interface would result in an increase in the pK_a value of the phenol because the protonated form would be the more stable form. The pK_a for benzoic acid changes only a modest amount and not as dramatic as the change in the pK_a value for phenol. The fact these compounds are impacted differently by the reverse micelle is consistent with a fundamentally different placement and interaction with the interface. We show here that HB is able to penetrate into a surfactant interface much deeper than the corresponding anion B[-], but that both compounds penetrate the surfactant/lipid interface.

2.3.9   Biological Implications

As a common preservative, it is important to investigate the interactions of HB with membranes. Especially considering that HB is able to preserve foods and drinks from both bacterial and eukaryotic cell growth. Generally, the data presented within this chapter suggests that HB is able to penetrate a membrane interface much more easily than B^-. This is most likely due to the difference in charge between HB and B^- which is supported by the observation that weak acid preservatives are more useful for food and drink preservation below their pK_a values (4.2 for HB in H_2O).[28] Below the pK_a value, the dominant species is HB, and therefore is able to cross penetrate the membrane of a cell. Once inside the cytoplasm (higher pH) the HB will deprotonate thus lowering the pH of the cytoplasm.

When relating to the biological effects of HB on *S. cerevisiae*, it is important to consider the futile cycle.[3, 9, 19] As described earlier, the futile cycle reforms HB outside of the cell.[3, 9, 19]This would be detrimental to the cell as HB is able to penetrate the membrane interface, as shown in this study. Therefore, there must be another method of resistance that *S. cerevisiae* employs to be able to cope for the presence of the weak acid preservative beyond excreting the weak acid conjugate base.[9, 39] To our knowledge, there is limited information about any further mechanisms of resistance.

Weak acid preservatives don't just protect food and beverages from eukaryotic species, but also bacterial species at low pH.[40] Generally, Gram-negative bacteria have a higher resistance to weak acid preservatives than Gram-positive bacteria [minimum inhibitory concentration (MIC) 100 mg/mL vs 1,600 mg/mL respectively].[40] The low pH value of the food that HB/B^- would allow for most of the HB/B^- to be in the HB form. When HB approaches the membrane from the outside of the bacterial cell in an acidic environment, it can readily penetrate the membrane and reach the neutral cytoplasm. Deprotonation of HB in the higher pH environment will provide a proton which will reduce the cytoplasmic pH as is commonly observed for uncouplers.[41-43] These considerations may explain the relative intrinsic resistance of Gram-negative bacteria to HB as compared to Gram-positive bacteria. The Gram-positive bacteria have

one membrane (Figure 2.10A), whereas the Gram-negative bacteria have two membranes (Figure 2.10B and 2.10C). Since HB deprotonates after passing through the first membrane, it will not be able to penetrate the second membrane (Figure 2.10). If the periplasmic space acidifies, then HB could diffuse through both membranes and reach the cytosol in the Gram-negative bacterium as illustrated in Figure 2.10, illustrating how the Gram-negative bacteria ultimately succumb to such compounds at higher concentration than Gram-positive bacteria.[40, 44]
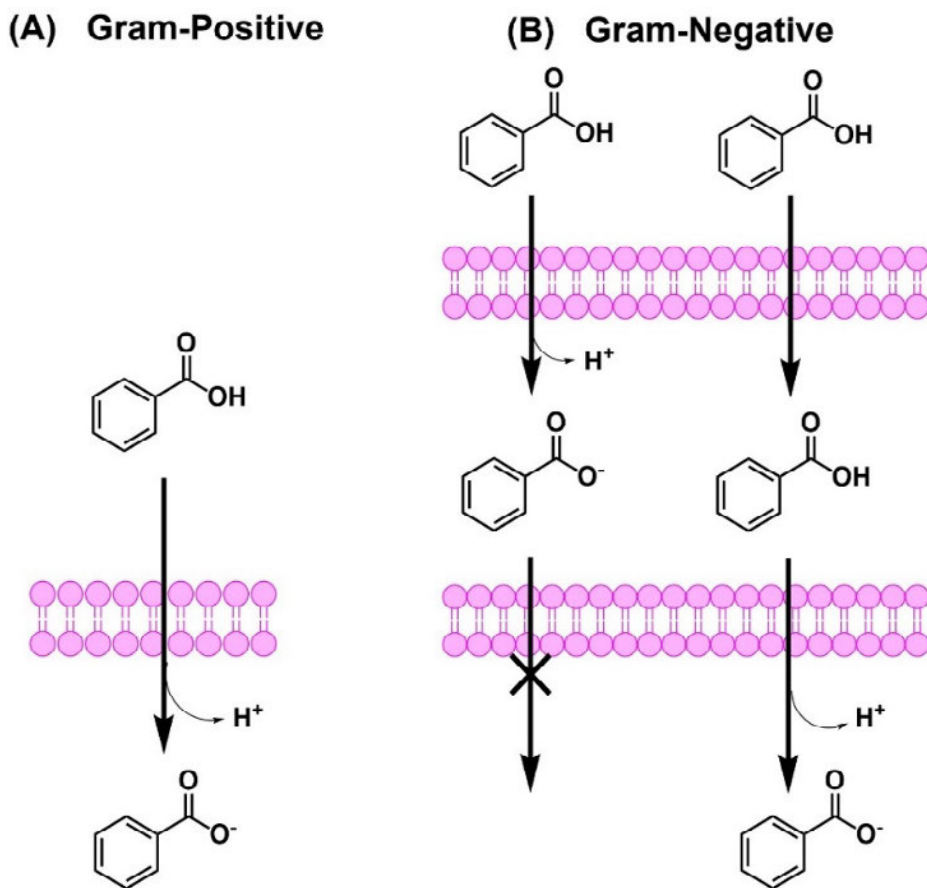
Figure 2.10. Illustration of HB diffusing across generalized Gram-positive (A) and Gram-Negative (B, C) membranes. The Gram-negative membranes show a dependence on protonation state for HB/B⁻ to be able to cross the second membrane when the periplasm is at higher pH (B) and at a lower pH (C).

2.4   Summary and Conclusions

We find that HB and B⁻ have very different placements at the water membrane-like interface in two different model membrane systems which supports our hypothesis that HB and B⁻ interact differently with

membrane interfaces. HB penetrates deeply while B⁻ will reside at the Stern layer in an AOT microemulsion system. This placement is supported by the Langmuir monolayer studies where pH dependence for the interactions with DPPC was determined, documenting that these results can be extended to interfaces prepared by common membrane phospholipids. These interactions are primarily attributed to the differences in charge (i.e., protonation state) and result in distinct interactions with the surfactant itself. In summary, we show here that the protonation state of a weak aromatic carboxylic acid can alter its interactions with a surfactant/lipid interface and that these observations can explain the properties of a very common food preserving agent, HB (HB).[20]

References

(1) Beales, N. Adaptation of Microorganisms to Cold Temperatures, Weak Acid Preservatives, Low pH, and Osmotic Stress: A Review. *Compr. Rev. Food Sci. Food Saf.* **2004,** *3* (1), 1-20.

(2) Brul, S.; Coote, P. Preservative Agents in Foods - Mode of Action and Microbial Resistance Mechanisms. *Int. J. Food Microbiol.* **1999,** *50* (1-2), 1-17.

(3) Piper, P.; Calderon, C. O.; Hatzixanthis, K.; Mollapour, M. Weak Acid Adaptation: The Stress Response That Confers Yeasts with Resistance to Organic Acid Food Preservatives. *Microbiology-Sgm.* **2001,** *147*, 2635-2642.

(4) Lambert, R. J.; Stratford, M. Weak-Acid Preservatives: Modelling Microbial Inhibition and Response. *J. Appl. Microbiol.* **1999,** *86* (1), 157-164.

(5) Krebs, H. A.; Wiggins, D.; Stubbs, M.; Sols, A.; Bedoya, F. Studies on the Mechanism of the Anti-Fungal Action of Benzoate. *Biochem. J.* **1983,** *214* (3), 657-663.

(6) Lou, P.-H.; Hansen, Birgit S.; Olsen, Preben H.; Tullin, S.; Murphy, Michael P.; Brand, Martin D. Mitochondrial Uncouplers with an Extraordinary Dynamic Range. *Biochem. J.* **2007,** *407* (Pt 1), 129-140.

(7) Silva, M. M.; Lidon, F. C. Food Preservatives - an Overview on Applications and Side Effects. *Emir. j. food agric.* **2016,** *28* (6), 366-373.

(8) Stratford, M.; Nebe-von-Caron, G.; Steels, H.; Novodvorska, M.; Ueckert, J.; Archer, D. B. Weak-Acid Preservatives: pH and Proton Movements in the Yeast Saccharomyces Cerevisiae. *Int. J. Food Microbiol.* **2013,** *161* (3), 164-171.

(9) Piper, P. W., Resistance of Yeasts to Weak Organic Acid Food Preservatives. In *Advances in Applied Microbiology, Vol 77*, Laskin, A. I.; Sariaslani, S.; Gadd, G. M., Eds. 2011; Vol. 77, pp 97-113.

(10) Mira, N. P.; Teixeira, M. C. Microbial Mechanisms of Tolerance to Weak Acid Stress. *Front. Microbiol.* **2013,** *4*, 1-2.

(11) Stratford, M.; Lambert, R. J. W. Weak-Acid Preservatives: Mechanisms of Adaptation and Resistance by Yeasts. *Food Aust.* **1999,** *51* (1-2), 26-29.

(12) Henriques, M.; Quintas, C.; LoureiroDias, M. C. Extrusion of Benzoic Acid in Saccharomyces Cerevisiae by an Energy-Dependent Mechanism. *Microbiology-Uk.* **1997,** *143*, 1877-1883.

(13) Holyoak, C. D.; Bracey, D.; Piper, P. W.; Kuchler, K.; Coote, P. J. The Saccharomyces Cerevisiae Weak-Acid-Inducible ABC Transporter Pdr12 Transports Fluorescein and Preservative Anions from the Cytosol by an Energy-Dependent Mechanism. *J. Bacteriol.* **1999,** *181* (15), 4644-4652.

(14) Kren, A.; Mamnun, Y. M.; Bauer, B. E.; Schuller, C.; Wolfger, H.; Hatzixanthis, K.; Mollapour, M.; Gregori, C.; Piper, P.; Kuchler, K. War1p, a Novel Transcription Factor Controlling Weak Acid Stress Response in Yeast. *Mol. Cell. Biol.* **2003,** *23* (5), 1775-1785.

(15) Mollapour, M.; Piper, P. W. Activity of the Yeast Zinc-Finger Transcription Factor War1 is Lost with Alanine Mutation of Two Putative Phosphorylation Sites in the Activation Domain. *Yeast.* **2012,** *29* (1), 39-44.

(16) Nygard, Y.; Mojzita, D.; Toivari, M.; Penttila, M.; Wiebe, M. G.; Ruohonen, L. The Diverse Role of Pdr12 in Resistance to Weak Organic Acids. *Yeast.* **2014,** *31* (6), 219-232.

(17) Papadimitriou, M. N. B.; Resende, C.; Kuchler, K.; Brul, S. High Pdr12 Levels in Spoilage Yeast (Saccharomyces Cerevisiae) Correlate Directly with Sorbic Acid Levels in the Culture Medium but Are Not Sufficient to Provide Cells with Acquired Resistance to the Food Preservative. *Int. J. Food Microbiol.* **2007,** *113* (2), 173-179.

(18) Piper, P. W.; OrtizCalderon, C.; Holyoak, C.; Coote, P.; Cole, M. Hsp30, the Integral Plasma Membrane Heat Shock Protein of Saccharomyces Cerevisiae, Is a Stress-Inducible Regulator of Plasma Membrane H$^+$-ATPase. *Cell Stress Chaperones.* **1997,** *2* (1), 12-24.

(19) Piper, P.; Mahe, Y.; Thompson, S.; Pandjaitan, R.; Holyoak, C.; Egner, R.; Muhlbauer, M.; Coote, P.; Kuchler, K. The Pdr12 Abc Transporter Is Required for the Development of Weak Organic Acid Resistance in Yeast. *EMBO J.* **1998,** *17* (15), 4257-4265.

(20) Peters, B. J.; Groninger, A. S.; Fontes, F. L.; Crick, D. C.; Crans, D. C. Differences in Interactions of Benzoic Acid and Benzoate with Interfaces. *Langmuir.* **2016,** *32* (37), 9451-9459.

(21) Samart, N.; Beuning, C. N.; Haller, K. J.; Rithner, C. D.; Crans, D. C. Interaction of a Biguanide Compound with Membrane Model Interface Systems: Probing the Properties of Antimalaria and Antidiabetic Compounds. *Langmuir.* **2014,** *30* (29), 8697-8706.

(22) Crans, D. C.; Schoeberl, S.; Gaidamauskas, E.; Baruah, B.; Roess, D. A. Antidiabetic Vanadium Compound and Membrane Interfaces: Interface-Facilitated Metal Complex Hydrolysis. *J. Biol. Inorg. Chem.* **2011,** *16* (6), 961-972.

(23) Crans, D. C.; Trujillo, A. M.; Bonetti, S.; Rithner, C. D.; Baruah, B.; Levinger, N. E. Penetration of Negatively Charged Lipid Interfaces by the Doubly Deprotonated Dipicolinate. *J. Org. Chem.* **2008,** *73* (24), 9633-9640.

(24) Sostarecz, A. G.; Gaidamauskas, E.; Distin, S.; Bonetti, S. J.; Levinger, N. E.; Crans, D. C. Correlation of Insulin-Enhancing Properties of Vanadium-Dipicolinate Complexes in Model Membrane Systems: Phospholipid Langmuir Monolayers and Aot Reverse Micelles. *Chem. - Eur. J.* **2014,** *20* (17), 5149-5159.

(25) Choi, Y.; Attwood, S. J.; Hoopes, M. I.; Drolle, E.; Karttunen, M.; Leonenko, Z. Melatonin Directly Interacts with Cholesterol and Alleviates Cholesterol Effects in Dipalmitoylphosphatidylcholine Monolayers. *Soft Matter.* **2014,** *10* (1), 206-213.

(26) Wang, Z. N.; Yang, S. H. Effects of Fullerenes on Phospholipid Membranes: A Langmuir Monolayer Study. *Chemphyschem.* **2009,** *10* (13), 2284-2289.

(27) Wehry, E. L., and Rogers, L. B. Deuterium Isotope Effects on the Protolytic Dissociation of Organic Acids in Electronically Excited States *J. Am. Chem. Soc.* **1966,** *88* (2), 351-354.

(28) Dempsy, E. P. S. a. B., *Ionisation Constants of Organic Acids in Aqueous Solution*. Permagamon Press: **1979**.

(29) Vermathen, M.; Stiles, P.; Bachofer, S. J.; Simonis, U. Investigations of Monofluoro-Substituted Benzoates at the Tetradecyltrimethylammonium Micellar Interface. *Langmuir.* **2002,** *18* (4), 1030-1042.

(30) Pham, H. H.; Taylor, C. D.; Henson, N. J. First-Principles Prediction of the Effects of Temperature and Solvent Selection on the Dimerization of Benzoic Acid. *J. Phys. Chem. B.* **2013,** *117* (3), 868-876.

(31) Fujii, Y.; Sobue, K.; Tanaka, M. Solvent Effect on Dimerization and Hydration Constant of Benzoic-Acid. *J. Chem. Soc., Faraday Trans.* **1978,** *74*, 1467-1476.

(32) Falcone, R. D.; Correa, N. M.; Biasutti, M. A.; Silber, J. J. Acid-Base and Aggregation Processes of Acridine Orange Base in N-Heptane/AOT/Water Reverse Micelles. *Langmuir.* **2002,** *18* (6), 2039-2047.

(33) Maitra, A. Determination of Size Parameters of Water Aerosol OT Oil Reverse Micelles from Their Nuclear Magnetic-Resonance Data. *J. Phys. Chem.* **1984,** *88* (21), 5122-5125.

(34) Jones, M. N., *Micelles, Monolayers, and Biomembranes*. New York : Wiley-Liss: New York, **1995**.

(35) Clarke, G. A.; Burton, J., Spectral Study of Aromatic Carboxylic Acids in Micellar Environments. In *Solution Behaviour of Surfactants: Theoretical and Applied Aspects*, K. L. Mittal, E. J. F., Ed. Plenum Press: New York and London, 1980; Vol. 2, pp 1047-1063.

(36)   Crans, D. C.; Rithner, C. D.; Baruah, B.; Gourley, B. L.; Levinger, N. E. Molecular Probe Location in Reverse Micelles Determined by NMR Dipolar Interactions. *J. Am. Chem. Soc.* **2006,** *128* (13), 4437-4445.

(37)   Luan, Y. X.; Song, A. X.; Xu, G. Y. Location of Probe Molecule in Double-Chain Surfactant Aggregates in Absence and Presence of Water-Soluble Polymer by NMR. *Soft Matter.* **2009,** *5* (13), 2587-2595.

(38)   Silva, O. F.; Fernandez, M. A.; Silber, J. J.; de Rossi, R. H.; Correa, N. M. Inhibited Phenol Ionization in Reverse Micelles: Confinement Effect at the Nanometer Scale. *Chemphyschem.* **2012,** *13* (1), 124-130.

(39)   Lindberg, L.; Santos, A. X. S.; Riezman, H.; Olsson, L.; Bettiga, M. Lipidomic Profiling of Saccharomyces Cerevisiae and Zygosaccharomyces Bailii Reveals Critical Changes in Lipid Composition in Response to Acetic Acid Stress. *PLoS One.* **2013,** *8* (9).

(40)   Rowe, R. C.; Shesky, P. J.; Quinn, M. E., *Handbook of Pharmaceutical Excipients*. 6th ed.; Pharmaceutical Press: **2009**; p 61-63.

(41)   Bakker, E. P.; Arents, J. C.; Hoebe, J. P. M.; Terada, H. Surface-Potential and Interaction of Weakly Acidic Uncouplers of Oxidative-Phosphorylation with Liposomes and Mitochondria. *Biochim. Biophys. Acta.* **1975,** *387* (3), 491-506.

(42)   Heytler, P. G. Uncouplers of Oxidative-Phosphorylation. *Pharmacol. Ther.* **1980,** *10* (3), 461-472.

(43)   Wilson, D. F.; Ting, H. P.; S., K. M. Mechanism of Action of Uncouplers of Oxidative Phosphorylation. *Biochemistry.* **1971,** *10* (15), 2897-2902.

(44)   Slonczewski, J. L.; Fujisawa, M.; Dopson, M.; Krulwich, T. A., Cytoplasmic Ph Measurement and Homeostasis in Bacteria and Archaea. In *Advances in Microbial Physiology, Vol 55*, Poole, R. K., Ed. 2009; Vol. 55, pp 1-79.

Chapter 3: Structural Importance of Small Molecules for Membrane Interactions

3.1   Structure Leads to Function

Small molecules (<500 Daltons) have been the cornerstone for medical treatment, supplements, and preservatives, with many diffusing through the cellular membrane to reach their target.[1-5] One such example is a very successful first line anti-tuberculosis drug, isoniazid (INH, Figure 1), which has been shown to diffuse across the membrane of *Mycobacterium tuberculosis*, where INH is then able to reach the target, KatG.[6-7] Similar to INH, the method of entry into a cell for many small molecules has been studied in detail,[8-12] but there is a lack of information pertaining to the specific interactions of small molecules with the membrane interfaces. This lack of information is in large part due to the difficulty of determining the specific interactions of molecules with the lipids that make up the membranes, and the complexity of the biological membranes themselves.[13-15] The specific small molecule-lipid interactions of a series of small aromatic compounds were studied here (Figure 3.1) to understand how small molecules are taken into cells, how they affect the membrane, and may elucidate aspects of the small molecule's mode of action.

Many of these small molecules used to treat diseases such as tuberculosis, contain a pyridine as their main structural component.[16-18] The presence and placement of nitrogen within the pyridine ring has great effects on these small molecules and their inter- and intramolecular interactions. For example, the amide group of picolinamide (PIC) is ortho to the pyridine nitrogen allowing for intramolecular hydrogen bonding (Figure 3.1).[19-21] This increases the molecule's hydrophobicity and allows it to penetrate a membrane interface deep enough to affect the packing of the phospholipid tails.[21-22] This behavior is not observed for nicotinamide (NIC, meta) nor isonicotinamide (iNIC, para) since the amide and pyridine nitrogen are

not in proximity for intramolecular hydrogen bond formation.[19-20] Despite this difference, Olsson et. al. were able to show that NIC tightly binds to plasma membrane extracts of human leukemic K-562 cells (K_d between 3.2 and 12.7 µM).[9] Because such small differences in structure have such profound effects on inter- and intramolecular interactions, we hypothesize here that these molecules may interact with a membrane interface differently despite having similar structures as shown in Figure 3.1. To test this hypothesis, Langmuir monolayer and RM studies were conducted to determine the interfacial interactions of the small molecules in Figure 3.1 with model membrane interfaces.
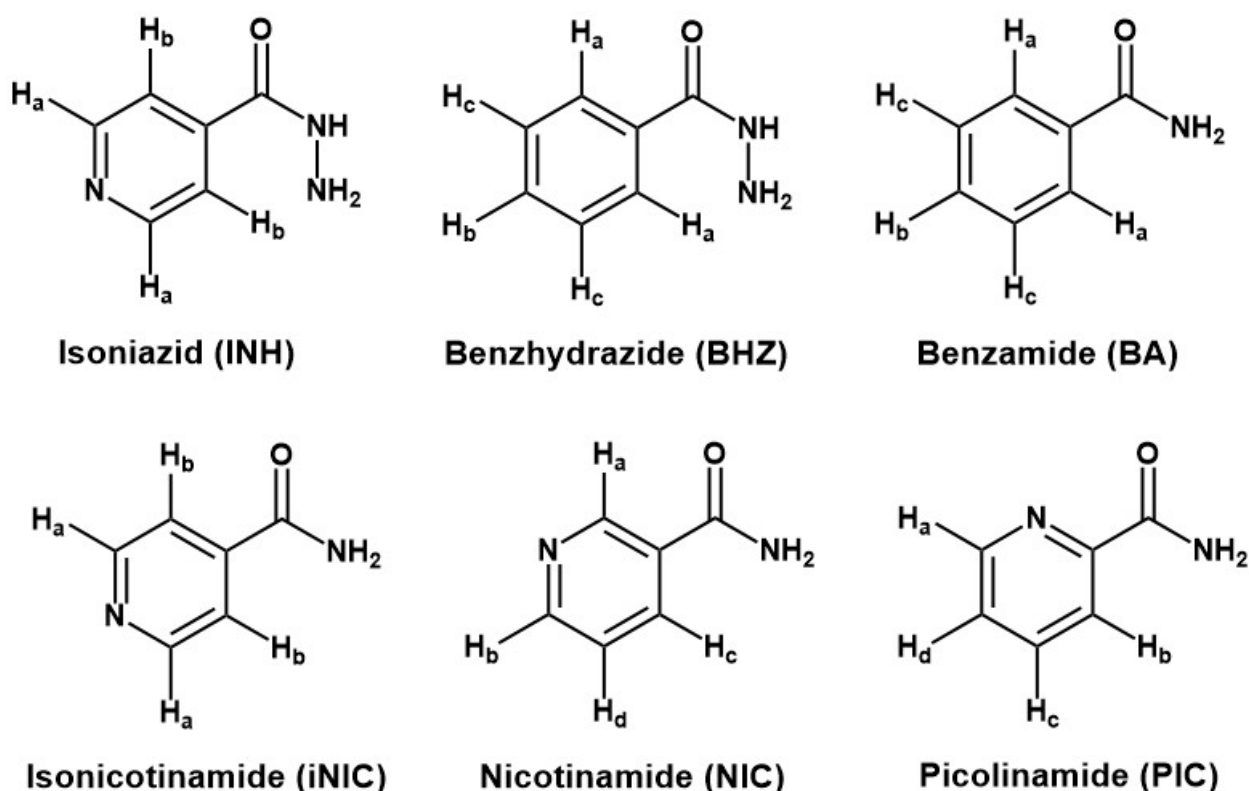
Figure 3.1. Structures of isoniazid (INH), benzhydrazide (BHZ), isonicotinamide (iNIC), benzamide (BA), nicotinamide (NIC), and picolinamide (PIC), with protons labeled for ^{1}H NMR peak labeling. The protons in the ^{1}H NMR spectra has H_a as the most downfield ^{1}H NMR peak, H_b the next one, etc.

3.2   Materials and Methods

3.2.1   Materials

Most materials were used without further purification. Benzamide (BA) (99%), PIC (98%), NIC (98%), iNIC (99%), INH (≥99%), benzhydrazide (BHZ) (98%), isooctane (2,2,4 trimethylpentane, 99.8%), methanol

(≥99.9%), activated charcoal (99.5%), chloroform (≥99.5%), deuterium oxide (99.9%), 2,2-dimethyl-2-silapentane-5-sulfonate sodium salt (DSS, 97%), monosodium phosphate (≥99.0%), disodium phosphate (≥99.0%), sodium hydroxide (≥98%), and hydrochloric acid (37%) were all purchased from Sigma Aldrich. DPPC (≥99%) and DPPE (99%) were purchased from Avanti Polar Lipids. Sodium AOT (aerosol OT, bis(2-ethylhexyl)sulfosuccinate sodium salt, ≥99.0%) was purchased from Sigma Aldrich and was purified further as has been reported previously to remove any acidic impurities.[23] Briefly, 50.0 g AOT was dissolved into 150 mL of methanol to which 15 g activated charcoal was added. This suspension was stirred for 2 weeks. After mixing, the suspension was filtered to re move the activated charcoal. The filtrate was then dried under rotary evaporation at 50 °C until the water content was below 0.2 molecules of water per AOT as determined by ^1H NMR spectroscopy. The pH was adjusted through-out this study using varying concentrations of NaOH or HCl dissolved/mixed in either D_2O or H_2O depending on experimental requirements. NaOH or HCl dissolved in D_2O is referred to as NaOD or DCl respectively.

3.2.2 Preparation of Langmuir Monolayers

Phospholipid stock solutions were prepared by dissolving DPPC (0.018 g, 0.025 mmol) or DPPE (0.017 g, 0.025 mmol) in 25 mL of 9:1 chloroform:methanol (v:v) for a final concentration of 1 mM phospholipid. The aqueous subphase consisted of 50 mL of 20 mM sodium phosphate buffer (pH 7.4) and varying concentrations of hydrazide of amide (10, 1.0, 0.10, or 0 mM hydrazide or amide). Sodium phosphate buffer (20 mM, pH 7.4) instead of double deionized H_2O (DDI H_2O) was used as the sub-phase for the compression isotherms for better pH control (Figure A5.1).[30] Before addition of the phospholipid monolayers, the surface of the subphase was cleaned using vacuum aspiration and to make sure the surface was clean, the surface pressure of a compression isotherm of just the subphase (no phospholipid present) was measured (surface pressure was consistently 0.0 +/- 0.5 mN/m throughout compression). To prepare the phospholipid monolayer, 20 µL of phospholipid stock solution (20 nmol of phospholipid, 112 $Å^2$/molecule) was added to the surface of the subphase in a dropwise manner using a Hamilton

syringe. The film was allowed to equilibrate for 15 minutes. The resulting phospholipid monolayer was then used for the compression isotherm experiments.

3.2.3   Compression Isotherm Surface Pressure Measurements of Langmuir Monolayers

The phospholipid monolayer was compressed from 2 sides with a total speed of 10 mm/min (5 mm/min from opposite sides) using a Kibron µTroughXS equipped with a Teflon ribbon (polytetrafluoroethylene, hydrophobic barrier). The temperature was maintained at 25 °C using an external water bath. The surface tension of the subphase during each com-pression was monitored using a wire probe as a Wilhemy plate. The surface pressure was calculated from the sur-face tension using equation 1 where π is the surface pressure, γ_0 is the surface tension of water (72.8 mN/m), and γ is the surface tension at a given area per phospholipid after the film has been applied.

$$\pi = \gamma_o - \gamma \tag{1}$$

Each compression isotherm experiment consisted of at least 3 replicates and the averages with standard deviations of the area per phospholipid at every 5 mN/m was calculated using Microsoft Excel. The worked-up data were transferred to OriginPro Version 9.1 to be graphed. From the averages of the compression isotherms, the percent difference from the control of each sample at 5mN/m, 30 mN/m, and 35 mN/m were calculated. The compression moduli were calculated using OriginPro Version 9.1 from the compression isotherm average results using equation 2, where C_s^{-1} is the compression modulus, A is the surface area, and π is the surface pressure.

$$C_s^{-1} = -A \left(\frac{d\pi}{dA} \right) \tag{2}$$

3.2.4   Preparation of RMs for Dynamic Light Scattering (DLS)

RMs were prepared as has previously been reported.[23] To prepare the 100 mM AOT stock solution, 2.2 g of purified AOT (4.9 mmol) was dissolved into 50 mL isooctane. The 10 mM aqueous stock solutions of amide or hydrazide were prepared by dissolving 50 µmol of amide or hydrazide into 5 mL DDI H_2O and then the pH was adjusted to pH 7.0. To prepare the RM solutions, specific volumes of the AOT stock

solution and aqueous solution were added for a total of 5 mL to form RM sizes of w_0 8, 12, 16, and 20 where w_0 = [H_2O]/[AOT]. Upon mixing the AOT stock solution with aqueous solution, a white aggregate formed at the water-isooctane interface. Then the mixture was vortexed until clear (~30 s), consistent with the formation of RMs.[23]

3.2.5   Parameters for DLS Analysis

Once the glass cuvettes (1 cm x 1 cm) had been washed with isooctane and RM sample (3 times each), the cuvettes were filled with 1 ml of sample, and analyzed using a Zetasizer nano-ZS. The wavelength of light used was 632.8 nm and scattering was obtained at an angle of 173°. Each sample was equilibrated for 700 s at 25 °C then run for 10 scans per acquisition for 15 acquisitions. Each sample was run in triplicate, and the hydrodynamic radii (R_h) and polydispersity index (PDI) were averaged with the standard deviations reported in Table S1.

3.2.6   Preparation of Aqueous solutions for RM studies

The aqueous solutions for the compounds of interest shown in Figure 3.1 were prepared in a similar manner as with HB in chapter one except for nicotinamide which the concentration was doubled to 20 mM for the stock solution (50 mmol).

3.2.7   Preparation of RMs and ^{1}H 1D NMR Spectroscopy

The RMs were prepared and ^{1}H NMR spectra were acquired in a similar manner as in chapter one except titrations were only conducted within the w_0 16 RMs for each of the molecules in Figure 3.1. The resulting spectra were processed in a similar manner as in chapter one.

3.2.8   Preparation of RMs for ^{1}H-^{1}H 2D NOESY and ROESY NMR Spectroscopy

The 750 mM AOT stock solution was prepared by dis-solving 0.34 g AOT (0.76 mmol) in 1 mL of isooctane. To form the RM (w_0 12), 839 µL of AOT stock solution was added to 161 µL of D_2O and vortexed until clear. This suspension was then mixed with 32 µmol of amide or hydrazide for an average

concentration of 200 mM amide or hydrazide within the RM water pool (32.2 mM overall). The mixture was vortexed until the solid dissolved into the RM microemulsion.

3.2.9 Parameters for Recording ^{1}H-^{1}H 2D NOESY and ROESY NMR Spectra

The ^{1}H-^{1}H 2D NOESY and ROESY experiments were con-ducted using a 400 MHz Varian NMR at 26 °C with 16 scans per transient and 256 transient pairs in the f1 dimension. The ^{1}H-^{1}H 2D NOESY spectrum was acquired using a standard pulse sequence with a mixing time of 200 ms and a 1.5 s relaxation delay. The ^{1}H-^{1}H 2D ROESY spectra were acquired using a standard pulse sequence with a 200, 100, or 0 ms mixing time and a 1.5 s relaxation delay. The resulting spectra were analyzed using MestReNova Version 10.0.1 by subjecting the spectra to a 90° sine^2 weighting function with a first point at 0.50. The spectra were then phased and baselined using a third order Bernstein polynomial baseline. Each spectrum was referenced to the isooctane methyl peak at 0.904 ppm in both dimensions.[23]

3.3 Results and Discussion

3.3.1 Interactions of Aromatic Hydrazides with Langmuir Monolayers

Surface pressure compression isotherms of DPPC and DPPE were measured to model phospholipids commonly found in eukaryotic and bacterial membranes.[24-27] The minor structural difference in the lipid headgroup results in significant differences in the properties of the resulting lipid monolayer. DPPE has a conical shape and packs much more tightly compared to DPPC which has a cylindrical shape. This is thought to be due to the hydrogen bonding capability of DPPE (ethanolamine head group) that DPPC (choline headgroup) is lacking.[28-29] For these reasons, both DPPC and DPPE zwitterionic phospholipids were used to form Langmuir monolayers to study the interactions of small molecules with phospholipid interfaces.

Surface pressure compression isotherms of DPPC or DPPE were initially conducted in the presence of INH or BHZ hydrazides (Figure 3.2 A-D). The area per phospholipid of the DPPC monolayer in the presence of 10 mM INH increased, until 20-25 mN/m. The area per phospholipid of the DPPE monolayer in the

presence of all concentrations of INH tested increased until 25-30 mN/m. In the presence of 10 mM BHZ, the area per phospholipid of the DPPC monolayer increased until 15-20 mN/m and the area per phospholipid of the DPPE monolayer was unaffected. Briefly, INH affected the area per phospholipid of both monolayers but at all concentrations only for the DPPE monolayer, while BHZ only affected the area per phospholipid of the DPPC monolayer.
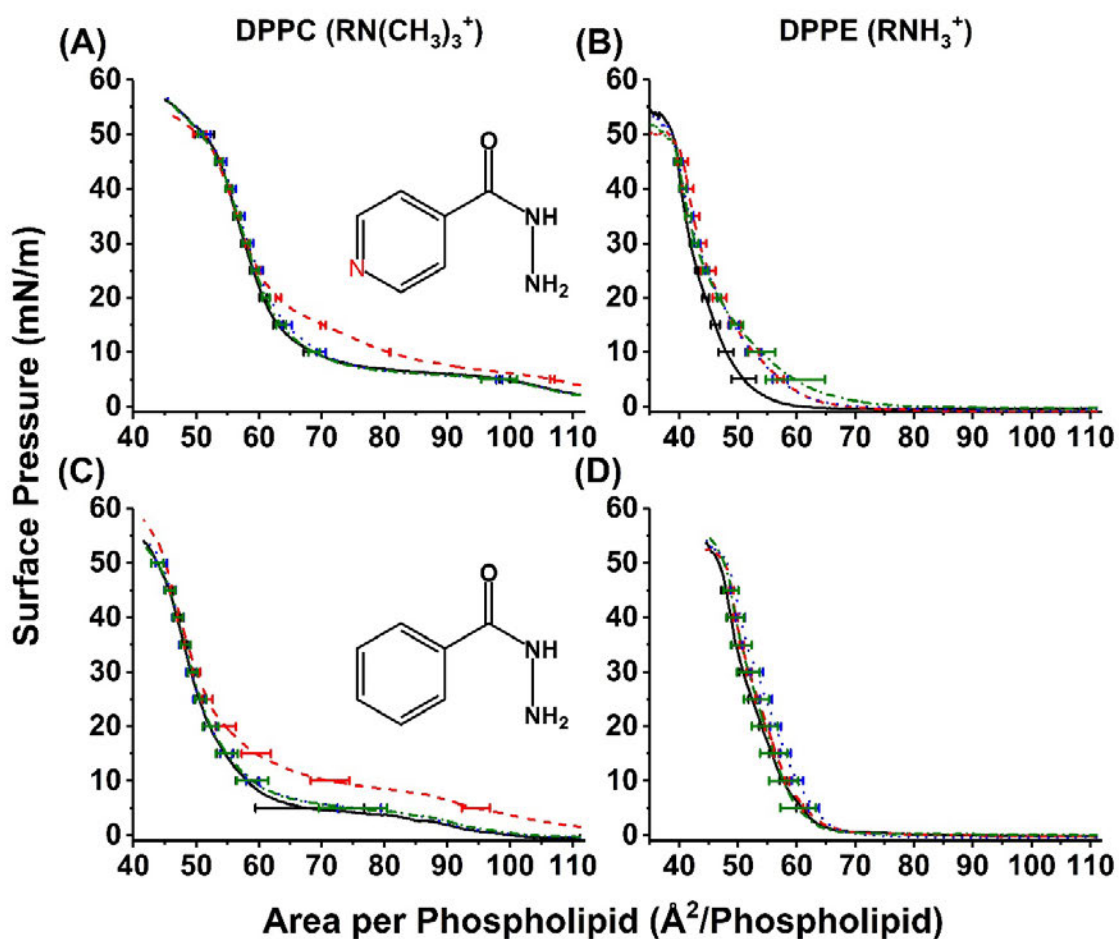
Figure 3.2. Compression isotherms of DPPC (left column) or DPPE (right column) in the presence of INH (A and B) or BHZ (C and D). The solid black curves correspond to the control films without any hydrazide present. The other curves correspond to 10 mM hydrazide (red dashed line), 1 mM (blue dotted line), and 0.1 mM (green dashed and dotted line) present in the 20 mM sodium phosphate buffered subphase (pH 7.4). Each curve is an average of at least 3 trials with standard deviations. The R group for each phospholipid includes the phosphate, glycerol, and fully saturated C_{16} tails.

To determine if the compressibility of the monolayers was affected, the compression modulus was calculated from the average compression isotherms (Figure 3.3 A-D). In the presence of 10 mM INH, the compression modulus of the DPPC monolayer decreased and all concentrations of INH tested, caused a decrease in the compression modulus of the DPPE monolayer. The presence of 10 mM BHZ decreased the compression modulus of the DPPC mono-layer and increased the compression modulus in the presence of 1 mM BHZ. All concentrations tested of BHZ present increased the compression modulus of the DPPE monolayer. In summary, INH decreased the compression modulus of both DPPC and DPPE monolayers, but only the DPPE monolayer was affected at all concentrations tested. BHZ decreased the compression modulus of the DPPC monolayer and with 1 mM BHZ present; the compression modulus of the DPPE monolayer increased.
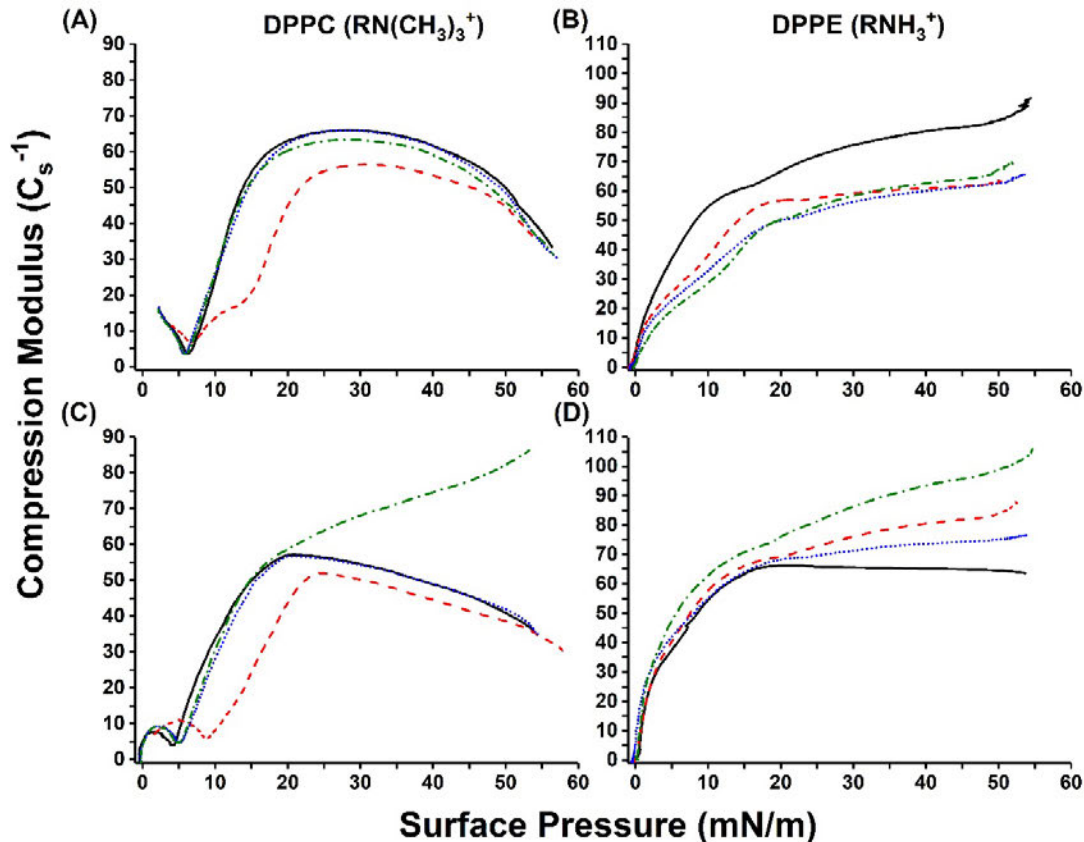
Figure 3.3. Compression moduli of DPPC (left column) or DPPE (right column) in the presence of INH (A and B) or BHZ (C and D). The solid black curves correspond to the control films without any hydrazide present. The other lines correspond to 10 mM hydrazide (red dashed line), 1 mM (blue dotted line), and 0.1 mM (green dashed and dotted line) present in the sodium phosphate buffered subphase (pH 7.4). Each curve is an average of at least 3 trials.

Generally, an increase in area per phospholipid of a monolayer indicates an uptake of the small molecule causing the monolayer to spread, and a decrease in area per phospholipid indicates either solubilization of lipid or a reorganization to allow for tighter packing of the phospholipid monolayer. A decrease in compression modulus has been commonly interpreted as an increase in compressibility and vice versa.[30-31] INH did increase the area per phospholipid of both the DPPC and DPPE monolayers indicating an uptake into the phospholipid monolayers, but did so at lower concentrations present for DPPE. A similar trend was observed with the decrease of compression moduli in the presence of INH. This suggests that INH has a higher affinity for DPPE than DPPC, indicating that INH would interact more

48

favorably with the ethanolamine than the choline head group. This is presumably due to hydrogen bonding with the ethanolamine head group which would disrupt the intermolecular hydrogen bonding between individual DPPE molecules of the DPPE monolayer.[28-29] BHZ affected the area per phospholipid of only the DPPC monolayer at 10 mM and decreased the compression modulus suggesting that at high concentration, BHZ is taken into and allows for easier compression of the DPPC monolayer. At 1 mM for DPPC and all concentrations tested for DPPE; BHZ does not affect the area per phospholipid but increases the compression modulus showing that the BHZ did not spread the phospholipids, but did cause the monolayer to be more difficult to compress than the control monolayers. This suggests that BHZ is reorganizing the phospholipid tails, but more information would be needed for confirmation. In summary, INH was shown to prefer the ethanolamine head group and allowed for easier compression than the control phospholipid monolayers, while BHZ allowed for easier compression and spread the DPPC monolayer when 10 mM was present in the subphase, but otherwise caused the phospholipid monolayers to be less compressible without affecting the area per phospholipid.

3.3.2   Interactions of Aromatic Amides with Langmuir Monolayers

To determine if the amides in Figure 3.1 interact with phospholipid interfaces differently, the surface pressure compression isotherms of DPPC and DPPE were conducted in the presence of BA, PIC, NIC, and iNIC, shown in Figure 3.4 and compression moduli are given in Figure 3.5.
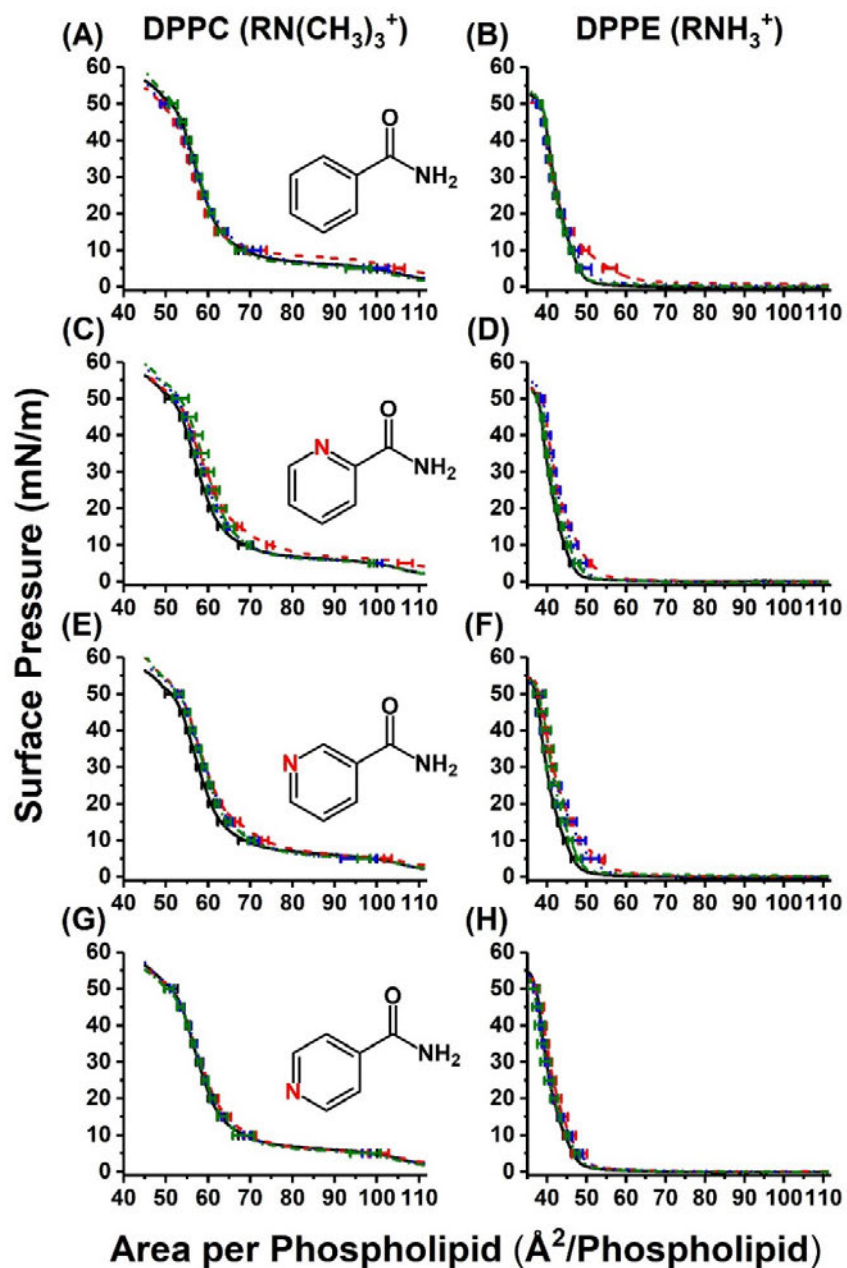
Figure 3.4. The resulting surface pressure compression isotherms of DPPC (left column) and DPPE (right column) in the presence of BA (A and B), PIC, (C and D), NIC (E and F), iNIC (G and H) at concentrations of 0 mM (black solid line), 0.1 mM (green dashed and dotted line), 1.0 mM (blue dotted line), and 10 mM (red dashed line) in the 20 mM sodium phosphate buffered subphase (pH 7.4). Each curve is an average of at least 3 trials with standard deviations. The R group for each phospholipid includes the phosphate, glycerol, and fully saturated C_{16} tails.
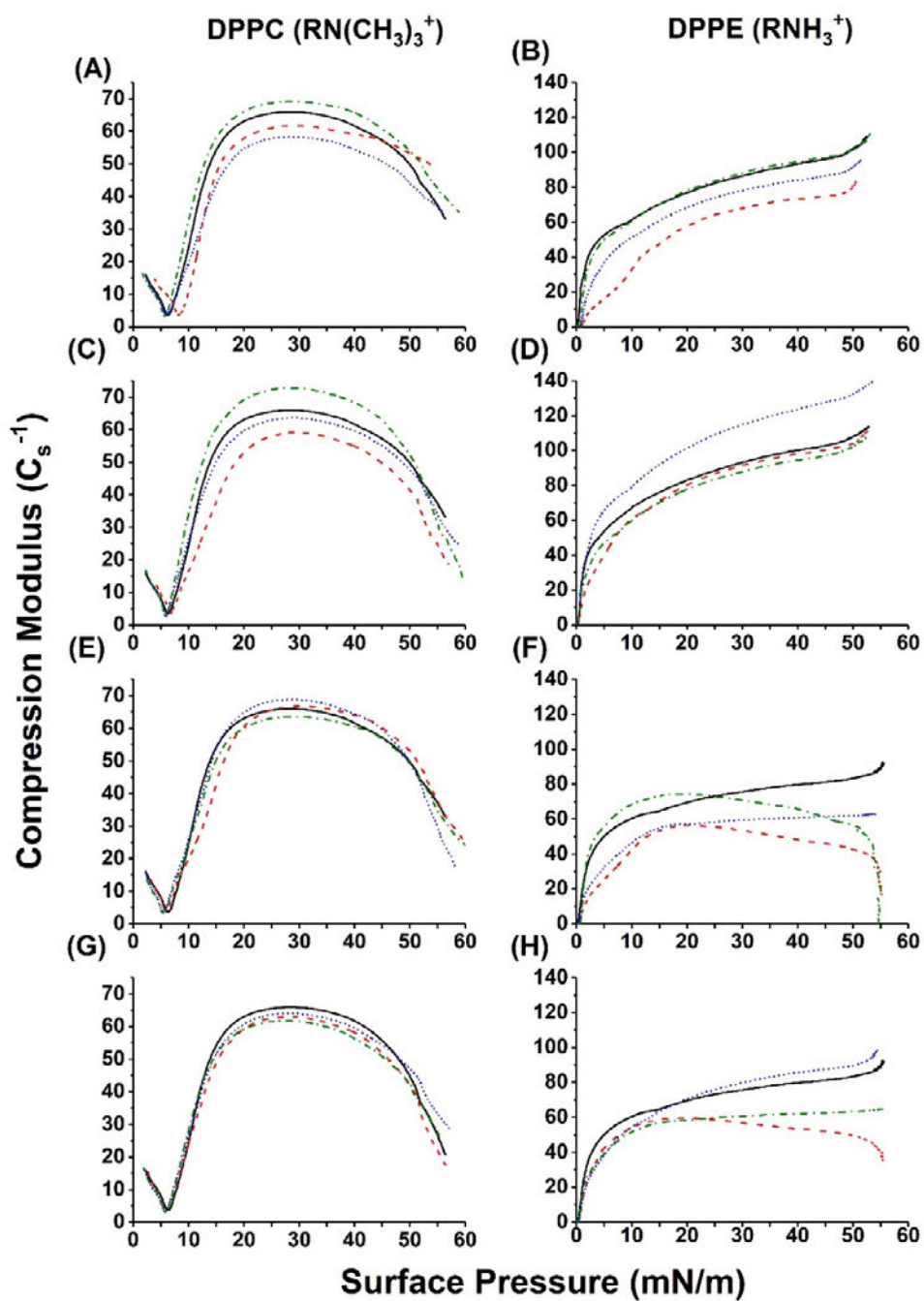
Figure 3.5. The resulting compression moduli of DPPC (left column) and DPPE (right column) in the presence of BA (A and B), PIC, (C and D), NIC (E and F), iNIC (G and H) at concentrations of 0 mM (black solid line), 0.1 mM (green dashed and dotted line), 1.0 mM (blue dotted line), and 10 mM (red dashed line) in the 20 mM sodium phosphate buffered subphase (pH 7.4). Each curve is an average of at least 3 trials.

First, the compression isotherm experiments using BA were conducted as a nitrogen deficient comparison. The presence of 10 mM BA, the DPPC monolayer exhibited an increase in pressure below 15-20 mN/m and then above 15-20 mN/m, exhibited a slight decrease in area per phospholipid. The DPPE monolayer increased in area per phospholipid until 15-20 mN/m. The compression modulus of the DPPC monolayer decreased in the presence of 10 mM and 0.1 mM BA and increased when 1.0 mM was present. Concentrations of 10 mM and 0.1 mM BA also decreased the compression modulus of the DPPE monolayer. This data suggests that BA can spread the phospholipids of both DPPC and DPPE until higher pressures, but it can still affect the compressibility of the phospholipid monolayers showing that BA still does interact with the monolayer at higher pressures.

In the presence of 10 mM PIC, the DPPC and DPPE monolayers exhibited an increase in area per phospholipid as compared to the control monolayers until 35-40 mN/m. Also, depending on the concentration of PIC within the subphase, the compression modulus either decreased for DPPC (10 mM), increased (1 mM), or no effect was observed (0.1 mM). The DPPE monolayer compression modulus was increased only by the presence of the 0.10 mM PIC. The increase in area per phospholipid of DPPC and DPPE in the presence of PIC suggests that PIC is spreading the lipids; but depending on the concentrations of PIC, the compressibility of the phospholipid monolayers is affected. The dependence of the compressibility on the concentration may be due to counter-acting effects where a large amount of PIC (10 mM) increases compressibility solely because PIC exists in excess within the monolayer, so it is compressed out of the monolayer. At lower concentrations (1 mM for DPPC and 0.10 mM for DPPE), PIC caused the monolayers to be-come more rigid and less compressible. Briefly, PIC did increase the area per phospholipid of both phospholipid monolayers, and had varying effects on the compression moduli of the phospholipid monolayers.

The DPPC and DPPE monolayers in the presence of NIC both exhibited an increase in area per phospholipid. All concentrations of NIC tested increased the area per phospholipid of DPPC above 10

mN/m. The DPPE monolayer was affected in a concentration dependent manner where 10 mM NIC increased the area per molecule the most. The presence of 10 mM NIC caused an increase in area per phospholipid of DPPE across at all surface pressures below collapse (55 mN/m). There was not much of an effect of NIC on the compression modulus on the DPPC monolayer; however, there was a decrease in the compression modulus for the DPPE monolayer at all concentrations of NIC tested. The presence of NIC caused a spreading of both phospholipid monolayers but only affected the compressibility of the DPPE monolayer allowing it to become more compressible than the control monolayer.

Unlike the other molecules tested, iNIC had no effect on either the DPPC nor the DPPE monolayer area per phospholipid. The presence of 10 and 1.0 mM iNIC did however decrease the compression modulus of the DPPE monolayer but did not have much of an effect on the compressibility of the DPPC monolayer. This suggests that iNIC has a higher affinity for DPPE than DPPC and allows the DPPE monolayer to be more easily compressed without spreading the phospholipids.

By comparing the interactions of all the molecules of interest with DPPC and DPPE monolayers, it is clear that not all of the small aromatic compounds interact with the phospholipid monolayers in the same manner (Table 3.1). Out of the six compounds tested, INH and iNIC exhibited more of an effect on the DPPE mono-layer than the DPPC monolayer suggesting a preference for the ethanolamine head group more so than the choline head group. This is most likely due to the ethanolamine's greater hydrogen bonding capacity than choline, allowing for intermolecular interaction. When comparing PIC, NIC, and the iNIC, the data is consistent with PIC and NIC affecting the phospholipid monolayers similarly, but iNIC had the least effect on the phospholipid monolayers. As shown in Table 1, NIC and PIC were the only compounds to significantly increase the area per phospholipid of the DPPC and DPPE monolayers at physiologically relevant surface pressures (30-35 mN/m),[32] whereas iNIC did not have much of an effect on the area per phospholipid. Of all the compounds, BA was the only molecule to cause a decrease in area per phospholipid for DPPC at higher surface pressures (above 15-20 mN/m, Table 1) suggesting that BA

was the only compound tested that either reorganized DPPC to condense further or assist in the solvation of the DPPC. Interestingly, BHZ did not have the same effect as BA, but still interacted with the phospholipid monolayers causing the phospholipids to spread. In summary, INH and iNIC both exhibited a preference for DPPE over DPPC, PIC and NIC affect the phospholipid monolayers similarly even at high pressures, BA reorganizes the DPPC monolayer or helps solubilize the DPPC, and BHZ does interact with both monolayers causing spreading of the phospholipids.

Table 3.1. Percent Difference of Monolayer Surface Area in the Presence of Small Aromatic Compounds.[a]
[a]Surface pressures were chosen based on initial curve (5 mN/m) and physiological relevance (30-35 mN/m).[32] Significance of the percent difference was determined using a Student's T test with *$p < 0.10$ and **$p < 0.05$.

Compound	Surface Pressure (mN/m)	DPPC	DPPE
		% Difference from Control	% Difference from Control
INH	5	7.36	12.25
	30	0.89	3.61
	35	0.10	3.22
BHZ	5	38.84	1.06
	30	1.86	2.02
	35	1.14	1.95
BA	5	6.21	16.19
	30	-2.20*	-0.92
	35	-2.19*	1.46
PIC	5	2.41	7.65
	30	3.32*	3.65**
	35	2.47**	3.44**
NIC	5	3.42	13.33
	30	3.01**	4.08**
	35	2.77**	3.62**
iNIC	5	1.22	3.32
	30	1.03	1.87
	35	0.55	1.89

3.3.3 Placement of Small Aromatic Hydrazides and Amides Within the AOT RM

Molecular information on the specific interaction and placement of the compounds with respect to a membrane interface was sought using AOT RMs and NMR spectroscopy.[23, 33-37] To this end, the ^{1}H NMR spectrum of each small aromatic compound was acquired in D_2O and varying sizes of RM. By varying the

sizes of the RM (w_0), small changes in the RM microenvironment occur. Comparing the chemical shifts of the N-containing compounds caused by varying environmental differences, it is possible to place the compounds within the RM.[23, 33-37] The following paragraphs describe the chemical shifting and our placement of compounds as a result of the observed chemical shifting patterns.
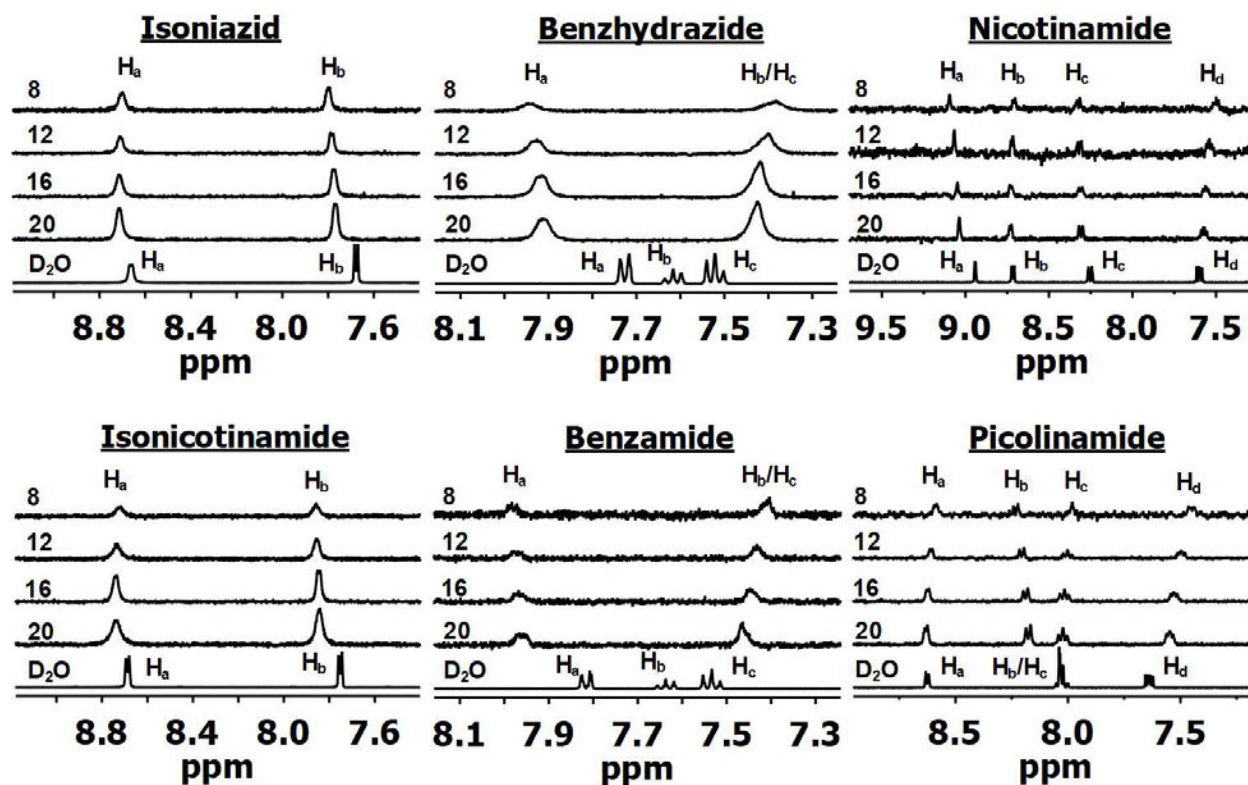
Figure 3.6. ^{1}H 1D NMR spectra obtained using a 400 MHz Varian NMR of INH, iNIC, BHZ, BA, NIC, and PIC in D_2O and varying sizes of RMs (w_0) given on the left of each stack of spectra. See Figure 3.1 for labeled structures corresponding to peak labels.

The ^{1}H NMR spectra of INH and iNIC are presented as stack plots of ^{1}H NMR spectra in D_2O at the bottom and the RM microemulsions with the smallest RMs as the top spectrum (w_0 8). In the INH spectra, the H_a doublet peak shifts slightly downfield from the D_2O spectrum at 8.67 to 8.71 ppm in the w_0 20 spectrum and then gradually shifts upfield to 8.70 ppm in w_0 8 spectrum. The doublet H_b peak for INH shifted gradually downfield from 7.69 ppm in D_2O to 7.80 ppm in the w_0 8 spectrum. A similar shifting pattern was observed with iNIC. The peak corresponding to the doublet H_a for iNIC barely shifts from 8.70 ppm in D_2O to 8.74 ppm in the w_0 20 spectrum and then a slight upfield shift to the w_0 8 spectrum at 8.72

55

ppm. The doublet peak corresponding to H_b shifts gradually downfield from 7.76 ppm in the D_2O spectrum to 7.86 ppm in the w_0 8 spectrum. The downfield shifting of both H_a and H_b peaks of INH and iNIC from the D_2O spectrum to the w_0 20 spectrum is consistent with a more charged (deshielded) environment such as near the sulfonates of the AOT.[38] The upfield shifting pattern of H_a of both compounds is consistent with the reduction of a charged environment as the RM sizes are reduced suggesting that H_a is more toward the hydrophobic region than H_b.[38] Together this data suggests that both INH and iNIC reside near the AOT headgroups with the pyridine nitrogen facing toward the AOT tails and the amide/hydrazide toward the water pool similar to benzoate and phenyl biguanide.[23, 37]

Next, the interactions of the benzene based hydrazide and amide, BHZ and BA, with the AOT RM interface are described by ^{1}H NMR. The doublet corresponding to H_a for BHZ shifted from 7.74 ppm in the D_2O spectrum to 7.94 ppm gradually as the RM sizes were reduced to the w_0 8 spectrum. The triplets corresponding to H_b and H_c for BHZ are at 7.62 ppm and 7.52 ppm respectively in the D_2O spectrum and then coalesce in the RM spectra while gradually shifting upfield to 7.38 ppm in the w_0 8 spectrum. The peak corresponding to H_a for BA shifts from 7.83 ppm in D_2O gradually to 7.99 ppm in the w_0 8 spectrum. The peaks corresponding to H_b and H_c of BA in the D_2O spectrum are at 7.64 ppm and 7.53 ppm respectively and then coalesce in the RM spectra and gradually shift upfield until 7.40 ppm in the w_0 8 spectrum. The down-field shifting pattern of H_a of both BHZ and BA from D_2O spectrum to the w_0 8 spectrum is consistent with the RM interface. The upfield shifting pattern of H_b and H_c of both BHZ and BA is consistent with a deep placement within the RM interface toward the AOT tails. Using this data, it is possible to place BHZ and BA within the water-AOT interface with the benzene ring of both compounds placed a little more toward the AOT tails than INH and iNIC, and with the amide/hydrazide toward the water pool. This is similar to, but not quite as deep within the interface as what has been previously found for benzoic acid.[23]

The position and orientation of NIC within the RM was explored by itself unlike the previous compounds. The doublet corresponding to H_a for NIC shifted gradually downfield from 8.94 ppm in the D_2O spectrum to 9.10 ppm in the w_0 8 spectrum. The H_b doublet shifts from 8.72 ppm in the D_2O spectrum to 8.74 ppm in the w_0 20 spectrum, and then shifts upfield to 8.71 ppm in the w_0 8 spectrum. The H_c doublet shifts from 8.27 ppm in the D_2O spectrum gradually to 8.34 ppm in the w_0 8 spectrum, and the H_d peak is the only peak for NIC to gradually shift up-field from 7.62 ppm in the D_2O spectrum to 7.52 ppm in the w_0 8 spectrum. The downfield shifting for the H_d and H_a peaks for NIC are consistent with placement toward the water-AOT interface. The H_c peak initially shifted downfield and then slightly upfield suggesting a placement near the water-AOT interface but more toward the AOT tails than H_d and H_a. The H_b peak was the only peak that consistently shifted upfield suggesting the deepest placement (toward AOT tails) of all the NIC protons. This data is consistent with NIC residing near the water-AOT interface with NIC tilted at the interface. This position would have H_a pointing toward the water pool and the amide tilted more toward the AOT headgroups. A similar finding was determined for the ortho-fluorobenzoate anion at the micellar interface.[38]

Finally, the placement and orientation of PIC within the RM samples was determined. The H_a doublet for PIC shifts slightly upfield from the 8.63 ppm in the D_2O spectrum to 8.60 ppm in the w_0 8 spectrum. The peaks corresponding to H_b and H_c are overlapping in the D_2O spectrum but then separate within the RM samples with H_b shifting downfield gradually from 8.04 ppm in the D_2O spectrum to 8.24 ppm in the w_0 8 spectrum and H_c gradually shifts upfield from 8.02 ppm in the D_2O spectrum to 7.98 ppm in in the w_0 8 spectrum. The H_d peak for PIC gradually shifts upfield from 7.64 ppm in the D_2O spectrum to 7.45 ppm in the w_0 8 spectrum. The upfield shifting pattern of H_a, H_c, and H_d peaks is consistent with the protons being placed toward the AOT tails. The downfield shifting pattern of H_b is consistent with it being placed more toward the AOT interface. This data is consistent with PIC residing near the AOT headgroups, with

only H_b being near the AOT head-groups and the other protons toward the AOT tails causing a tilt of the molecule within the interface.

In summary, this data shows that these N-containing molecules interact differently with the AOT RM, but reside at similar positions within the water-AOT interface. INH and iNIC were shown to reside within the AOT interface with the pyridine nitrogen facing toward the AOT tails and the hydrazide/amide toward the AOT head groups. BHZ and BA were shown to reside deeper toward the AOT tails than INH or iNIC but with the same orientation. PIC was shown to reside at the AOT interface as INH and iNIC, but slightly tilted at the interface with the nitrogen of the pyridine and the amide facing toward the AOT head group and water pool. NIC was also shown to be tilted with the proton between the amide and pyridine nitrogen facing the water pool. Generally, each molecule resided in similar positions, but the pyridine nitrogen to amide orientation did affected the overall molecular orientation at the water-AOT RM interface. This finding is similar to what has been shown for fluorobenzoate derivatives with micelles.[38]

3.3.4 ^{1}H-^{1}H NMR of Hydrazides and Amides Within the AOT RM Interface

More information was sought to confirm the placement and orientation based on ^{1}H 1D NMR experiments, there-fore through space ^{1}H-^{1}H 2D NOESY and ROESY experiments were conducted.[23, 34-36] Both ^{1}H-^{1}H 2D NOESY and ROESY spectra with a 200 ms mixing time and higher concentration of BA was acquired to explore which experiment would provide the best signal to noise ratio. With the ROESY data producing a better signal to noise ratio than the NOESY for these samples, other ROESY spectra were sought using 100 or 0 ms mixing times. The 0 ms mixing time serves as a negative control to confirm no magnetization transfer was observed between magnetically different protons.

A portion of the ^{1}H-^{1}H 2D ROESY NMR spectra for INH within w_0 12 RMs are shown in Figure 3.7. The spectra of INH within the w_0 12 RM microemulsion show a diagonal with two, negative, blue peaks corresponding to the H_a and H_b peaks of INH at 7.71 ppm and 7.77 ppm respectively. The positive, red, off diagonal cross peaks corresponding to H_a and H_b are observed in the spectra of 200 and 100 ms mixing

time whereas no cross peaks were observed in the 0 ms mixing time spectrum as would be expected. In

the 200 ms mixing time spectrum for INH, an off diagonal cross peak corresponding to H_b on INH and the

methyl peak of either AOT or isooctane at 0.90 ppm on the f2 axis. In the 100 ms mixing time spectrum,

off diagonal cross peaks for both H_a and H_b at 0.90 ppm on the f2 axis were observed and correspond to

the AOT or isooctane methyl peak. Considering that the previous ^1H 1D NMR experiments have shown

that INH and iNIC reside within the water-AOT interface, INH is most likely residing near the AOT ethyl CH_3

protons with the CH_3 protons tilted toward the interface (see Figure A3.1 for AOT assignments).
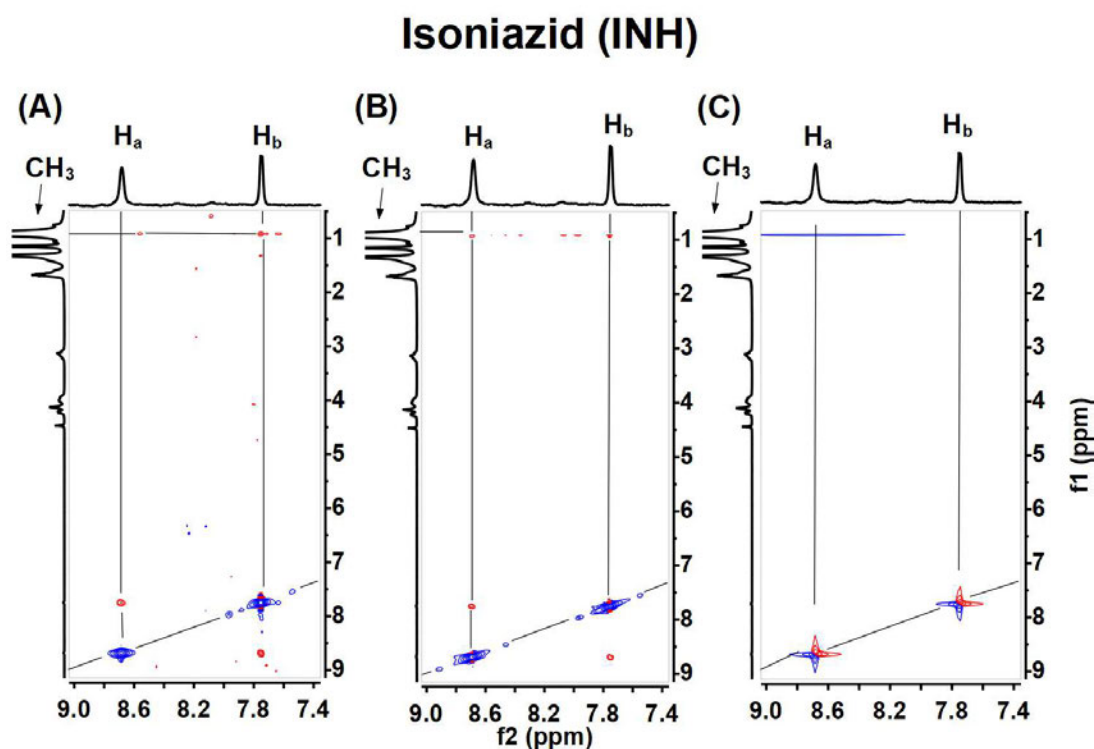
Figure 3.7. ^1H-^1H 2D ROESY NMR spectra acquired using a 400 MHz Inova NMR of INH using 200 ms (A), 100 ms (B), and 0 ms (C) mixing time and a relaxation delay of 1.5 s. The diagonal is indicated by the diagonal line. The lines also highlight any off diagonal cross peaks. Peaks are labeled according to Figure 3.1 and Figure A3.1.

The ^1H-^1H 2D ROESY NMR spectra of the w_0 12 RM microemulsion with iNIC also indicated an

interaction with the AOT interface similar to INH. Along the diagonal shown in Figure 3.8, two, negative,

blue peaks corresponding to iNIC protons H_a and H_b at 8.70 ppm and 7.80 ppm respectively. Positive, red,

off diagonal cross peaks between H_a and H_b in the 200 and 100 ms mixing time spectra are observed.

59

Finally, no cross peaks were observed in the 0 ms mixing time spectrum. In the 200 ms mixing time spectrum, positive, red, off diagonal cross peaks with H_a and H_b of iNIC are observed at 1.30 ppm and 0.90 ppm on the f2 axis corresponding to the AOT CH_2 and an isooctane or AOT CH_3 peak, respectively. These peaks were not observed in either the 100 ms nor 0 ms mixing time spectra. Due to iNIC's insolubility in isooctane and its similar placement determined by the ^1H 1D NMR studies, these results support the interpretation that iNIC interacts within the RM water-AOT resides at the interface near the sulfonate headgroups of the AOT similar to the vanadium dipicolinate complex.[39]

Isonicotinamide (iNIC)

Figure 3.8. ^{1}H-^{1}H 2D ROESY NMR spectra acquired using a 400 MHz Inova NMR of iNIC using 200 ms (A), 100 ms (B), and 0 ms (C) mixing time and a relaxation delay of 1.5 s. The diagonal is indicated by the diagonal line. The lines also highlight any off diagonal cross peaks. Peaks are labeled according to Figure 3.1 and Figure A3.1.

The ^{1}H-^{1}H 2D ROESY spectra of RMs containing BHZ and BA (Figure 3.9) were very similar. In the following these compounds will be discussed concurrently. As can be seen on the diagonal of the spectra of BHZ, there are two negative, blue peaks at 7.97 ppm and 7.43 ppm corresponding to H_a and H_b/H_c respectively. Within the 200 and 100 ms mixing time spectra, positive, red, off diagonal cross peaks are observed between the H_a and H_b/H_c peaks whereas no cross peaks are observed for the 0 ms mixing time spectrum. In the 200 ms mixing time spectrum positive, red, off diagonal cross peaks at 1.30 ppm and 0.90 ppm on the f1 axis corresponding to the AOT CH_2 peak, the AOT CH_3, or isooctane CH_3 peak and H_a and H_b/H_c can be observed. In the spectrum using 100 ms mixing time the same off diagonal peaks are observed except for the off diagonal cross peak at 1.30 ppm on the f1 axis and 7.97 ppm on the f2 axis corresponding to the AOT CH_2 and the H_a protons respectively. These cross peaks were also observed for

BA where the only differences in the spectra were from the placement of the BA negative, blue peaks on the diagonal at 7.92 ppm for H_a and 7.39 ppm for H_b/H_c. This data suggests that BHZ and BA are both positioned nearby the AOT ethyl with the hydrazide/amide facing the water pool consistent with the ^1H 1D NMR studies.

Benzhydrazide (BHZ)

(A1) **(A2)** **(A3)**

## Benzamide (BA)

(B1) **(B2)** **(B3)**

Figure 3.9. ^{1}H-^{1}H 2D ROESY NMR spectra acquired using a 400 MHz Inova NMR of BHZ (A) or BA (B) using 200 ms (1), 100 ms (2), and 0 ms (3) mixing time and a relaxation delay of 1.5 s. The diagonal is indicated by the diagonal line. The lines also highlight any off diagonal cross peaks. Peaks are labeled according to Figure 3.1 and Figure A3.1.

The ^{1}H-^{1}H 2D ROESY spectra of PIC, within RMs were acquired to confirm placement and orientation within the RM water-AOT interface. Figure 3.10 shows the ^{1}H-^{1}H 2D ROESY NMR spectra of PIC within w_0 12 RM microemulsion acquired using 200, 100, and 0 ms mixing times. Observed in each of these spectra are negative, blue peaks along the diagonal corresponding to H_a (8.60 ppm), H_b (8.19 ppm), H_c (7.99 ppm), and H_d (7.47 ppm). In the spectra acquired using 200 and 100 ms mixing times, there are positive, red, off diagonal cross peaks between the peaks corresponding to the PIC peaks whereas no off diagonal cross peaks are observed in the spectrum acquired using a 0 ms mixing time. In the 200 ms mixing time spectrum, positive, red, off diagonal cross peaks at 0.90 in the f1 dimension corresponding to all the PIC peaks observed. The same positive, red, off diagonal cross peaks are observed using 100 ms mixing time with the exception of the off diagonal cross peak at 0.90 ppm in the f1 dimension and 7.99 ppm in the f2 dimension corresponding to H_c of PIC. This confirms that PIC resides within the AOT interface and does interact with the CH_3 of the ethyl of AOT.
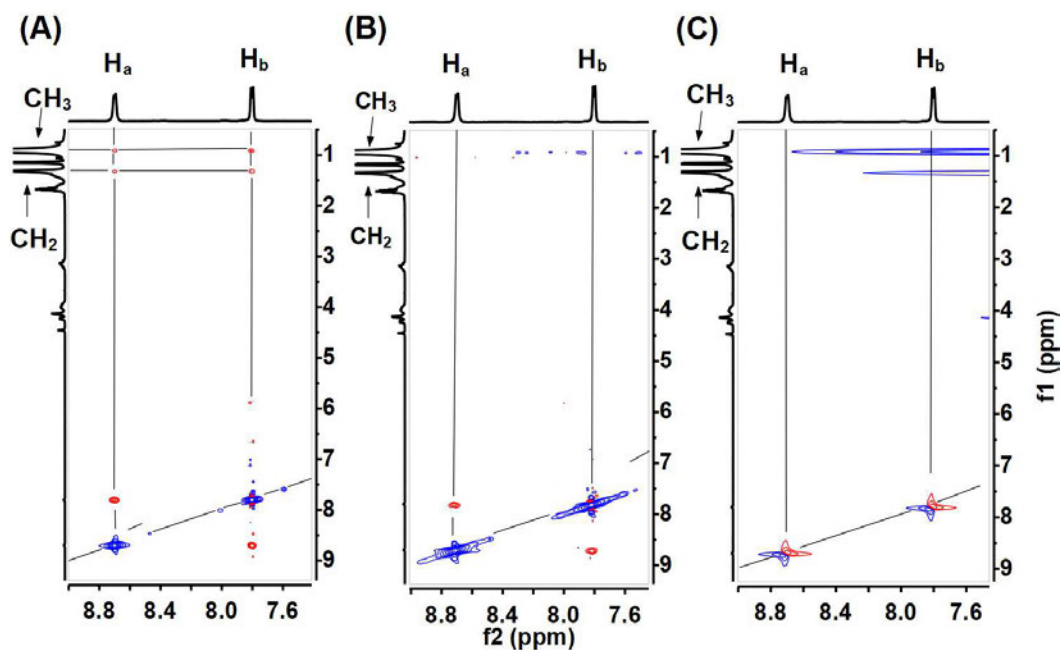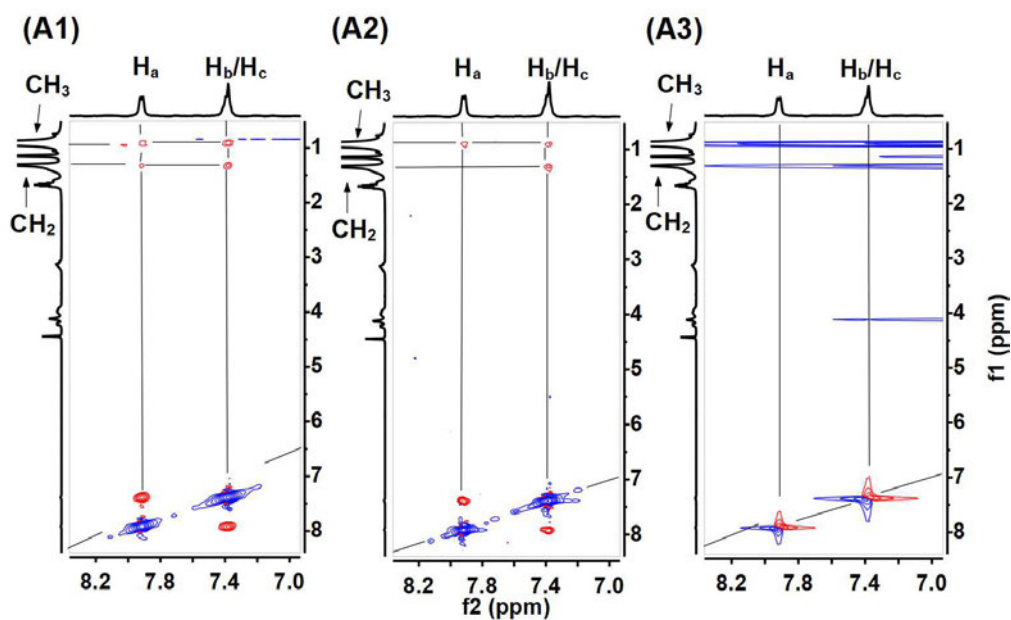
Picolinamide (PIC)
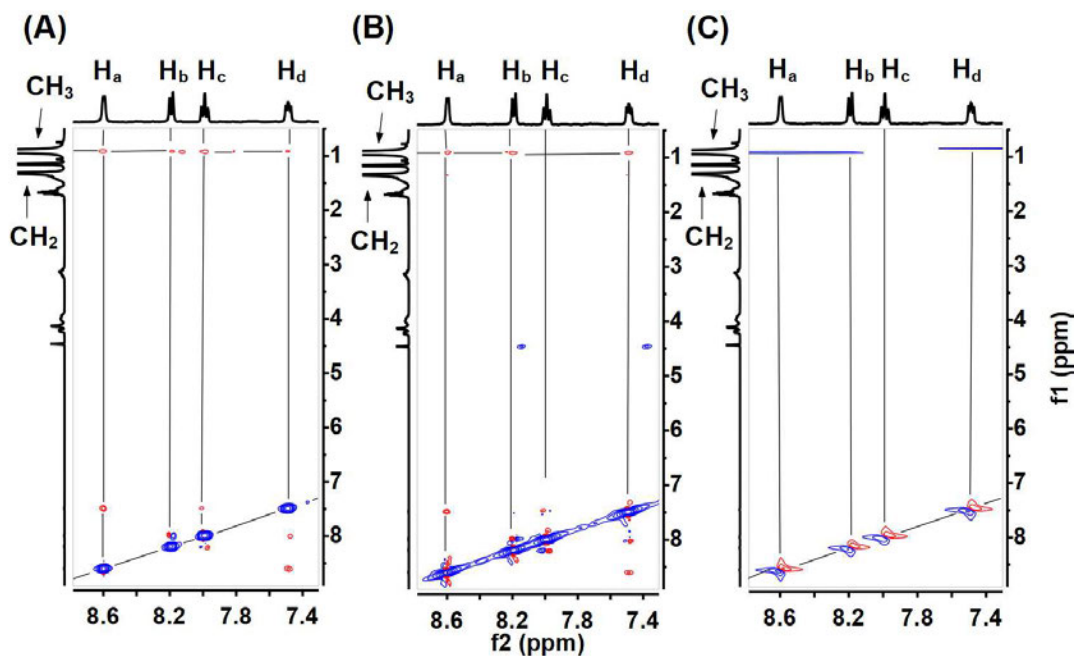
Figure 3.10. ^{1}H-^{1}H 2D ROESY NMR spectra acquired using a 400 MHz Inova NMR of PIC using 200 ms (A), 100 ms (B), and 0 ms (C) mixing time and a relaxation delay of 1.5 s. The diagonal is indicated by the diagonal line. The lines also highlight any off diagonal cross peaks. Peaks are labeled according to Figure 3.1 and Figure A3.1.

The placement and orientation within RMs of NIC was explored using ^{1}H-^{1}H 2D ROESY NMR in the w_0 12 RM spectra shown in Figure 3.11. The peaks on the diagonal are negative, blue peaks corresponding to H_a (9.02 ppm), H_b (8.68 ppm), H_c (8.29 ppm), and H_d (7.50 ppm). Positive, red, off diagonal cross peaks between the NIC aromatic protons can be observed in the spectra acquired using 200 ms and 100 ms mixing times but not for the 0 ms mixing time spectrum. Positive, red, off diagonal cross peaks corresponding to AOT peaks can be observed at 0.90 ppm in the f1 dimension and at 9.02 ppm, 8.68 ppm, 8.29 ppm, and 7.50 ppm in the f2 dimension. These peaks suggest that all the aromatic protons of NIC reside near a methyl. Three other positive, red, off diagonal cross peaks can be observed at 1.30 ppm in the f1 dimension and at 8.68 ppm, 8.29 ppm, and 7.50 ppm in the f2 dimension corresponding to the CH_2 AOT peak and H_b, H_c, and H_d. This data is consistent with NIC residing at the same position within the RM

interface as the other probe molecules but H_a is not in proximity to the CH_2 of the AOT ethyl. By rotating the C-C bonds of the ethyl of AOT, the CH_3 of the ethyl can reach further than the CH_2 suggesting that H_a is in a position away from the CH_2. This would suggest a tilt in the NIC at the water-AOT interface supporting the interpretation of the ^{1}H 1D NMR spectra.

Nicotinamide (NIC)
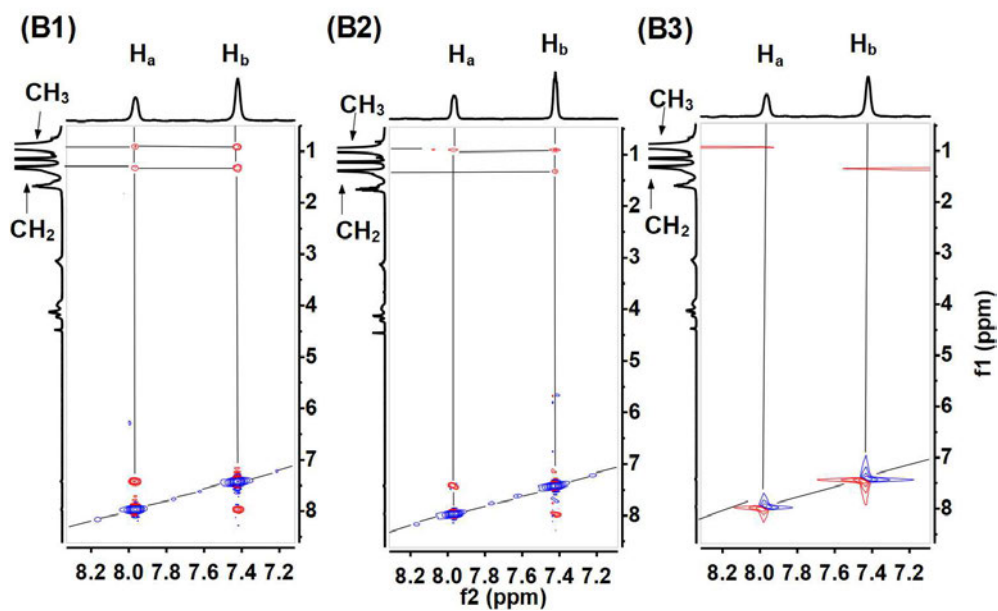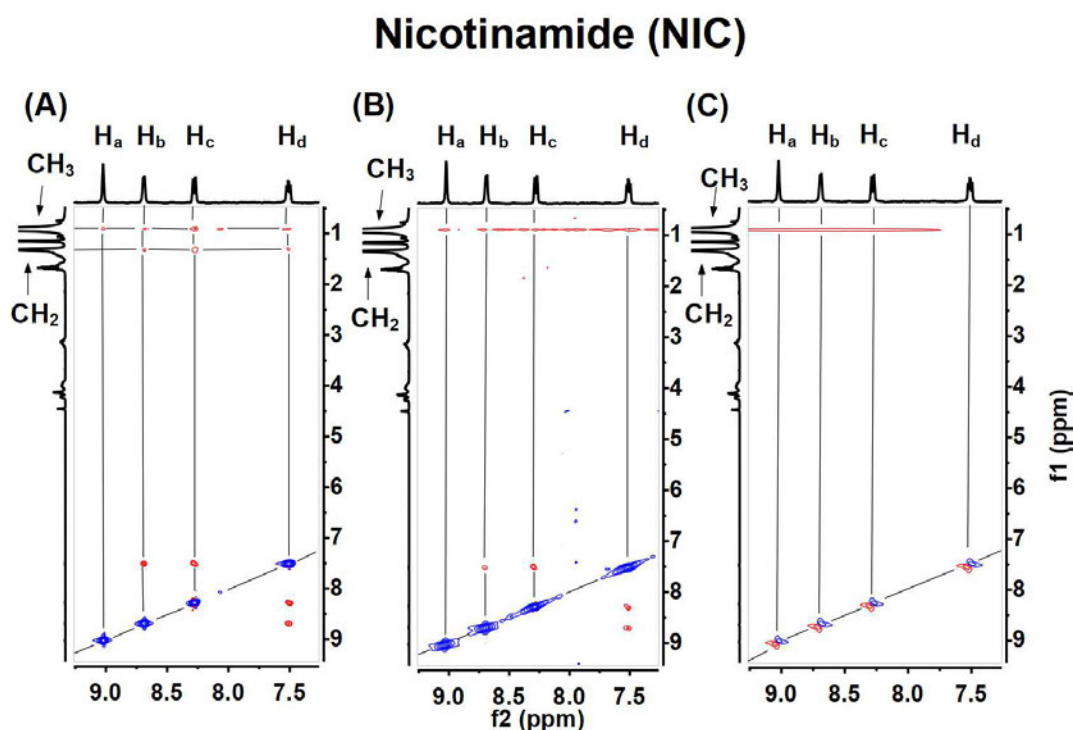

Figure 3.11. ^{1}H-^{1}H 2D ROESY NMR spectra acquired using a 400 MHz Inova NMR of NIC using 200 ms (A), 100 ms (B), and 0 ms (C) mixing time and a relaxation delay of 1.5 s. The diagonal is indicated by the diagonal line. The lines also highlight any off diagonal cross peaks. Peaks are labeled according to Figure 3.1 and Figure A3.1.

In summary, the ^{1}H-^{1}H 2D ROESY NMR spectra of w_0 12 RMs containing the compounds of interest did support the results from the ^{1}H 1D NMR spectra. The placement of each of these molecules using data from both the 1D and 2D NMR experiments is illustrated in Figure 3.12. First of which, INH and iNIC both can be positioned near the AOT ethyl. Since iNIC exhibited interactions with the CH_2 of the ethyl of AOT, iNIC is placed slightly deeper toward the tails of the AOT than INH. BHZ and BA both can be placed at the same position and slightly deeper than iNIC. The 2D NMR of PIC confirmed that it does reside within the inter-face of the water pool and AOT while the 1D NMR suggested a tilt at the water-AOT interface. Briefly,

66

all the molecules resided near the water-AOT interface however, PIC and NIC exhibited a tilted orientation within the interface (see Figure 3.12).
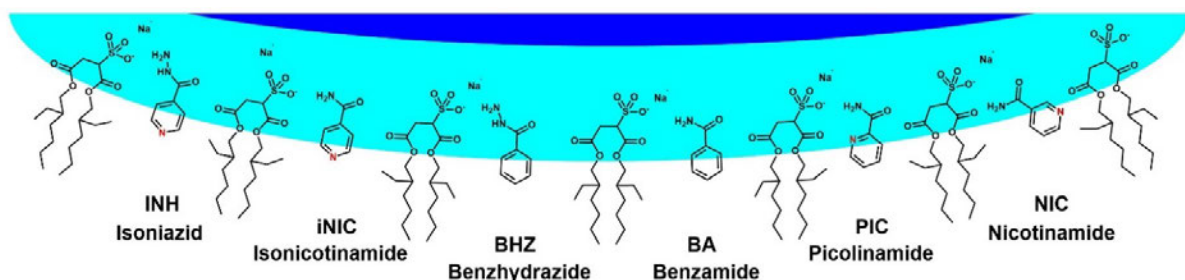
Figure 3.12. Pictorial representation of the placement of INH, iNIC, BHZ, BA, PIC, and NIC within the RM as determined through 1D and 2D ^{1}H NMR studies. It is important to note that this system is highly dynamic and therefore these are average positions/orientation within the AOT interface based on the 1D and 2D NMR data presented in this study.

3.3.5   pK$_a$ Measurement of the Hydrazides and Amides Within the AOT RM

To explore how the AOT interface affects the small aromatic molecules, the pK$_a$ values of the small aromatic molecules were determined. The pH within the RM water pool is not just simply the $-\log[H^+]$ as is normally used in the United States to calculate pK$_a$ in aqueous solutions.[39] The pH value within the RM water pool is much more complicated. Depending on the charge of the head group surfactant used to form the RM microemulsion, a proton gradient can form.[40-41] The AOT RMs used in this study have a negative charge and therefore can cause an increase in proton concentration at the interface.[42] The pK$_a$ of molecules have also been known to change within varying environments, such as the difference in pK$_a$ values of a specific amino acid depends on whether or not it is in the center or on surface of a protein, therefore the RM may affect the small aromatic molecules' pK$_a$ value.[43]

The pK$_a$ values of the aromatic small aromatic molecules in D$_2$O and in w_0 16 RMs are shown and compared to literature and calculated values in Table 3.2 The pK$_a$ for BA was not determined in this study, because of BA's low pK$_a$ value. The pK$_a$ of each of the probe molecules in D$_2$O are all very similar to both the predicted pK$_a$ values and the experimentally determined pK$_a$ values.[44] The small differences between the pK$_a$ values found in this study and the experimental studies in aqueous solutions is most likely caused by differences in ionic strength, temperature, and differences caused by H$_2$O (reported pK$_a$ values) or D$_2$O (this study). Within the RMs, the pK$_a$ of each molecule lowered beyond measurement. This would support an interaction with the AOT itself or an effect of the high ionic strength of the interface.[23, 42, 45-47] Either possibility supports that the molecules reside within the RM interface.

Table 3.2. pK$_a$ Values of the Hydrazides and Amides of Interest in Aqueous and RM Solutions.[a] [a]The table above outlines the pK$_a$ values determined using the method outlined in Appendix IV. The pK$_a$ of the amine protons for INH and BZH are given by*. The predicted pK$_a$ values are from http://www.chemicalize.org. The reported pK$_a$ values are from Maitra.[48]

Compound	Predicted pK$_a$	Reported pK$_a$[44]	pK$_a$ in D$_2$O	pK$_a$ in w_o 16 RM
INH	3.4, 2.4*	3.5, 1.9*	3.3	<1
BHZ	2.8*	3.0*	2.8*	<1
BA	-0.4	N.A.	N.A.	N.A.
PIC	2.2	2.1	2.4	<1
NIC	3.6	3.3	3.7	<1
iNIC	3.5	3.6	3.9	<1

3.3.6   DLS of RMs Containing Aromatic Hydrazides and Amides

DLS was used to determine that RMs formed. In addition to confirming that the RMs form, we also demonstrated that the sizes of the systems measured were consistent with that reported in the literature (Table 3.3).[48] Furthermore, the measurements were done to investigate whether the addition of the compound alter the overall structure of the RMs studied. As shown in Table 3.3 no differences in sizes of RMs with and without the aromatic hydrazides and aromatic amides were observed.[48]

Table 3.3. Size Parameters for RMs of Varying w_0 Values.[a] [a]The table outlines the content of the RM, the observed hydrodynamic radius (R_h), polydispersity index (PDI), the reported water pool radius (R_w), aggregation number (number of AOT per RM on average, η_{agg}), and the average number of probe molecules per RM. Literature values are from Maitra et al.[44]

w_0	RM Contents	R_h (nm)	PDI	R_h Reported[44] (nm)	R_w Reported[44] (nm)	η_{agg}[44]	Probe/RM
20	H$_2$O	4.0 +/- 0.8	0.4 +/- 0.2	4.4	3.5	302	0
	INH	4.7 +/- 0.4	0.1 +/- 0.1				1.1
	BHZ	4.6 +/- 0.3	0.2 +/- 0.1				1.1
	BA	4.5 +/- 0.8	0.2 +/- 0.1				1.1
	PIC	4.5 +/- 0.2	0.2 +/- 0.1				1.1
	NIC	4.3 +/- 0.3	0.3 +/- 0.1				1.1
	iNIC	4.5 +/- 0.5	0.4 +/- 0.2				1.1
16	H$_2$O	3.9 +/- 0.3	0.3 +/- 0.1	4.2	2.9	215	0
	INH	4.4 +/- 0.3	0.1 +/- 0.1				0.6
	BHZ	5 +/- 1	0.2 +/- 0.1				0.6
	BA	4.3 +/-0.2	0.2 +/- 0.1				0.6
	PIC	4.1 +/- 0.3	0.2 +/- 0.1				0.6
	NIC	4.0 +/- 0.2	0.2 +/- 0.1				0.6
	iNIC	4.0 +/- 0.3	0.3 +/- 0.1				0.6
12	H$_2$O	3.8 +/- 0.2	0.2 +/- 0.1	3.7	2.2	129	0
	INH	3.9 +/- 0.2	0.1 +/- 0.1				0.3
	BHZ	3.7 +/- 0.1	0.2 +/- 0.1				0.3
	BA	3.4 +/- 0.3	0.4 +/- 0.2				0.3
	PIC	3.8 +/- 0.1	0.2 +/- 0.1				0.3
	NIC	3.8 +/- 0.1	0.2 +/- 0.1				0.3
	iNIC	3.5 +/- 0.3	0.3 +/- 0.1				0.3
8	H$_2$O	3.2 +/- 0.3	0.3 +/- 0.1	3.2	1.6	72	0
	INH	3.4 +/- 0.2	0.2 +/- 0.1				0.1
	BHZ	4.3 +/- 0.6	0.2 +/- 0.1				0.1
	BA	3.3 +/- 0.3	0.3 +/- 0.1				0.1
	PIC	3.4 +/- 0.2	0.2 +/- 0.1				0.1
	NIC	3.7 +/- 1.6	0.3 +/- 0.1				0.1
	iNIC	3.3 +/- 0.2	0.2 +/- 0.1				0.1

3.3.7 Evaluation of Findings of Langmuir Monolayer Studies and AOT RM Studies

Studies in model systems are done to obtain information that may not be accessible in studies of the biological membranes. The two model systems used in the studies here both have advantages and limitations. Regardless, it is important to note that there are substantial differences between the AOT interface and a phospholipid interface. The differences in structure, curvature, surfactant/lipid density, and head group charge (negative vs. zwitterionic respectively), may impact the interactions of the

molecules under investigation with regard to their interaction with interfaces.[14, 33, 45-46] Although these differences exist, there are similarities between how the molecules of interest interact with the AOT interface and the phospholipid interface. By comparing the findings of the RM experiments with phospholipid Langmuir monolayer experiments, the combination can shed light on crucial differences behind the interactions of molecules with the surfactant or lipid interfaces.[23, 36]

Interestingly, all the molecules studied here were found to reside near the head group of the AOT surfactant interface. The RM studies provide information about how small structural changes in the aromatic amide or hydrazide can affect compound placement and orientation at a surfactant interface. This finding, albeit on a different type of interface, is consistent with the results reported in computational studies of NIC and PIC with phosphatidyl-choline and phosphatidylethanolamine phospholipids[21-22] along with experimental studies with INH interacting with a liposome consisting of phosphotidylcholine.[49-50] We found that the distance of amide to the pyridine nitrogen and the molecular orientation of the amide can impact the interactions with the water-AOT interface. Similarly using computational methods in studies by Borba et al. and Martini et al. specific hydrogen bonding with NIC and PIC were found using phosphatidylcholine and phosphatidylethanolamine phospholipids.[21-22] Although the findings in our studies with the RMs do not directly demonstrate the specific interactions with the phospholipid headgroups found in these computational studies, but the locations identified in our studies of the small aromatics N-containing molecules with the sulfonate head group of AOT were comparable, that is placing the drug near the interface.

Conversely if the small aromatic compounds interacted primarily with the phospholipid tails, then the head group would not have affected the overall interactions with the phospholipids and the area per phospholipid would have been affected similarly between DPPC and DPPE. Since this was shown to not be the case in the Langmuir monolayer studies, the molecules of interest most likely also reside near the phospholipid head groups as found in the AOT RM experiments. The difference in interaction with DPPC

vs. DPPE was especially evident with INH and iNIC (see Figure 3.2 and Figure 3.4). The previous study by Marques *et al.* was able to determine a dissociation constant (K_d) of INH with dimyristoylphosphatidylcholine (DMPC) supported bilayers to be 0.031 μmol by plasmon waveguide resonance.[49, 51] With the observation that INH most likely prefers DPPE to DPPC, the K_d of INH with DPPE would most likely be lower than that found by Marques et al. More studies are needed to determine the exact values and whether the difference in tail length would affect the K_d.

The Langmuir monolayer studies also support the interpretation that the orientation of the amide to pyridine nitrogen affect the phospholipid interface. This result was apparent from the differences in compression isotherm area per phospholipid caused by the presence of iNIC compared to NIC and PIC. NIC and PIC affected the monolayers similarly, in contrast to iNIC that affected the monolayers differently. INIC was more similar to INH where it preferred DPPE, but iNIC did not spread the lipids like NIC and PIC did. The similar overall effects on the phospholipid monolayers by PIC and NIC were most likely caused by different molecular interactions that happen to have similar outcomes as supported by a difference in tilting at the RM interface. To summarize, the specific structural characteristics of these compounds can influence their interactions with phospholipid and surfactant interfaces in a comparable manner.

When combining the information from these two model membrane systems, a few conclusions about the placement and interactions of the molecules of interest with surfactant and phospholipid interfaces can be made. The RM experiments show that despite a similar placement of all the molecules of interest within the water-AOT interface, the orientation of the pyridine nitrogen to the amide can affect the specific orientation of the whole molecule of interest within an interface. This tilt of PIC and NIC suggests that within other interfaces, such as a phospholipid interface, the small difference between these molecules can allow for differences in the interactions with a phospholipid monolayer. Although, those interactions will likely not be the same as determined from the RM experiments.[21] The phospholipid Langmuir monolayer studies build on this idea by also supporting the expectation that the specifics behind

the interactions of the head group of the phospholipid with the molecule of interest can affect binding such as what was observed with INH and iNIC. To summarize, the hypothesis that small differences in structure can lead to differences in the interactions of these small molecules with membrane interfaces, was supported by these observations.

Although this study focused exclusively on monolayers, the observations gathered can cautiously be used to provide some projections about how these molecules might pass through a bilayer membrane. With each molecule studied here, they all resided within the water-AOT RM interface and interacted differently with phospholipids containing the same tail but different head groups. Together, these observations would support a head group based interaction of the drugs in contrast to interactions with the choline, phosphate, or glycerol of phospholipids. Therefore these compounds may not passively diffuse through a bilayer membrane like weak acid preservatives (ex. benzoic acid and formic acid) or protonophores (ex. carbonyl cyanide m-chlorophenyl hydrazine).[8, 10, 23] If the molecules are able to traverse a membrane by passive diffusion, then it would be expected that the molecules would reside deeper within the RM tails/organic solvent.[23] The data obtained in this study does not support passive transport of these small aromatic compounds.

Other methods for crossing a bilayer has been extensively studied using different cations and anions. In these method, cations or anions are transported through forming a complex with phospholipids and then flip with the phospholipid across the bilayer, or through a hydrophobic pore that may form allowing traversing of ions.[52-56] Some of these mechanisms have been studied through computational studies, and Borba et al. was able to show that the binding of PIC and NIC to the phosphatidylcholine or phosphatidylethanolamine head groups can cause con-formational differences in the phospholipid tails.[22] Considering that all of the molecules within this study inter-acted with the headgroups of AOT and the phospholipids, it is feasible that at least some of these molecules may affect the phospholipid tails as well. If these molecules affect the phospholipid tails then such interaction might aid in the crossing of the drugs

across the phospholipid bilayer. Additional studies are needed to determine if these small molecules passively diffuse across bilayers, but these studies provide the framework to build a more in depth understanding of small molecule interactions with membrane interfaces.

3.4   Summary and Conclusions

We found that the interactions of INH, BHZ, BA, PIC, NIC, and iNIC, all interact with phospholipid and surfactant interfaces with the phospholipid/surfactant head groups, but have different effects on phospholipid interfaces. The phospholipid Langmuir monolayer studies show a difference in interaction of the small molecules that were not only dependent on the structure of the small molecules but also the phospholipids themselves. All the molecules tested reside within the water AOT surfactant interface of RMs with the amide/hydrazide facing toward the water pool except of NIC and PIC. NIC and PIC resided at the interface but were tilted with the amide of NIC facing more away from the water pool than the amide of PIC. In summary, we show here that interactions of small aromatic molecules with lipid surfactant interfaces are not straight forward and that structural changes of the small aromatic compounds can alter their affinity for different phospholipid interfaces, how they affect different phospholipid interfaces, and the specifics behind the interactions with these interfaces.[57]

References

(1)   Azuma, K.; Ouchi, Y.; Inoue, S. Vitamin K: Novel Molecular Mechanisms of Action and Its Roles in Osteoporosis. *Geriatr Gerontol Int.* **2014,** *14* (1), 1-7.

(2)   Lambert, R. J.; Stratford, M. Weak-Acid Preservatives: Modelling Microbial Inhibition and Response. *J. Appl. Microbiol.* **1999,** *86* (1), 157-164.

(3)   Ullah, A.; Orij, R.; Brul, S.; Smits, G. J. Quantitative Analysis of the Modes of Growth Inhibition by Weak Organic Acids in Saccharomyces Cerevisiae. *Appl. Environ. Microbiol.* **2012,** *78* (23), 8377-8387.

(4)   Westfall, D. A.; Krishnamoorthy, G.; Wolloscheck, D.; Sarkar, R.; Zgurskaya, H. I.; Rybenkov, V. V. Bifurcation Kinetics of Drug Uptake by Gram-Negative Bacteria. *PLoS One.* **2017,** *12* (9), 1-18.

(5)   Zhang, Y.; Wade, M. M.; Scorpio, A.; Zhang, H.; Sun, Z. H. Mode of Action of Pyrazinamide: Disruption of Mycobacterium Tuberculosis Membrane Transport and Energetics by Pyrazinoic Acid. *J. Antimicrob. Chemother.* **2003,** *52* (5), 790-795.

(6)   Bardou, F.; Raynaud, C.; Ramos, C.; Laneelle, M. A.; Laneelle, G. Mechanism of Isoniazid Uptake in Mycobacterium Tuberculosis. *Microbiology-Uk.* **1998,** *144*, 2539-2544.

(7)   Unissa, A. N.; Subbian, S.; Hanna, L. E.; Selvakumar, N. Overview on Mechanisms of Isoniazid Action and Resistance in Mycobacterium Tuberculosis. *Infect., Genet. Evol.* **2016,** *45*, 474-492.

(8)   Finkelst.A Weak-Acid Uncouplers of Oxidative Phosphorylation - Mechanism of Action on Thin Lipid Membranes. *Biochim. Biophys. Acta.* **1970,** *205* (1), 1-6.

(9)   Olsson, A.; Olofsson, T.; Pero, R. W. Specific Binding and Uptake of Extracellular Nicotinamide in Human Leukemic K-562 Cells. *Biochem. Pharmacol.* **1993,** *45* (6), 1191-1200.

(10)   Piper, P.; Mahe, Y.; Thompson, S.; Pandjaitan, R.; Holyoak, C.; Egner, R.; Muhlbauer, M.; Coote, P.; Kuchler, K. The Pdr12 ABC Transporter Is Required for the Development of Weak Organic Acid Resistance in Yeast. *EMBO J.* **1998,** *17* (15), 4257-4265.

(11)   Silve, A.; Mir, L. M., *Cell Electropermeabilization and Cellular Uptake of Small Molecules: The Electrochemotherapy Concept*. **2011**; p 69-82.

(12)   Wilson, D. F.; Ting, H. P.; S., K. M. Mechanism of Action of Uncouplers of Oxidative Phosphorylation. *Biochemistry.* **1971,** *10* (15), 2897-2902.

(13)   Ivanova, N.; Ivanova, A. Testing the Limits of Model Membrane Simulationsbilayer Composition and Pressure Scaling. *J. Comput. Chem.* **2018,** *39* (8), 387-396.

(14)   Singer, S. J.; Nicolson, G. L. The Fluid Mosaic Model of the Structure of Cell Membranes. *Science.* **1972,** *175* (4023), 720-731.

(15)   van Meer, G.; Voelker, D. R.; Feigenson, G. W. Membrane Lipids: Where They Are and How They Behave. *Nat. Rev. Mol. Cell Biol.* **2008,** *9* (2), 112-124.

(16)   Alvarez, R.; Aramburu, L.; Puebla, P.; Caballero, E.; Gonzalez, M.; Vicente, A.; Medarde, M.; Pelaez, R. Pyridine Based Antitumour Compounds Acting at the Colchicine Site. *Curr. Med. Chem.* **2016,** *23* (11), 1100-1130.

(17)   Nayyar, A.; Jain, R. Recent Advances in New Structural Classes of Anti-Tuberculosis Agents. *Curr. Med. Chem.* **2005,** *12* (16), 1873-1886.

(18)   Prachayasittikul, S.; Pingaew, R.; Worachartcheewan, A.; Sinthupoom, N.; Prachayasittikul, V.; Ruchirawat, S.; Prachayasittikul, V. Roles of Pyridine and Pyrimidine Derivatives as Privileged Scaffolds in Anticancer Agents. *Mini-Rev. Med. Chem.* **2017,** *17* (10), 869-901.

(19)   Borba, A.; Albrecht, M.; Gomez-Zavaglia, A.; Lapinski, L.; Nowak, M. J.; Suhm, M. A.; Fausto, R. Dimer Formation in Nicotinamide and Picolinamide in the Gas and Condensed Phases Probed by Infrared Spectroscopy. *PCCP.* **2008,** *10* (46), 7010-7021.

(20)   Borba, A.; Gomez-Zavaglia, A.; Fausto, R. Molecular Structure, Vibrational Spectra, Quantum Chemical Calculations and Photochemistry of Picolinamide and Isonicotinamide Isolated in Cryogenic Inert Matrixes and in the Neat Low-Temperature Solid Phases. *J. Phys. Chem. A.* **2008,** *112* (1), 45-57.

(21)   Martini, M. F.; Disalvo, E. A.; Pickholz, M. Nicotinamide and Picolinamide in Phospholipid Monolayers. *Int. J. Quantum Chem.* **2012,** *112* (20), 3289-3295.

(22)   Borba, A.; Lairion, F.; Disalvo, A.; Fausto, R. Interaction of Nicotinamide and Picolinamide with Phosphatidylcholine and Phosphatidylethanolamine Membranes: A Combined Approach Using Dipole Potential Measurements and Quantum Chemical Calculations. *Biochim. Biophys. Acta, Biomembr.* **2009,** *1788* (12), 2553-2562.

(23)   Peters, B. J.; Groninger, A. S.; Fontes, F. L.; Crick, D. C.; Crans, D. C. Differences in Interactions of Benzoic Acid and Benzoate with Interfaces. *Langmuir.* **2016,** *32* (37), 9451-9459.

(24)   Nowotarska, S. W.; Nowotarski, K. J.; Friedman, M.; Situ, C. Effect of Structure on the Interactions between Five Natural Antimicrobial Compounds and Phospholipids of Bacterial Cell Membrane on Model Monolayers. *Molecules.* **2014,** *19* (6), 7497-7515.

(25)   Veldhuizen, E. J. A.; Haagsman, H. P. Role of Pulmonary Surfactant Components in Surface Film Formation and Dynamics. *Biochim. Biophys. Acta, Biomembr.* **2000,** *1467* (2), 255-270.

(26)   Veldhuizen, R.; Nag, K.; Orgeig, S.; Possmayer, F. The Role of Lipids in Pulmonary Surfactant. *Biochim. Biophys. Acta, Mol. Basis Dis.* **1998,** *1408* (2-3), 90-108.

(27)   Wustneck, R.; Perez-Gil, J.; Wustneck, N.; Cruz, A.; Fainerman, V. B.; Pison, U. Interfacial Properties of Pulmonary Surfactant Layers. *Adv. Colloid Interface Sci.* **2005,** *117* (1-3), 33-58.

(28)   Leekumjorn, S.; Sum, A. K. Molecular Simulation Study of Structural and Dynamic Properties of Mixed DPPC/DPPE Bilayers. *Biophys. J.* **2006,** *90* (11), 3951-3965.

(29)   Leekumjorn, S.; Sum, A. K. Molecular Investigation of the Interactions of Trehalose with Lipid Bilayers of DPPC, DPPE and Their Mixture. *Mol. Simul.* **2006,** *32* (3-4), 219-230.

(30)   Choi, Y.; Attwood, S. J.; Hoopes, M. I.; Drolle, E.; Karttunen, M.; Leonenko, Z. Melatonin Directly Interacts with Cholesterol and Alleviates Cholesterol Effects in Dipalmitoylphosphatidylcholine Monolayers. *Soft Matter.* **2014,** *10* (1), 206-213.

(31)   Wang, Z. N.; Yang, S. H. Effects of Fullerenes on Phospholipid Membranes: A Langmuir Monolayer Study. *Chemphyschem.* **2009,** *10* (13), 2284-2289.

(32)   Jones, M. N., *Micelles, Monolayers, and Biomembranes*. New York : Wiley-Liss: New York, **1995**.

(33)   Crans, D. C.; Peters, B. J.; Wu, X.; McLauchlan, C. C. Does Anion-Cation Organization in Na$^+$-Containing X-Ray Crystal Structures Relate to Solution Interactions in Inhomogeneous Nanoscale Environments: Sodium-Decavanadate in Solid State Materials, Minerals, and Microemulsions. *Coord. Chem. Rev.* **2017,** *344*, 115-130.

(34)   Crans, D. C.; Trujillo, A. M.; Bonetti, S.; Rithner, C. D.; Baruah, B.; Levinger, N. E. Penetration of Negatively Charged Lipid Interfaces by the Doubly Deprotonated Dipicolinate. *J. Org. Chem.* **2008,** *73* (24), 9633-9640.

(35)   Crans, D. C.; Trujillo, A. M.; Pharazyn, P. S.; Cohen, M. D. How Environment Affects Drug Activity: Localization, Compartmentalization and Reactions of a Vanadium Insulin-Enhancing Compound, Dipicolinatooxovanadium(V). *Coord. Chem. Rev.* **2011,** *255* (19-20), 2178-2192.

(36)   Koehn, J. T.; Magallanes, E. S.; Peters, B. J.; Beuning, C. N.; Haase, A. A.; Zhu, M. J.; Rithner, C. D.; Crick, D. C.; Crans, D. C. A Synthetic Isoprenoid Lipoquinone, Menaquinone-2, Adopts a Folded Conformation in Solution and at a Model Membrane Interface. *J. Org. Chem.* **2018,** *83* (1), 275-288.

(37) Samart, N.; Beuning, C. N.; Haller, K. J.; Rithner, C. D.; Crans, D. C. Interaction of a Biguanide Compound with Membrane Model Interface Systems: Probing the Properties of Antimalaria and Antidiabetic Compounds. *Langmuir.* **2014,** *30* (29), 8697-8706.

(38) Vermathen, M.; Stiles, P.; Bachofer, S. J.; Simonis, U. Investigations of Monofluoro-Substituted Benzoates at the Tetradecyltrimethylammonium Micellar Interface. *Langmuir.* **2002,** *18* (4), 1030-1042.

(39) Crans, D. C.; Rithner, C. D.; Baruah, B.; Gourley, B. L.; Levinger, N. E. Molecular Probe Location in Reverse Micelles Determined by Nmr Dipolar Interactions. *J. Am. Chem. Soc.* **2006,** *128* (13), 4437-4445.

(40) Baruah, B.; Roden, J. M.; Sedgwick, M.; Correa, N. M.; Crans, D. C.; Levinger, N. E. When Is Water Not Water? Exploring Water Confined in Large Reverse Micelles Using a Highly Charged Inorganic Molecular Probe. *J. Am. Chem. Soc.* **2006,** *128* (39), 12758-12765.

(41) Majumder, R.; Sarkar, Y.; Das, S.; Ray, A.; Parui, P. P. Interfacial Ph and Polarity Detection of Amphiphilic Self-Assemblies Using a Single Schiff-Base Molecule. *New J. Chem.* **2017,** *41* (16), 8536-8545.

(42) Crans, D. C.; Levinger, N. E. The Conundrum of pH in Water Nanodroplets: Sensing pH in Reverse Micelle Water Pools. *Acc. Chem. Res.* **2012,** *45* (10), 1637-1645.

(43) Moran, L.; Scrimgeour, K.; Horton, H.; Ochs, R.; Rawn, J., *Biochemistry*. 2 ed.; Neil Patterson: **1994**.

(44) Perrin, D. D.; International Union of, P.; Applied Chemistry. Commission on Electrochemical, D., *Dissociation Constants of Organic Bases in Aqueous Solution*. Butterworths: London :, **1965**.

(45) De, T. K.; Maitra, A. Solution Behavior of Aerosol OT in Nonpolar-Solvents. *Adv. Colloid Interface Sci.* **1995,** *59*, 95-193.

(46) Eicke, H. F.; Rehak, J. Formation of Water-Oil-Microemulsions. *Helv. Chim. Acta.* **1976,** *59* (8), 2883-2891.

(47) Sohlenkamp, C.; Geiger, O. Bacterial Membrane Lipids: Diversity in Structures and Pathways. *FEMS Microbiol. Rev.* **2016,** *40* (1), 133-159.

(48) Maitra, A. Determination of Size Parameters of Water Aerosol OT Oil Reverse Micelles from Their Nuclear Magnetic-Resonance Data. *J. Phys. Chem.* **1984,** *88* (21), 5122-5125.

(49) Marques, A. V.; Trindade, P. M.; Marques, S.; Brum, T.; Harte, E.; Rodrigues, M. O.; D'Oca, M. G. M.; da Silva, P. A.; Pohlmann, A. R.; Alves, I. D.; de Lima, V. R. Isoniazid Interaction with Phosphatidylcholine-Based Membranes. *J. Mol. Struct.* **2013,** *1051*, 237-243.

(50) Rodrigues, C.; Gameiro, P.; Prieto, M.; de Castro, B. Interaction of Rifampicin and Isoniazid with Large Unilamellar Liposomes: Spectroscopic Location Studies. *Biochim. Biophys. Acta, Gen. Subj.* **2003,** *1620* (1-3), 151-159.

(51) Tollin, G.; Salamon, Z.; Hruby, V. J. Techniques: Plasmon-Waveguide Resonance (PWR) Spectroscopy as a Tool to Study Ligand-Gpcr Interactions. *Trends Pharmacol. Sci.* **2003,** *24* (12), 655-659.

(52) Contreras, F. X.; Sánchez-Magraner, L.; Alonso, A.; Goñi, F. M. Transbilayer (Flip-Flop) Lipid Motion and Lipid Scrambling in Membranes. *FEBS Lett.* **2010,** *584* (9), 1779-1786.

(53) Gurtovenko, A. A.; Vattulainen, I. Molecular Mechanism for Lipid Flip-Flops. *J. Phys. Chem. B.* **2007,** *111* (48), 13554-13559.

(54) Henseleit, U.; Plasa, G.; Haest, C. Effects of Divalent-Cations on Lipid Flip-Flop in the Human Erythrocyte-Membrane. *Biochim. Biophys. Acta.* **1990,** *1029* (1), 127-135.

(55) Kandasamy, S. K.; Larson, R. G. Cation and Anion Transport through Hydrophilic Pores in Lipid Bilayers. *J. Chem. Phys.* **2006,** *125* (7), 07491.

(56) Smeets, E. F.; Comfurius, P.; Bevers, E. M.; Zwaal, R. F. A. Calcium-Induced Transbilayer Scrambling of Fluorescent Phospholipid Analogs in Platelets and Erythrocytes. *Biochim. Biophys. Acta, Biomembr.* **1994,** *1195* (2), 281-286.

(57)   Peters, B. J.; Van Cleave, C.; Haase, A. A.; Hough, J. P. B.; Giffen-Kent, K. A.; Cardiff, G. M.; Sostarecz, A. G.; Crick, D. C.; Crans, D. C. Structure Dependence of Pyridine and Benzene Derivatives on Interactions with Model Membranes. *Langmuir.* **2018**.

Chapter 4: Membrane Phospholipid Density and Its Effects on Electron Transporters

4.1   Electron Transport and Quinones

Quinones have vital roles in biological systems, and of those roles, the most recognized is them as proton and electron carriers of electron transport systems.[1-7] As shown in Figure 4.1, three of the most commonly discussed quinones are ubiquinone (UBQ), menaquinone (MK), and plastoquinone (PQ). Despite structural differences in electron transport systems and between these three quinones, they all are commonly illustrated as moving through the bilayer in a cyclic motion (Figure 4.1).[1, 6]

(A) Schematic of Mitochondrial Inner-Membrane Electron Transport System Q-Loop

(B) Schematic of *Mycobaterium Tuberculosis* Electron Transport System Q-Loop

(C) Schematic of Chloroplast Electron Transport System Q-Loop

Ubiquinone (UBQ)   Menaquinone (MK)   Plastoquinone (PQ)
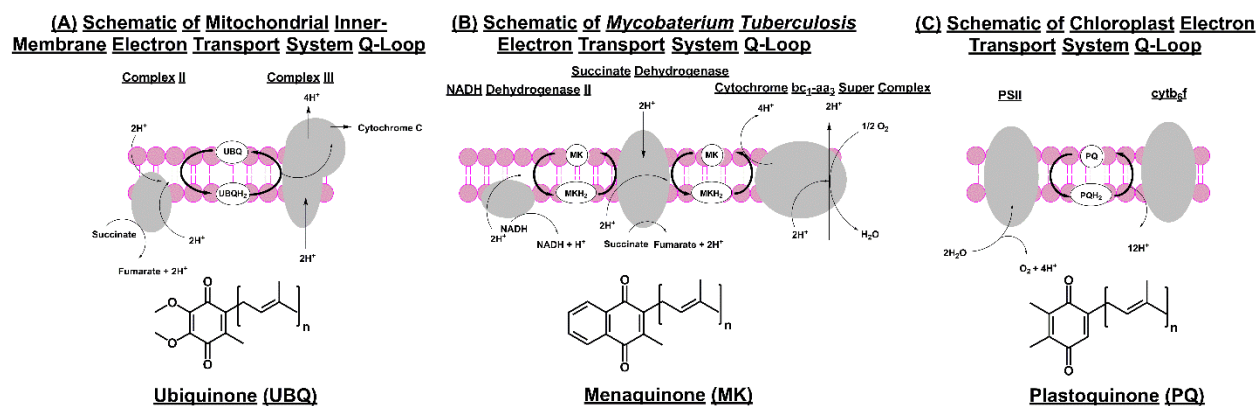
Figure 4.1. Partial schematic of electron transport systems of mitochondria (A), gram positive bacteria with menaquinone (B), and of the chloroplast (C) outlining the importance of each specific quinone within each system. This Figure was adapted from Kurosu *et al.* and Rochaix.[1, 6]

For this cyclic motion to occur, quinones are either highly mobile through the membrane, or the translocation is facilitated by proteins. Considering the high hydrophobicity of the quinones, it is likely that they are mobile through the lipid bilayer and therefore, their interactions with lipids have been explored in detail.[4-5, 7-19] Quinn et al. and Hoyo *et al.* have both shown using Langmuir monolayer techniques that UBQ and PQ both interact similarly with phospholipid interfaces.[13, 18] The tail length was found to affect the collapse pressure of monolayers formed using UBQ of varying isoprene tail lengths (1-

10 isoprenes), which was attributed to aggregation of UBQ.[13, 18] These studies were also able to show that at higher pressures (>15 mN/m) of mixed phospholipid monolayers with UBQ or PQ, both quinones are compressed out of the monolayer into the tails of the phospholipids.[11-13, 18] This finding is consistent with a computational study by Kaurola *et al.* where UBQ was found to be able to traverse the bilayer but prefer to reside within the hydrophobic region of the bilayer.[16] Despite the detailed knowledge of the interactions of UBQ and PQ with phospholipid interfaces, there have been few studies that explore the interactions of MK with phospholipid interfaces.[20-21]

Unlike UBQ and PQ, MK analogs are more commonly thought of as being a part of the vitamin K family of compounds.[1, 22] Additionally to being used for vitamins, MK has an important role in the electron transport system of *Mycobacterium tuberculosis,* with the main electron transporter being MK-9 (H2), or menaquinone with nine isoprene units and a saturation at the β isoprene position (second isoprene from the quinone).[1] MK-9 contains a more hydrophobic headgroup than the other quinone electron transporters mentioned in Figure 4.1, but the majority of the structure (isoprenoid tail) is very similar with only the length and saturation of the isoprenoid tail being varied.[1, 4, 6] Considering the similar structures and depictions within biological systems, here we hypothesize that MK-9 (without β isoprene saturation) interacts with phospholipids in a similar manner as UBQ and PQ with phospholipid interfaces.[3, 6, 16] Specifically, MK-9 will interact with a phospholipid interface in a pressure dependent manner.[3, 6, 16]

Previously, Langmuir monolayers have been used to explore the interactions between lipids, quinones, hydrophilic molecules with lipids, and proteins with lipids.[8, 11-13, 18, 23-27] Specifically, compression isotherm experiments of Langmuir monolayers of mixed lipids can give information about the specific interactions between the components of the monolayer.[8, 11-13, 18, 23] In this study, the interactions of the electron transporter, MK-9, with the phospholipids dipalmitoylphosphatidylcholine (DPPC) and dipalmitoylphosphatidylethanolamine (DPPE) were examined using Langmuir monolayer techniques to determine if MK-9 interacts with phospholipid interfaces in a similar manner as the other electron

transporters shown in Figure 4.1. In conjunction with Brewster angle microscopy (BAM), a visualization of the monolayer allowing for observations of morphological differences can elucidate how the MK-9 interacts with the phospholipids. Using compression isotherms of Langmuir monolayers of MK-9, phospholipids, mixed monolayers, and BAM this study aims to describe the interactions between MK-9 and common phospholipids found biological membranes.

4.2   Materials and Methods

4.2.1   Materials

The following chemicals were used without further purification. DPPC (>99%) and DPPE (99%) were purchased from Avanti Polar Lipids. MK-9 (≥98%) was purchased Santa Cruz Biotechnology. Chloroform (≥99.5%), methanol (≥99.9%), monosodium phosphate (≥99.0%), and disodium phosphate (≥99.0%), were all purchased from Sigma Aldrich.

4.2.2   Preparation of Langmuir Monolayers

Phospholipid stock solutions were prepared by dissolving 18 mg (0.025 mmol) DPPC or 17 mg (0.025 mmol) DPPE into 25 mL of 9:1 chloroform:methanol (v:v) for a final concentration of 1 mM. The stock solution of MK-9 was prepared by dissolving 3.9 mg of MK-9 (0.005 mmol) into 5 mL of 9:1 chloroform:methanol (v:v) for a final concentration of 1 mM MK-9. The subphase for the monolayers for compression isotherm experiments consisted of 50 mL of 20 mM sodium phosphate buffer (pH 7.4). Before addition of the stock solution to the subphase, the subphase was cleaned using aspiration and with the barriers near the center of the trough. After aspirating the subphase surface, the barriers were spread and the cleanliness of the subphase surface was determined by conducting a compression isotherm experiment without MK-9 or phospholipid present. By cleaning the subphase with the barriers close to the center of the trough, the reproducibility of the compression isotherm measurements was greatly increased. The subphase was considered clean when the surface pressure was consistently 0.0 +/- 0.5 mN/m throughout compression without lipid present. To form the pure monolayers of phospholipid or

MK-9, 20 μL of stock solution (20 nmol) was added to the subphase (112 Å^2/molecule) in a dropwise

manner using a 50 μL Hamilton Syringe. To prepare the mixed monolayers of MK analog and phospholipid,

specific volumes MK analog and phospholipid from the stock solutions were mixed to prepare solutions

containing 25:75, 50:50, and 75:25 mole fractions of MK-9 to phospholipid. Then 20 μL (20 nmol) of the

mixed solutions were added to the subphase in a similar manner as the pure monolayers. Once the pure

solutions or mixed solutions were added to the subphase, the applied solution was then allowed to

equilibrate for 15 minutes to allow for solvent evaporation and spreading of the phospholipids and MK-9.

4.2.3 Surface Pressure Compression Isotherms of Pure and Mixed Monolayers

Once the monolayers were prepared, they were compressed from 2 sides at a total rate of 10 mm/min

(5 mm/min from each side) using a Kibron μTroughXS equipped with a Teflon ribbon (hydrophobic

barriers). The temperature of the subphase was kept constant at 25 °C using an external water bath.

During each compression, the surface tension was monitored using the Wilhemy plate method where a

wire probe was used as the Wilhemy plate. The surface pressure was calculated from the surface tension

using Equation 4.1 where π is the surface pressure, γ_0 is the surface tension of water without monolayer

present (72.8 mN/m), and γ is the surface tension of water with monolayer present.

$$\pi = \gamma_o - \gamma \qquad (4.1)$$

4.2.4 Analysis of the Surface Pressure Compression Isotherms

The compression isotherms were conducted in triplicate and averaged with standard deviations of

the area per molecule (phospholipid and MK-9) every 5 mN/m. Using the compression isotherm curves,

the ideal area was determined using equation 4.2 where A_i is the ideal area, x_{MK} is the mole fraction of MK

analog, x_{PL} is the mole fraction of phospholipid, A_{MK} is the area per molecule of the pure MK-9 monolayer

at a specific surface pressure, A_{PL} is the area per molecule of the pure phospholipid monolayer at a given

surface pressure.[28-29] The ideal area curves were then compared to the actual data by calculating a percent

difference of the area per molecule at specific surface pressures.

$$A_I = x_{MK}A_{MK} + x_{PL}A_{PL} \qquad (4.2)$$

The area per molecule of the mixed monolayers compression isotherm curves were then normalized to the amount of phospholipid present within each monolayer (area per molecule excluding MK-9) as has been previously reported.[18, 24, 30] The compression moduli were calculated from the average compression isotherm curves using Equation 4.3 where C_s^{-1} is the compression modulus, A is the area per molecule, and π is the surface pressure.[18, 23, 25] The data were analyzed using OriginPro Version 9.1.

$$C_s^{-1} = -A\left(\frac{d\pi}{dA}\right) \qquad (4.3)$$

4.2.5 Brewster Angle Microscopy (BAM) of Pure and Mixed Langmuir Monolayers

BAM experiments were conducted using a Biolin Scientific (NIMA) medium sized Langmuir Blodgett trough (364 cm x 75 cm) equipped with a MicroBAM (resolution of 12 µm) and delrin bariers (hydrophilic). The MicroBAM was equipped with a 30 mW laser emitting 659 nm laser light that was p-polarized. The subphase consisted of ~200 µL of 20 mM sodium phosphate buffer (pH 7.4). The surface of the subphase was cleaned in the same manner as with the compression isotherm experiments (section 4.2.2). The pure and mixed lipid solutions were prepared in the same manner as for the compression isotherm experiments. The amount of pure and mixed lipid solution added to the surface of the subphase varied between 40 and 100 µL (40-100 nmol) to ensure full compression of the monolayer. Once the lipid solutions were added to the surface of the subphase, they were allowed to equilibrate for 15 minutes before compression at a total rate of 10 mm/min from two sides (5 mm/min from opposite sides). During compression, the surface pressure was monitored using the Wilhemy plate method with a platinum plate as the Wilhemy plate. Beginning at a surface pressure of 1 mN/m, BAM images were collected every second until end of compression (collapse of monolayer or end of trough). These experiments were conducted in triplicate to ensure the observations of the monolayer morphologies were consistent at specific surface pressures. The images presented here are for 10 mN/m, 20 mN/m and 30 mN/m of the pure phospholipid and mixed monolayers. In appendix VII (DPPC) and VIII (DPPE, Figures A7.1 and 8.1

respectively), the images for the surface pressures ranging from 10 mN/m to 40 mN/m are given every 2.5 mN/m. Given in appendix VI are images of a time dependent equilibration of an MK-9 monolayer after compression (Figure A6.1).

4.3   Results and Discussion

4.3.1   Compression Isotherms of Pure and Mixed Monolayers of MK-9 and Phospholipids

Compression isotherms of pure and mixed monolayers of MK-9, DPPC, and DPPE were conducted to probe for interactions between the MK-9 and common phospholipids (Figure 4.2). The DPPC compression isotherm curve exhibits the characteristic gas-liquid phase transition at 4 mN/m and a collapse pressure at 45 mN/m similar to findings in literature.[20-21, 25-26, 31-32] The DPPE compression isotherm collapses at 45 mN/m and the curve is similar to reported findings.[30, 33] The MK-9 compression isotherm curve exhibits a collapse at 9.5 mN/m which is similar to the low collapse pressures of UBQ, PQ, and vitamin K_1 under inert atmosphere.[11-13, 18, 20, 31, 34] The low collapse pressure is likely due to the limited hydrogen bonding capacity of MK-9 and therefore it has limited interactions with the water interface. This would limit the observed surface activity of MK-9. The large isoprenoid tail could also allow for aggregation as was observed with ubiquinone limiting interactions with the water surface.[13, 18]
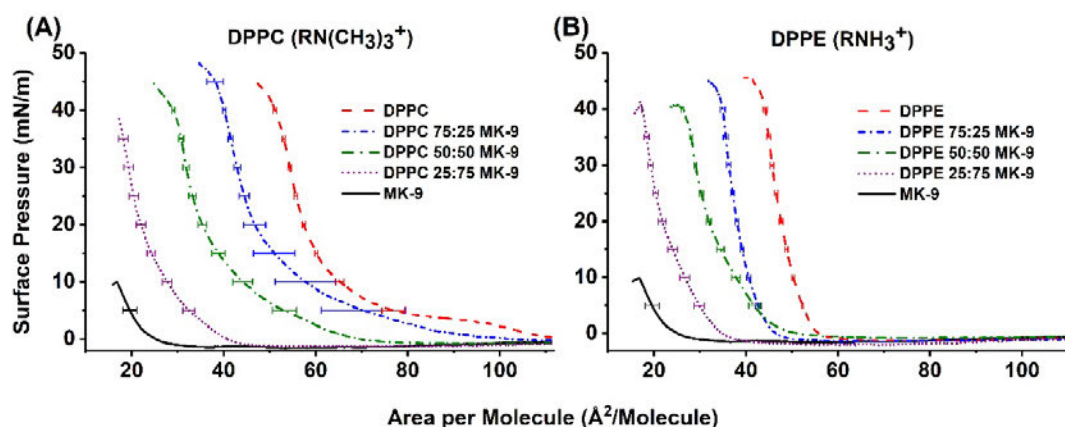
Figure 4.2. Compression isotherms of mixed and pure monolayers of MK-9 and DPPC (A) or DPPE (B). The compression isotherm curves correspond to the pure MK-9 monolayer (solid black line), 75:25 MK-9: phospholipid monolayer (dotted purple line), 50:50 MK-9:phospholipid monolayer (dashed and dotted green line), 25:75 MK-9:phospholipid monolayer (short dash and dot blue line), and the pure phospholipid monolayer (dashed red line). The ratios correspond to mole fractions of MK-9 to phospholipid of the monolayers.

When mixing MK-9 with DPPC or DPPE, some alterations of the compression isotherm curves from the pure phospholipid compression isotherm curves can be observed in Figure 4.2. The gas-liquid phase transition of the DPPC compression isotherm curve is not present in the mixed monolayers (present at 4 mN/m for DPPC monolayer). The lack of this phase transition, is consistent with either MK-9 disordering the DPPC phospholipids causing a prevention of a phase transition or having a condensing effect on the DPPC thus the DPPC would begin the compression in the liquid phase.[32, 35] For the DPPE and MK-9 mixed monolayers, the compression isotherm curves exhibit a decrease in slope of the curves below 15 mN/m from the DPPE control monolayer curve. This difference is consistent the presence of MK-9 spreading the DPPE phospholipids more so than observed in the pure DPPE monolayer. Further analysis of the slope of the DPPE curves is provided in the compression modulus section (section 4.3.4). Above 15-20 mN/m, the mixed monolayers of MK-9 and either phospholipid decreases in area per molecule by what seems to be a fixed amount as the MK-9 content is increased and an analysis of this phenomenon is conducted in section 4.3.3. This trend is similar to observations by Quinn *et al*. with UBQ.[18] In summary, the presence

of MK-9 prevents the gas-liquid phase transition of DPPC, the DPPE curves seem to have a decrease in slope, and the area per molecule of the mixed monolayer curves decrease in fixed intervals according to the MK-9 composition.

4.3.2 Ideal Area vs. Actual Area Comparison

To determine if MK-9 and DPPC or DPPE are interacting in a way that is causing a condensing or expanding effect, the ideal curves were calculated and compared to the experimental compression isotherm curves. Due to the low collapse pressure of MK-9, the ideal curves do not go above 9.5 mN/m as shown in Figure 4.3.
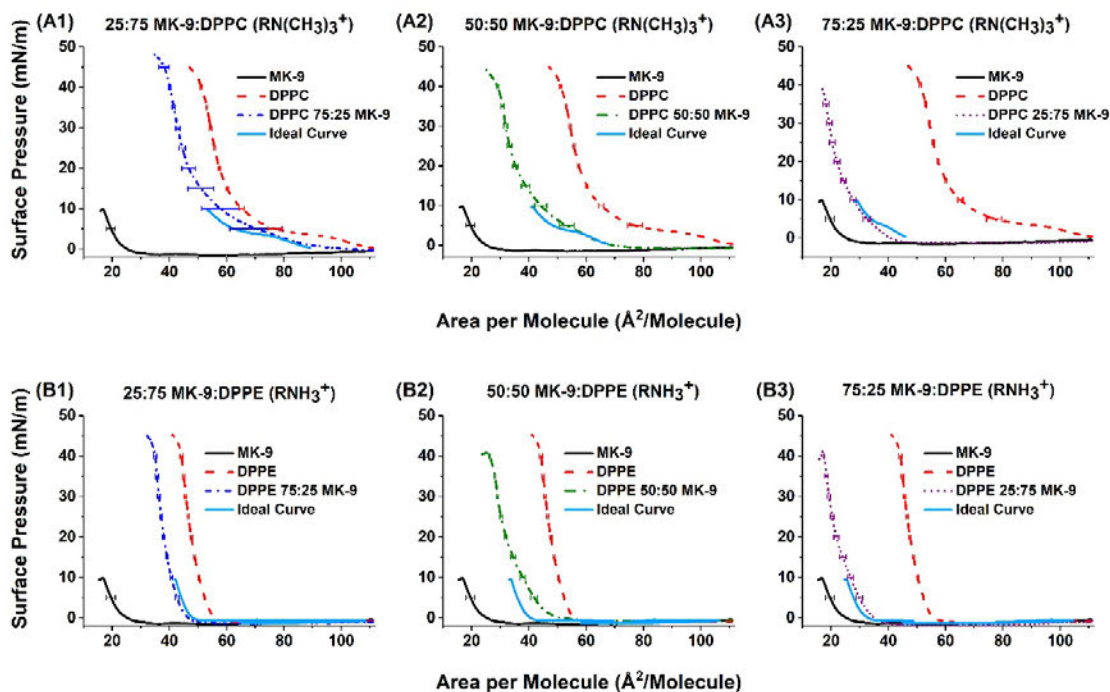
Figure 4.3. Compression isotherms of pure monolayers of MK-9 and DPPC (A), DPPE (B), or the ideal area curve (solid light blue line). The compression isotherm curves correspond to the pure MK-9 monolayer (solid black line), 25:75 MK-9:phospholipid monolayer (1, short dash and dot blue line), 50:50 MK-9:phospholipid monolayer (2, dashed and dotted green line), 75:25 MK-9: phospholipid monolayer (3, dotted purple line), and the pure phospholipid monolayer (dashed red line). The ratios correspond to mole fractions of MK-9 to phospholipid of the monolayers.

As shown in Figure 4.3 (A1-3), the MK-9 and DPPC compression isotherms exhibit varying condensing or expanding effects from ideality. The 25% and 50% MK-9 (25:75 and 50:50 MK-9:DPPC, mole fractions)

85

monolayers may exhibit an increase in area per molecule above 4 mN/m while the 75% MK-9 monolayer exhibited a decrease in area per molecule below 4 mN/m. The possible expansion effects of the monolayers consisting of 25% or 50% MK-9 are likely due to DPPC spreading the MK-9 molecules more, inhibiting as much aggregation as when the monolayer consists of pure MK-9 (See Figures 4.7 and A6.1). This interpretation is made with hesitation as the deviations of the data are very close to the ideal area curve. The spreading of DPPC is not likely as DPPC spreads very well across the aqueous interface and therefore it would be difficult to spread the DPPC further.[36-37] The condensing effect of the 75% MK-9 monolayer from ideality below 4 mN/m is likely due to the phase transition within the ideal curve. This observation would be consistent with MK-9 preventing the gas-liquid phase transition of DPPC at 4 mN/m. As shown in Figure 4.4, the percent difference from the ideal area of each curve exhibits an increase at 4 mN/m suggesting that all MK-9 mole fractions tested prevent or reduce the gas-liquid phase transition of DPPC. These observations are consistent with MK-9 reorganizing the DPPC tails, and DPPC possibly preventing aggregation of the MK-9.
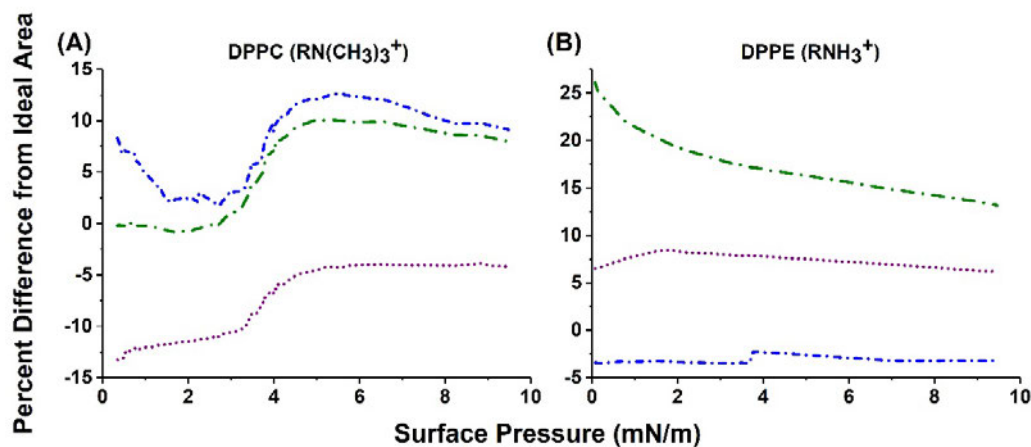
Figure 4.4. The percent difference of area per molecule from the ideal curve at specific surface pressure of the mixed monolayers of MK-9 and DPPC (C) or DPPE (B). The graphs depict the percent difference in area of the 75:25 MK-9:phospholipid (dotted purple line), 50:50 MK-9:phospholipid(dashed and dotted green line), or 25:75 MK9:phospholipid (small dashed and dotted blue line)

The mixed monolayers of MK-9 and DPPE also had variable expansion or condensing effects from the ideal curves. The 25% MK-9 monolayer exhibited a slight increase in area per molecule, the 50% MK-9

monolayer exhibited a large increase in area per molecule, and the 75% MK-9 monolayer exhibited a slight decrease in area per molecule from the ideal curves (Figures 4.3 and 4.4). The increase in area at 50% or less MK-9 mixed monolayers is likely due to the presence of the MK-9 disrupting the packing of the DPPE. The 75% MK-9 monolayer exhibited a small decrease in area per molecule which is likely caused by the small amount of DPPE causing a greater amount of packing for the MK-9 than just MK-9 by itself. The 25% MK-9 curve is very close to ideality suggesting limited interaction between DPPE and MK-9.

4.3.3   Normalization to Phospholipid Content

Due to the collapse pressure of the MK-9 monolayer compression isotherm, the ideal area calculations were unable to give information about the interactions of MK-9 and the phospholipids above 9.5 mN/m. Therefore, more information about the interactions of MK-9 with phospholipids was sought by normalizing each monolayer to the phospholipid content as shown in Figure 4.5.[18] In this instance, normalizing the compression isotherms to the phospholipid content is simply ignoring the MK-9 content of the monolayers for the area per molecule calculations (area per phospholipid in Figure 4.5).
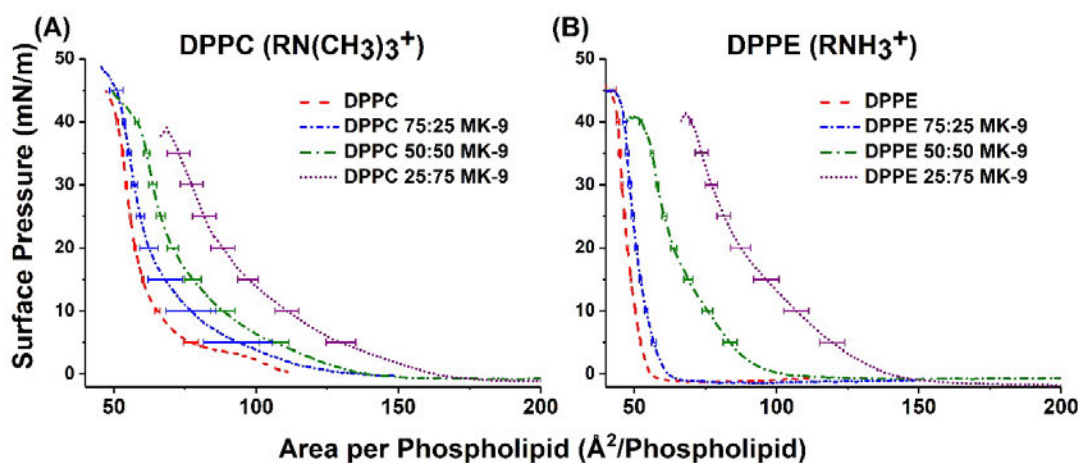
Figure 4.5. Compression isotherms of pure monolayers of MK-9 and DPPC (A) or DPPE (B) normalized to the phospholipid content. These curves ignore the presence of MK-9 for the calculation of the area per molecule. The compression isotherm curves correspond to the 75:25 MK-9: phospholipid monolayer (dotted purple line), 50:50 MK-9:phospholipid monolayer (dashed and dotted green line), 25:75 MK-9:phospholipid monolayer (short dash and dot blue line), and the pure phospholipid monolayer (dashed red line). The ratios correspond to mole fractions of MK-9 to phospholipid of the monolayers. MK-9 monolayer compression isotherm curves are not present as there was no phospholipid present within the monolayer.

When the MK-9 mole fraction is increased, the isotherms shift toward a greater area per phospholipid. None of the mixed monolayers exhibited MK-9 being compressed completely out of the monolayer which would have been shown by overlapping normalized isotherm curves.[18] UBQ has previously been shown to be compressed out of the monolayer by Quinn *et al.*[18] As shown in table 4.1, the difference in the area per phospholipid when MK-9 is present from the control monolayer decreases when the surface pressure is above 20 mN/m. This is consistent with partially compressing MK-9 out of the monolayer.

Table 4.1. Percent Difference in Area per Phospholipid of Normalized Mixed Monolayers from Pure Phospholipid Monolayers.[a]

Surface Pressure (mN/m)	DPPC			DPPE		
	25% MK-9	50% MK-9	75% MK-9	25% MK-9	50% MK-9	75% MK-9
5	21.6	38.1	68.5	8.7	59.9	128.5
10	18.0	35.2	69.8	7.6	50.4	112.5
15	13.1	29.3	61.6	6.9	41.3	97.3
20	8.5	23.1	53.7	6.4	34.0	83.3
25	6.4	19.2	46.7	6.2	30.1	74.9
30	5.2	17.0	42.2	5.9	27.2	68.7
35	4.3	15.9	37.1	5.7	25.2	64.0
40	4.7	13.7	N.A	5.4	18.3	58.0

4.3.4 Compression Moduli of Mixed and Pure Monolayers of MK-9 and Phospholipids

For further confirmation that MK-9 is not being completely compressed out of the mixed monolayers but still affect the monolayers at higher pressures, the compression moduli of the mixed and pure monolayers were compared (Figure 4.6). The compression moduli were also compared to determine if the presence of MK-9 causes the monolayers to be compressed more easily.
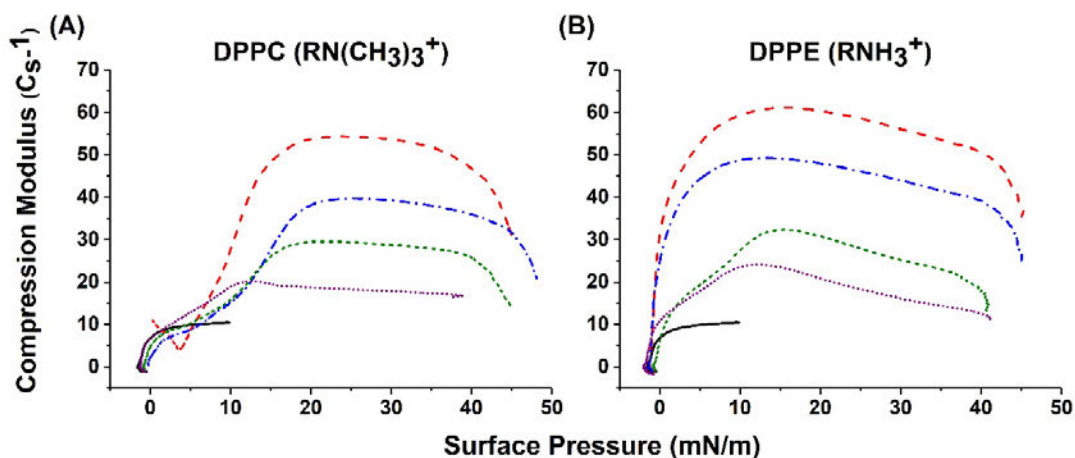
Figure 4.6. Compression moduli of pure monolayers of MK-9 and DPPC (A) or DPPE (B). The compression moduli curves correspond to pure MK-9 monolayer (solid black line), 75:25 MK-9: phospholipid monolayer (dotted purple line), 50:50 MK-9:phospholipid monolayer (dashed and dotted green line), 25:75 MK-9:phospholipid monolayer (short dash and dot blue line), and the pure phospholipid monolayer (dashed red line). The ratios correspond to mole fractions of MK-9 to phospholipid of the monolayers.

The DPPC, DPPE, and MK-9 compression moduli curves are similar to reported curves for the phospholipids and other quinones.[11-13, 20] The compression moduli decrease as the mole fraction of MK-9 increases for both phospholipid monolayers. This observation is consistent with previous findings.[11-13, 20] In the presence of MK-9, the DPPC compression moduli no longer exhibit the characteristic gas-liquid phase transition at 4 mN/m as shown by the minimum compression modulus of the DPPC control monolayer compression modulus. The gas-liquid phase transition disappearance in the mixed monolayers is consistent with observations from the compression isotherm curves. The 75% MK-9 and 25% DPPC monolayer exhibited a small maximum compression modulus and the 50% MK-9 and 25% MK-9 monolayers exhibited sharp increases in the compression modulus after the collapse pressure of the pure MK-9 monolayer. Similarly, the mixed monolayers of MK-9 and DPPE (75% and 50% MK-9) exhibited a local maximum at slightly higher pressures than the collapse pressure of the pure MK-9 monolayer (~13 mN/m). This is interpreted as being an energy barrier for the collapse of the MK-9 within the monolayers which would lead to compressing the MK-9 out of the monolayer into the phospholipid tails. This interpretation is consistent with previous studies and would still affect the compressibility of the monolayers.[11-13, 20]

4.3.5   BAM of Mixed and Pure Monolayers of MK-9 and Phospholipids

To further examine the interactions of MK-9 with DPPC or DPPE, compression isotherms of mole fractions of MK-9 with one of the phospholipids were conducted while BAM images were collected. BAM has been successfully used previously to explore the morphology of Langmuir monolayers and therefore was used in this study to do the same.[11-13, 31]

The BAM images of pure monolayers consisting of either 50 nmoles or 100 nmoles of MK-9 are shown in Figure 4.7. The collapse pressure of MK-9 during these experiments were found to be 15 mN/m. The vairability between the collapse pressure of the compression isotherm experiments and the BAM experiments is likely due to the intermolecular interactions of MK-9. As can be observed in the 50 nmol

MK-9 images, MK-9 forms a flat surface until the 15 mN/m. After the 15 mN/m, small aggregates can be observed. With the 100 nmol images, aggregates can be observed at all the pressures shown. These observations are interpreted as MK-9 aggregating as the MK-9 comes in closer proximity with other MK-9 molecules.

After the collapse at 15 mN/m, BAM images were also recorded every 5 minutes for 20 minutes to observe any post-collapse alterations of the MK-9 monolayer (See Figure A6.1). As the monolayer was left to equilibrate, the aggregations (1 min) tended toward dissapearing into an image with larger aggregates and a flate surface (20 min). This data shows that as MK-9 is allowed to equilibrate, it tends to spread across the interface slowly. This slow equilibration post-collapse of MK-9 is likely why the collapse pressure of the MK-9 monolayer was found to be variable.

50 nmol MK-9

5 mN/m

100 nmol MK-9

7 mN/m

10 mN/m
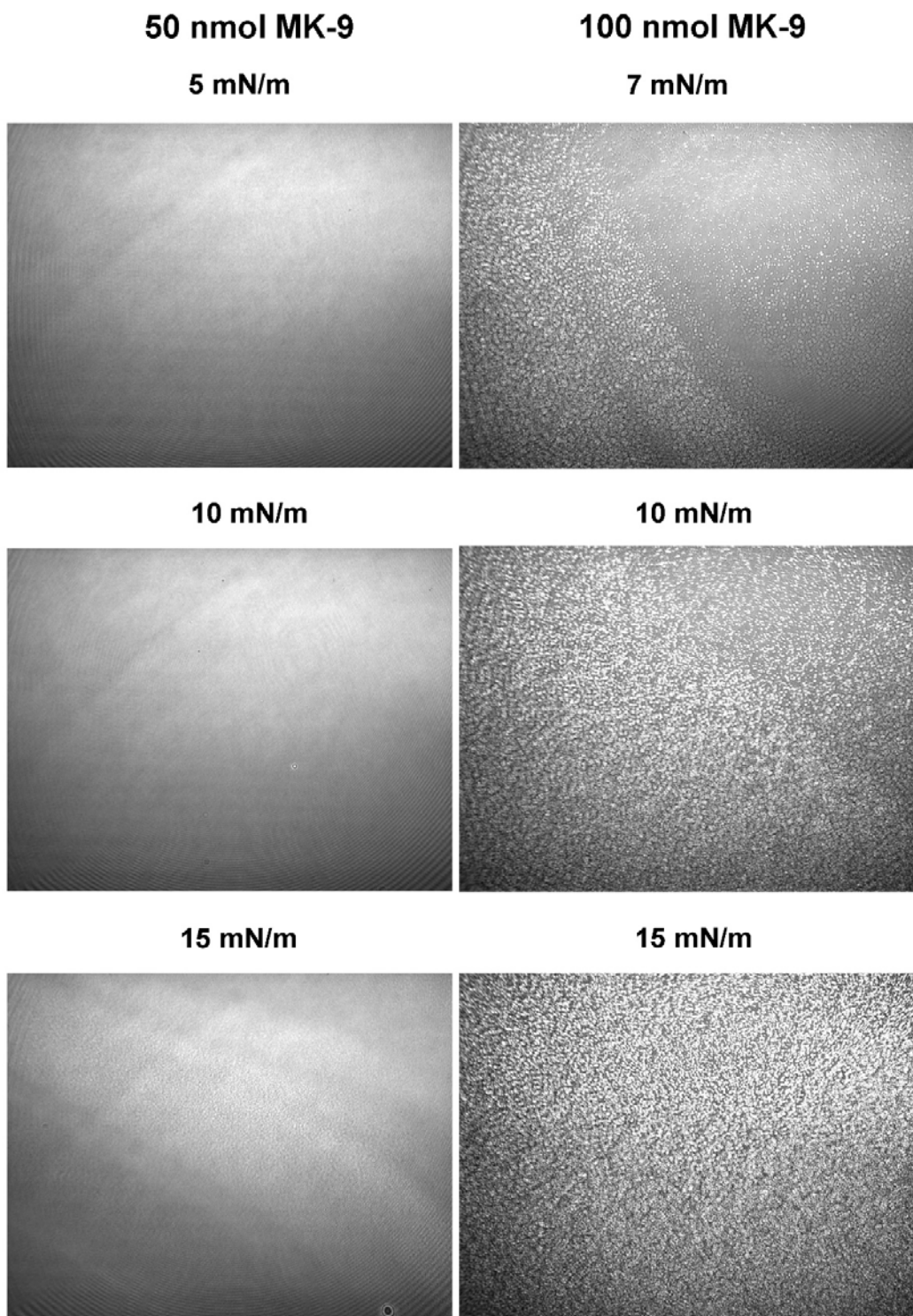
10 mN/m

15 mN/m

15 mN/m

Figure 4.7. BAM images of compression isotherms of monolayers consisting of 50 nmoles (left column) or 100 nmoles (right column) of MK-9. Surfaces pressures are given with corresponding images below. See Figure A6.1 for BAM images post collapse of the monolayer consisting of 50 nmoles of MK-9.

In Figure 4.8 the BAM images of DPPC and DPPC mixed monolayers with MK-9 are presented at 10 mN/m, 20 mN/m, and 30 mN/m. As can be seen with the DPPC monolayer images, DPPC tends to form an even coverage across the subphase surface.[36-37] A phase transition from the liquid to solid phase can be observed as very small aggregates in the 20 mN/m DPPC monolayer image. When MK-9 is present, the DPPC liquid to solid phase transition is no longer observed. Also, as the MK-9 content is increased, more dark spots can be observed on the monolayer surface. The appearance of these dark spots is interpreted as portions of the DPPC interface being more fluid and reorganizing with the presence of MK-9. This interpretation is consistent with the lack of a liquid to solid phase transition. Spots similar to these can also be interpreted as dust particles affecting the monolayer. This is not likely as the spots are more prevalent as the MK-9 content is increased within the monolayer. This phenomenon was consistent through multiple trials which would not be expected if the spots were dust particles as they should be equally distributed in different monolayers.

Figure 4.8. BAM images of DPPC (top row), 25% MK-9 and 75% DPPC (second row), 50% MK-9 and 50% DPPC, and 75% MK-9 and 25% DPPC monolayers at 10 mN/m, 20 mN/m and 30 mN/m. For images presented every 5 mN/m, see Figure A7.1.

The BAM images of DPPE and DPPE mixed monolayers at 10 mN/m, 20 mN/m and 30 mN/m can be observed in Figure 4.9. The pure DPPE monolayers at 10 mN/m exhibit dark spots within the image that corresponds to empty space within the DPPE monolayer. This is consistent with DPPE being involved in intermolecular hydrogen bonding leading to a greater amount of aggregation than what was observed for DPPC. By 30 mN/m the surface of the subphase was completely covered by DPPE. As the MK-9 content is increased, small aggregates can be observed in the 10 mN/m and 20 mN/m images (specifically 50% and 75% MK-9 images). The 30 mN/m image of the monolayer consisting of 75% MK-9 is then of a mostly flat

surface. This can be interpretted as either that at high pressure the MK-9 is compressed out of the monolayer forming a flat surface on the top of the monolayer or the pressure is causing the MK-9 to disperse within the DPPE instead of aggregating. Considering the compression isotherm data and analysis, it is likely that a mixture of the interpretations is what is occuring. The MK-9 being compressed out of the monolayer would also be consistent with previous findings by Hoyo *et al.* and Quinn *et al.*[11-13, 18]
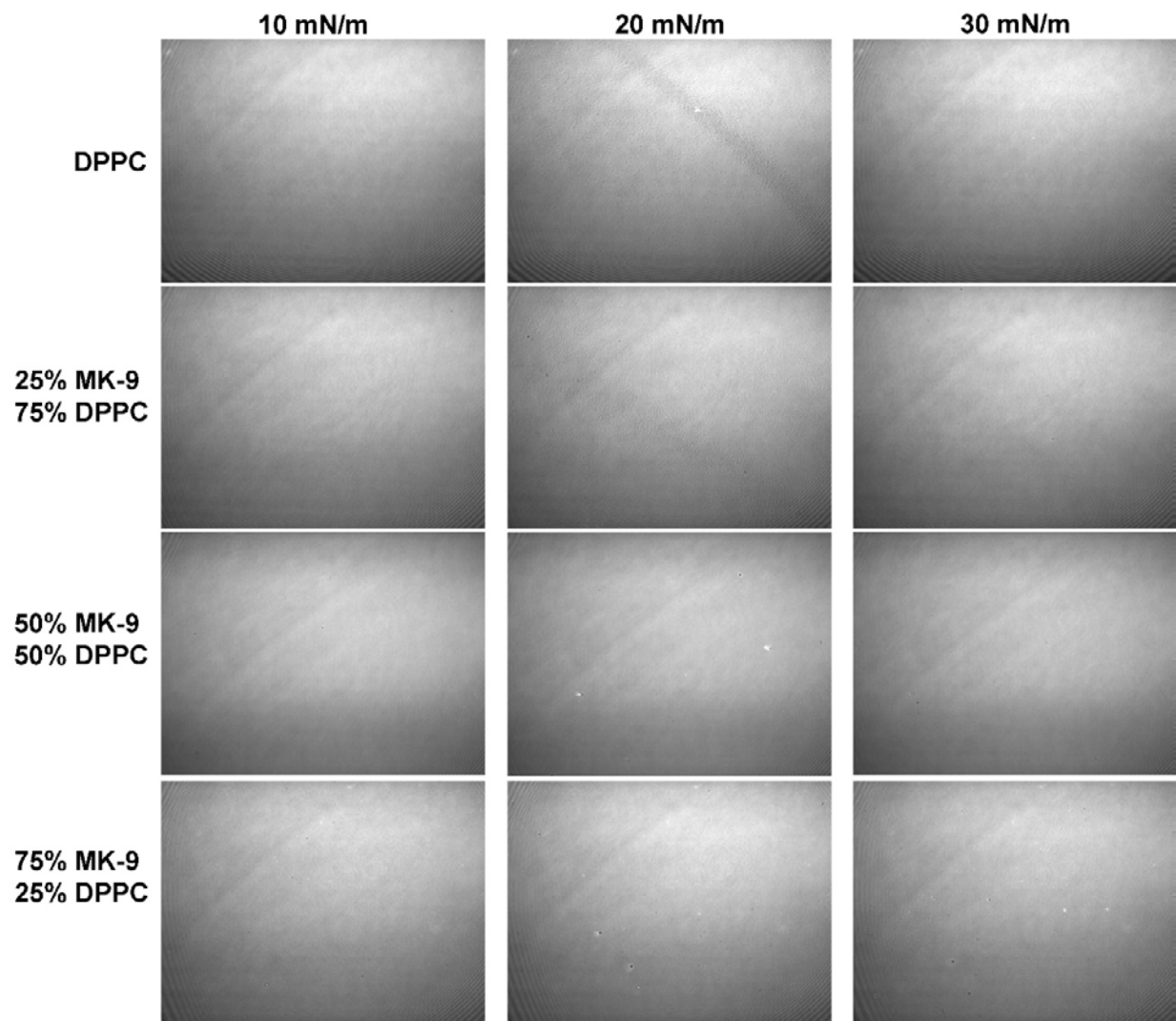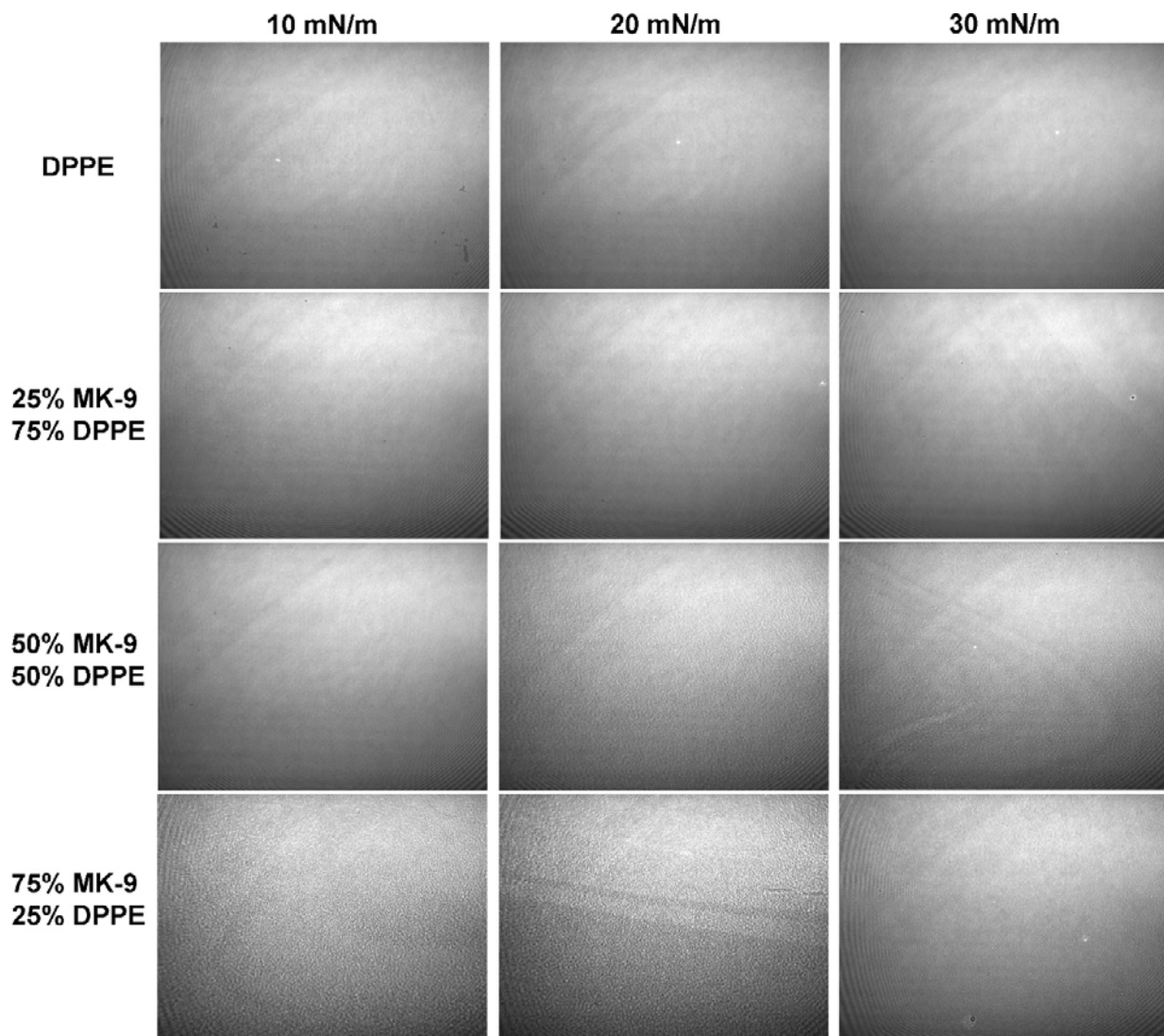

Figure 4.9. BAM images of DPPE (top row), 25% MK-9 and 75% DPPE (second row), 50% MK-9 and 50% DPPE, and 75% MK-9 and 25% DPPE monolayers at 10 mN/m, 20 mN/m and 30 mN/m. For images presented every 5 mN/m, see Figure A8.1.

4.3.6 Evaluation of Findings and Comparison to Literature

Through the compression isotherm experiments and BAM images, the surface pressure dependent interactions of MK-9 and DPPC were determined. Through the compression isotherm experiments of pure and mixed monolayers of DPPC, a disappearance of gas to liquid phase transitions and a low collapse of the pure MK-9 monolayer were observed. The ideal area gave variable results, but the compression isotherm curves normalized to the phospholipid content suggested that MK-9 is partially compressed out of the monolayer. The compression modulus data suggests that the MK-9 does affect the monolayer throughout compression and allows for easier compression as the MK-9 content is increased. The BAM suggests that the presence of MK-9 can cause tail rearrangements of DPPC in distinct positions. All of this data is in agreement with MK-9 being partially compressed out of the DPPC monolayer, but still affecting the DPPC monolayer allowing it to be easier to compress. This would suggest that the MK-9 is still within the lipid monolayer and not simply residing on top of the monolayer.

The compression isotherm and BAM experiments were also used to determine the surface pressure dependent interactions of MK-9 and DPPE. The compression isotherm experiments of pure and mixed monolayers suggested MK-9 was affecting the DPPE monolayers more at lower surface pressures than at higher surface pressures (above 20 mN/m). Ideal area results were variable, but the isotherm curves normalized to the phospholipid content exhibited MK-9 being partially compressed out of the monolayer similar to the DPPC results.[11-13, 18, 31, 38] The presence of MK-9 also caused the DPPE monolayer to be compressed easier in the same manner as the DPPC monolayer. Through imaging the monolayers using BAM, the MK-9 would still aggregate, but at high pressures (30 mN/m) MK-9 is either compressed out of the monolayer or intercalates into the DPPE regions. In summary, the data is consistent with MK-9 being partially compressed out of the monolayer and likely residing within the monolayer instead of residing on top of the monolayer similarly as with DPPC (see Figure 4.10 for illustration of interpretation).
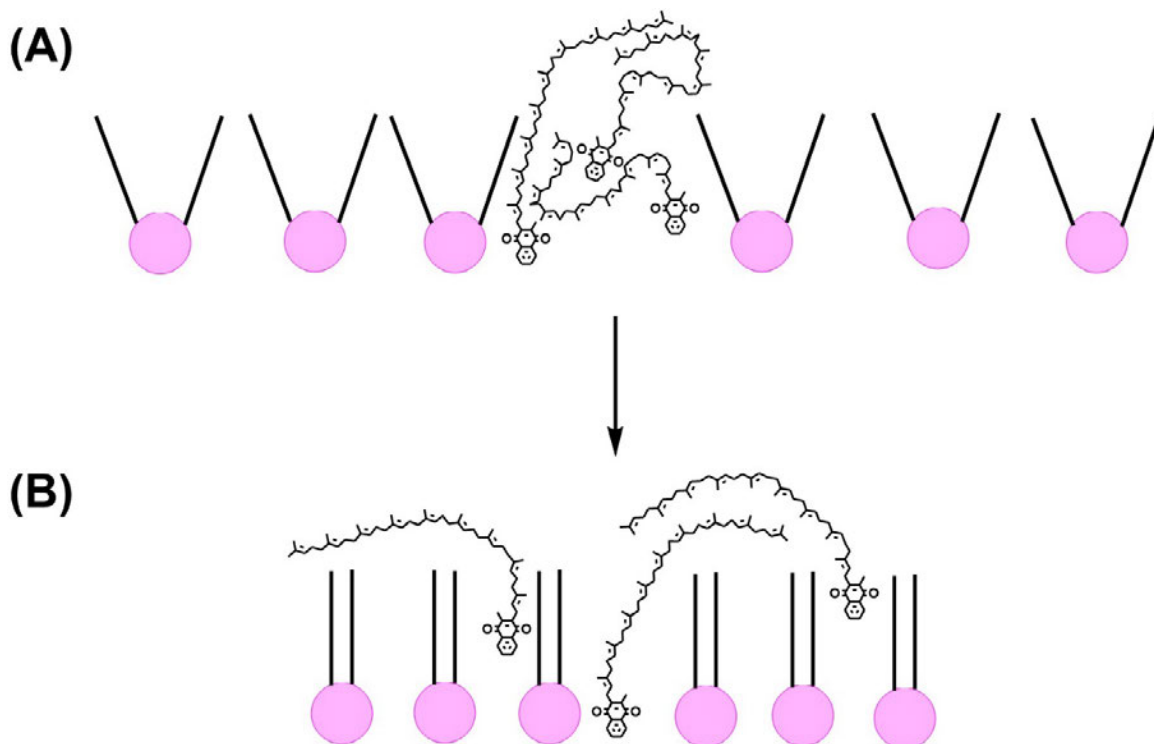
Figure 4.10. Pictorial representation of the interpretations of the current study. Initially the MK-9 aggregates within the lipids (A) and as the lipids are compressed closer to one another, the MK-9 molecules are compressed out of the water interface toward the lipid tails (B). MKs are depicted as being folded as is consistent with literature.[16, 20, 39]

These findings are similar to previous findings, but there are small differences from previous studies. Quinn *et al*. found through compression isotherm experiments of UBQ of varying tail length and phospholipids, that ubiquinone is completely compressed out of the monolayer to the top of the phospholipids tails.[18] In this study, MK-9 was not completely compressed out of the monolayer, but instead still affected the area per molecule and compressibility of the monolayer. This discrepancy may be due to the headgroups of the quinones, or the improvements in sensitivity of Langmuir monolayer experimental setups over time.[18] In either case, this does demonstrate that MK-9 does interact with phospholipids similarly to UBQ. Also similar to current findings, Hoyo *et al*. and Kruk *et al.* found that UBQ and PQ both are partially compressed out of the phospholipid monolayers using AFM, BAM and compression isotherms.[11-13, 38] Considering the current findings and these studies, the three quinones

considered interact with phospholipid interfaces very similarly.[11-13, 18, 38] This suggests that the main factor in the transport of these quinones across membranes is the isoprenoid tails.[11-13, 18, 38]

In a biological setting, MK-9 would have to transverse a bilayer instead of a monolayer as was used within this study. Although there are clear differences between a bilayer and a monolayer, this study still provides information on aspects of the ability of MK-9 to traverse the membrane.[14-16] The conclusion that MK-9 partially being compressed out of the monolayers suggests that MK-9 does not strongly interact with the water inerface. This is likely due to a limited amount of hydrogen bonding with the water interface compared to DPPC or DPPE.[40-41] Therefore once the lipid density becomes sufficiently high (above ~20 mN/m), MK-9 is compressed into the lipid tails. With many biological membranes having a lipid density relating to 30-35 mN/m, MK-9 most likely resides within the lipid tails for the majority of time.[36-37, 42] The rest of the time, MK-9 likely resides near the headgroups of the phospholipids.[16] Considering MK-9 resides within the tails of the phospholipid monolayers at physiological lipid densities as shown in this study, MK-9 likely is able to traverse the bilayer easily.[11-13, 16, 18]

4.4   Summary and Conclusions

The current studies explored the interactions of the electron transporter of *Mycobacterium tuberculosis*, MK-9, with common phospholipids using Langmuir monolayers. The compression isotherm experiments of mixed and pure monolayers of MK-9 and the phospholipids DPPC or DPPE, suggested that MK-9 and the phospholipids do interact with one another. Through analysis of the compression isotherm curves, the ideal area, isotherm curves normalized to the phospholipid content, and the compression modulus were calculated and shows that MK-9 is partially compressed out of the monolayers into the tails of the phospholipids. The BAM images were able to corroborate these findings. Therefore, these studies were able to show that MK-9 is partially compressed out of the monolayer in a surface pressure (lipid density) dependent manner similar to that of other quinones.[11-13, 16, 18]

References

(1)   A Kurosu, M.; A Begari, E. Vitamin K2 in Electron Transport System: Are Enzymes Involved in Vitamin K2 Biosynthesis Promising Drug Targets? *Molecules.* **2010,** *15*, 1531-1553.

(2)   Crane, F. L.; Sun, I. L.; Barr, R.; Low, H. Electron and Proton Transport across the Plasma-Membrane. *J. Bioenerg. Biomembr.* **1991,** *23* (5), 773-803.

(3)   Haapanen, O.; Sharma, V. A Modeling and Simulation Perspective on the Mechanism and Function of Respiratory Complex I. *Biochim. Biophys. Acta, Bioenergetics.* **2018,** *1859* (7), 510-523.

(4)   Nowicka, B.; Kruk, J. Occurrence, Biosynthesis and Function of Isoprenoid Quinones. *Biochim. Biophys. Acta, Bioenergetics.* **2010,** *1797* (8), 1587-1605.

(5)   Ragan, C. I.; Cottingham, I. R. The Kinetics of Quinone Pools in Electron-Transport. *Biochim. Biophys. Acta.* **1985,** *811* (1), 13-31.

(6)   Rochaix, J. D., Regulation and Dynamics of the Light-Harvesting System. In *Annu. Rev. Plant Biol.*, Merchant, S. S., Ed. 2014; Vol. 65, pp 287-309.

(7)   Tikhonov, A. N.; Vershubskii, A. V. Computer Modeling of Electron and Proton Transport in Chloroplasts. *BioSyst.* **2014,** *121*, 1-21.

(8)   Hoyo, J.; Guaus, E.; Torrent-Burgues, J. Influence of Membrane Galactolipids and Surface Pressure on Plastoquinone Behaviour. *Bioelectrochemistry.* **2016,** *111*, 123-130.

(9)   Hoyo, J.; Guaus, E.; Torrent-Burgues, J. Tuning Ubiquinone Position in Biomimetic Monolayer Membranes. *Eur. Phys J. E.* **2017,** *40* (6), 1-8.

(10)   Hoyo, J.; Guaus, E.; Torrent-Burgues, J.; Sanz, F. Electrochemical Behaviour of Mixed LB Films of Ubiquinone - DPPC. *J. Electroanal. Chem.* **2012,** *669*, 6-13.

(11)   Hoyo, J.; Guaus, E.; Torrent-Burgues, J.; Sanz, F. Biomimetic Monolayer Films of Digalactosyldiacylglycerol Incorporating Plastoquinone. *Biochim. Biophys. Acta, Biomembr.* **2015,** *1848* (6), 1341-1351.

(12)   Hoyo, J.; Guaus, E.; Torrent-Burgues, J.; Sanz, F. Biomimetic Mono Layer Films of Monogalactosyldiacylglycerol Incorporating Plastoquinone. *J. Phys. Chem. B.* **2015,** *119* (20), 6170-6178.

(13)   Hoyo, J.; Torrent-Burgues, J.; Guaus, E. Biomimetic Monolayer Films of Monogalactosyldiacylglycerol Incorporating Ubiquinone. *J. Colloid Interface Sci.* **2012,** *384*, 189-197.

(14)   JemiolaRzeminska, M.; Kruk, J.; Skowronek, M.; Strzalka, K. Location of Ubiquinone Homologues in Liposome Membranes Studied by Fluorescence Anisotropy of Diphenyl-Hexatriene and Trimethylammonium-Diphenyl-Hexatriene. *Chem. Phys. Lipids.* **1996,** *79* (1), 55-63.

(15)   Jemiota-Rzeminska, M.; Latowski, D.; Strzalka, K. Incorporation of Plastoquinone and Ubiquinone into Liposome Membranes Studied by HPLC Analysis. The Effect of Side Chain Length and Redox State of Quinone. *Chem. Phys. Lipids.* **2001,** *110* (1), 85-94.

(16)   Kaurola, P.; Sharma, V.; Vonk, A.; Vattulainen, I.; Rog, T. Distribution and Dynamics of Quinones in the Lipid Bilayer Mimicking the Inner Membrane of Mitochondria. *Biochim. Biophys. Acta, Biomembr.* **2016,** *1858* (9), 2116-2122.

(17)   Leidner, C. R.; Patterson, D. H.; Scheper, W. M.; Liu, M. D. Reduction of Phospholipid Quinones in Bilayer-Membranes - Kinetics and Mechanism. *ACS Symp. Ser.* **1992,** *493*, 202-217.

(18)   Quinn, P. J.; Esfahani, M. A. Ubiquinones Have Surface-Active Properties Suited to Transport Electrons and Protons across Membranes. *Biochem. J.* **1980,** *185* (3), 715-722.

(19)   Rokitskaya, T. I.; Murphy, M. P.; Skulachev, V. P.; Antonenko, Y. N. Ubiquinol and Plastoquinol Triphenylphosphonium Conjugates Can Carry Electrons through Phospholipid Membranes. *Bioelectrochemistry.* **2016,** *111*, 23-30.

(20)   Koehn, J. T.; Magallanes, E. S.; Peters, B. J.; Beuning, C. N.; Haase, A. A.; Zhu, M. J.; Rithner, C. D.; Crick, D. C.; Crans, D. C. A Synthetic Isoprenoid Lipoquinone, Menaquinone-2, Adopts a Folded Conformation in Solution and at a Model Membrane Interface. *J. Org. Chem.* **2018,** *83* (1), 275-288.

(21)   Bernard, S.; Roche, Y.; Etienne, F.; Peretti, P. Interaction between Ubiquinones and Dipalmitoylphosphatidylcholine in Mixed Langmuir Monolayers. *Mol. Cryst. Liq. Cryst.* **2000,** *338*, 207-221.

(22)   Azuma, K.; Ouchi, Y.; Inoue, S. Vitamin K: Novel Molecular Mechanisms of Action and Its Roles in Osteoporosis. *Geriatr. Gerontol. Int.* **2014,** *14* (1), 1-7.

(23)   Choi, Y.; Attwood, S. J.; Hoopes, M. I.; Drolle, E.; Karttunen, M.; Leonenko, Z. Melatonin Directly Interacts with Cholesterol and Alleviates Cholesterol Effects in Dipalmitoylphosphatidylcholine Monolayers. *Soft Matter.* **2014,** *10* (1), 206-213.

(24)   Paul, P. K.; Che, D. C.; Hiroyuki, K.; Araki, K.; Matsumoto, T. Adsorption Characteristics of Cytochrome C/DNA Complex Langmuir Molecular Assemblies at the Air-Water Interface: A Surface Area-Normalized Isotherm Study. *Rsc Advances.* **2017,** *7* (60), 37755-37764.

(25)   Peters, B. J.; Groninger, A. S.; Fontes, F. L.; Crick, D. C.; Crans, D. C. Differences in Interactions of Benzoic Acid and Benzoate with Interfaces. *Langmuir.* **2016,** *32* (37), 9451-9459.

(26)   Sostarecz, A. G.; Gaidamauskas, E.; Distin, S.; Bonetti, S. J.; Levinger, N. E.; Crans, D. C. Correlation of Insulin-Enhancing Properties of Vanadium-Dipicolinate Complexes in Model Membrane Systems: Phospholipid Langmuir Monolayers and Aot Reverse Micelles. *Chem. - Eur. J.* **2014,** *20* (17), 5149-5159.

(27)   Thong, A.; Tsoukanova, V. Cytochrome-C-Assisted Escape of Cardiolipin from a Model Mitochondrial Membrane. *Biochim. Biophys. Acta, Biomembr.* **2018,** *1860* (2), 475-480.

(28)   Miyoshi, T.; Kato, S. Detailed Analysis of the Surface Area and Elasticity in the Saturated 1,2-Diacylphosphatidylcholine/Cholesterol Binary Monolayer System. *Langmuir.* **2015,** *31* (33), 9086-9096.

(29)   Taira, T.; Ikeda, S.; Kawamura, D.; Sakai, H.; Abe, M.; Kitamoto, D.; Imura, T. Monolayer Behavior of Cyclic and Linear Forms of Surfactins:Thermodynamic Analysis of Langmuir Monolayers and Afm Study of Langmuir-Blodgett Monolayers. *J. Oleo. Sci.* **2014,** *63* (4), 407-412.

(30)   Petelska, A. D.; Figaszewski, Z. A. The Equilibria of Phosphatidylethanolamine-Cholesterol and Phosphatidylcholine-Phosphatidylethanolamine in Monolayers at the Air/Water Interface. *J. Macromol. Sci., Pure Appl. Chem.* **2009,** *46* (6), 607-614.

(31)   Nerdal, W.; Nilsen, T. R. S.; Steinkopf, S. Coenzymeq(10), Localizations in Model Membranes. A Langmuir Monolayer Study. *Biophys. Chem.* **2015,** *207*, 74-81.

(32)   Knobler, C. M.; Desai, R. C. Phase-Transitions in Monolayers. *Annu. Rev. Phys. Chem.* **1992,** *43*, 207-236.

(33)   Borrell, J. H.; Domenech, O. Critical Temperature of 1-Palmitoyl-2-Oleoyl-Sn-Glycero-3-Phosphoethanolamine Monolayers and Its Possible Biological Relevance. *J. Phys. Chem. B.* **2017,** *121* (28), 6882-6889.

(34)   Capuzzi, G.; LoNostro, P.; Kulkarni, K.; Fernandez, J. E.; Vincieri, F. F. Interactions of 6-O-Stearoylascorbic Acid and Vitamin K-1 in Mixed Langmuir Films at the Gas/Water Interface. *Langmuir.* **1996,** *12* (22), 5413-5418.

(35)   Kaganer, V. M.; Mohwald, H.; Dutta, P. Structure and Phase Transitions in Langmuir Monolayers. *Rev. Mod. Phys.* **1999,** *71* (3), 779-819.

(36)   Veldhuizen, R.; Nag, K.; Orgeig, S.; Possmayer, F. The Role of Lipids in Pulmonary Surfactant. *Biochim. Biophys. Acta, Mol. Basis Dis.* **1998,** *1408* (2-3), 90-108.

(37)   Veldhuizen, E. J. A.; Haagsman, H. P. Role of Pulmonary Surfactant Components in Surface Film Formation and Dynamics. *Biochim. Biophys. Acta, Biomembr.* **2000,** *1467* (2), 255-270.

(38)   Kruk, J.; Strzalka, K.; Leblanc, R. M. Monolayer Study of Plastoquinones, Alpha-Tocopherol Quinone, Their Hydroquinone Forms and Their Interaction with Monogalactosyldiacylglycerol - Charge-Transfer Complexes in a Mixed Monolayer. *Biochim. Biophys. Acta.* **1992,** *1112* (1), 19-26.

(39)   Szterk, A.; Zmysłowski, A.; Bus, K. Identification of Cis/Trans Isomers of Menaquinone-7 in Food as Exemplified by Dietary Supplements. *Food Chem.* **2018,** *243*, 403-409.

(40)   Leekumjorn, S.; Sum, A. K. Molecular Investigation of the Interactions of Trehalose with Lipid Bilayers of DPPC, DPPE and Their Mixture. *Mol. Simul.* **2006,** *32* (3-4), 219-230.

(41)   Leekumjorn, S.; Sum, A. K. Molecular Simulation Study of Structural and Dynamic Properties of Mixed DPPC/DPPE Bilayers. *Biophys. J.* **2006,** *90* (11), 3951-3965.

(42)   Jones, M. N., *Micelles, Monolayers, and Biomembranes*. New York : Wiley-Liss: New York, **1995**.

Chapter 5: Physical and Chemical Characteristics Affecting Membrane Interactions

As presented in the previous chapters, many factors play a role in the interactions of small molecules with lipid interfaces and inter-lipid interactions. The factors presented here are likely not the only factors that affect small molecule and inter-lipid interactions within membranes.[1-2] These other factors that were not explored within these studies may, but are not limited to include lipid density, ionic strength of the water, charge of molecules or ions, and structure and composition of the lipids.[1-14] Understanding these characteristics is crucial for the development of drugs and further understanding of biological systems. The following discusses a few of these factors that affect small molecule interactions with lipids and inter-lipid interactions.

5.1 Interactions of Small Molecules and Ions with Cell Membranes
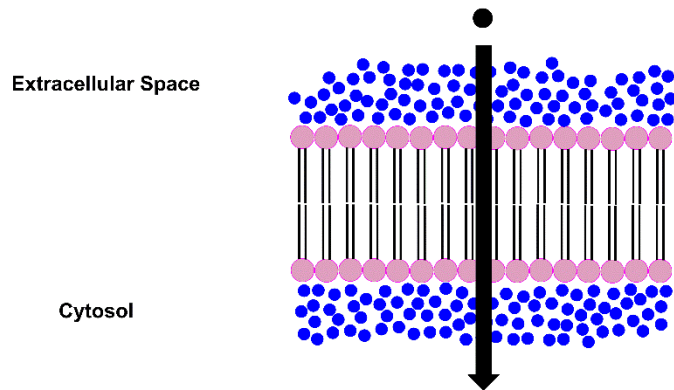
When considering small molecules diffusing into and across the cell membrane, it is important to consider the steps by which the small molecules go through to cross the membrane. First, the small molecule must be sufficiently hydrophobic to bind to the cell membrane interface. Once at the interface, the molecule is thought to diffuse across the membrane by itself or with assistance of a channel protein.[7, 15-21] If the molecule is too hydrophobic (logP > 5.6), it will be trapped within the membrane hydrophobic region or if the molecule is too hydrophilic (logP < -0.4), then it will not bind to the membrane and to enter a cell it must go through a transporter.[17, 22] Therefore, an appropriate hydrophobicity is sought for diffusion across the cell membrane. These generalities are good estimates for drug development, but there are examples of ions and molecules that do not follow this generalization and diffusion across the cell membrane may be much more complicated.[2, 23-26] There are many factors that may affect the interactions of small molecules with lipid interfaces and the following discusses a few of those factors.

5.1.1 Diffusion of Ions through Lipid Bilayers

For decades, it has been known that cells are able to uptake needed ions through the lipid membrane.[27-32] To do this, there are many protein transporters, but the cell can also uptake ions through the lipid bilayer.[13, 24, 27-34] Considering the ions are charged, it is commonly assumed that the ions do not interact with the lipid interfaces (primarily hydrophobic). Interestingly, these cations are still able to cross lipid bilayers.[9, 13, 24, 34]

To cross the lipid bilayer, cations bind to the phosphates of the membrane phospholipids and the nearby water molecules.[9, 13, 33-35] Assuming there is enough of concentration gradient of the ions across the membrane, a hydrophilic pore may form.[20, 25, 36] This pore can consist of ~100 H_2O molecules, cations, and anions, which can then cross to the other side of the lipid bilayer.[20, 33, 35-36] This method of crossing the bilayer is one of the currently, most accepted mechanisms of ions traversing a lipid bilayer and is called the pore mechanism (see Figure 5.1 for illustration of pore formation).[9, 20, 35] Alternatively, some anions are able to diffuse across lipid bilayers using the solubility-diffusion mechanism.[13, 25, 34] This is the mechanism that is commonly described for passive diffusion.[13, 25, 34] For this method, the anion would have to be sufficiently soluble in the lipid hydrophobic region to where, through Brownian motion, it is able to traverse the bilayer (see Figure 5.1). For an anion to be able to cross the bilayer in this method, the basicity and polarity of the anion are important factors.[13, 34] The basicity is important for the anion to be able to ionically bind to a proton while if the anion is too charged, it will not be able to cross the membrane easily.[13, 34] Therefore, ions are able to cross membranes through at least two accepted mechanisms of diffusion including the pore method and the solubility-diffusion mechanism.[9, 13, 20, 33-36]

(A) Solubility-Diffusion Model

Extracellular Space

Cytosol

(B) Pore Model

(a) Lipid Bilayer

Extracellular Space

Cytosol

(b) Initial Disruption of Bilayer

(c) Initial Pore Formation
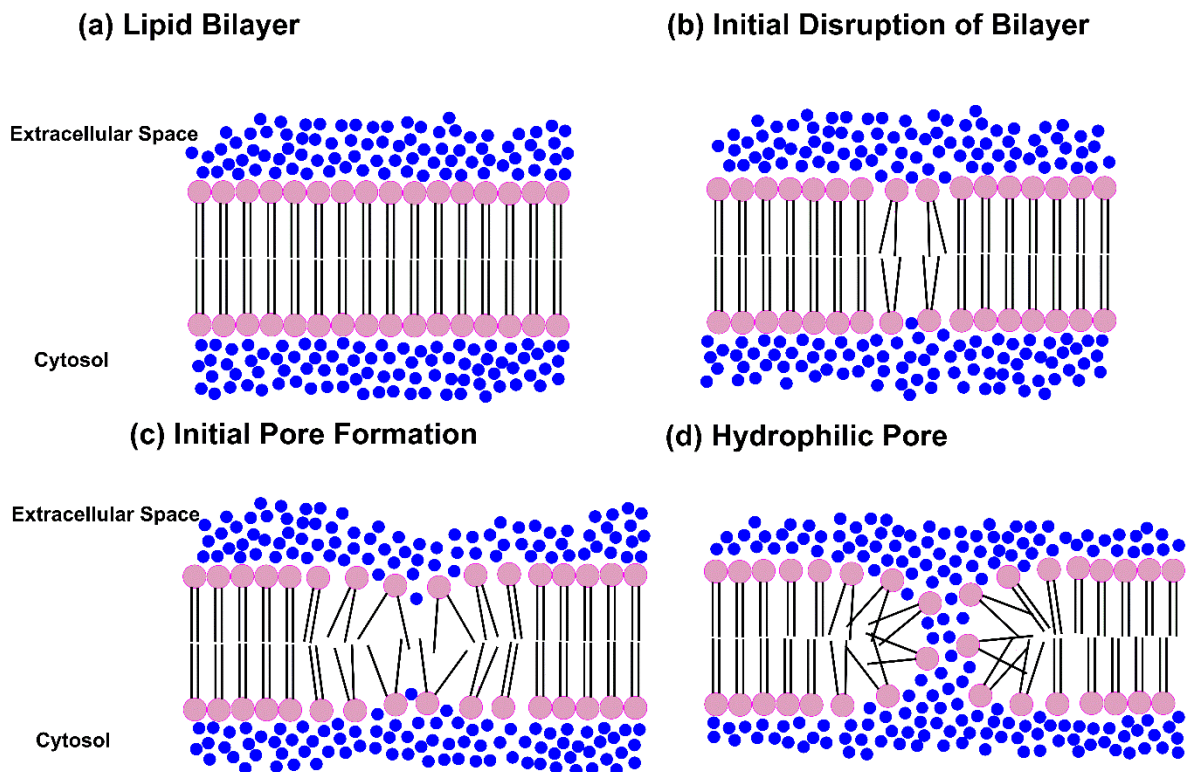
Extracellular Space

Cytosol

(d) Hydrophilic Pore

Figure 5.1. Schematic diagrams of the solubility-diffusion method (A) for an uptake of an anion into a cell (black circle and arrow) and a schematic of the formation of a hydrophilic pore (pore method of uptake, B). The figures outlining the pore formation beginning with the cell bilayer (a), followed by a small disruption of the bilayer (b), initial pore formation (c), and pore formation (d). This figure is based on computational studies where the pore formation is caused by larger differences in concentrations of ions across the membrane.[20, 25, 36] The blue circles represent water molecules.

5.1.2   Small Structural Differences Affecting Small Molecule Interactions with Lipids

The specific structures of small molecules used to treat illnesses are typically thought of in terms of binding to proteins or DNA.[37-40] The specific structures can be altered to make sure the molecules form tight bonds with the target protein or DNA which would then allow for better inhibition of the target.[37-40] Less is done to affect the binding and interactions with the lipids that make up the membrane. As was observed in chapter 3, the small structural differences of small molecules can affect the molecular interactions with general membrane-like interfaces.[2] With advances in the understanding of the interactions of small molecules with specific lipids, it may be possible to direct the small molecules to specific regions of the cell membrane, which could contain the target of interest.[2, 41-44] By targeting the lipids near the protein of interest, the drug molecule would be brought in proximity of the target allowing for a greater chance for the drug to reach its target.[2, 41-44]

5.1.3   pH Dependence of Membrane Interactions of Small Molecules

The pH dependence is well known for the uptake of weak acid preservatives and some small molecule drugs. For carboxylic acids, within solutions of pH values below the pK_a value of the weak acid, the neutral acid form is primarily present and therefore the weak acid interacts more with the lipid bilayer than the conjugate base.[1, 7, 18-19, 45-47] As discussed in chapter 2, benzoic acid was able to reside within the reverse micelle tails which was in a much more hydrophobic region than where benzoate resided which was at the water pool- AOT interface.[1] This likely extends to other weak acid food preservatives shown in Figure 5.2.[1, 7, 18, 46-47] With the neutral acid able to diffuse into the hydrophobic region, the weak acid should be able to completely diffuse across the lipid bilayer similar to the solubility-diffusion method that the anions described previously could use to traverse the membrane bilayer.[13, 34] More information about the mechanistic insights are given in section 5.1.5.
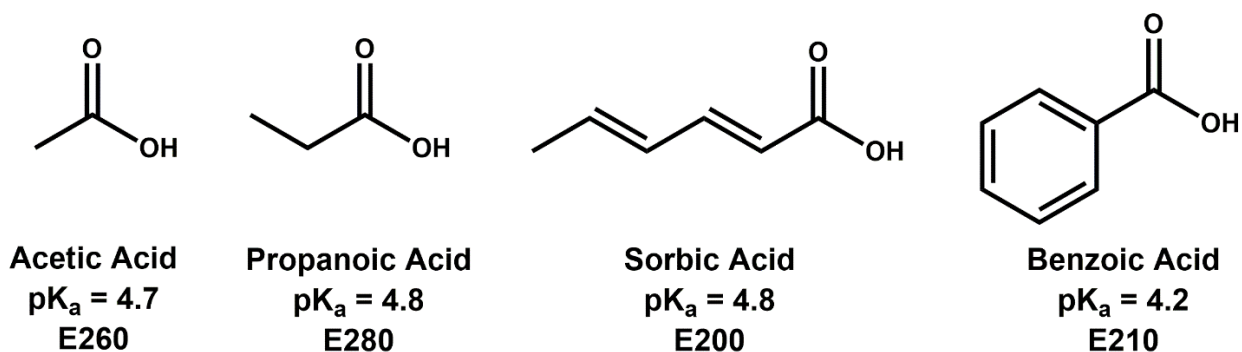
Figure 5.2. Structures, pK_a, and E number (number used to identify preservatives) of acetic acid, propanoic acid, sorbic acid, and benzoic acid. pK_a values are from reference 48.[48]

5.1.4   Lipid Density and Uptake of Small Molecules

For many cells, the density of lipids of membranes corresponds to about 30-35 mN/m, but may vary in organs such as the lungs.[12, 14, 49] Within the alveoli of the lungs, the primary phospholipid is dipalmitoylphosphatidylcholine (DPPC).[14, 49] This lipid is known to have complete coverage of an interface even near 0 mN/m.[14, 49] The decrease in lipid density can allow for rapid gas molecule diffusion through the alveolar surface.[14, 49] With other systems where the lipid density relates to the surface pressure of 30-35 mN/m, the uptake of small molecules is severely reduced unless the cell allows for greater uptake of the molecule through protein channels.[15, 50-51] This has been demonstrated using insertion profiles of small molecules and N-Ras protein into Langmuir monolayers.[52] At higher surface pressures (greater lipid densities) the uptake of small molecules is reduced.[52] Generally, the more dense the lipid interface, the less a small molecule is able to penetrate into the lipid interface.[15, 50-52]

5.1.5   Comparison of Mechanisms for Small Molecule Diffusion Across Cell Membranes

There are two commonly accepted mechanisms for small molecule diffusion across membrane bilayers.[25] The mechanisms have the same names as with the ions, but the specifics behind the diffusion are altered due to clear differences in structures between organic molecules and inorganic ions.[25] For instance, when the molecule is using the Solubility-diffusion method for traversing a lipid bilayer, it may tilt parallel with the water-bilayer interface and exist in a perpendicular state to the water-lipid interface

when the molecule is near the interface (see Figure 5.3).[16, 25] This was shown to be the case by Jambeck *et al*. for ibuprofen and aspirin, and is likely to be the situation for many sufficiently hydrophobic molecules.[16, 25] One such molecule that likely follows this pattern is benzoic acid, but more studies would be needed for confirmation.[1, 16, 25]
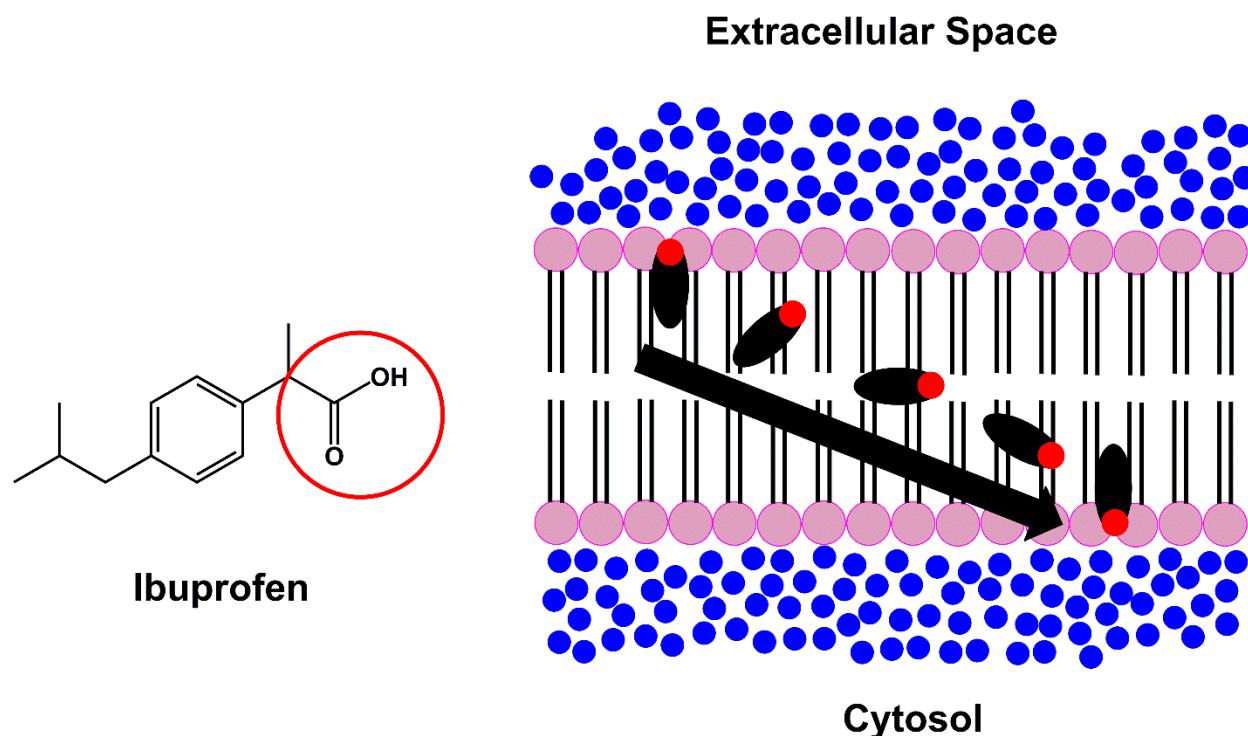

Figure 5.3. Chemical structure and schematic of the diffusion of ibuprofen through a cell membrane. As depicted by the black ovals, the orientation of ibuprofen changes depending on its placement within the lipid bilayer. The red circle around the carboxylic acid of ibuprofen corresponds to the red spot on the black oval in the bilayer. The blue circles represent water molecules.

The second method for small molecule diffusion across the membrane is the pore method similar to that described for ions.[25] This method has been described for curcumin in a concentration dependent manner, where pores form within the lipid bilayers as the curcumin aggregates within the lipid bilayer as shown by solid state NMR by Barry *et al*.[25, 53] Once the pore is formed, the curcumin is able to cross the lipid bilayer.[25, 53] This mechanism of bilayer traversing is likely used by molecules that have hydrophilic structural motifs across the molecule along with being sufficiently hydrophobic allowing for membrane adsorption.[25, 53]

A small molecule that has a membrane dependent interaction that is used to treat tuberculosis is pyrazinamide (PZA).[45, 54-55] The active form, pyrazinoic acid (POA), is known to have a pH dependent effect on *Mycobacterium tuberculosis* (*Mtb*) where at a lower pH of 5.5, PZA has a greater effect on *Mtb* than at pH 6.5.[45, 55] The current mode accepted mechanism of action of PZA is still debated.[56] PZA first crosses the bacterial membrane either through passive diffusion or active transport.[56-57] Once inside the bacterium, PZA is hydrolyzed by PncA to form the carboxylic acid POA and a molecule of ammonia.[21, 56] After formation of POA, the POA may inhibit trans-translation and is also excreted by an efflux system.[56, 58] When POA is introduced to the acidic environment, it is thought that POA becomes protonated and then can diffuse across the cell membrane (pK_a = 2.9).[45, 47, 55, 59] This would then decrease the cytosolic pH and affect many functions of the cell including reducing ATP synthesis.[21, 45, 55-56] The mechanism just described is very similar to that of the futile cycle described by Piper *et al.* for benzoic acid.[7, 18-19, 46] Although for weak acid food preservatives, the pH collapse is only observed below the pK_a of the food preservative.[7, 18-19, 46, 60] This would suggest that for this same mode of action to be relevant for PZA/POA, the pH of the extracellular space would have to be below pH 2.9 or the pK_a of POA would have to change drastically to have the same pH reducing effect on the cytosol.[7, 18, 47, 60] For the pK_a to change there may be some specific interaction with the lipid interface making the protonated state of POA more favorable or there may be some intramolecular hydrogen bonding similar to that of picolinamide.[6, 61-62] In contrast and seemingly more likely, the pK_a of POA may not be altered much at the interface, but instead, POA along with increased ionic strength may allow for a hydrophilic pore to form.[9, 20, 24-25, 33] This would allow for ions, such as protons, to cross the lipid bilayer for the limited time the pore exists (ns) causing the observed effects of POA.[9, 20, 24-25, 33, 55] More studies are needed to confirm the exact interactions of POA with the membrane interface which would lead to an understanding of the effect POA has on the membrane of the bacterium.[21, 24, 45, 55-56, 59] In summary, the pH dependent effect of PZA/POA on *Mtb* is an

example of a pH dependent drug that likely interacts in a specific way with the membrane interface.[21, 45, 55-56, 59]

5.2   Characteristics Affecting Inner Membrane Dynamics

Cell membranes are highly dynamic structures. Within these structures many proteins, and lipids are constantly moving and there are a few characteristics that are able to affect the cell membrane dynamics.[12, 63-64] This is necessary to allow for processes of the membrane to function properly.[12, 63-64] The following sections discuss a couple of the characteristics of the lipid portion of the membrane that may affect the membrane fluidity and local membrane structure.

5.2.1   Saturation of the Lipid Fatty Acid Tails

As mentioned in chapter 1, the degree of saturation of the fatty acid tails of lipids can affect the membrane. Normally saturations (double bonds) of the tails are in the cis orientation to induce a "kink", which then causes the tail of the lipid to not stack as easily within the compact lipid membrane.[12, 63-65] The limited stacking can be observed with Langmuir monolayers, where an increase in lipid saturation, decreases the collapse pressure of the monolayer and the area per molecule is increased at a given surface pressure compared to a lipid with a saturated tail.[11, 66-68] This would suggest that the lipids do not pack as closely as with saturated tails.[11, 66-68] This "kink" can also cause a spreading of the lipids nearby and an overall increase in fluidity of that specific membrane region.[11, 66-68] The fluidity stems from the fact that with a "kink" in the lipid tails, a portion of the hydrophobic tail region becomes less occupied.[12, 63-65] The less occupied region can be filled with tails that are able to occupy the space that would otherwise be tightly packed.

5.2.2   Specialized Lipids

Cholesterol

Beyond changing the structure of the lipid portion of the membrane, the composition of the membrane may be altered as well. To alter the fluidity of the membrane, a cell can change the cholesterol

content of its membrane.[69-71] If the cell needs a more fluid membrane, the cholesterol content can be reduced, while if the cell needs a more rigid membrane, the cholesterol content can be increased.[69-71] Cholesterol has known condensing effects on the surrounding lipids which would cause the apparent increase in rigidity.[70, 72-73] These effects are caused by the structure of cholesterol. The fused ring structure of cholesterol causes a more straight conformation of the tails of the neighboring lipids, which cause the local area of the cholesterol to become more ordered and rigid.[70, 74] Along with the rigidity being affected by the presence of cholesterol, the lipid flip/flop (flip to inner membrane, flop to outer membrane) rate is increased.[4-5, 64, 69] The exact mechanism of how cholesterol increases this rate is unknown, but there have been studies showing how cholesterol flips/flops within the bilayer.[4-5, 64, 69] Cholesterol is normally drawn within the lipid bilayer as being parallel to the lipids surrounding it, but there have been findings that show a significant amount of cholesterol resides perpendicular to the lipids (parallel with the middle of the bilayer).[74-75] This means that there are two orientations of cholesterol within the lipid bilayer and flips across the bilayer similar to ibuprofen.[74-75] One major orientation is with the hydroxyl of the cholesterol near the headgroups of the lipids, and the other is with the cholesterol residing parallel to membrane interface similar to the solvation-diffusion method of ion and small molecule of diffusion across the lipid bilayer.[64, 74-75] This would suggest that cholesterol is able to rotate within the lipid bilayer and affect both sides of the lipid bilayer in similarly.[74-75]

Quinones

Quinones (specifically ubiquinone, plastoquinone, and menaquinone) have all been shown to interact similarly within the cell membrane.[76-83] As discussed in chapter 4, menaquinone-9 (MK-9, nine isoprene units) is partially compressed out of the monolayer at higher surface pressures that relate to physiological densities (30-35 mN/m).[12] Similar findings have been found for Ubiquinone-10 (UBQ-10) and plastoquinone-9 (PQ-9) with varying lipid types composing the mixed monolayers.[76-79, 81-82] This suggests that these quinones are all hydrophobic enough to be able to reside within the hydrophobic region of the

bilayer easily and therefore should be able to flip/flop from one side of the bilayer quickly (ns).[82, 84] This was found to be the case through a computational study by Kaurola *et al*. where UBQ-10 was found to have a folded conformation within the lipid tails when flipping/flopping to the other side of the bilayer.[84] The fold within this computational study is similar to findings by Koehn *et al*. and Szterk *et al.* where the different menaquinone analogs (MK-2, and MK-7 respectively) were found to have folded conformations.[80, 85] considering that the quinones do act similarly throughout many studies, it is likely that the isoprenoid tail is the main structural component that affects the motion of quinones through the bilayer.[82, 84] With the large isoprenoid tail of the quinones (>MK-4), it is possible that the lipids around the quinones are less packed allowing for higher flip/flop rates.[84] The high rate of flip/flop would then allow for the quinones to be able to accomplish the necessary function of transporting electrons and protons through a membrane necessary for cell survival.[3, 82, 84, 86-87]

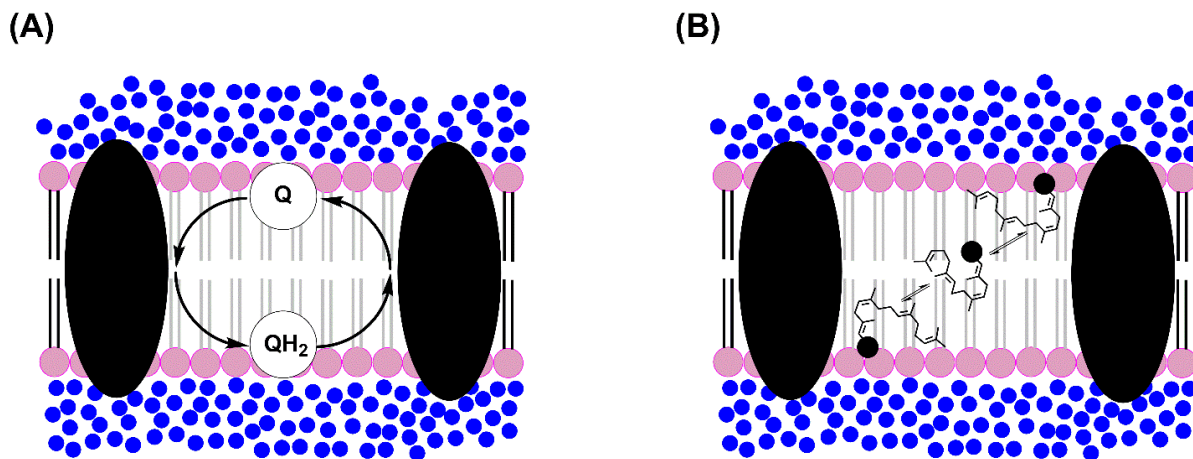**(A)**   **(B)**

Figure 5.4. Comparison between the illustration normally utilized to depict the motion of a general quinone (Q) through the bilayer (A) and a schematic showing that a general quinone (variable headgroup shown by black circle) and that the isoprenoid tail is likely bent.[80, 84-85] The blue circles represent water molecules.

5.3 Summary of Implications of Studying the Interactions between Lipids and Small Molecules and Electron Transporters

5.3.1 Implications for Rational Drug Design

The implications for understanding the chemical and physical characteristics that affect membrane interactions are far reaching into many disciplines, but specifically the research within this thesis is important for rational drug design. When drugs are being rationally designed, they are normally designed to maximize their binding affinity with a target of choice.[17, 38, 40] This less commonly done with lipids as the target. It may be possible to improve on the efficacy of the drug by considering the environment (as shown in chapter 2), along with the specific drug-lipid interactions (chapter 3).[1-2]

5.3.2 Implication for Understanding Electron Transport Systems

Many studies have been conducted on UBQ-10 and PQ-9, but previously, there have been no studies on the interactions of MK-9 with lipid interfaces (chapter 4).[3, 77-79, 81-82, 84] By comparing the interactions of these three quinones, it is clear that these three electron transporters interact with cell membranes in a very similar way.[3, 77-82, 84] Therefore, the isoprenoid tail is likely the important structural component of the quinones that allow for the high flip/flop rate.[84] This would suggest that the headgroup differences likely has a more important role in the specifics with their respective redox potential and possibly binding to the proteins that act on them.[3, 8, 86-88]

5.4 Concluding Remarks

The research presented in this thesis builds a foundation for further research into understanding the factors that play roles in the interactions of molecules with lipid interfaces. The pH dependence of benzoic acid on its placement within the reverse micelle interface is an example of how the environment can affect molecular interactions with an interface.[1] Chapter 3 is an example of how small structural differences can affect the molecular orientation, placement, and membrane interactions.[2] Chapter 4 is an example of how

lipid density can play a role in the lipid interface interactions. These studies together are examples of many factors that play roles in the interactions of different molecules with model membranes, and together point to that membranes are very complicated structures that still have many avenues to explore.

References

(1)   Peters, B. J.; Groninger, A. S.; Fontes, F. L.; Crick, D. C.; Crans, D. C. Differences in Interactions of Benzoic Acid and Benzoate with Interfaces. *Langmuir.* **2016,** *32* (37), 9451-9459.

(2)   Peters, B. J.; Van Cleave, C.; Haase, A. A.; Hough, J. P. B.; Giffen-Kent, K. A.; Cardiff, G. M.; Sostarecz, A. G.; Crick, D. C.; Crans, D. C. Structure Dependence of Pyridine and Benzene Derivatives on Interactions with Model Membranes. *Langmuir.* **2018**.

(3)   A Kurosu, M.; A Begari, E. Vitamin K2 in Electron Transport System: Are Enzymes Involved in Vitamin K2 Biosynthesis Promising Drug Targets? *Molecules.* **2010,** *15*, 1531-1553.

(4)   Allhusen, J. S.; Conboy, J. C. The Ins and Outs of Lipid Flip-Flop. *Acc. Chem. Res.* **2017,** *50* (1), 58-65.

(5)   Allhusen, J. S.; Kimball, D. R.; Conboy, J. C. How the Structural Aspects of Cholesterol Mediate Lipid Flip-Flop. *Biophys. J.* **2016,** *110* (3), 17A-17A.

(6)   Andersson, M. P.; Olsson, M. H. M.; Stipp, S. L. S. Predicting the pK_a and Stability of Organic Acids and Bases at an Oil-Water Interface. *Langmuir.* **2014,** *30* (22), 6437-6445.

(7)   Brul, S.; Coote, P. Preservative Agents in Foods - Mode of Action and Microbial Resistance Mechanisms. *Int. J. Food Microbiol.* **1999,** *50* (1-2), 1-17.

(8)   Crane, F. L.; Sun, I. L.; Barr, R.; Low, H. Electron and Proton Transport across the Plasma-Membrane. *J. Bioenerg. Biomembr.* **1991,** *23* (5), 773-803.

(9)   Delemotte, L.; Dehez, F.; Treptow, W.; Tarek, M. Modeling Membranes under a Transmembrane Potential. *J. Phys. Chem. B.* **2008,** *112* (18), 5547-5550.

(10)   Gurtovenko, A. A.; Vattulainen, I. Molecular Mechanism for Lipid Flip-Flops. *J. Phys. Chem. B.* **2007,** *111* (48), 13554-13559.

(11)   Hac-Wydro, K.; Wydro, P. The Influence of Fatty Acids on Model Cholesterol/Phospholipid Membranes. *Chem. Phys. Lipids.* **2007,** *150* (1), 66-81.

(12)   Jones, M. N., *Micelles, Monolayers, and Biomembranes*. New York : Wiley-Liss: New York, **1995**.

(13)   Tse, E. C. M.; Barile, C. J.; Gewargis, J. P.; Li, Y.; Zimmerman, S. C.; Gewirth, A. A. Anion Transport through Lipids in a Hybrid Bilayer Membrane. *Anal. Chem.* **2015,** *87* (4), 2403-2409.

(14)   Veldhuizen, R.; Nag, K.; Orgeig, S.; Possmayer, F. The Role of Lipids in Pulmonary Surfactant. *Biochim. Biophys. Acta, Mol. Basis Dis.* **1998,** *1408* (2-3), 90-108.

(15)   Citovsky, V.; Zambryski, P. Transport of Nucleic-Acids through Membrane Channels - Snaking through Small Holes. *Annu. Rev. Microbiol.* **1993,** *47*, 167-197.

(16)   Jambeck, J. P. M.; Lyubartsev, A. P. Exploring the Free Energy Landscape of Solutes Embedded in Lipid Bilayers. *J. Phys. Chem. Lett.* **2013,** *4* (11), 1781-1787.

(17)   Lipinski, C. A. Drug-Like Properties and the Causes of Poor Solubility and Poor Permeability. *J. Pharmacol. Toxicol. Methods.* **2000,** *44* (1), 235-249.

(18)   Piper, P.; Calderon, C. O.; Hatzixanthis, K.; Mollapour, M. Weak Acid Adaptation: The Stress Response That Confers Yeasts with Resistance to Organic Acid Food Preservatives. *Microbiology-Sgm.* **2001,** *147*, 2635-2642.

(19)   Piper, P. W., Resistance of Yeasts to Weak Organic Acid Food Preservatives. In *Advances in Applied Microbiology, Vol 77*, Laskin, A. I.; Sariaslani, S.; Gadd, G. M., Eds. 2011; Vol. 77, pp 97-113.

(20)   Wang, S. H.; Larson, R. G. Water Channel Formation and Ion Transport in Linear and Branched Lipid Bilayers. *PCCP.* **2014,** *16* (16), 7251-7262.

(21)   Zhang, Y.; Mitchison, D. The Curious Characteristics of Pyrazinamide: A Review. *Int. J. Tuberc. Lung Dis.* **2003,** *7* (1), 6-21.

(22)   Veber, D. F.; Johnson, S. R.; Cheng, H.-Y.; Smith, B. R.; Ward, K. W.; Kopple, K. D. Molecular Properties That Influence the Oral Bioavailability of Drug Candidates. *J. Med. Chem.* **2002,** *45* (12), 2615-2623.

(23)   Estrada-Tejedor, R.; Sabate, N.; Broto, F.; Nonell, S. Octanol-Water Partition Coefficients of Highly Hydrophobic Photodynamic Therapy Drugs: A Computational Study. *Afinidad.* **2013,** *70* (564), 250-256.

(24)   Kandasamy, S. K.; Larson, R. G. Cation and Anion Transport through Hydrophilic Pores in Lipid Bilayers. *J. Chem. Phys.* **2006,** *125* (7), 07491.

(25)   Loverde, S. M. Molecular Simulation of the Transport of Drugs across Model Membranes. *J. Phys. Chem. Lett.* **2014,** *5* (10), 1659-1665.

(26)   Vraka, C.; Mijailovic, S.; Frohlich, V.; Zeilinger, M.; Klebermass, E. M.; Wadsak, W.; Wagner, K. H.; Hacker, M.; Mitterhauser, M. Expanding Logp: Present Possibilities. *Nucl. Med. Biol.* **2018,** *58*, 20-32.

(27)   Bernardi, P. Mitochondrial Transport of Cations: Channels, Exchangers, and Permeability Transition. *Physiol. Rev.* **1999,** *79* (4), 1127-1155.

(28)   Brown, E. M.; MacLeod, R. J. Extracellular Calcium Sensing and Extracellular Calcium Signaling. *Physiol. Rev.* **2001,** *81* (1), 239-297.

(29)   Lang, F.; Stehle, T.; Haussinger, D. Ion Fluxes During Cell-Volume Regulation in Rat-Liver. *Biol. Chem. Hoppe Seyler.* **1988,** *369* (9), 862-862.

(30)   Lewis, D. L.; Lechleiter, J. D.; Kim, D.; Nanavati, C.; Clapham, D. E. Intracellular Regulation of Ion Channels in Cell-Membranes. *Mayo Clin. Proc.* **1990,** *65* (8), 1127-1143.

(31)   Raab, J. L.; Humphreys, T. Potassium-Ions and Regulation of Cell-Growth in Culture. *Exp. Cell Res.* **1974,** *89* (2), 407-410.

(32)   Traynelis, S. F.; Wollmuth, L. P.; McBain, C. J.; Menniti, F. S.; Vance, K. M.; Ogden, K. K.; Hansen, K. B.; Yuan, H. J.; Myers, S. J.; Dingledine, R. Glutamate Receptor Ion Channels: Structure, Regulation, and Function. *Pharmacol. Rev.* **2010,** *62* (3), 405-496.

(33)   Kirsch, S. A.; Bockmann, R. A. Membrane Pore Formation in Atomistic and Coarse-Grained Simulations. *Biochim. Biophys. Acta, Biomembr.* **2016,** *1858* (10), 2266-2277.

(34)   Paula, S.; Volkov, A. G.; Deamer, D. W. Permeation of Halide Anions through Phospholipid Bilayers Occurs by the Solubility-Diffusion Mechanism. *Biophys. J.* **1998,** *74* (1), 319-327.

(35)   Lin, J. Q.; Dargazany, R.; Alexander-Katz, A. Lipid Flip-Flop and Pore Nucleation on Zwitterionic Bilayers Are Asymmetric under Ionic Imbalance. *Small.* **2017,** *13* (22), 1-10.

(36)   Marrink, S. J.; de Vries, A. H.; Tieleman, D. P. Lipids on the Move: Simulations of Membrane Pores, Domains, Stalks and Curves. *Biochim. Biophys. Acta, Biomembr.* **2009,** *1788* (1), 149-168.

(37)   Dror, R. O.; Green, H. F.; Valant, C.; Borhani, D. W.; Valcourt, J. R.; Pan, A. C.; Arlow, D. H.; Canals, M.; Lane, J. R.; Rahmani, R.; Baell, J. B.; Sexton, P. M.; Christopoulos, A.; Shaw, D. E. Structural Basis for Modulation of a G-Protein-Coupled Receptor by Allosteric Drugs. *Nature.* **2013,** *503* (7475), 295-302.

(38)   Khan, T.; Sankhe, K.; Suvarna, V.; Sherje, A.; Patel, K.; Dravyakar, B. DNA Gyrase Inhibitors: Progress and Synthesis of Potent Compounds as Antibacterial Agents. *Biomed. Pharmacother.* **2018,** *103*, 923-938.

(39)   Liu, Q. S.; Sabnis, Y.; Zhao, Z.; Zhang, T. H.; Buhrlage, S. J.; Jones, L. H.; Gray, N. S. Developing Irreversible Inhibitors of the Protein Kinase Cysteinome. *Chem. Biol.* **2013,** *20* (2), 146-159.

(40)   Rossetti, M.; Porchetta, A. Allosterically Regulated DNA-Based Switches: From Design to Bioanalytical Applications. *Anal. Chim. Acta.* **2018,** *1012*, 30-41.

(41)   Gajate, C.; Mollinedo, F. Lipid Rafts and Fas/Cd95 Signaling in Cancer Chemotherapy. *Recent Pat. Anticancer Drug Discov.* **2011,** *6* (3), 274-283.

(42)   Patra, S. K.; Rizzi, F.; Silva, A.; Rugina, D. O.; Bettuzzi, S. Molecular Targets of (-)-Epigallocatechin-3-Gallate (Egcg): Specificity and Interaction with Membrane Lipid Rafts. *J. Physiol. Pharmacol.* **2008,** *59*, 217-235.

(43)   van Spriel, A. B.; van den Bogaart, G.; Cambi, A. Editorial: Membrane Domains as New Drug Targets. *Front. Physiol.* **2015,** *6*.

(44)   Verma, S. P. Hiv: A Raft-Targeting Approach for Prevention and Therapy Using Plant-Derived Compounds (Review). *Curr. Drug Targets.* **2009,** *10* (1), 51-59.

(45)   Zhang, Y.; Scorpio, A.; Nikaido, H.; Sun, Z. H. Role of Acid Ph and Deficient Efflux of Pyrazinoic Acid in Unique Susceptibility of Mycobacterium Tuberculosis to Pyrazinamide. *J. Bacteriol.* **1999,** *181* (7), 2044-2049.

(46)   Piper, P.; Mahe, Y.; Thompson, S.; Pandjaitan, R.; Holyoak, C.; Egner, R.; Muhlbauer, M.; Coote, P.; Kuchler, K. The Pdr12 Abc Transporter Is Required for the Development of Weak Organic Acid Resistance in Yeast. *EMBO J.* **1998,** *17* (15), 4257-4265.

(47)   Perrin, D. D.; International Union of, P.; Applied Chemistry. Commission on Electrochemical, D., *Dissociation Constants of Organic Bases in Aqueous Solution*. Butterworths: London :, **1965**.

(48)   Dempsy, E. P. S. a. B., *Ionisation Constants of Organic Acids in Aqueous Solution*. Permagamon Press: **1979**.

(49)   Veldhuizen, E. J. A.; Haagsman, H. P. Role of Pulmonary Surfactant Components in Surface Film Formation and Dynamics. *Biochim. Biophys. Acta, Biomembr.* **2000,** *1467* (2), 255-270.

(50)   Mandery, K.; Glaeser, H.; Fromm, M. F. Interaction of Innovative Small Molecule Drugs Used for Cancer Therapy with Drug Transporters. *Br. J. Pharmacol.* **2012,** *165* (2), 345-362.

(51)   Zeth, K.; Thein, M. Porins in Prokaryotes and Eukaryotes: Common Themes and Variations. *Biochem. J.* **2010,** *431*, 13-22.

(52)   Chimote, G.; Banerjee, R. Evaluation of Antitubercular Drug Insertion into Preformed Dipalmitoylphosphatidylcholine Monolayers. *Colloids Surf. B. Biointerfaces.* **2008,** *62* (2), 258-264.

(53)   Barry, J.; Fritz, M.; Brender, J. R.; Smith, P. E. S.; Lee, D. K.; Ramamoorthy, A. Determining the Effects of Lipophilic Drugs on Membrane Structure by Solid-State Nmr Spectroscopy: The Case of the Antioxidant Curcumin. *J. Am. Chem. Soc.* **2009,** *131* (12), 4490-4498.

(54)   Scorpio, A.; Zhang, Y. Mutations in PncA, a Gene Encoding Pyrazinamidase/Nicotinamidase, Cause Resistance to the Antituberculous Drug Pyrazinamide in Tubercle Bacillus. *Nat. Med.* **1996,** *2* (6), 662-667.

(55)   Lu, P.; Haagsma, A. C.; Pham, H.; Maaskant, J. J.; Mol, S.; Lill, H.; Bald, D. Pyrazinoic Acid Decreases the Proton Motive Force, Respiratory ATP Synthesis Activity, and Cellular ATP Levels. *Antimicrob. Agents Chemother.* **2011,** *55* (11), 5354-5357.

(56)   Laborde, J.; Deraeve, C.; Bernardes-Genisson, V. Update of Antitubercular Prodrugs from a Molecular Perspective: Mechanisms of Action, Bioactivation Pathways, and Associated Resistance. *Chemmedchem.* **2017,** *12* (20), 1657-1676.

(57)   Zhang, Y.; Wade, M. M.; Scorpio, A.; Zhang, H.; Sun, Z. H. Mode of Action of Pyrazinamide: Disruption of Mycobacterium Tuberculosis Membrane Transport and Energetics by Pyrazinoic Acid. *J. Antimicrob. Chemother.* **2003,** *52* (5), 790-795.

(58)   Shi, W. L.; Zhang, X. L.; Jiang, X.; Yuan, H. M.; Lee, J. S.; Barry, C. E.; Wang, H. H.; Zhang, W. H.; Zhang, Y. Pyrazinamide Inhibits Trans-Translation in Mycobacterium Tuberculosis. *Science.* **2011,** *333* (6049), 1630-1632.

(59)   Kalinda, A. S.; Aldrich, C. C. Pyrazinamide: A Frontline Drug Used for Tuberculosis. Molecular Mechanism of Action Resolved after 50 Years? *Chemmedchem.* **2012,** *7* (4), 558-560.

(60)   Krebs, H. A.; Wiggins, D.; Stubbs, M.; Sols, A.; Bedoya, F. Studies on the Mechanism of the Anti-Fungal Action of Benzoate. *Biochem. J.* **1983,** *214* (3), 657-663.

(61) Borba, A.; Lairion, F.; Disalvo, A.; Fausto, R. Interaction of Nicotinamide and Picolinamide with Phosphatidylcholine and Phosphatidylethanolamine Membranes: A Combined Approach Using Dipole Potential Measurements and Quantum Chemical Calculations. *Biochim. Biophys. Acta, Biomembr.* **2009,** *1788* (12), 2553-2562.

(62) Borba, A.; Albrecht, M.; Gomez-Zavaglia, A.; Lapinski, L.; Nowak, M. J.; Suhm, M. A.; Fausto, R. Dimer Formation in Nicotinamide and Picolinamide in the Gas and Condensed Phases Probed by Infrared Spectroscopy. *PCCP.* **2008,** *10* (46), 7010-7021.

(63) Cantor, R. S. Lipid Composition and the Lateral Pressure Profile in Bilayers. *Biophys. J.* **1999,** *76* (5), 2625-2639.

(64) Mouritsen, O. G., *Life - as a Matter of Fat : Lipids in a Membrane Biophysics Perspective*. Second edition. ed.; Cham : Springer: **2016**.

(65) Stillwell, W.; Stillwell, W., *An Introduction to Biological Membranes Composition, Structure and Function Second Edition Preface*. **2016**; p IX-X.

(66) Gew, L. T.; Misran, M. Interaction between C18 Fatty Acids and Dope Peg2000 in Langmuir Monolayers: Effect of Degree of Unsaturation. *J. Biol. Phys.* **2017,** *43* (3), 397-414.

(67) Gew, L. T.; Misran, M. Energetic Mixing of Anti-Snap25 on Lipid Monolayers: Degree of Saturation of C18 Fatty Acids. *Surf. Interface Anal.* **2017,** *49* (5), 388-397.

(68) Hac-Wydro, K.; Jedrzejek, K.; Dynarowicz-Latka, P. Effect of Saturation Degree on the Interactions between Fatty Acids and Phosphatidylcholines in Binary and Ternary Langmuir Monolayers. *Colloids Surf. B. Biointerfaces.* **2009,** *72* (1), 101-111.

(69) Chabanel, A.; Flamm, M.; Sung, K. L. P.; Lee, M. M.; Schachter, D.; Chien, S. Influence of Cholesterol Content on Red-Cell Membrane Viscoelasticity and Fluidity. *Biophys. J.* **1983,** *44* (2), 171-176.

(70) Choi, Y.; Attwood, S. J.; Hoopes, M. I.; Drolle, E.; Karttunen, M.; Leonenko, Z. Melatonin Directly Interacts with Cholesterol and Alleviates Cholesterol Effects in Dipalmitoylphosphatidylcholine Monolayers. *Soft Matter.* **2014,** *10* (1), 206-213.

(71) Hong, Z. K.; Ersoy, I.; Sun, M. Z.; Bunyak, F.; Hampel, P.; Hong, Z. L.; Sun, Z.; Li, Z. H.; Levitan, I.; Meininger, G. A.; Palaniappan, K. Influence of Membrane Cholesterol and Substrate Elasticity on Endothelial Cell Spreading Behavior. *J. Biomed. Mater. Res. A.* **2013,** *101* (7), 1994-2004.

(72) Bhattacharya, S.; Haldar, S. Interactions between Cholesterol and Lipids in Bilayer Membranes. Role of Lipid Headgroup and Hydrocarbon Chain-Backbone Linkage. *Biochim. Biophys. Acta, Biomembr.* **2000,** *1467* (1), 39-53.

(73) Lintker, K. B.; Kpere-Daibo, P.; Fliesler, S. J.; Serfis, A. B. A Comparison of the Packing Behavior of Egg Phosphatidylcholine with Cholesterol and Biogenically Related Sterols in Langmuir Monolayer Films. *Chem. Phys. Lipids.* **2009,** *161* (1), 22-31.

(74) Marquardt, D.; Kucerka, N.; Wassall, S. R.; Harroun, T. A.; Katsaras, J. Cholesterol's Location in Lipid Bilayers. *Chem. Phys. Lipids.* **2016,** *199*, 17-25.

(75) Jo, S.; Rui, H. A.; Lim, J. B.; Klauda, J. B.; Im, W. Cholesterol Flip-Flop: Insights from Free Energy Simulation Studies. *J. Phys. Chem. B.* **2010,** *114* (42), 13342-13348.

(76) Bernard, S.; Roche, Y.; Etienne, F.; Peretti, P. Interaction between Ubiquinones and Dipalmitoylphosphatidylcholine in Mixed Langmuir Monolayers. *Mol. Cryst. Liq. Cryst.* **2000,** *338*, 207-221.

(77) Hoyo, J.; Guaus, E.; Torrent-Burgues, J.; Sanz, F. Biomimetic Monolayer Films of Digalactosyldiacylglycerol Incorporating Plastoquinone. *Biochim. Biophys. Acta, Biomembr.* **2015,** *1848* (6), 1341-1351.

(78) Hoyo, J.; Guaus, E.; Torrent-Burgues, J.; Sanz, F. Biomimetic Mono Layer Films of Monogalactosyldiacylglycerol Incorporating Plastoquinone. *J. Phys. Chem. B.* **2015,** *119* (20), 6170-6178.

(79) Hoyo, J.; Torrent-Burgues, J.; Guaus, E. Biomimetic Monolayer Films of Monogalactosyldiacylglycerol Incorporating Ubiquinone. *J. Colloid Interface Sci.* **2012,** *384*, 189-197.

(80) Koehn, J. T.; Magallanes, E. S.; Peters, B. J.; Beuning, C. N.; Haase, A. A.; Zhu, M. J.; Rithner, C. D.; Crick, D. C.; Crans, D. C. A Synthetic Isoprenoid Lipoquinone, Menaquinone-2, Adopts a Folded Conformation in Solution and at a Model Membrane Interface. *J. Org. Chem.* **2018,** *83* (1), 275-288.

(81) Nerdal, W.; Nilsen, T. R. S.; Steinkopf, S. Coenzymeq(10), Localizations in Model Membranes. A Langmuir Monolayer Study. *Biophys. Chem.* **2015,** *207*, 74-81.

(82) Quinn, P. J.; Esfahani, M. A. Ubiquinones Have Surface-Active Properties Suited to Transport Electrons and Protons across Membranes. *Biochem. J.* **1980,** *185* (3), 715-722.

(83) Ragan, C. I.; Cottingham, I. R. The Kinetics of Quinone Pools in Electron-Transport. *Biochim. Biophys. Acta.* **1985,** *811* (1), 13-31.

(84) Kaurola, P.; Sharma, V.; Vonk, A.; Vattulainen, I.; Rog, T. Distribution and Dynamics of Quinones in the Lipid Bilayer Mimicking the Inner Membrane of Mitochondria. *Biochim. Biophys. Acta, Biomembr.* **2016,** *1858* (9), 2116-2122.

(85) Szterk, A.; Zmysłowski, A.; Bus, K. Identification of Cis/Trans Isomers of Menaquinone-7 in Food as Exemplified by Dietary Supplements. *Food Chem.* **2018,** *243*, 403-409.

(86) Rokitskaya, T. I.; Murphy, M. P.; Skulachev, V. P.; Antonenko, Y. N. Ubiquinol and Plastoquinol Triphenylphosphonium Conjugates Can Carry Electrons through Phospholipid Membranes. *Bioelectrochemistry.* **2016,** *111*, 23-30.

(87) Tikhonov, A. N.; Vershubskii, A. V. Computer Modeling of Electron and Proton Transport in Chloroplasts. *BioSyst.* **2014,** *121*, 1-21.

(88) Hoyo, J.; Guaus, E.; Torrent-Burgues, J.; Sanz, F. Electrochemical Behaviour of Mixed LB Films of Ubiquinone - DPPC. *J. Electroanal. Chem.* **2012,** *669*, 6-13.

Appendix I: Contributions to Works

The material in chapter one is primarily review and background knowledge of lipids and cell membrane composition. Figures 1.2-1.5 were originally prepared or adapted for this thesis. Table 1.1 is partially from literature and partially from calculations performed using literature values for this thesis.

The material in chapter two is published in *Langmuir* with Benjamin J. Peters as the primary author. Coauthors include Allison S. Groninger, Fabio L. Fontes, Dean C. Crick, and Debbie C. Crans. Allison Groninger was an undergraduate student who contributed by working through many of the issues related to method development for the Langmuir monolayer studies. Fabio Fontes and Dean Crick, contributed valuable advice and direction. Debbie Crans guided me through the process of writing this manuscript and taught me many lessons along the way about communicating science along with writing the majority of the ^{1}H-^{1}H 2D NOESY NMR section. For this work, Benjamin Peters acquired all data presented, analysis of the data, and did most of the preparation of the published manuscript.[1]

The material in chapter three was submitted and accepted with minor revisions to *Langmuir* with Benjamin J. Peters as the primary author. Coauthors include Cameron Van Cleave, Allison A. Haase, John Peter B. Hough, Keisha A. Giffen-Kent, Gabriel M. Cardiff, Audra G. Sostarecz, Dean C. Crick, and Debbie C. Crans. Cameron Van Cleave, Allison A. Haase, and John Peter B. Hough contributed to the DPPE Langmuir monolayer experiments. Keisha A. Giffen-Kent and Gabriel M. Cardiff contributed by assisting in the isoniazid and benzhydrazide titrations in both D_2O and reverse micelle samples through ^{1}H 1D NMR experimentation. Audra G. Sostarecs contributed very valuable advice for interpretation of the Langmuir monolayer studies. Dean C. Crick, was always there for support for determining the story and always willing to talk about the science. Debbie C. Crans helped set up meetings, give valuable insight into the story, and help with interpretation of the data. I would like to give a special thanks to Chris Rithner for

valuable input on preparing the ^{1}H-^{1}H 2D NMR spectra. For this work, Benjamin Peters acquired all the DPPC Langmuir monolayer data, all the ^{1}H-^{1}H 2D NOESY and ROESY data, determined the pK$_a$ values, acquired the ^{1}H 1D NMR data for isonicotinamide, nicotinamide, picolinamide, and benzamide, prepared all NMR data, and prepared the majority of the manuscript.[2]

The material in chapter four is in preparation to be submitted to *Langmuir* with Benjamin J. Peters as the primary author. Coauthors include Cameron Van Cleave, Allison A. Haase, Katarina R. Werst, Brandon Allen, Dean C. Crick, and Debbie C. Crans. For this work, Cameron Van Cleave, Allison A. Haase, and Katarina R. Werst acquired most of the data for the compression isotherm experiments for the MK-9 and phospholipid pure and mixed monolayers. Brandon Allen computed the ideal area isotherm curves. Cameron Van Cleave prepared data that was used for the GIF (graphical image format) videos. Dean C. Crick and Debbie C. Crans provided valuable insight and advice. Benjamin Peters designed and determined experimental parameters, conducted the Brewster angle microscopy experiments, interpreted the data, and is currently preparing the manuscript for publication.

The material in chapter 5 is an outline of where Benjamin Peters believes this data fits with current knowledge of membrane interactions and diffusion across cell membranes. All figures were originally prepared for this thesis.

The following appendices state my contributions to the published works that are not discussed within the chapters of this thesis or are supplementary figures useful for further interpretation of the data.

References

(1)   Peters, B. J.; Groninger, A. S.; Fontes, F. L.; Crick, D. C.; Crans, D. C. Differences in Interactions of Benzoic Acid and Benzoate with Interfaces. *Langmuir.* **2016,** *32* (37), 9451-9459.

(2)   Peters, B. J.; Van Cleave, C.; Haase, A. A.; Hough, J. P. B.; Giffen-Kent, K. A.; Cardiff, G. M.; Sostarecz, A. G.; Crick, D. C.; Crans, D. C. Structure Dependence of Pyridine and Benzene Derivatives on Interactions with Model Membranes. *Langmuir.* **2018.**

Appendix II: ^{1}H 1D NMR spectrum of Benzoic Acid in Isooctane
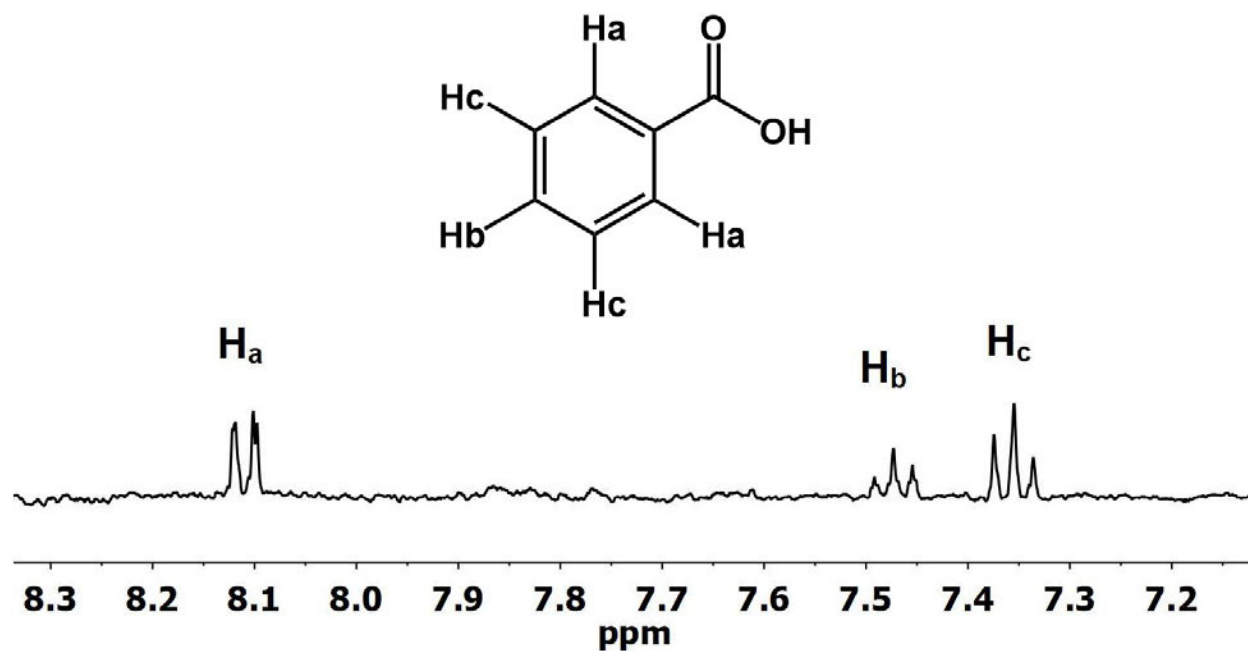
Figure A2.1: ^{1}H 1D NMR spectrum of 10 mM benzoic in 95% isooctane/5% d_{12}-cyclohexane (referenced to the tetramethyl silane peak at 0 ppm). Labeled protons refer to HB structure given.[1]

Reference

(1)   Peters, B. J.; Groninger, A. S.; Fontes, F. L.; Crick, D. C.; Crans, D. C. Differences in Interactions of Benzoic Acid and Benzoate with Interfaces. *Langmuir.* **2016,** *32* (37), 9451-9459.

Figure A3.1. ^{1}H NMR spectrum and chemical structure depicting sodium aerosol-OT (AOT) with protons labeled for NMR interpretation forming w_0 12 reverse micelles (RMs) with D_2O. It is important to note that regions near the sulfonate of the AOT molecule may reside within an aqueous environment, while the AOT hydrocarbon tails reside within isooctane. The HOD chemical shift is consistent with the chemical shift found by *Maitra et al* showing the w_0 of the reverse micelle used to obtain this spectrum is consistent with literature.[1-2]

References

(1)   Maitra, A. Determination of Size Parameters of Water Aerosol OT Oil Reverse Micelles from Their Nuclear Magnetic-Resonance Data. *J. Phys. Chem.* **1984,** *88* (21), 5122-5125.

(2)   Peters, B. J.; Van Cleave, C.; Haase, A. A.; Hough, J. P. B.; Giffen-Kent, K. A.; Cardiff, G. M.; Sostarecz, A. G.; Crick, D. C.; Crans, D. C. Structure Dependence of Pyridine and Benzene Derivatives on Interactions with Model Membranes. *Langmuir.* **2018**.

Appendix IV: Determination of pKₐ values through ^{1}H 1D NMR Titrations
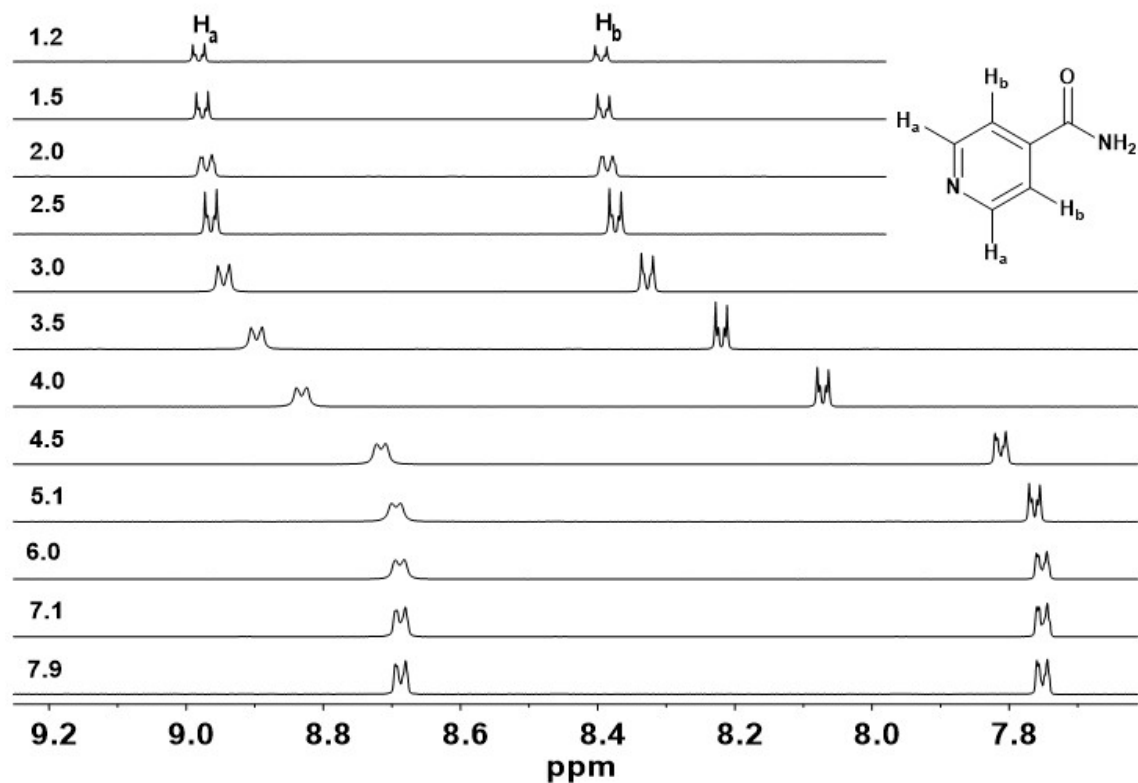
Figure A4.1. an example titration of iNIC in D_2O. The pH is indicated on the left of each 1D ^{1}H spectrum in the stack plot. The chemical shifts of the H_a peak were then plotted as a function of pH as shown in Figure A4.2.[1-2]
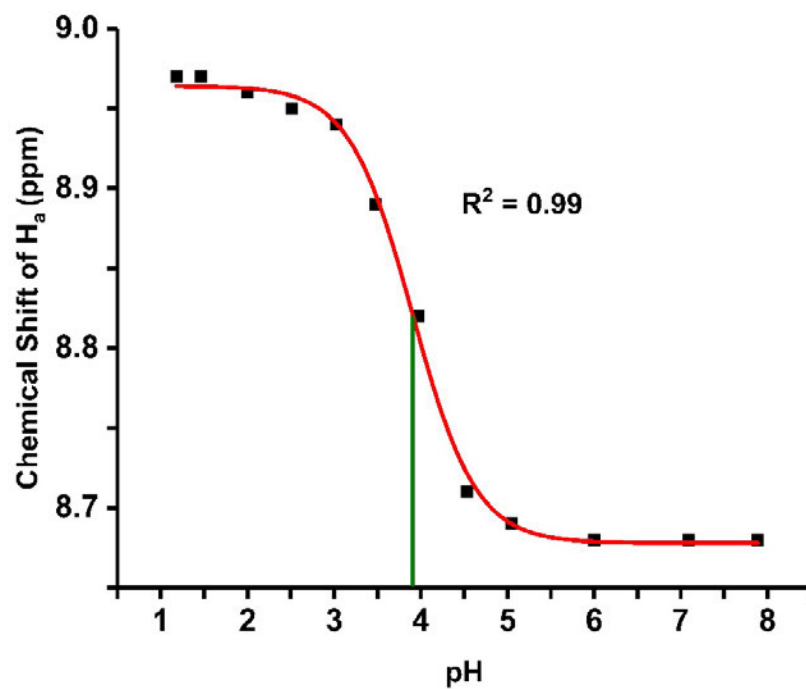
Figure A4.2. To determine the pK_a of each compound, the chemical shifts of H_a was graphed as a function of pH (right) and a best fit sigmoidal curve was fit to the points. The first derivative was taken of this best fit curve to determine the pH at which the slope was the largest (green line) and this was reported as the pK_a value of each compound. This method was used for all compounds of interest in reverse micelles and D_2O.[1-2]

References

(1)   Peters, B. J.; Groninger, A. S.; Fontes, F. L.; Crick, D. C.; Crans, D. C. Differences in Interactions of Benzoic Acid and Benzoate with Interfaces. *Langmuir.* **2016,** *32* (37), 9451-9459.

(2)   Peters, B. J.; Van Cleave, C.; Haase, A. A.; Hough, J. P. B.; Giffen-Kent, K. A.; Cardiff, G. M.; Sostarecz, A. G.; Crick, D. C.; Crans, D. C. Structure Dependence of Pyridine and Benzene Derivatives on Interactions with Model Membranes. *Langmuir.* **2018**.
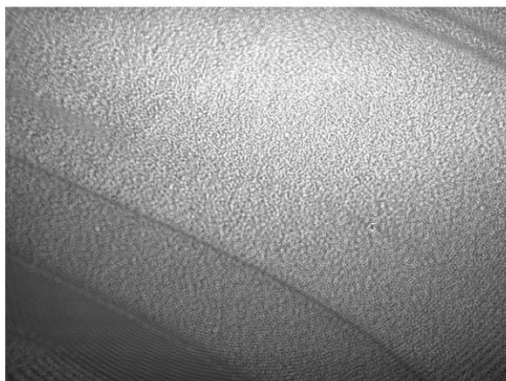
Appendix V: Compression Isotherms Comparison of Different Subphases
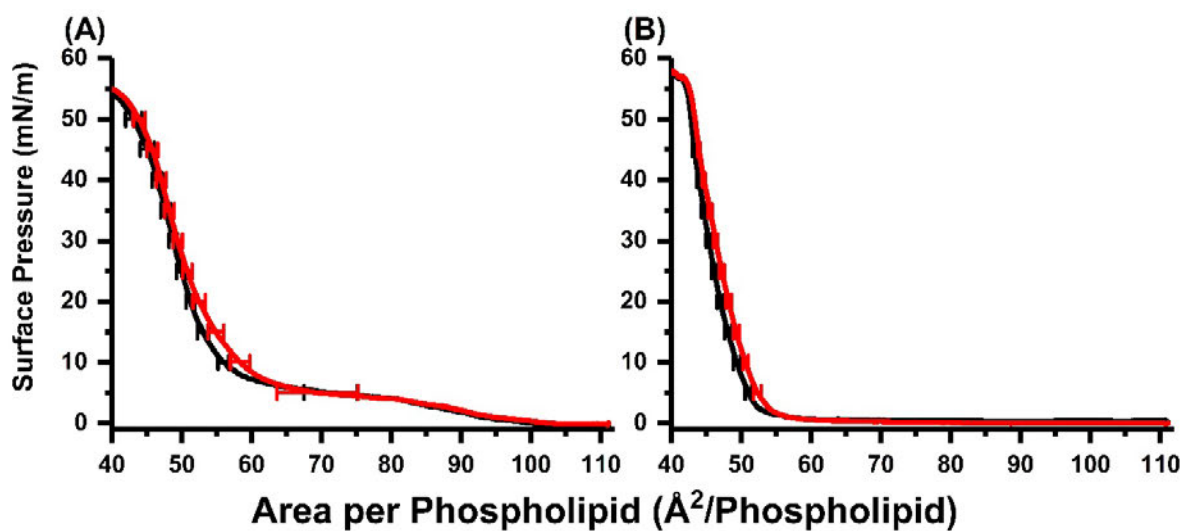
Figure A5.1. Surface pressure compression isotherms of DPPC (A) or DPPE (B) film on a subphase containing 20 mM phosphate buffer (pH 7.4, red) and DPPC film on a subphase consisting of only DDI H_2O (pH 7.4 black).[1-2]

References

(1)   Peters, B. J.; Groninger, A. S.; Fontes, F. L.; Crick, D. C.; Crans, D. C. Differences in Interactions of Benzoic Acid and Benzoate with Interfaces. *Langmuir.* **2016,** *32* (37), 9451-9459.

(2)   Peters, B. J.; Van Cleave, C.; Haase, A. A.; Hough, J. P. B.; Giffen-Kent, K. A.; Cardiff, G. M.; Sostarecz, A. G.; Crick, D. C.; Crans, D. C. Structure Dependence of Pyridine and Benzene Derivatives on Interactions with Model Membranes. *Langmuir.* **2018**.

Appendix VI: Brewster Angle Microscopy of MK-9 Post-Collapse
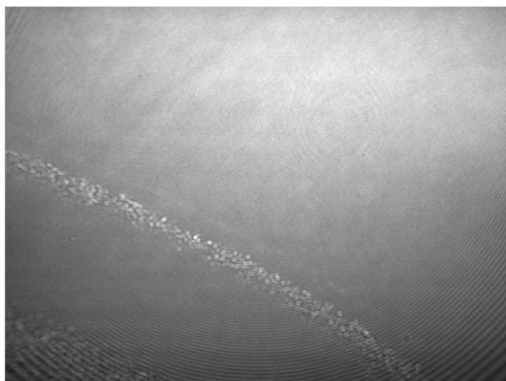

50 nmol MK-9 Post-Collapse

1 min

5 min   **10 min**
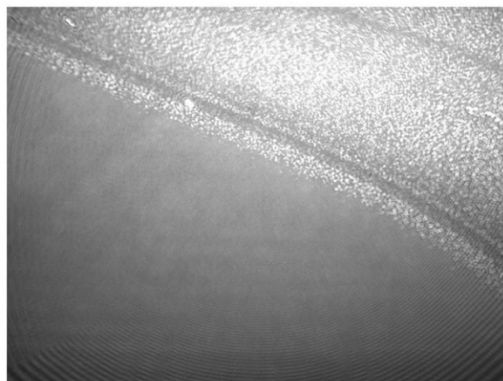
15 min   **20 min**

Figure A6.1. BAM images of post compression isotherm collapse of monolayers consisting of 50 nmoles of MK-9. Times post-collapse are given with corresponding images below.

Appendix VII: Brewster Angle Microscopy of Mixed and Pure
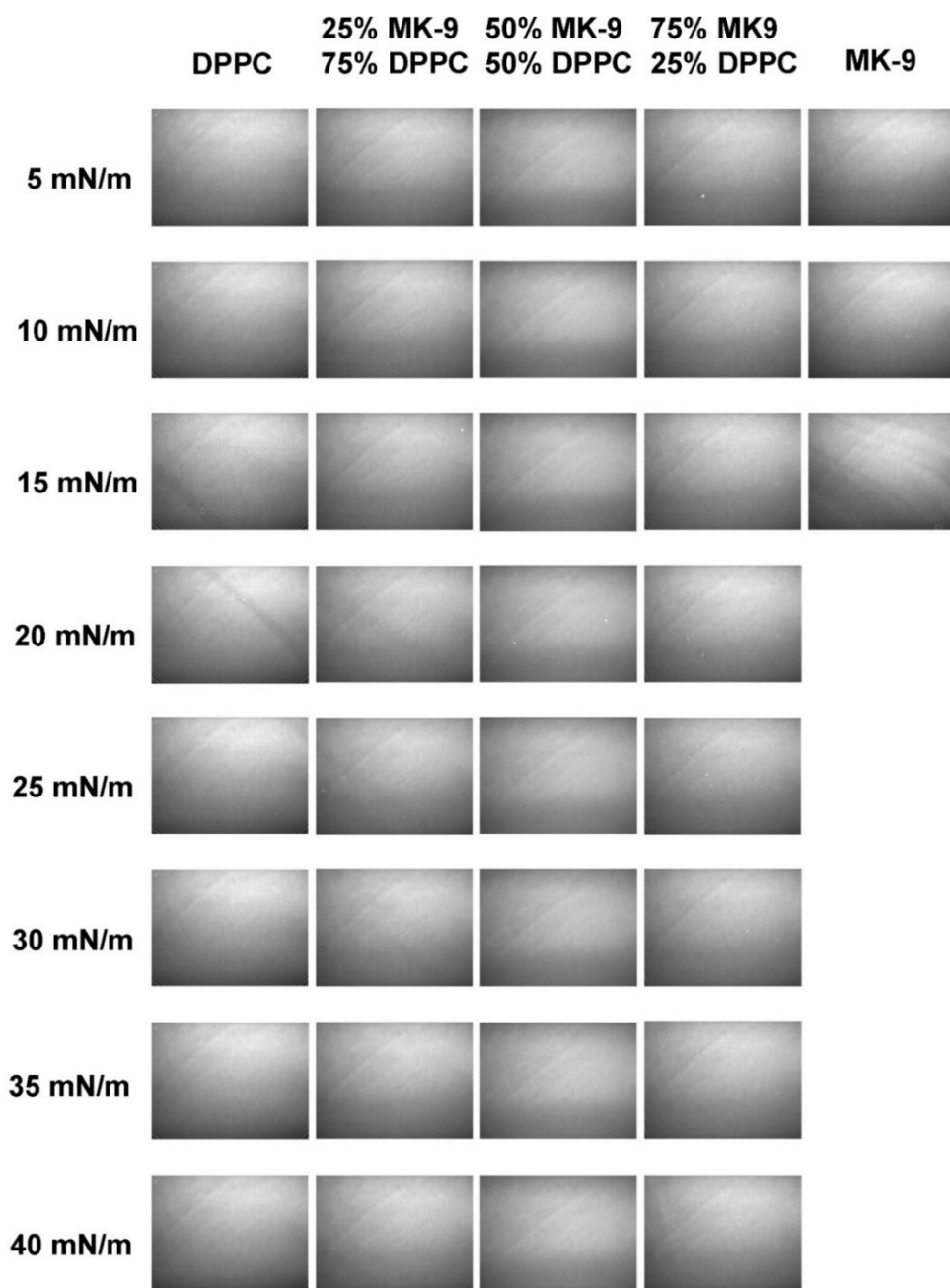
Monolayers of MK-9 and DPPC

Figure A7.1 BAM images of DPPC, 25% MK-9 and 75% DPPC, 50% MK-9 and 50% DPPC, 75% MK-9 and 25% DPPC monolayers and a monolayer consisting of 50 nmol of MK-9 (left column to right column respectively). Surface pressures are given on the left every 5 mN/m until 40 mN/m.

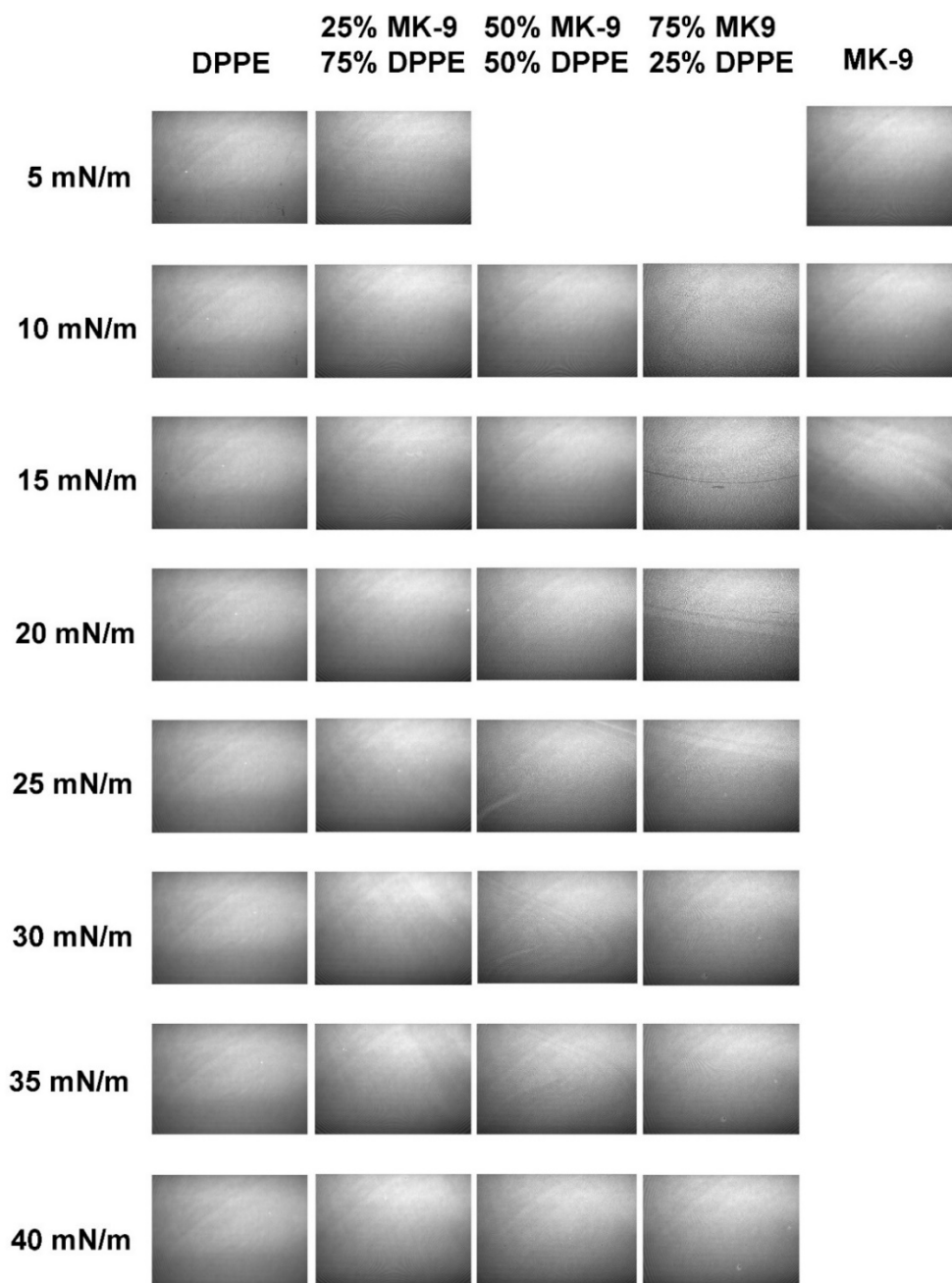# Appendix VIII: Brewster Angle Microscopy of Mixed and Pure Monolayers of MK-9 and DPPE

Figure A8.1. BAM images of DPPE, 25% MK-9 and 75% DPPE, 50% MK-9 and 50% DPPE, 75% MK-9 and 25% DPPE monolayers and a monolayer consisting of 50 nmol of MK-9 (left column to right column respectively). Surface pressures are given on the left every 5 mN/m until 40 mN/m.

Appendix IX: Vanadium-phosphatase complexes: Phosphatase Inhibitors Favor the Trigonal Bipyramidal Transition State Geometries

Reference

(1)   McLauchlan, C. C.; Peters, B. J.; Willsky, G. R.; Crans, D. C. Vanadium-Phosphatase Complexes: Phosphatase Inhibitors Favor the Trigonal Bipyramidal Transition State Geometries. *Coord. Chem. Rev.* **2015,** *301*, 163-199.

Contents lists available at ScienceDirect

Coordination Chemistry Reviews

journal homepage: www.elsevier.com/locate/ccr

Review

Vanadium–phosphatase complexes: Phosphatase inhibitors favor the trigonal bipyramidal transition state geometries

Craig C. McLauchlan[a,*], Benjamin J. Peters[b], Gail R. Willsky[c], Debbie C. Crans[b,*]

[a] Department of Chemistry, Illinois State University, Campus Box 4160, Normal, IL 61790, USA
[b] Department of Chemistry, Colorado State University, Fort Collins, CO 80523, USA
[c] Department of Biochemistry, School of Medicine and Biomedical Sciences, University at Buffalo (State University of New York, SUNY), Buffalo, NY 14214, USA

Contents

ABSTRACT

Over the past two decades increasing information about the function and structural detail of phosphatases has become available detailing the interaction with vanadate or other vanadium compounds. Considering the importance of the phosphorylation reaction in signal transductions the structural details of the inter-action of vanadate or other vanadium species with many phosphatases are used to provide information on the nature of successful inhibitors of these enzymes. Analysis shows that most of the available X-ray

structures of vanadium–phosphatase complexes contain vanadium with five coordinating atoms in trigonal bipyramidal coordination geometries even though corresponding small molecule analog compounds may have square pyramidal geometries. This finding for the static structures in their solid state documents the fact that the variety of phosphatases all stabilize a vanadium geometry that is closer to the trigonal bipyramidal geometry than square pyramidal geometry. We also review the efficacy of vanadium-based inhibitors and examine both oxometalates and vanadium coordination complexes. The evaluation of the inhibitory efficacies of the oxometalates provides the opportunity to identify product-based inhibitors and transition-state-based inhibitors. Whether initial coordination geometry is important to inhibitor design geometry was examined. For vanadium–phosphatase complexes, regardless of what form was added to the protein crystal in all but one case vanadate was found bound in the phosphatase. Because of speciation considerations and prior hydrolysis of potential vanadium complexes, this result may be a consequence of the experimental conditions. With regard to inhibition we find that the coordination geometry of the starting complex does not need to be trigonal bipyramidal to result in a effective phosphatase inhibitor and that all reported phosphatase inhibitors span a range of only three orders of magnitude in K_i across all phosphatases examined.

1. Introduction

Removing a phosphate group from a biomolecule is a central reaction in biology and catalyzed by a range of enzymes, collectively named phosphatases [1–5]. Phosphorylation/dephosphorylation is currently recognized as a major metabolic control system that activates or inhibits metabolic reactions by affecting the phosphorylation state of metabolites and enzymes [1,6–8]. A number of chemical signaling systems have been used throughout molecular evolution. Examples include ribosylation, adenylation, isoprenylation and methylation [9]. Because phosphorylation introduces a charge and sometimes even a double charge, often a dramatic change of a protein properties result, which will impact how the different parts of protein folds associate with each other and the protein surface. Specifically, in some cases phosphorylations change a hydrophobic surface or neutral surface into a hydrophilic surface, thus destroying an interaction that may have been favorable prior to the phosphorylation [5,10]. Therefore, phosphorylation is a well suited process to alter properties of peptides and thus modulate the activity of enzymes in crucial metabolic pathways. For phosphorylation of proteins, several different types of amino acid side chains are typically phosphorylated inducing various regulatory responses in the cell; serine, threonine, tyrosine, and aspartate result in an O-phosphate group, histidine, arginine, and lysine result in an N-phosphate group, and cysteine results in a S-phosphate group, each of which result in a different response. Phosphatases are enzymes that remove these phosphate group by dephosphorylation [1,11], and thus important contributors in signal transduction pathways. This process supports a simple switch system, which is easily adopted to "turn on" and "turn off" important processes by phosphorylation/dephosphorylation of the enzymes in question. Alternatively, understanding the inhibition of these enzymes is important, and this manuscript concerns how vanadate and related vanadium compounds inhibit phosphatases [12–15].

The introduction of the charged phosphate group is also important for the small molecules of intermediary metabolism. For example, the intracellular phosphorylation of glucose by hexokinase is well known to trap glucose inside the cell as the charged glucose-6-phosphate, which is not recognized by the GLUT facilitated diffusion transporters located in the plasma membranes whether or not their presence in the plasma membrane is strongly insulin sensitive [16,17]. Whether the phosphorylated form of the metabolite or protein is active or inactive, it is critical to recognize that the dephosphorylated form will have the opposite action. Nature chose well because multiple chemical moieties (OH, NH, SH) can be phosphorylated making phosphorylation a widely applicable system with several levels of control.

Indeed, the specificity of phosphatases is an important part of metabolic regulation and changing concentrations of substrates and inhibitors of phosphatases can have a large effect. Specificity of the phosphatases for a particular phosphatase inhibitor leading to an effect in some metabolic pathways, but not others is critical for this regulation. This process can occur if the inhibitor contains some recognition feature on the organic part of the substrate or a specific part of the enzyme as an allosteric regulator.

Of the alternative mechanisms for signaling processes, methylation is the system of choice for fine tuning metabolic signaling via epigenetic (or post-translational) modification [9,18]. Methylation is increasingly found to be important in other biological processes such as translation [19] and protein degradation of other cellular proteins [9]. Because methylation generally changes the hydrophobicity, the changes in peptide structure by methylation, although significant, will not be as large as the introduction of a charge. The change in hydrophobicity by a methyl group is however sufficient to affect the conformation and shape of the peptide fragment in a protein. Specifically, DNA is not likely to bind to hydrophobic regions in the histones. Although there are no charge changes in these modifications and interactions, increased hydrophobicity could modulate the affinity of the DNA for the histone protein and thus fine-tune the associations between hydrophobic surface in the histone and DNA. Therefore, from a chemical and biophysical perspective the choice of chemical modification distribution on major and minor signal transduction control pathways makes sense. The methylation of amines or thiols are changes that will affect the conformation choice of a peptide in contrast to the phosphorylation which dramatically affects the peptide properties; as a result methylation is used for fine-tuning the histone binding to DNA and phosphorylation is used as the major regulatory control in biological systems on a wide range of systems.

Because of the key role of phosphatases in signal transduction, it is not surprising that these enzymes have become a key target for studying metabolism [10], for modifying cell signaling [20,21], and for treatment of diseases [10,22]. Specifically, phosphatases have been targeted as an entry for treatment of diabetes [23–29] and trypanosomal diseases such as Chagas disease and leishmaniasis [30–34], often with vanadium species. Orthovanadate, the simple vanadium oxoanion often called just vanadate (VO_4^{3-}), is a well-known inhibitor of phosphatases [12–15], and because of its potency has been studied with many different enzymes [35,36]. The effects of vanadate have stimulated the development and testing of many other vanadium compounds as phosphatase inhibitors [37–40]. This review will investigate the reported X-ray structures of phosphatases with a vanadium bound in the active site as illustrated in Fig. 1 [41]. We chose to use X-ray crystallographic data, because they provide the opportunity to observe molecular details,
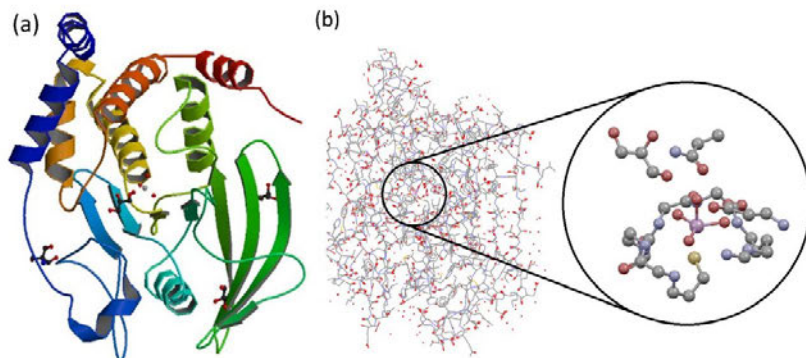
Fig. 1. The X-ray structure from *H. sapiens* protein tyrosine phosphatase 1B, PDB ID 3i80 [41], displayed as (a) a ribbon diagram of the vanadium–protein complex and (b) a ball and stick representation along with an inset of the environment surrounding the active site containing vanadate. Key to atom coloring: C, gray; N, blue; O, red; S, yellow; V, lilac.

albeit of the static structures in the solid state. After removing the layers of protein in silico, the details of the binding in the active site can be investigated. The crystallographic studies require the formation of single crystals for analysis by X-ray diffraction but with different crystallizing techniques it becomes possible to "trap" a protein in many different conformations along its reaction pathway [42]. Accordingly one would expect that protein–vanadium complexes might form containing different types of bound vanadium. In this work we analyze the coordination environment around the vanadium with a focus on the groups immediately near the vanadium, i.e. whether the vanadium is four- or five-coordinate and if the five-coordinate structure has geometry better described as trigonal bipyramidal or square pyramidal. Although some effects are clearly induced by the second coordination sphere [43] the main focus of this review is on the first coordination sphere around the vanadium.

Enzyme and phosphatase nomenclature, in general, can follow several strategies. The importance of accurate descriptions is critical, though, as there are at least 424 synonyms compiled for protein-tyrosine-phosphatases alone [44]. The strategy taken by the Enzyme Commission (EC) is to classify the proteins by the *reaction* they catalyze (see below) [45]. When two different proteins catalyze the same reaction, they then share the same EC number. From a mechanistic perspective we can also classify the phosphatases by the nature of the amino acid that serves as the nucleophile in the active site of the enzyme, i.e. transferases [46]. This organization is that which historically has been termed acid, alkaline, and protein phosphatases and other phosphatases that do not follow any of these categories such as purple acid phosphatase and some of the bacterial phosphatases [37,47]. The reader is referred to previous literature describing the enzymology of many known phosphatases [47–49], whereas the original work describing the inhibition by vanadate and other vanadium compounds is highlighted in this review. While this work was underway, an analysis of the vanadium in structural biology was reported [50] cataloging all the protein complexes containing vanadium from the Protein Data Bank (PDB) [51]. That study provides a list of amino acid residues within 5 Å of the vanadium and also analyzes enzyme classes other than those that perform hydrolysis, such as transferases and oxidoreductases. Thus, they did not focus on the phosphatases, nor was the chemistry and structural detail of any of the five-coordinate vanadium compounds considered, which likely impacted their conclusions [50]. In this review, we will analyze the coordination geometry of the vanadium in the active sites of these protein structures and their coordination geometries.

It is the objective of this work to determine if the observed and reported structure contains a trigonal bipyramidal (TBP) vanadium or a square pyramidal (SP) vanadium. We aim to examine whether known inhibitors have the same geometry as the protein complexes and to consider the possibility that such geometry would produce more potent inhibitor design.

2. Fundamentals of phosphate ester hydrolysis; reaction, transition state and categorization

2.1. Enzyme-catalyzed hydrolysis of phosphate esters

Generally, phosphatases catalyze the hydrolysis reaction of an organic phosphate ester, illustrated in Fig. 2. The reaction has been observed over a wide pH range and thus is likely to involve different protonation states of the phosphate ester [5,52]. The reaction mechanism has been studied in aqueous solution and differences in the detailed reaction mechanism have been reported in the monoprotonated phosphoester and deprotonated phosphoester hydrolysis. Because the pK_a values of most phosphate monoesters are in the pH range 7–8, the hydrolysis reaction under physiological pH is taking place in a pH range where two protonation states of the phosphoester exist, namely $ROPO_3^{2-}$ and $ROPO_3H^-$.

Historically phosphatases were classified as belonging to one of five well-characterized classes of hydrolases, namely (1) alkaline phosphatases (containing a serine OH in the active site) [48], (2) low molecular weight acid phosphatases (containing histidine or lysine NH in the active site) [53], (3) high molecular weight acid phosphatases (containing histidine or lysine NH in the active site) [54], (4) protein phosphatases (containing cysteine SH in the active site) [55] and (5) purple acid phosphatases (containing a dinuclear metal complex) [56]. Because many of the phosphatases catalyze phosphate ester hydrolysis through an associative mechanism forming a covalent intermediate with an enzyme residue, the
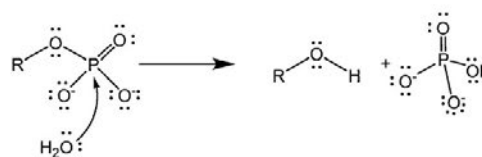

Fig. 2. The hydrolysis of an organic phosphate to form an alcohol and inorganic phosphate [52].
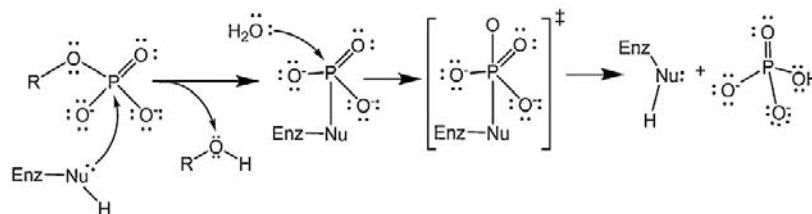
138

Fig. 3. The schematic drawings illustrating potentially intermediate forms of five-coordinate covalent protein–phosphorus complexes in the form of transition states or high energy intermediates [1,58].

protein complexes often have the phosphorus in a five-coordinate geometry during a high energy intermediate and/or the transition state (‡), Fig. 3, regardless of the exact nature of the phosphatase, the nature of the active site, or the protonation state of the complex. Because the associative transition state of phosphoester hydrolysis is trigonal bipyramidal, it is anticipated that the vanadium inhibitors in these protein complexes will adopt the trigonal bipyramidal geometry as an effective transition state analog [1,57].

2.2. Enzyme categorization of phosphatases

The Enzyme Commission (EC) number describes the numerical categorization of enzymes based on the reaction that they catalyze [45,59]. Enzymes with EC numbers of the form 3.#.#.# include phosphatases, lipases, amylases, and peptidases because all catalyze the hydrolysis of a substrate to form two products. Phosphatases are classified as hydrolases because they catalyze the hydrolysis reaction of a wide range of organic phosphates. Because the hydrolysis acts on an ester bond, phosphatases are given the EC number of 3.1.#.# because class 3.1 contains all esterases, including phosphoesters. Phosphoric monoester hydrolases, which are of primary interest to this review, belong to 3.1.3.# and act on small metabolites to large phosphoprotein substrates, Table 1. Because there is a large number of substrates that are phosphorylated, the number of enzymes and proteins catalyzing this process is very large; there are over 90 different classes of phosphatases spanning a broad diversity. In Table 1, we only list the enzymes that are pertinent for this review and described further below.

The most common enzymes catalyzing phosphoester monoester hydrolysis are less specific, being able to dephosphorylate a number of substrates. Alkaline and acid phosphatases are examples of less specific enzymes. Alkaline phosphatase received its name because its activity was greatest at high pH [52,60]. Alkaline phosphatase is important for bone processing and metabolic processing and the widespread presence of this enzyme in many cell types serves an important purpose [1–8]. The more specific phosphatases are often regulatory enzymes, with the reaction impacting the cellular events [1,6–8]. A number of these phosphatases are membrane associated, and thus linking

the phosphate ester hydrolysis reaction with a cellular event such as nutrient uptake or proton transport [61,62]. The action of protein tyrosine phosphatases are therefore intricately associated with cellular regulation such the insulin signaling pathways [11]. These enzymes are only present in small amounts and are not yet commercially available or prohibitively expensive for most researchers. Inhibition of such protein phosphatases is likely to be important in diseases such as diabetes and cancer [11].

2.3. Five-coordinate transition-state geometry – ideal and alternative possibilities

As noted above, the transition state of phosphatases is believed to go through a five-coordinate phosphorus species. The geometric restrictions imposed by the ligands coordinated to a metal ion often distort the coordination geometry from ideal trigonal bipyramidal (TBP) or square pyramidal (SP) geometries. Because five-coordinate geometries are either SP or TBP both geometries seem possible for the protein active sites, although distortions in-between are also possible and, in fact, quite common.

Describing the geometry of five-coordinate complexes can be nontrivial because the geometries are often distorted in between the ideal TBP and SP geometries. The simple index parameter, tau (τ), was introduced by Addison et al. to calculate any potential distortion, where $\tau = (\beta - \alpha)/60$ [63]. Although there are some limitations to τ and other descriptions such as the continuous shape measure are also used [64–66], we have used the τ parameter in this review. At one extreme, $\tau = 0$ for a simple ideal SP geometry: where B, C, D, E, and M are co-planar, the two basal angles α and β (Fig. 4) are each 180°. For the ideal TBP geometry, $\tau = 1$ because the α and β angles (Fig. 4) lead to $\tau = (180 - 120)/60 = 60/60$. The more common distorted structures "in between" these extremes, then, will have a τ value between 0 and 1 and thus help to classify systems with less-ideal geometries.

Examination of the five-coordinate geometry of the metal center in detail is important because the ligands are likely to impact the specific structure at the metal ion. We recently demonstrated in an analysis of five-coordinate vanadium complexes [67], that the SP geometry is more common in small-molecule vanadium

Table 1
Representative phosphatases and their enzyme commission (EC) numbers based on the chemical reactions that the respective enzymes are catalyzing.

| EC number	Phosphatase name; reflecting chemical reaction	Reaction
3.1	Hydrolases	Hydrolysis of ester
3.1.3	Phosphoester monoester hydrolase	Hydrolysis of phosphoester
3.1.3.1	Alkaline phosphatase	Hydrolysis of phosphoester
3.1.3.2	Acid phosphatase	Hydrolysis of phosphoester
3.1.3.3	Phosphoserine phosphatase	Hydrolysis of phosphoester
3.1.3.16	Protein–serine/threonine phosphatase	Hydrolysis of phosphoester
3.1.3.29	N-Acylneuraminate-9-phosphatase	Hydrolysis of phosphoester
3.1.3.41	4-Nitrophenylphosphatase	Hydrolysis of phosphoester
3.1.3.48	Protein-tyrosine-phosphatase	Hydrolysis of phosphoester
3.1.3.70	Mannosyl-3-phosphoglycerate phosphatase	Hydrolysis of phosphoanhydride
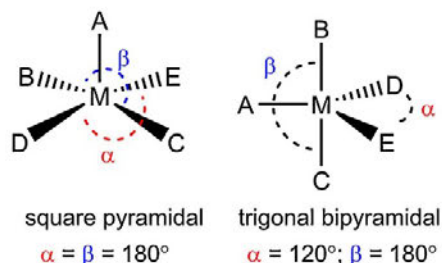
Fig. 4. Two schematic drawings of five-coordinate covalent protein–vanadate complexes with the vanadium in a (a) square pyramidal geometry and (b) trigonal bipyramidal geometry. Angles are drawn for clarity and are less than 180°. Reproduced with permission from Ref. [67].

compounds. In contrast, the TBP geometry is more common for vanadium complexes in protein structures as generally presumed and demonstrated in this work in Section 3. Because the vanadium complexes in the protein are in the geometry that is less prevalent (and therefore presumably less stable), this analysis suggested that the protein stabilizes the geometry of the vanadium.

2.4. Speciation of vanadate, vanadyl cation and vanadium complexes

As an early transition metal ion, vanadium exists in several oxidation states of which vanadium(V), (IV), and (III) are most relevant for the vanadium–protein complexes described in this review [68,69]. The highest oxidation state vanadium(V) can exist both as an anion (VO_4^{3-}, HVO_4^{2-}, $H_2VO_4^{-}$) and a cation (VO_2^{+}) under physiological conditions [68–74]. This V(V) is the form of vanadium that is compatible with oxygen and at neutral pH exists in the form of vanadate, which is often considered an electronic and

structural analog of phosphate [71]. The vanadate monomer can exist in three different forms; at high pH it exists as VO_4^{3-}, and at neutral pH it can be in two forms: HVO_4^{2-} and $H_2VO_4^{-}$. The fully protonated form, H_3VO_4, is not believed to exist in any appreciable amount [70,72]. However, as the concentration increases oligomeric vanadate species are formed in a quantity that depends on pH. The structures of these species are shown in Fig. 5. The dinuclear species ($V_2O_7^{4-}$) can have a charge up to 4−, analogous to pyrophosphate, $P_2O_7^{4-}$, however at neutral pH the anion mono- or di-anionic species dominate. At higher concentration at neutral pH the major species are the cyclic tetranuclear and pentanuclear species [70,72,73], which are *much* less common for phosphate analogs, but not unknown [75,76]. These oxovanadate species are rapidly interconverting [77], and it was demonstrated that the different species have a long enough lifetime to exhibit different biological responses [78]. V_1, V_2, V_4 and V_5 are the major species, but additional species can form such as the linear vanadate trimer (V_3, $V_3O_9^{5-}$), which can be observed at lower concentrations from pH 8.5 to 9.0 [79]. The exchange of species, although well-known by chemists, is more indirectly appreciated by biochemists. For example, biologists and biochemists commonly "activate vanadate" by taking a sodium orthovanadate solution that is adjusted to pH 10.0 (although any pH above 7 will suffice), boil it, and re-adjust to pH 10.0 [14] to ensure that the vast majority of the vanadium species present is monomeric vanadate (that is a mixture of HVO_4^{2-} and VO_4^{3-}) [80–83].

The cationic form of vanadium(V) is found at low pH (VO_2^{+}) and in complexes and protein active sites [58,68–70,72]. At higher concentrations and in the acidic pH range 3.0–6.5 the major vanadium species is decavanadate, $V_{10}O_{28}^{6-}$. This modestly sized polyoxovanadate is kinetically stable in acidic conditions with dimensions of 5 Å × 7.8 Å × 8.3 Å [84]. The specific protonation state is dependent on pH ($H_nV_{10}O_{28}^{6-n-}$) and can have up to a minus 6 charge. In this acidic pH region the vanadate monomer concentration is very low, although at sub-millimolar concentrations decavanadate does not form spontaneously even at pH 6.
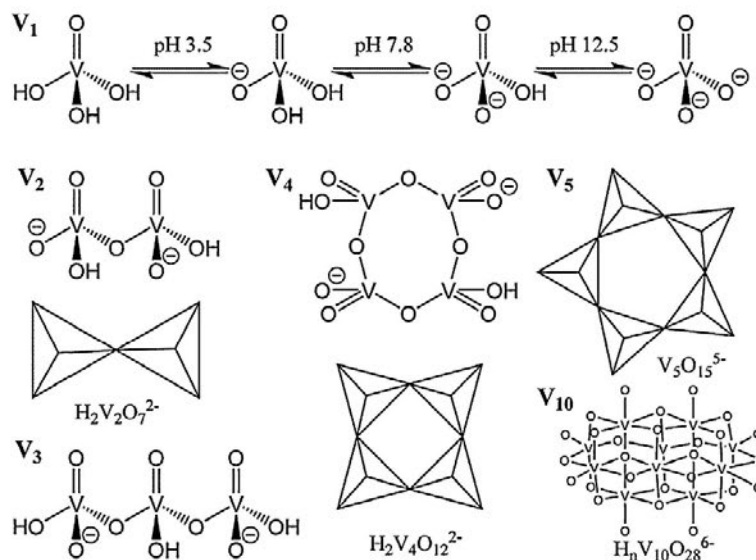
Fig. 5. Scheme of known equilibrating oxovanadate (vanadium (V)) oligomers in solution. The species existing at neutral and high pH (V_1, V_2, V_4, V_5) and the species at low pH VO_2^{+} and V_{10} [68,70,72,79,82]. The V_3 and other minor contributors are present at lower concentrations but have been observed between pH 8.5 and 9 at higher concentrations [79]. The solution at neutral and high pH is colorless and the V_{10} is yellow/orange depending on concentration and cation in solution.

The speciation of vanadium(IV) has also been examined and at neutral pH the monomeric vanadium species concentration are very low [68,85–87]. It is the VO^{2+} and $VOOH^+$ species that predominate at low pH and at high pH an anionic form is present, $VO(OH)^{3-}$. The concentration is so low that no species can by be observed by EPR spectroscopy [68,85]. Solutions are EPR silent, because the stable form is an oligomeric–polymeric species in which the free electrons are coupled. The presence of the vanadium(IV) species can be observed by adding a buffer which will then complex with the vanadium(IV) and render the material EPR active [85].

The speciation of vanadium(III) has also been characterized, and as free salts these solutions are very sensitive to oxygen, time and specific conditions [68,88,89]. Various protonation steps exist for monomer, dimer, and trimer species. These species are sensitive to air, and must be handled under an inert atmosphere. In addition, as a complex vanadium(III) materials can be stable, and exert an effect in biological conditions. For example, with regard to anti-diabetic properties, some vanadium(III) complexes have been reported to have an effect, but it seems to be less than the effects of the two higher oxidation states [89,90]. Indeed, vanadium(III) typically converts to the vanadium(IV) species in aqueous solution.

In addition to these speciation issues, vanadium species readily react with most ligands [71,74,85,91,92]. As a result, new coordination complexes form with buffers, substrates and other metabolites present under the conditions of the assay or under physiological conditions [71,74,85,91,92]. Early studies documented that both vanadate and vanadium(IV) react with most buffers, however, generally the complexes that form are weak and thus not isolated [74,91]. The interaction of, for example, HEPES with vanadium(IV) prevented formation of the EPR-silent oligomeric form of vanadium(IV), which impacted the response time observed with enzymes of solutions of vanadium(IV) [85]. This problem of interactions with buffers is profound: if no buffer is used it is difficult to maintain pH; however, if a buffer is used it is not clear how much of the observed effect is due to buffer-vanadate complex formation. Therefore researchers do the best they can, and as long as the limitations are recognized, studies are informative regardless of what approach is used.

2.5. Methods of inhibition of phosphatase

Phosphatases can be inhibited in several ways, including substrate inhibition, transition state inhibition, and product inhibition [93]. Phosphatases catalyze the hydrolysis of phosphate esters and the resulting organic part and the phosphate products can inhibit the enzyme when the product slowly falls off. Because vanadate is a phosphate analog, vanadate can also interact with phosphatases as a product analog [37]. Vanadate as a product inhibitor binds to the protein in a four-coordinate geometry in the protein complex. It would be anticipated that product analog inhibitors would be weaker inhibitors than transition state analog inhibitors. The comparison of vanadate and phosphate inhibition of the phosphatases will reflect the mode of action of the inhibitor. There are known examples of protein complexes with the vanadium in the tetrahedral coordination geometry [41,94,95]. The reported vanadium–phosphatase protein complexes include some complexes that do not have the vanadium in five-coordinate geometries.

In the phosphatase–vanadium complexes where the vanadate acts as a product inhibitor the vanadium will be in a four-coordinate geometry as has been found for *Bacteroides thetaiotamicron* HPP D10A (PDB ID [96] 2rar) [94] and *Drosophila melanogaster* PTP10D (PDB ID 3s3f) [95]. In these complexes the major differences from the vanadium–protein complexes with five-coordinate vanadium are the bond distances because the angles of the vanadium center do not change significantly. However, in some cases a bond
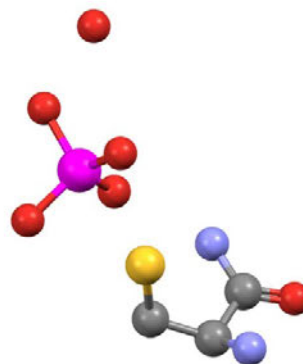

Fig. 6. In the structure of a *Homo sapiens* receptor-like protein tyrosine phosphatase γ (RPTPγ) a vanadate, VO_4, is bound in the active site; ID 3qcc in the PDB database. The authors consider the nearby S-atom, which is at a distance where a respectable bond could have formed at 2.716 Å [100], whereas the PDB entry ignores it. Key to the atom coloring is: C, gray; N, blue; O, red; S, yellow; V, magenta.

distance can be so long that one begins to wonder how long a bond can be before it is no longer considered a bond. The importance of these considerations depends on the nature of the VO-unit and whether there are single, double, or even triple bonds [97,98]. This is important, because bond lengths are not incorporated into the determination of τ. Of the over 49,000 unique V···O bonds are in the Cambridge Crystal Structural Database (CCSD), ranging from 1.473 to 2.909 Å [99], for those defined as V—O regardless of oxidation state, the mean bond distance is 1.94 Å, whereas for V=O, it is 1.60 Å and for V≡O it is 1.67 Å. Clearly those descriptions and values are some cause for concern, but that is beyond the scope of this review.

Another example of how coordination geometries impact the analysis of bound inhibitors is demonstrated in the structure of a *Homo sapiens* receptor-like protein tyrosine phosphatase γ (RPTPγ) with vanadate bond in the active site, PDB ID 3qcc [100]. It is a protein phosphatase complex which contains a vanadate with four VO bonds in the range of 1.628–1.676 Å, Fig. 6. The inter O—V—O angles are 107°, 107°, 109°, and 116°. This vanadium derivative, then, could be described as tetrahedral VO_4. However, there is also a V···S_{Cys} distance of 2.716 Å which exemplifies a fifth bond, at least as a V coordination chemist would define it. In the CCSD [99] for small molecules, there are 1681 unique V—S bonds, which range from 2.045 to 2.945 Å. The mean and median value are both 2.370 Å, so this 2.716 Å could be considered a long bond, even though there are several examples with such bonds and even longer [101–106]. The angles indicate that this is a TBP environment, with a τ value of 0.98 ($\beta = 175.0°$, $\alpha = 116.1°$). The authors describe this vanadium atom to be "liganded to Cys" along with four oxygen atoms. Including the long V—S bond in the vanadium–protein complex describes an enzyme with a TBP vanadium coordination environment. The PDB, however, described this structure with a vanadate ion ligand (Ligand ID VO4).

3. X-ray structural characterization of protein–inhibitor complexes: resolution and experimentally imposed limitations

In the past 100 years, X-ray crystallography has become an important tool in understanding structure on the molecular level across many disciplines of science [58,107–110]. Improvements in crystal growth techniques, collection and detection systems, and computational power have also served to advance the field
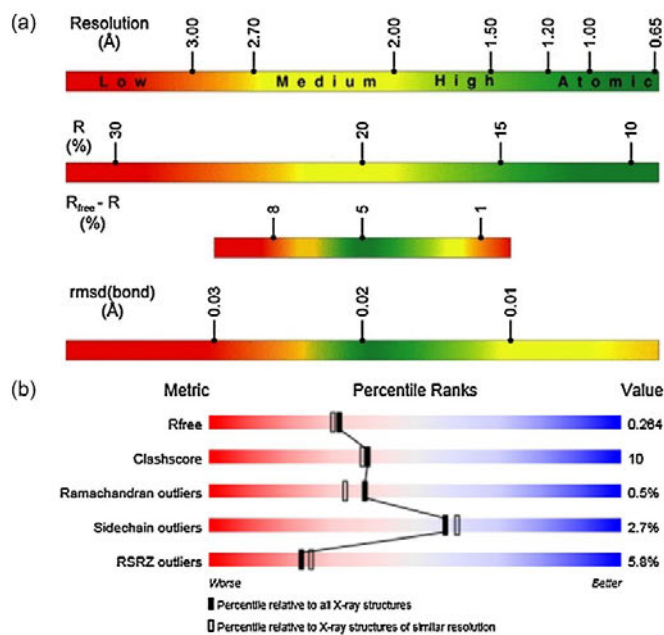
Fig. 7. Several parameters that help indicate quality of protein crystallography structural data exist. (a) Values in red indicate likely lower reliability data whereas those in green are generally of higher quality. Reproduced with permission from Ref. [108]. (b) Sample PDB validation summary of 3qcc [118].

and allow it to contribute valuable insights in many disciplines. As important as this tool has become, limitations in what X-ray crystallography can and cannot demonstrate exist [111]. Extensive discussion is beyond the scope of this review, but interested readers are referred to several texts on the subject [112–115] as well as two insightful reviews on the topic of protein crystallography by Wlodawer et al. [108,116]. Briefly, there are several key factors to keep in mind when analyzing protein crystallographic data and the limitations in a particular structure i.e. resolution, reliability indices (R and R_{free}), and root mean square deviations of bonds from typical geometric standards (rmsd(bond)), Fig. 7a. As shown, the structures can be represented using a color code that describes the quality of the model. Any one parameter does not define the quality of the structure, but taken together, these parameters give a good sense of the structural quality. Such limitations can impact the validity of the interpretation and conclusions based on the data. For example, from low resolution (red color) to high resolution (green color) the differences in the bond distances typically vary from 0.03 to 0.01 Å, so over-interpretation of small differences should be avoided. This color scheme is, however, not to be confused with the color scheme used to describe charge on protein surfaces, with blue describing a cationic surface and red an anionic surface. The PDB itself now includes structural validation reports for each structure, emphasizing slightly different parameters, but still giving the viewer a sense of the likely validity of a different structure. Their metrics show the values for the structure relative to all structures in the database as well as against only other structures with similar resolution [117]. A representative validation report from the structure designated as 3qcc in the PDB is shown in Fig. 7b.

In solving the X-ray crystallographic structure, one is minimizing the difference between the predicted intensities and positions and those observed in the X-ray diffraction study resulting in a computed structural solution [107,112]. This fact is often not

appreciated, but solutions can lead to computed models ("structures") that poorly represent the true system, exemplified by small molecule crystallographic studies when the computed solutions do not describe reasonable chemical structures. In less-well-defined protein systems, this problem is only magnified. One key issue is reflected in the resolution of the structure. The resolution can be defined as the minimum distance between structural features that can be distinguished [108]. For example, one can point to the progression of structures of the FeMo-cofactor in nitrogenase to illustrate how the issue of resolution can confine the possible conclusions. Initially there was a void in the middle of the structure, then an unknown atom X (identification of the nature of X was not possible), but as the structures achieved better resolution, X was identified first as a N-atom and ultimately as a C-atom (Fig. 8) [119–123] and the assignment was reinforced by spectroscopy [123,124]. Some comparisons can be made while attempting to pull out details when the resolution is low, perhaps even so low that the lengths being discussed are not well defined, but the ability to draw too many conclusions may be limited. So, for instance, it may be quite possible to discern a four-coordinate species from a five- or six-coordinate species even at poor resolution (e.g. 3.0 Å), but the uncertainty in atom positions and, therefore, angles should limit the confidence in the results when specifying differences between two five-coordinate geometries. This is particularly important for the discussion in this review because, as we previously documented [67], the differences in TBP and SP coordination environments can be very small and subtle. The problem arises because protein structures contain a large number of atoms that must *all* be modeled because in crystallography one models the entire ensemble of atoms; it is not possible to examine *just* the active site. Therefore, crystallographers may need to impose certain restrictions to achieve stable refinements, and such solutions may include limitations on the geometries in the enzymes active site. Because there is
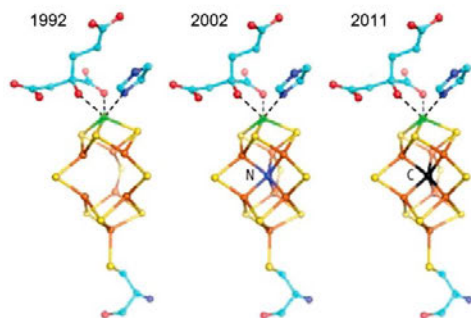
Fig. 8. Molecular structures of the iron molybdenum cofactor (FeMoco) as determined by X-ray crystallography over the years. The resolution was 2.7 Å in 1992, 1.16 Å in 2002 and 1.0 Å in 2011. The iron, sulfur, and molybdenum atoms are apparent, even at the lowest of resolution. However, only at the 1.0 Å resolution is it possible to say with certainty that the missing atom at the center of the cluster is a C. Reproduced with permission from Ref. [125]. Key to atom coloring: C, aqua/black; Fe, orange; Mo, green; N, blue; O, red; S, yellow.

no absolute decisive value for trustworthy structural data, we have used the published data as they were and have included some of the reliability indicators in our tables in this review to assist the reader in seeing the limitations on some of the τ values.

In crystallography it is common to begin the modeling process with a previous model solution for as much as is deemed reasonable (molecular replacement) so as to learn quickly about the part of the molecule one presumes to impact. Many authors are very forthright in their manuscripts or depositions about these restraints, e.g. Zhang et al. state in their structure of Bovine Low Molecular Weight PTPase (refcode 1z12) [126], "In order to avoid any model bias for the trigonal bipyramidal geometry suggested by the electron density map, the tetrahedral vanadate was first used in the refinement, but with loose constraints on the bond lengths (10 Å) and bond angles (20°). After 40 cycles of positional and individual B-factor refinement, the model showed that three of the four oxygen atoms on the vanadate ion became nearly coplanar with the vanadium atom. Forty more cycles of refinement were done with increasingly tighter constraints of vanadate geometry on the previously refined model. In the final round of refinement, the three oxygen atoms and the vanadium were fixed in the same plane [126]." The conclusions drawn are likely correct, but the geometry of the final model was effectively fixed to be planar and, therefore, described as TBP when the "nearly coplanar" angles may have led to a different description. However, such important discussions regarding structural limitations can be lost with a database query, or by reviewers, or by an editorial decision to condense a manuscript.

The particular form of the protein "captured" in an X-ray structure can also be an issue. X-ray crystallography averages structure over the repeating unit all in the same orientation and small deviations are eliminated by the method. This is why crystals must be formed for single crystal diffraction and the materials cannot be powders or microcrystals. With the relatively slow growth conditions for many crystals, though, it becomes possible to "trap" a protein in many stages of the catalytic process. Sometimes this is intentional and valuable information can be compiled, as noted by Brandão et al. [41]. In other cases, the expected enzyme form is not isolated. In the structures by Hengge and co-workers, for example, both divanadate [127] and trivanadate [128] structures were captured from soaking with vanadate (VO_4^{3-}) in acidic conditions even though trivanadate is not stable in observable amounts in such a solution. The long-standing discussion of whether the X-ray structures are an accurate reflection of what is occurring in

solution is, therefore, only more complicated when considering protein structures.

Another complexity of X-ray crystallography being an average structure is that of disorder and "partial occupancy". The proteins trapped in the above example could be trapped across a range of possible conformations in the crystal, leading to disorder in the model. A crystal may also not have every single equivalent site occupied by a metal or cofactor, which would lead to lower electron density than expected for the system, a phenomenon usually referred to as partial occupancy. It then becomes important to consider both disorder and partial occupancy in such a large macromolecular structure.

4. PDB structures of phosphatases containing a bound vanadium

4.1. Search parameters

The search for protein–vanadium complexes was done in the Protein Data Bank (PDB) [51] which contained 103,015 structures (on September 2, 2014). We focused only on structures solved by X-ray crystallography, of which there were 91,382 structures. Only the structures in which the enzymes were phosphatases and designated as hydrolases were selected. Of the 1713 structure hits for phosphatases in the PDB, 1610 of those were derived from X-ray data along with another 48 unreleased structures. Within that set, 8 contain "vanadium" and 46 contain "vanadate" resulting in a list of 38 unique codes and 4 more unreleased structures leading to the structures tabulated in Table 2. Several control searches were also conducted and searches were analyzed selecting all vanadium-containing systems to be sure to capture the largest number of structures. Not all of these systems contain V, some are repeats and some contain multiple V's per structure, so the true number of unique proteins is 29. Database searches do not always contain the correct information regarding pH, ligand form, etc. when comparing to the publication. Coordinates were downloaded from PDB and distances and angles were analyzed using Mercury [129]. Data were compiled and calculated for τ [63] in Table 2 as described previously [67]. With only 29 structures, each was also compared to the original reference and details sought in the manuscript and deposition regarding description, refinement constraints, etc. This left 29 different structures, which are summarized in Table 2. It should be noted that some structures of phosphatases with other oxoanions exist, including molybdate [130,131], tungstate [132,133], and phosphate [133], but those are not reviewed comprehensively because they are not the focus of this review.

The parameters for vanadium–protein complexes for each class of phosphatases were analyzed and include the method by which the crystal was obtained and some details of the conditions, the resulting resolution of the structure, and the active site residue coordinated to the vanadium in the active site. Because the resolution of the structures of the vanadium-containing phosphatase varies from 3.0 to 1.0 Å, there is a wide range of the quality of these structures, and, therefore, the reliability of the details in the coordination environment that is obtained. For example, the structure with resolution of 3.0 Å is not precise enough to allow a completely reliable description of the coordination environment. Regardless of differences in the protein, the active site environments in most cases contained a VO_4 covalently coordinated to an active site nucleophile from the phosphatase and are depicted in Fig. 9. When examining putative active sites of phosphatase enzymes co-crystallized or soaked with a vanadium-containing species the τ calculation allowed for assignment of TBP or SP geometries.

Table 2
The known phosphatase structures containing vanadium and some details about them.

PDB id	Source	Enzyme	EC #	Form of V	Exposure to V[a]	Geometry	5th ligand	τ value	Res (Å)	R_{Obs}	pH[b]	Ref.
1rpt	*Rattus norvegicus*	Acid phosphatase	3.1.3.2/5	VO₄···His	Soak	TBP	N	0.91	3.00	0.215	5.4	[131]
4qih	*Mycobacterium tuberculosis H37Rv*	Glucosyl-3-phosphoglycerate phosphatase	3.1.3.70	VO₄···His	NR	TBP	N	0.81	2.30	0.192	7.50	[137]
3e81	*Bacteroides thetaiotaomicron*	Bact KDN-9P	NR	VO₃···Asp.cofactor	Soak	TBP	O	0.95	1.63	0.176	8.50	[143]
1b8j	*Escherichia coli*	Alkaline phosphatase	3.1.3.1	VO₄···Ser	Soak	TBP	O	0.77, 0.85	1.90	0.171	7.50	[144]
3t00	*Sinorhizobium melioti*	Phosphoacetate hydrolase	3.6.1.9	VO₄···Thr	Soak	TBP	O	0.83	1.80	0.207	7.50	[148]
1h2f	*Bacillus stearothermophilus*	Phosphatase PhoE (fka YhfR)	3.1.3.2/5	V₃O₈ chains···His, Glu covalent	Soak	Distorted tetrahedral	–	c	2.00	0.214	5.00ᵉ	[128]
1j9l	*Thermotoga maritima*	Survival protein E (SurE)	3.1.3.5	VO₄ + H bonds	Soak	Distorted tetrahedral	–	0.43d	1.90	0.199	7.50	[149]
2gso	*Xanthomonus ananopodis*	NPP	3.6.1.9	VO₄···Thr	CO	TBP; 6th O at 3Å	O	0.55	1.45ᵉ	0.173	6.00	[150]
2d1g	*Francisella tularensis*	Acid phosphatase A (AcpA)	3.1.3.2	HVO₅²⁻	Soak	TBP	O	0.76ᶜ	1.75	0.198d	6.00	[151]
2rbk	*Bacteroides thetaiotaomicron*	HPP wild type		O···VO₃···Asp	Soak	TBP	O	0.78	1.00	0.123	5.50	[94]
2rar	*Bacteroides thetaiotaomicron*	HPP D10A mutant		VO₃···Asp	CO	Tetrahedral	–	c	1.52	0.167	7.00	[94]
3zwk	*Thermus thermophilus*	Mannosyl-3-phosphoglycerate	3.1.3.70	VO₃···W···Asp	Soak	TBP	O	0.56	2.10	0.158	6.50	[154]
3zx5	*Thermus thermophilus*	Mannosyl-3-phosphoglycerate	3.1.3.70	VO₃···Asp···MG	Soak	TBP	O	0.89	1.81	0.170	6.50	[154]
4knw	*Homo sapiens*	N-Acylneuraminate-9-phosphatase	3.1.3.29	VO₄···Asp	Soak	TBP	O	1.07	2.70	0.255	7.50	[155]
3zwu	*Pseudomonas fluorescens*	Alkaline phosphatase Phox	3.1.3.1ᶜ	VO₅	NR	TBP	O	0.94	1.39	0.159	8.00	[170]
4kkz	*Phaseolus vulgaris*	Purple acid phosphatase	3.1.3.2	VO₄···OEt	NR	TBP	O	0.83	2.20	0.153	4.0	[171]
1z12	*Bos taurus*	Low Mr PTP	3.1.3.2/48	VO₄···Cys	Soak	TBP	S	0.88	2.20	0.173	7.50	[126]
3qcc	*Homo sapiens*	RPTPγ	3.1.3.48ᶜ	VO₄···Cys	Soak	TBP	S	0.98	2.10	0.225	6.50	[100]
3qcd	*Homo sapiens*	RPTPγ	3.1.3.48ᶜ	VO₄···Cys	Soak	TBP	S	0.91	1.80	0.241	7.00	[100]
2hy3	*Homo sapiens*	RPTPγ	3.1.3.48	VO₄···Cys	NR	TBP	S	0.76	2.60	0.206	8.00	[164]
2i4e	*Homo sapiens*	HPTP-b-CD	3.1.3.48	VO₄···Cys	Soak	TBP	S	0.82	1.75	0.180	8.00	[159]
3i80	*Homo sapiens*	PTP1B	3.1.3.48	VO₄···Cys	CO	TBP	S	0.90	2.25	0.201	7.50	[41]
3i7z	*Homo sapiens*	PTP1B	3.1.3.48	VO₃···Cys···DADEYL peptide	CO	TBP	S	0.83	2.30	0.207	7.50	[41]
3qkq	*Homo sapiens*	PTP1B W179F	3.1.3.48ᶜ	VO₃···W···Cys	CO	TBP	S	0.88	2.20	0.199	7.50	[166]
3f9b	*Yersinia enterocolitica (type O:9)*	W354F PTPase	3.1.3.48	V₂O₇ (VO4···Cys; VO5)	CO	TBP, TBP	O, S	0.07, 0.78	1.42	0.174	7.50	[127]
2i42	*Yersinia enterocolitica*	YopH protein tyrosine phosphatase	3.1.3.48	VO₄···Cys	CO	SP	S	0.30	2.20	0.170	8.50	[168]
3omx	*Drosophila melanogaster*	SSu72 phosphatase	3.1.3.16	VO₄···Cys	Soak	TBP	S	0.73	2.34	0.208	7.50	[169]
3s3f	*Drosophila melanogaster*	PTP10D	3.1.3.48	VO₄	Soak	Tetrahedral	–	c	2.70	0.240	6.50	[95]
4erc	*Homo sapiens*	VHZ – short PTP	3.1.3.16/48	VO₃···Cys···Arg	CO	Trigonal planar	–	0.35d	1.15	0.129	7.50	[157]

a Method of exposure to vanadium. CO, co-crystallization; soak, soaking; NR, not reported. See text and references for details.
b pH of crystallization as reported in PDB or literature.
c No fifth coordination ligand.
d Extremely long fifth coordination ligand.
e Publication details differ from database details.

144

Table 3
Selected angles (°) and bond lengths (Å) for the coordination environment immediately surrounding the vanadium center(s) for the structures listed in Table 2. The assumed coordination is VO_4X except as noted.

| PDB id	X	τ	O_1VO_2	O_1VO_3	O_1VO_4	O_1VX	O_2VO_3	O_2VX	O_3VX	O_4VO_2	O_4VO_3	O_4VX	$V-O_1$	$V-O_2$	$V-O_3$	$V-O_4$	$V-X$
1rpt	N	0.91	118.12	86.46	123.14	91.45	91.31	88.42	177.47	118.29	85.73	96.61	1.654	1.532	1.757	1.656	1.966
4qjh	N	0.81	126.52	111.15	88.01	96.78	113.23	106.66	95.94	68.89	83.89	174.91	1.574	1.584	1.607	2.253	2.058
3e81	O	0.95	117.84	121.52	82.24	99.06	119.75	89.72	90.57	89.5	88.9	178.69	1.751	1.787	1.798	2.107	2.101
1b8j	O	0.77	115.71	122.28	86.77	101	121.74	76.14	97.32	93.05	85.28	168.62	1.709	1.752	1.749	1.879	1.699
3r00	O	0.83	106.97	111.99	116.34	77.27	107.17	166.24	82.54	99.01	113.86	67.72	1.896	1.911	1.921	1.897	2.039
1h2f	N[a]	N/A	111.64	114.03		104.93	112.8	100.66	111.7				1.728	1.743	1.727		1.765
1h2f	O[a]	N/A	104.45	109.44	105.73		110.68			115.16	110.94		1.745	1.748	1.736	1.776	
1h2f	O[a]	N/A	104.89	109.92		139.87	108.07	83.04	104.37				1.76	1.732	1.729		1.809
1j9l	O	0.43	124.6	93.49	99.49	82.08	130.23	107.33	41.87	91.72	114.17	155.8	1.735	1.7	1.675	1.74	3.617
2gso	O	0.55	113.18	123.03	88.35	94.15	123.8	102.36	74.73	97.83	84.52	156.75	1.989	1.702	2.025	1.944	1.894
2d1g	O	0.76	99.55	99.54	96.67	165.61	114.36	88.69	87.59	120.16	118.95	68.94	1.921	1.858	1.86	1.848	2.237
2rbk	O	0.78	120.66	124.5	79.63	91.82	110.89	91.04	107	93.66	77.94	171.45	1.664	1.76	1.837	2.124	2.021
2rar	O[a]	N/A	117.8	121.46	101.69		112.78			96.07	100.32		1.687	1.688	1.756	2.001	
3zwk	O	0.56	118.68	118.18	111.03	82.78	119.3	78.66	127.88	83.74	57.46	161.5	1.907	1.906	1.912	2.944	2.477
3zx5	O	0.89	121.57	115.93	94.72	86.47	116.91	72.55	87.66	102.75	96.12	174.98	1.879	1.878	1.902	2.021	2.731
4knw	O	1.07	108.23	108.75	109.93	175.62	111.36	67.67	74.69	109.71	108.85	70.87	1.912	1.909	1.907	1.905	2.124
3zwu	O	0.94	98.04	97.43	101.87	177.17	120.76	81.49	80.48	113.14	118.78	80.85	1.763	1.758	1.733	1.732	2.396
4klz	O	0.83	90.01	90.5	178.7	89.79	115.38	128.78	115.84	89.65	90.78	89.45	1.668	1.691	1.69	1.69	1.691
1z12	S	0.88	82.91	90.55	85.53	173.7	120.61	102.05	83.58	120.13	118.02	95.18	1.715	1.601	1.624	1.605	2.158
3qcc	S	0.98	104.16	107.34	107.43	175.04	116.1	73.93	70	109.32	111.86	77.52	1.678	1.631	1.626	1.672	2.716
3qcd	S	0.91	102.07	103.26	107.64	175.74	120.93	74.61	76.61	108.88	112.59	76.16	1.732	1.709	1.709	1.676	2.778
2hy3	S	0.76	107.8	111.13	106.12	161.43	103.25	73.62	85.96	115.74	112.78	58.7	1.946	1.91	1.938	1.901	2.976
2i4e	S	0.82	117.44	116.75	87.44	97.61	125.5	91.08	87.25	88.68	88.35	174.42	1.741	1.756	1.718	1.978	2.468
3i80	S	0.90	120.54	122.32	89.84	87.91	117.1	92.72	87.74	91.22	90.73	176.05	1.909	1.912	1.909	2.103	2.514
3i7z	S	0.83	116.63	117.79	91.11	86.09	125.58	92.55	91.41	92.17	86.74	175.22	1.905	1.883	1.893	2.123	2.648
3qkq	S	0.88	120.5	122.36	89.95	93.1	117.11	83.98	90.91	91.23	90.73	175.17	1.908	1.912	1.91	2.102	2.588
3f9b	S	0.90	120.46	119.88	87.27	90.48	119.01	92.98	94.63	92.79	81.87	174.17	1.893	1.886	2.044	2.054	2.445
3f9b	O	0.07	101.4	106.15	101.02	103.54	141.03	129.53	69.37	67.24	80.68	145.37	1.898	1.913	2.07	2.078	1.907
2i42	S	0.30	145.08	103.2	113.07	83.43	111.71	102.01	81.21	67.63	90.24	162.91	1.708	1.676	1.611	1.938	2.156
3omx	S	0.73	83.01	84.61	81.57	172.66	113.23	90.41	95.08	128.84	113.42	105.19	1.966	1.884	1.961	1.882	2.318
3s3f	S	0.88	109.79	109.14	109.43	55.42	109.89	163.66	83.48	107.92	110.65	74.4	1.912	1.913	1.915	1.905	4.513
4erc	S	0.35	117.09	117.14	69.45	99.09	116.61	103.68	97.74	54.76	123.42	138.35	1.686	1.724	1.727	4.059	2.38

[a] No 5th ligand, i.e. VO_3X.

1B8J τ = 0.77   1Z12 τ = 0.88   1RPT τ = 0.91
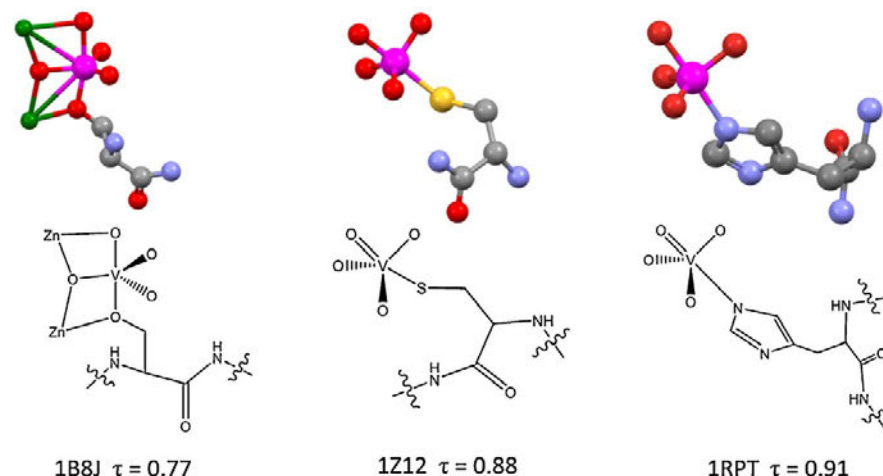
Fig. 9. Examples of active site environments for VO₄O, VO₄S, and VO₄N coordination environments of known structure species with the pertinent PDB ID and τ values. Each is shown as a ball and stick model of the first coordination sphere of the active site as well as the chemical connectivity. Key to atom coloring: C, gray; Mg, green; N, blue; O, red; S, yellow; V, magenta.

Because the phosphatases contain an active site coordination geometry of ~VO₄X, where X can be O, N and S we organized these phosphatase into these three groups based on the nature of the active site nucleophile, the O for Ser/Thr, N-His, and S-containing Cys. This allowed the comparison of these protein structures with different classes of coordination environments in small molecules from the CCSD. Previously we analyzed the known vanadium-containing small molecules with five-coordinate geometries which were divided into three groups; VO₄X, VO₄N, and VO₄O [67]. We found only one VO₄S complex in the group of 44 structures with X being everything else than N or O, about 300 VO₄N species and about 1100 species with VO₄O coordination environments, Fig. 10. In this report we demonstrated that nearly all VO₄O complexes regardless of author-reported oxidation state of vanadium or the nature of the O-containing ligand have a τ value of less than 0.5 and should thus be described as containing a vanadium with SP coordination geometry [67]. In fact more than 97% have a τ value of less than 0.1. For compounds with the VO₄N coordination geometry the results are similar, but with *only* 75% less than 0.5 [67]. For a large, random subpopulation of those identified as V⁵⁺ small molecule species in the CCSD searches, the results are 91% and 77% SP, respectively. Related analysis employing the continuous shape measure methodology [65] leads to subtly different individual results, but a similar conclusion [134]. These findings are strikingly in contrast to the TBP coordination environments found in the enzyme active sites, and tabulated in Tables 2 and 3. All the species in Table 2 have vanadium in oxidation state 5+ (only one V⁴⁺-protein complex has been reported in the PDB, although not with a phosphatase, but rather with hen egg white lysozyme) [135,136]. The V−O bond lengths in Table 3 are all quite long, too, and are much longer than might be expected for V=O or V≡O (*c.f.* Section 2.5 and Ref [99]).

4.2. Descriptors of structurally characterized species

Relevant information about the structures available in the PDB is shown in Table 2 and Table S1. Values are generally derived from that in the database, but are changed as indicated where the values in the published description do not match those in the database. One common area for disagreement is the pH of crystallization, which is usually listed as the value the native crystals

are grown in, not the soaking solution. In several of the structures more than one crystallographically unique monomer of the protein exists. In such cases, only one monomeric unit was chosen at random (although we tried to align with the site authors discussed in their manuscripts where possible) for more in-depth analysis and inclusion in Table 2. Angles and distances used for calculations are shown in Table 3.

Supplementary Table S1 related to this article can be found, in the online version, at http://dx.doi.org/10.1016/j.ccr.2014.12.012.

4.2.1. Nitrogen-containing active sites
4.2.1.1. Rat acid phosphatase. The acid phosphatase from *Rattus norvegicus* is a versatile phosphatase classified as both EC 3.1.3.2 and 3.1.3.5. Crystals of purified rat acid phosphatase were soaked in 15% PEG 6000 in 0.1 M sodium acetate, pH 5.4, containing 5 mM Na₃VO₄ for two days and analyzed by X-ray diffraction [131]. The crystal structure was solved by molecular displacement from the native enzyme and deposited as PDB ID 1rpt. The model is based on low resolution (3.0 Å) data, but the authors noted electron density in the active site that could not be modeled as tetrahedral VO₄. Instead a trigonal bipyramidal geometry (τ = 0.91) with VO₄ and an axial N_His was "built into the difference model and refined" [131]. Additional side chains (His and Arg) stabilize the environment. The fixed refinement and low resolution do not allow many conclusions to be drawn from this structure itself, but similar VO₄N coordination geometries in known structures of vanadium-dependent haloperoxidases [139–142] support this motif. Surprisingly, despite being known for twenty years, 1rpt is the only reported acid phosphatase with vanadium in the PDB. The second enzyme with a VO₄N coordination environment in Table 2, 4qih [137], represents one of several enzymes that are in the PDB but have not yet appeared in the original literature.

4.2.2. All-oxygen-containing active sites
4.2.2.1. Bacterial KDN-9P. The bacterial 2-keto-3-deoxy-D-glycero-D-galacto-9-phosphononic acid (KDN-9P) phosphatase is a hydrolase from *Bacteroides thetaiotaomicron*, and included in this analysis even though it is described as a transferase in the PDB and not classified within the EC category 3.1.3. Because the aspartic acid is the active site nucleophile this enzyme can
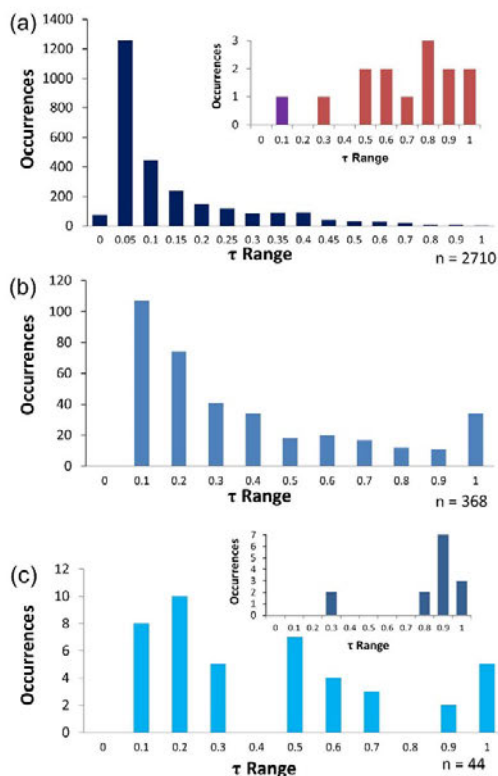
Fig. 10. Combined figures comparing search results from the CCSD (large figure) and PDB (insets) databases. Histogram showing number of occurrences in the CCSD [99] of five-coordinate complexes with (a) VO$_4$O coordination. The region $\tau = 0$–0.5 is expanded with twice as many bins for clarity because over 97% of the complexes have $\tau < 0.5$ [67]. The inset shows the same distribution only for phosphatase structures in the PDB. The outlier shown in purple is one of the vanadium atoms in a divanadate structure PDB id: 3f9b [127]. In the divanadate structure the two vanadium atoms are different; the bound vanadium is TBP, but the free vanadium is SP (shown in purple). (b) Likewise for VO$_4$N coordination. The only reported phosphatases with VO$_4$N in the PDB have $\tau = 0.91$ (PDB id: 1rpt) [131] and $\tau = 0.81$ (PDB id: 4qih) [137]. (c) As in (a), but for VO$_4$X coordination. In the PDB X is always S. Of the outliers, one is the YopH-vanadate (2i42) and the other is the VHZ (4erc), neither of which are best described as TBP according to the authors. The only small molecule VO$_4$S in the CSD has $\tau = 0.17$ [138].

be classified within several groups within EC 3.1.3. The enzyme crystals grown from PEG were soaked at room temperature for 15 min with "20 mM activated NaVO$_3$" (which generally implies a solution of vanadate that has been heated in order to hydrolyze any decavanadate content) and 100 mM of the model sialic acid substrate N-acetylneuraminate (Neu5Ac) in 35% PEG, 0.06 M TAPS buffer, and 10 mM MgCl$_2$ at pH 8.50 resulting in the crystals deposited in the database as PDB ID 3e81 [143]. The structure was solved by molecular replacement. The observed vanadium can be described as a five-coordinate vanadium in which a planar VO$_3$ is bound apically (axially to a coordination chemist) by an aspartic acid residue and an O from the substrate Neu5Ac. A cofactor Mg^{2+} ion is also located in the vicinity, 2.0 Å from one of the O atoms in the VO$_3$ plane, and there are secondary interactions with additional side chains. The τ value for the vanadium is calculated to 0.95 making this an almost ideal TPB geometry. It is unclear from the crystallographic files and published materials how many

restrictions were placed on the geometries of the four vanadium centers in the structure (1 per chain) during the processing leading to the solution of the vanadium–protein complex.

4.2.2.2. Escherichia coli alkaline phosphatase. The *E. coli alkaline phosphatase* is a hydrolase from group 3.1.3.1 with a serine active site nucleophile. Crystals of the enzyme were stabilized at pH 7.50 and washed to remove residual phosphate, and then treated with 100 mM Tris buffer and 100 μM NH$_4$VO$_3$ vanadate resulting in the crystals used to determine the structure deposited in the database as PDB ID 1b8j [144]. The *E. coli* alkaline phosphatase has a different affinity for vanadium than for example the mammalian alkaline phosphatases, which is reflected by the added potency by with vanadium inhibits this enzyme [145,146]. Although the *E. coli* enzyme was the first for which inhibition by aqueous V(IV) was documented [145] it has since then been reported that mammalian alkaline phosphatases are also inhibited by aqueous V(IV) (see below for additional information) [147]. In the deposited structure, there are two vanadium putative active sites that are very similar in their coordination bonds and angles. Each comprises a VO$_5$ unit with a nearly planar VO$_3$ unit axially bound to an oxygen from serine and a Zn^{2+}-coordinated water molecule. The coordination chemistry of the vanadium, then, is distorted TBP with a τ value of 0.77 in one site and 0.85 in the other. These values and the quite long V—O distances (ca. 1.72 Å) demonstrate distortion of the TBP geometry in the active site, consistent with the assumption that the vanadium geometry was allowed to refine freely inferred from the discussion and conclusions. Alkaline phosphatases have an interesting extended active site in which the active site is strongly influenced by the presence of other metals. The active site is commonly thought to be a dinuclear metalloenzyme with coordinating Mg^{2+} and/or Zn^{2+} ions [4,48]. Two of the equatorial oxygens in the VO$_3$ are positioned to be able to form hydrogen bonds with additional side chains, whereas the third is positioned between two Zn^{2+} ions.

4.2.2.3. Sinorhizobium melitoti phosphonoacetate hydrolase (PhnA) [148]. Phosphonoacetate hydrolase (PhnA) from the bacterium *S. melitoti* catalyzes the hydrolysis of phosphonates and is the only enzyme covered in this review that reacts with phosphonates not phosphates. Because it catalyzes the breaking of P–C bonds it is therefore classified as EC 3.6.1.9, however the sequence is very similar to that of alkaline phosphatases [148]. Crystals of the apo protein were soaked on ice for 10 min with 2 mM freshly boiled sodium orthovanadate solution to afford the tetragonal crystals used for this study. The structure was solved with a 1.8 Å resolution and deposited as PDB ID 3t00. In this complex the vanadium is in a slightly distorted TBP VO$_4$O geometry ($\tau = 0.83$), with VO$_4$ bound to an axial O$_{Thr}$ located 2.04 Å away. The VO$_3$ equatorial unit is also non-planar. The protein contains two Zn^{2+} ions which facilitate the interaction of the protein with vanadate inhibitor through multiple H-bonding systems. Specifically, one equatorial oxygen of the vanadate unit is electrostatically stabilized by interaction with both of the metal ions and one of the other oxygen atoms is stabilized by interacting with the amino acid side chains.

4.2.2.4. Bacillus stearothermophilus phosphatase. The PhoE phosphatase from *Geobacillus stearothermophilus* is a multifunctional nonspecific enzyme, as evidenced by classification of (at least) both EC# 3.1.3.2 and 3.1.3.5. The structure of crystals of PhoE-phosphate that had been soaked in 50.0 mM of ammonium metavanadate, 30.0% ethylene glycol, and 20.0 mM sodium acetate buffer (pH 5.0) for three days is deposited as PDB ID 1h2f [128]. Although the authors had expected to see a bound vanadate in the active site when solving the structure by molecular replacement, instead an oligomeric form of vanadate, trivanadate, nominally

$V_3O_8{}^{2-}$, is observed. The trivanadate species occupies the putative active site of the enzyme with minimal conformational changes to the backbone, but one end covalently binds to a His residue and the other end of the chain has a vanadium bound to a Glu residue. The center vanadium, then, has tetrahedral VO_4 geometry, whereas the two ends of the chain have distorted tetrahedral VO_3N and distorted tetrahedral VO_3O geometry respectively. The fact that an oligomer which is not normally observed in aqueous solution in significant amounts [80] is sufficiently stable to bind in the active site highlights the stabilizing role of the enzyme information of these protein–vanadate complexes.

4.2.2.5. Thermotoga maritime SurE protein.

The survival protein of the microbe *T. maritime* of previously unknown function was identified as a phosphatase of classification EC 3.1.3.5 in this study [149]. The crystals of SurE with vanadate (PDB ID: 1j9L) were grown from purified recombinant, native SurE protein in the presence of 80-fold excess of "vanadate" (likely activated) in a reservoir comprising 100 mM HEPES, pH 7.5, 200 mM calcium chloride and 25% (v/v) PEG 400. The structure was solved based beginning with a lower resolution structure of a selenomethionine (SeMet)-substituted protein as a starting point and subsequently refined. The presence of a di-metal-containing active site was observed, with both a Ca^{2+} ion and VO_4 unit. With no prior model of the active site to depend on, the authors appear to have allowed free refinement of vanadium-containing moiety and the vanadium coordination environment generates flags in both electron density and bond lengths by validation checks. That being said, the vanadium coordination environment as deposited is best described as very distorted tetrahedral with long V—O bonds (1.675–1.740 Å) and a very long fifth interaction (either 2.6 Å (authors) or 3.6 Å (deposited coordinates)) to a serine. If that fifth ligand is included, a τ of 0.43 can be calculated, which would be best described as distorted square pyramidal, an unusual geometry for vanadium–protein complexes as we have seen, but very typical for small molecules with VO_4O environments. The O atom of the VO_4 unit with the longest distance bridges to the nearby Ca^{2+} ion.

4.2.2.6. Xanthamonas axonopodis pv. citri nucleotide pyrophosphatase/phosphodiesterase (NPP).

Crystals of nucleotide pyrophosphatase/phosphodiesterase (NPP) of *X. axonopodis pv. citri* were grown at room temperature at pH 6.0 by hanging drop method [150]. These crystals were then soaked in 0.1 M NaHEPES (pH 7.5), 19% PEG 3350, and 500 μM sodium orthovanadate for 10 min to obtain the $P2_12_12_1$ crystals used to solve the structure deposited in the database as PDB ID 2gso. The NPP active site contains a VO_4 moiety covalently bound to an O_{Thr}. The O atoms on the VO_4 also interact with two Zn^{2+} ions and N atoms from side chains (Asn and Thr) at 2.8–2.9 Å. The model was constructed beginning with the holoenzyme (enzyme and cofactors) model and refined to "clearly indicated the presence of vanadate in a trigonal bipyramidal geometry in the active site." The VO_5 unit (where one O is O_{Thr}) was restrained by bond length (2.0 ± 0.1 Å) and bond angle ($\pm 3°$) from the ideal TBP in the final refinements. The authors, then, describe the structure as TBP and emphasize the "trigonal plane" of VO_3 despite the τ of 0.55.

4.2.2.7. Francisella tularensis acid phosphatase A (AcpA).

The acid phosphatase A (AcpA) of the pathogenic bacterium *F. tularensis* is a "highly expressed 57-kDa polyspecific periplasmic acid phosphatase [151]." The purified enzyme crystals soaked in 0.1 M NaHEPES (pH 7.5), 19% PEG 3350, and 500 μM sodium orthovanadate for 10 min to afford the orthorhombic crystals studied here. The authors collected two crystals at different wavelengths for anomalous difference Fourier analysis to solve the structure, deposited as PDB ID 2d1g. Although the structure is solved at 1.75 Å

resolution, there are several interesting parts to this structure and each draw some concern. In the authors' words: "Each AcpA molecule contains one orthovanadate ($HVO_4{}^{2-}$) and one metal ion bound to the active site. The metal ion was modeled as Ca^{2+} for purposes of crystallographic refinement, but appears with atom name UNK... in the PDB... to indicate that that the identity of the metal is unknown at this time." It is at least a Ca^{2+} and likely a 1st row transition metal. "There is also a decavanadate ion ($V_{10}O_{28}{}^{6-}$) bound in a crystal contact region, where it interacts with the carboxyl-terminal histidine affinity tag of one of the AcpA molecules." The orthovanadate species appears to be VO_4O distorted TBP based on the geometry ($\tau = 0.76$), although many of the V—O interactions are at ca. 1.9 Å and the O_{Ser} is 2.2 Å away. The authors call the species vanadate and do not indicate covalent bonding to O_{Ser}. The vanadate also shows interactions with neighboring His and Asp residues. This enzyme is similar to enzymes of "AlkP superfamily, which has been described in detail [152]."

4.2.2.8. Bacteroides thetaiotaomicron hexose phosphate phosphatase.

The structures of a wild-type and derivative hexose phosphate phosphatase (HPP) BT4131 from *B. thetaiotaomicron* VPI-5482 have been determined and deposited. The wild-type enzyme is proposed by the authors to be a member of the haloalkanoic acid dehalogenase enzyme superfamily, dominated by the phosphatases of interest to this review, but perhaps not appropriately assigned to that enzyme class [94]. Crystals of the wild-type and mutant enzyme complexed with vanadate were grown from equal volumes of purified proteins in 1 mM HEPES (pH 7.0) and 30% wt/vol polyethelene glycol (PEG) 1500, 10 mM $MgCl_2$, and 5 mM sodium orthovanadate at room temperature by the hanging drop method. The crystals used for data collection for the wild type were grown by soaking pre-formed apo crystals from a crystallization solution (10 mM $MgCl_2$, 0.2 M ammonium acetate, 0.1 M Bis-Tris (pH = 5.5) and 25% PEG 3350) in 2 mM sodium orthovanadate for 2 h before data collection. Orthorhombic crystals of each were isolated and the respective structures solved using the molecular replacement method from the published native protein structure, and deposited as PDB ID 2rbk (wild-type, 1.00 Å resolution) and 2rar (mutant, 1.52 Å resolution). In the wild-type HPP structure the vanadate is bound in a distorted TBP geometry ($\tau = 0.78$), with a VO_3 unit bound to a water molecule (2.1 Å) and covalently to O_{Asp} (2.0 Å) along with additional stabilization by hydrogen bonds/secondary interactions with other side chains and an Mg^{2+} ion cofactor. In a mutant where the Asp has been replaced by Ala (HPP D10A) the vanadate binds in a distorted tetrahedral geometry with only four bound O atoms, including to the same O_{Asp} as in the wild type, but no longer bound to a water molecule. Vanadate is a potent inhibitor and binds tighter than substrate [153].

4.2.2.9. Thermus thermophilus mannosyl-3-phosphoglycerate phosphatase.

Mannosyl-3-phosphoglycerate phosphatase is a phosphatase of class EC 3.1.3.70 found in many thermophilic microorganisms, including the bacteria *T. thermophilus* [154]. Crystals of the apo enzyme of mannosyl-3-phosphoglycerate phosphatase were soaked with substrate α-D-mannopyranosyl-(1,2)-O-D-glycerate (MG) HB27 in the presence of vanadate and magnesium ion for 1 h. Two structures were characterized of protein–vanadate complexes one containing substrate (PDB ID 3zwk) and one without substrate (PDB ID 3zx5). In the structure of the complex of protein, vanadate and substrate MG the vanadium is coordinated with Asp (V–Asp distance 2.0 Å) and MG substrate (V–MG distance 2.7 Å). The geometry is distorted VO_5 TBP environment ($\tau = 0.89$) and the VO_3 has fixed bond lengths resulting from the restricted optimization. The second structure, PDB ID 3zx5, was from mannosyl-3-phosphoglycerate phosphatase soaked for 14 h in the presence of vanadate, gadolinium, and magnesium ion,

but no substrate. This structure was solved to 2.1 Å resolution. The coordination geometry of the vanadium is distorted TBP ($\tau = 0.56$) with the VO$_3$ being combined with an Asp residue and a water molecule completing the VO$_5$ coordination sphere. This structure shows many similarities with the first structure, with the exception that the protein and water molecules in 3zx5 are replacing the interactions that involved the MG substrate in 3zwk.

4.2.2.10. H. sapiens N-acetylneuraminate-9-phosphate phosphatase. Human *N*-acetylneuraminate-9-phosphate phosphatase is a hydrolase classified as E.C. 3.1.3.29 [155]. Details for this structure and its determination are limited, despite its publication. Based on the description in the PDB it is surmised that crystals of the apo protein were grown using a vapor diffusion, hanging drop technique at room temperature and then soaked with vanadate and/or magnesium. The structure was solved at 2.70 Å resolution and deposited as PDB ID 4knw. The structure appears to have a VO$_4$ moiety bound to an O$_{Asp}$ at 2.12 Å. The VO$_4$O coordination geometry is best described as distorted TBP and exhibits the mathematically allowed oddity when β–α > 60° (see Section 2.3 and Refs. [65,67]) of $\tau = 1.07$. Indeed this is observed because of shape of the coordination arrangement and the fact that the τ analysis used here is meaningful only for structures along the Berry pathway, as described elsewhere [64–66]. In this particular complex the coordination environment may deviate from the square pyramid and from the Berry pathway, and an analysis using the continuous shape measure methodology would be desirable.

4.2.3. Sulfur-containing active sites

4.2.3.1. Protein tyrosine phosphatases. Comparison of protein tyrosine phosphatase domains across many different organisms all seem to show extensive sequence conservation with very similar mechanisms [95,156,157]. This entry therefore describes vanadate complexes of several different enzymes, some cytosolic and others membrane bound, subdivided further by extracellular domain. Vanadate is tetrahedral in solution, but in active sites of PTPs often forms stable pentavalent structures exhibiting trigonal bipyramidal geometries [126,158,159]. A common feature of many of these species is a sulfur atom of a cysteine amino acid residue [157]. However, some reports have suggested that vanadate supports a more associative mechanism which is not consistent with all the experimental data that suggest that the transition state is dissociative [160].

4.2.3.2. Bovine low molecular weight phosphotyrosyl phosphatase (low Mr PTPase) [126]. Samples of purified, desalted, and crystallized recombinant *Bos taurus* heart low Mr PTPase [161] were "soaked in 0.5 mM Na$_2$VO$_4$ [sic] for 1 day prior to X-ray data collection." The added vanadium species was likely to actually be sodium orthovanadate, Na$_3$VO$_4$, which would most likely be present in solution as H$_2$VO$_4^-$ at this pH. The crystallization occurred at pH 7.5 for the crystals, the structure of which was deposited as PDB ID 1z12. The crystal structure was solved in the *C*2 space group beginning with the isomorphous model from the native enzyme and a VO$_4$ moiety covalently bound (2.16 Å) to S$_{Cys}$ in the active site was observed. After several refinement cycles the authors fixed a VO$_3$ plane (vide supra, Section 3), enforcing TBP geometry and resulting in a τ of 0.88.

4.2.3.3. H. sapiens receptor-like protein tyrosine phosphatase γ (RPTPγ). Two unique crystallographic settings of apo (substrate-free) crystals of the human receptor-like protein tyrosine phosphatase γ (RPTPγ) were grown at room temperature using hanging-drop vapor-diffusion techniques at pH 6.5 in buffered crystal growth solutions with slightly varying conditions [162].

Each crystal form of apo crystals was soaked in 25% (w/v) PEG 3350, 0.2 M magnesium chloride, 0.1 M HEPES, pH 7.5, and 10 mM sodium orthovanadate for 6 h. Both crystal forms of vanadate-containing species were reported and deposited, one in an orthorhombic setting ($P2_12_12_1$, PDB ID: 3qcc) and one in a trigonal setting ($P3_221$, PDB ID: 3qcd). [100] The trigonal setting only had one chain in the asymmetric unit. Both were solved using molecular replacement; the apo form of RPTPγ served as an initial model for 3qcc and one chain of 3qcc served as the initial model for 3qcd. The structures both show a closed WPD-loop (Trp-Pro-Asp), which is one of the characteristic structural motifs found in PTPs, and is thought to be critical to the enzymes activity. In each crystal system the active site is very similar with a VO$_4$ unit liganded (bound) to a S$_{Cys}$ in a near TBP geometry ($\tau = 0.98$, 3qcc; $\tau = 0.91$, 3qcd).

The Protein Structure Initiative (PSI) of the U.S. National Institute of General Medical Sciences (NIGMS) [163] has made dozens of depositions of structures to the PDB related to phosphatase [164], including an open WPD-loop conformation of RPTPγ with vanadate solved at 2.60 Å resolution as PDB ID 2hy3. This phase of the PSI project was designed to be high throughput and these depositions offer valuable contributions to the knowledge base, but do not offer author commentary as there is no accompanying manuscript and limited experimental information. The coordination geometry of vanadium in this structure is loosely described as distorted TBP, but all the bond lengths are very long; the four shortest bonds are V—O and all are over 1.9 Å, whereas a V···S$_{Cys}$ is observed at 2.9 Å. If one includes all those interactions, a value of τ of 0.76 can be calculated. Even more so than 3qcc [100], though, the reality of the 5th bond may be questioned and one may also describe this as a distorted tetrahedral VO$_4$ coordination (O—V—O angles range from 103° to 115°).

4.2.3.4. H. sapiens protein tyrosine phosphatase (PTP1b). Several structures with the human PTP1b enzyme and variants have been reported. Andersen et al. appear to have determined the structure of wild-type human PTP1b as well as a mutant (F182H) [165], but those coordinates do not seem to have been deposited in the PDB (or are unreleased).

4.2.3.5. H. sapiens receptor-like protein tyrosine phosphatase β (HPTPβ). The human protein tyrosine phosphatase β (HPTPβ) is also a receptor-based protein that is classified as EC 3.1.3.48 and has been a target for inhibition studies. Evdokimov and co-workers cloned, expressed, purified, and crystallized several catalytic domain regions of HPTPβ along with a number of inhibitors, including vanadate [159]. To isolate the crystals studied, monoclinic ($P2_1$) crystals of the apo species of the third catalytic domain were soaked in vanadate at a concentration of 1–10 mM in crystallization buffer (21% PEG 8000, 220 mM MgCl$_2$, 1% BME, 0.1% BOG, 5 mM DTT) for 2–24 h. The structure was solved at 1.75 Å resolution by molecular replacement from the apo species and is deposited as PDB ID 2i4e. The putative active site of this catalytic domain is similar to that of human PTP1B, with a nearby WPD loop and a VO$_4$ moiety attached to a S$_{Cys}$ in a distorted TBP VO$_4$S geometry ($\tau = 0.82$). The three equatorial V—O bonds are all in the range of 1.72–1.74 Å, whereas the axial/apical V—O is at 1.98 Å and the opposite V···S$_{Cys}$ is observed at 2.47 Å.

4.2.3.6. H. sapiens protein tyrosine phosphatase (PTP1b). Brandão et al. obtained several structures of human PTP1B with vanadate and with and without a peptide substrate fragment DADEYL [41]. Crystals were grown by sitting drop diffusion at 4 °C with mixtures of 0.5 μL of 30% (w/v) sucrose, and 3 μL of precipitant solution (0.1 M HEPES, pH 7.5, 0.2 M magnesium acetate, and 15–17% PEG 8000) and a variable protein solution containing preincubated Na$_3$VO$_4$ and DADEYL (pH 8.5–9.0) with native PTP1B in

149

10 mM Tris, pH 7.5, 25 mM NaCl, 0.2 mM EDTA, and 3 mM dithio-threitol. Different ratios of protein, peptide and vanadate were used to get crystals containing DADEYL substrate and vanadate (30:3:1; peptide:V:protein) and to obtain free protein–vanadate crystal (3:30:1). The protein–vanadate crystal structure was solved at 2.25 Å resolution and deposited as PDB ID 3i80. The tetrahedral vanadate in solution binds to the PTP1B forming a pentacoordinate transition state analog complex with the protein in nearly perfect TBP geometry ($\tau = 0.90$). The vanadium has a VO_4S coordination geometry and is bound as a VO_4 unit to a S_{Cys}. Vanadate is stabi-lized in the active site and binds better than a tetrahedral species that cannot expand its coordination geometry, e.g. phosphate and arsenate. The substrate-containing crystal was solved at 2.30 Å res-olution and deposited as PDB ID 3i7z. When vanadate is bound to PTP1B in the presence of DADEYL it is still VO_4S in the crystal struc-ture, but is now bound to Cys and an O of the DADEYL with a VO_3 unit in a five-coordinate transition state manner ($\tau = 0.83$). Both structures showed the closed loop and similar hydrogen bonding were found between the Q, R, D, Y and P-loops for both.

4.2.3.7. H. sapiens protein tyrosine phosphatase (PTP1b) W179F. Brandão et al. have also obtained a structure of the mutant human PTP1B (W179F) in the presence and absence of vanadate [166]. Their crystallization methods were similar to those employed for those in 3i80, i.e. sitting drop diffusion at 4 °C with mixtures of 0.5 μL of 30% (w/v) sucrose, and 3 μL of precipitant solution (0.1 M HEPES, pH 7.5, 0.2 M magnesium acetate, and 15–20% PEG 8000) and an excess of W179F PTP1B with 60 mM Na_3VO_4 in 10 mM Tris, pH 7.5, 25 mM NaCl, 0.2 mM EDTA, and 3 mM dithiothre-itol. The structure was solved at 2.20 Å resolution using molecular replacement and deposited as PDB ID 3qkq. The structural solution was modeled as "two conformations observed with approximately equal occupancy: a WPD loop-open ligand-free form and a closed vanadate-bound form." The 48/52% refined occupancies offer some insight as to how an X-ray crystal structure is an average model. In the vanadium-containing form, the vanadate has VO_4S coordi-nation geometry in a TBP arrangement ($\tau = 0.88$). The vanadium consists of a VO_3 unit with apical/axial positions occupied by the S_{Cys} and an oxygen atom from a water molecule. There are also addi-tional hydrogen bonding interactions to the P-loop and neighboring amino acids.

4.2.3.8. Yersinia enterocolitica YopH protein tyrosine phos-phataseW354F mutant. A mutant of the protein tyrosine phosphatase YopH from the bacterium *Yersinia enterocolitica* (type O:9) was isolated and crystallized. YopH is a powerful phos-phatase that is very effective in catalyzing phosphate monoester dianions and is classified as EC 3.1.3.48 [127,167]. The W345F mutant of YopH was produced to probe the catalytic impact of removing the tryptophan in the WPD loop. Crystals were obtained by co-crystallization in solution of 0.5 μL of activated 5 mM Na_3VO_4 with 2 μL of protein solution (20 mg/mL in 100 mM sodium acetate, 100 mM NaCl, 1 mM EDTA, and 1 mM DTT, pH 5.7) and 3 μL of precipitant solution (12–19% PEG 3350 and 0.1 M HEPES, pH 7.5). Orthorhombic crystals of the protein–vanadate complex were collected, solved at 1.4 Å resolution, and deposited as PDB ID 3f9b [127]. The structure reveals a "quasi-open con-formation" of the WPD loop, unlike in the wild-type version of the protein. The vanadium species present in the solution is also described as a divanadate moiety, i.e. V_2O_7. The authors claim that this is not merely a disordered, partially occupied vanadate VO_4 species. That is, because crystallography shows average structure over an entire crystal, it is reasonable to imagine that a vanadate could occupy one place or the other *in a random, non-periodic manner* over the whole of the structure which could appear in the electron density model to be less than a fully present V_2O_7

species. The authors describe the V_2O_7 structure as "a double distorted trigonal bipyramid containing a cyclic $[VO]_2$ core" which is coordinated to a S_{Cys} at a distance of 2.44 Å. Each of the V–O bonds are quite long (1.89–2.08 Å). The two vanadium centers have coordination geometries best described as SP VO_4O and TBP VO_4S, then, with τ values of 0.07 and 0.78, respectively. The vanadium site of divanadate covalently bound to the protein is more TBP and the unbound end is SP, like nearly all small-molecule VO_4O species [67].

4.2.3.9. Yersinia enterocolitica YopH protein tyrosine phosphatase. The structure of the wild-type YopH protein with vanadate is unpublished, but the coordinates for the structure (solved at 2.20 Å resolution) have been deposited as PDB ID 2i42 [168] and some details can be gleaned from the PDB and also a preliminary report [158]. That species was isolated by co-crystallization of the native protein with orthovanadate at pH 8.0. In their preliminary report of the structure, Denu et al. state, "The structure demonstrated a distorted trigonal bipyramidal geometry that may mimic the tran-sition state for thiol-phosphate hydrolysis [158]." The vanadium center has VO_4S geometry with a 2.51 Å V—S_{Cys} distance, however the angles lead to a τ of 0.30 and a description of SP seems more appropriate. Shape measures, however, purport that 2i42 is not well described by either TBP or SP [134].

4.2.3.10. D. melanogaster SSu72 phosphatase. The Ssu72 phos-phatase is an essential phosphatase in eukaryotes that acts on serine in the C-terminal domain (CTD) of RNA polymerase II [169]. The protein–vanadate complex of Ssu72 from *drosophila*, classi-fied as EC 3.1.3.16 was crystallized at pH 7.5. The vanadate–protein crystal for data collection was formed by soaking the apo protein in 2 mM Na_3VO_4 for 2 h. The structure was solved by molecular replacement to a resolution of 2.35 Å and deposited as PDB ID 3omx. The vanadium center is bound to Cys with a bond 2.31 Å in the active site of the protein and a distorted TBP VO_4S coordination geometry with a τ value of 0.73. The complex also shows H bonding between the vanadate and neighboring Asp and Arg.

4.2.3.11. D. melanogaster receptor protein tyrosine phosphatase PTP10D. The fruit fly receptor protein tyrosine phosphatase PTP10D is a well-studied, highly efficient enzyme classified as EC 3.1.3.48 [95]. The PTP domain of PTP10D was purified and crystal-lized at pH 6.50, then soaked in 5 mM sodium vanadate to afford the crystals studied. The structure was solved at 2.70 Å resolu-tion using molecular replacement from the apo PTP10D structure and deposited as PDB ID 3s3f. The protein supports a tetrahedral vanadate with four long V—O interactions of over 1.90 Å and 6 O—V—O angles between 107.9° and 110.6°, supporting a tetrahedral assignment. However, there is also a Cys residue 4.5 Å that is not covalently bonded, but is poised for bonding. The authors described this V-atom as being associated "loosely" to a Lys154 (3.6 Å) and Cys 242 (4.5 Å). Inclusion of this Cys ligand as the 5th ligand, results in a τ value of 0.88. The authors conclude that despite conservation in sequence, this study has shown that the less concerted domains can be very important for inhibitor-protein complexes as well.

4.2.3.12. H. sapiens VH1-related protein, Z member (VHZ). Human VH1-related protein, Z member (VHZ) is a 150-residue human PTP classified as EC 3.1.3.16 and 3.1.3.48. It "contains only the minimal structural elements common to all PTPs [157]." In the authors' screening of over 300 peptides, the enzyme was specific for hydrolysis of phosphotyrosine-containing peptides, but not phos-phoserine or phosphothreonine. Crystals of VHZ with vanadate were grown at room temperature by sitting drop vapor depo-sition from purified wild-type VHZ and sodium vanadate mixed with an equal volume of L-malate (pH 7.0) and 15–20% of PEG

3350. The structure of the orthorhombic crystals was solved at 1.1 Å resolution and deposited as PDB ID 4erc. The structure contains a metavanadate (VO_3) unit that is nearly planar with an apical/axial S_{Cys} at 2.4 Å, but the authors claim that structural and computational studies both support an electrostatic interaction, not covalent binding. The VO_3 is also hydrogen bound to several side chains. The authors also indicate an interaction of over 3.1 Å axially opposite the Cys to an Arg from neighboring molecule and likely H-bond interacts with Glu and Asp.

Several other, as yet unpublished structures are in the PDB including PDB ID 4qih [137], a *Mycobacterium tuberculosis* glucosyl-3-phosphoglycerate phosphatase with VO_4N coordination ($\tau = 0.81$), PDB ID 3zwu [170], a *Pseudomonas fluorescens* PhoX with a very complex multinuclear VO_4O geometry (also two Fe^{2+} and three Ca^{2+} nearby) with $\tau = 0.84$, and PDB ID 4kkz [171], a *Phaseolus vulgaris* purple acid phosphatase with a multinuclear complex with VO_4O geometry ($Fe^{2+}/Zn^{2+}/Na^+$ also nearby) with $\tau = 0.83$. We resist the temptation to discuss them more fully here.

5. Inhibition of phosphatase by vanadium compounds

5.1. Measuring inhibition of vanadium compounds

The inhibition of vanadium salts or compounds can be measured using a range of different enzyme assays [172]. The mode of inhibition – whether competitive, non-competitive, or a mixed type inhibitor – is determined by varying the inhibitor concentration and measuring the associated activity at a range of substrate concentrations [93]. Measuring the compound concentration may be trivial for other compounds, but it is non-trivial for vanadium compounds because of the many hydrolytic and redox reactions vanadium compounds generally undergo (*c.f.* Section 2.4) [15,69]. Indeed, the speciation of vanadium compounds is generally complex, and depending on ligand, oxidation state and concentration, the species that form in solution will vary and be very sensitive to the pH of the specific conditions under considerations [15,69]. Considering the complications with speciation the experimentation needed for determination of a K_i is, therefore, much more demanding than measuring EC_{50}, which can be done by simply varying the inhibitor concentration.

Measuring K_i is particularly complex with materials such as vanadium compounds that interact with buffers and whose stability is closely linked to pH and the conditions of the solution [74,91]. The measurement of K_i will require first determining the mode of inhibition before varying the inhibitor concentration, a step which is not needed for measuring the EC_{50}. For example, in the case of measuring the K_i of dipicolinate dioxovanadium(V), the mechanism of inhibition against alkaline phosphatase is competitive [173]. If we determine the K_i values of the vanadate and free ligand, dipicolinate, then the K_i value for the complex can be calculated using Michaelis–Menten kinetics according to the equations shown in Eq. (1). This calculation requires that concentrations of complex, free ligand, and vanadate be known. Because the compound is dissociating to form vanadate and free ligand, dipicolinate, the speciation must be known under the varying assay conditions [173].

$$\text{slope} = \frac{K_m}{V_{max}} \left(1 + \frac{[V^V\text{dipic}]}{K_{iV^V\text{dipic}}} + \frac{[V^V\text{dipic}]}{K_{iV_i} K_f [\text{dipic}]} + \frac{[\text{dipic}]}{K_{i\text{dipic}}} \right) \quad (1)$$

This type of analysis is non-trivial because it does require known speciation under conditions of the assay [173]. Because most vanadium compounds are not stable under physiological conditions, many researchers choose to measure the EC_{50} values for the vanadium compounds, which can be measured without knowing the speciation in solution. Indeed, often the chemical analyses are not carried out, which then will result in the description of an K_i which

is larger and suggests that the compound is less potent than what the compound actually is. That is, the measured effect is a result of the combination of the complex, vanadate, and free ligand and not simply complex. Measuring the K_i provides information on the mode of inhibition, however, such studies require that the concentration of complex is known so that several series of measurements can be carried out. In contrast, measuring EC_{50} values simply requires one series of studies, and the absence of speciation data can be accounted for when considering the potency of the compound. The current recommendations of the International Union of Biochemistry have recently been updated and also address these issues [45].

In addition to the complications described above, there is a matter of compound compatibility with the assay conditions. Vanadate, vanadyl cation, and even vanadium compounds interact with most buffers and carbonate [73,74]. Unfortunately the speciation of the salts and materials are commonly not considered. This is particularly critical for routine conditions for PTPases assays for vanadium(V) systems [15]. Generally, the concentration of vanadium(V) salts and complexes are changed under the reduced environment needed to assay the PTPases. As a result, there are particularly few studies carried out with vanadium(V) complexes, and even fewer studies in which the complex remains intact during the assay. However, some studies, particularly enzyme studies, have been carried out while the speciation studies have been done concurrently.

An early study by van Etten and coworkers investigated the differences in activities between the alkaline and acid phosphatases with vanadate [12]. Since then detailed studies have been done comparing sequences within the groups of phosphatases leading to much more sophisticated comparisons [174]. Differences in enzyme activities in sources of phosphatases are to be expected when similarities are less. Human protein tyrosine phosphatase, PTP1B, was first obtained from placenta, but is also expressed in many tissues [175,176]. The reports are not always clear with regard to the proteins that are used and from which sources making comparisons difficult. Recently some authors have even expressed the human PTP1B catalytic domain using *E. coli* [177]. If the phosphatases have similar protein sequence the origin of the source becomes less critical. Importantly, the reader should recognize the variation in the K_i values obtained in different studies may not only be due to the complicated chemistry involved [178]. The reader is referred to the original literature for more information on this subject [126].

5.2. Oxoanions (phosphate, arsenate, vanadate, chromate, molybdate and tungstate)

Although our primary focus is vanadates, several oxoanions are known inhibitors of phosphatases. Oxometalates in particular are well-known inhibitors for phosphatases [12,68,145,147]. This inhibition is either attributed to the binding of the oxometalate in the product (phosphate) binding site or the binding of the oxometalate as a transition state analog [12,15,68,126,132,145,179]. We review here studies that reported K_i values for different oxometalates. Such a compilation of necessarily narrower studies permits a comparison extending over the different oxometalates within one phosphatase and its source, and also a comparison among enzyme sources and a particular inhibiting anion. We and others previously reported that less inhibition is observed when the inhibitor is binding in the product (phosphate) binding site, as seen for phosphate and arsenate [12,68,91,147]. Larger differences are observed when the inhibitor is binding as a transition-state analog such as vanadate, molybdate and tungstate. The previous literature reports suggest that the higher the coordination number the more potently the enzyme will be inhibited. The analysis of the data shown in Table 4 furthermore

151

Table 4
The K_i values for simple oxometalate anions against phosphatases.

Inhibitor	EC #	Origin of phosphatase	Active site nucleophile	pH of assay	K_i (M)	Substrate	Assay buffer	Ref.
Inorganic phosphate $P_i/H_2PO_4{}^{2-}/HPO_4$	3.1.3.48	Bovine heart	S/Cys	5.0	$2.2 \pm 0.4 \times 10^{-3}$	pNPP	Sodium acetate	[126]
	3.1.3.48[a]	Bovine liver	S/Cys	5.5	3×10^{-3}	pNPP	Sodium acetate	[180]
	3.1.3.48	Human[c]	S/Cys	7.0	1.7×10^{-2}	pNPP	3.3-Dimethylglutarate	[181]
	3.1.3.16	λ Phage	DNM	7.8	$7.1 \pm 1.3 \times 10^{-4}$	pNPP	Tris	[182]
	3.1.3.3	Human[d]	DNM	8.0	$1.2 \pm 0.2 \times 10^{-3}$	pNPP	2-Amino-2-methyl-1.3-propanediol	[183]
	3.1.3.2	Human abdominal epidermis	N/His	5.0	1.0×10^{-3}	pNPP	Sodium 3-3-dimethylglutarate	[184]
	3.1.3.2	Human liver	N/His	5.0	8.0×10^{-4}	pNPP	Sodium acetate	[12]
	3.1.3.2	Human seminal fluid	N	5.5	1.8×10^{-2}	MUP	Sodium acetate	[185]
	3.1.3.2	Human seminal fluid	N	7.1	$>8.0 \times 10^{-4}$	MUP	Imidazole	[185]
	3.1.3.2	Bovine spleen[g,h]	DNM	6.0	5.4×10^{-3}	pNPP	MES	[186]
	3.1.3.2	Porcine uterine fluid[g,h]	DNM	5.5	$3.4 \pm 0.4 \times 10^{-3}$	pNPP	Sodium acetate	[47]
	3.1.3.2	Labeo rohita Liver	N	5.5	1.9×10^{-7}	pNPP	Sodium acetate	[187]
	3.1.3.2	Drosophila melanogaster	N	5.0	5.2×10^{-4}	pNPP	Sodium acetate	[188]
	3.1.3.2	Banana	N	5.8	9.7×10^{-5}	PEP	Sodium acetate	[189]
	3.1.3.2	Potato	N/His	6.0	$1.0 \pm 0.2 \times 10^{-3}$	pNPP	HEPES	[147]
	3.1.3.2	Wheat germ	N/His	5.0	1.3×10^{-3}	pNPP	Sodium acetate	[12]
	3.1.3.2	Wheat germ	N/His	6.0	$3.5 \pm 0.6 \times 10^{-4}$	pNPP	HEPES	[190]
	3.1.3.2	Penicillium chrysogenum	N	5.5	4.2×10^{-4}	pNPP	Sodium acetate	[191]
	3.1.3.2	Aspergillus ficuum	N	6.0	1.6×10^{-4}	pNPP	Imidazole	[192]
	3.1.3.1	Chicken intestine	O	8.0	$9.5 \pm 1.3 \times 10^{-5}$	pNPP	HEPES	[147]
	3.1.3.1	Pigeon intestine	O	8.0	$8.4 \pm 1.2 \times 10^{-5}$	pNPP	HEPES	[147]
	3.1.3.1	Calf intestine	O/Ser	8.0	$1.3 \pm 2.0 \times 10^{-4}$	pNPP	HEPES	[147]
	3.1.3.1	Dog intestine	O/Ser	8.0	$4.1 \pm 0.6 \times 10^{-4}$	pNPP	HEPES	[147]
	3.1.3.1	Horse intestine	O/Ser	8.0	$2.1 \pm 0.3 \times 10^{-4}$	pNPP	HEPES	[147]
	3.1.3.1	Rabbit intestine	O/Ser	8.0	$3.8 \pm 0.3 \times 10^{-4}$	pNPP	HEPES	[147]
	3.1.3.1	Sheep intestine	O/Ser	7.5	$2.1 \pm 0.4 \times 10^{-4}$	pNPP	HEPES	[147]
	3.1.3.1	Sheep intestine	O/Ser	8.0	$1.0 \pm 0.2 \times 10^{-4}$	pNPP	HEPES	[147]
	3.1.3.1	Sheep intestine	O/Ser	8.5	$3.0 \pm 0.6 \times 10^{-4}$	pNPP	TAPS	[147]
	3.1.3.1	Sheep intestine	O/Ser	9.0	$6.2 \pm 1.2 \times 10^{-4}$	pNPP	CHES	[147]
	3.1.3.1	Bovine mucosa	O/Ser	8.0	$8.1 \pm 0.9 \times 10^{-5}$	pNPP	HEPES	[147]
	3.1.3.1	Porcine mucosa	O/Ser	8.0	$4.4 \pm 0.5 \times 10^{-5}$	pNPP	HEPES	[147]
	3.1.3.1	Chicken intestine	O/Ser	8.0	$4.7 \pm 0.3 \times 10^{-4}$	pNPP	HEPES	[173]
	3.1.3.1	Human liver	O/Ser	7.4	4×10^{-5}	pNPP	2-Methyl-2-aminopropan-1-ol, Tes. and Tris	[146]
	3.1.3.1	Human liver	O/Ser	9.0	9×10^{-5}	pNPP	2-Methyl-2-aminopropan-1-ol, Tes. and Tris	[146]
	3.1.3.1	Scylla serrata viscera	O	10	9.5×10^{-4}	pNPP	Sodium carbonate	[193]
Arsenate $AsO_4{}^{2-}$	3.1.3.48	Human[c]	S/Cys	7.0	1.5×10^{-4}	pNPP	3.3-Dimethylglutarate	[181]
	3.1.3.48[a]	Bovine liver	S/Cys	5.5	3×10^{-4}	pNPP	Sodium acetate	[180]
	3.1.3.48	Yersinia	S/Cys	7.0	$8.9 \pm 0.5 \times 10^{-4}$	pNPP	3.3-Dimethylglutarate	[194]
	3.1.3.16	λ Phage	DNM	7.8	$6.0 \pm 1.4 \times 10^{-3}$	pNPP	Tris	[182]
	3.1.3.2	Human liver	N/His	5.0	1.8×10^{-4}	pNPP	Sodium acetate	[12]
	3.1.3.2	Human seminal fluid	N	5.5	$>4.0 \times 10^{-3}$	MUP	Sodium acetate	[185]
	3.1.3.2	Human seminal fluid	N	7.1	1.0×10^{-5}	MUP	Imidazole	[185]

152

Table 4 (*Continued*)

180

Inhibitor	EC #	Origin of phosphatase	Active site nucleophile	pH of assay	K_i (M)	Substrate	Assay buffer	Ref.
	3.1.3.2	Bovine spleen[g,h]	DNM	6.0	1.8×10^{-4}	pNPP	MES	[186]
	3.1.3.2	Porcine uterine fluid[g,h]	DNM	5.5	6.4×10^{-4}	pNPP	Sodium acetate	[47]
	3.1.3.2	Potato	N/His	6.0	$1.7 \pm 0.3 \times 10^{-5}$	pNPP	HEPES	[147]
	3.1.3.2	Wheat germ	N/His	6.0	$3.2 \pm 0.5 \times 10^{-5}$	pNPP	HEPES	[147]
	3.1.3.2	Wheat germ	N/His	5.0	6.1×10^{-4}	pNPP	Sodium acetate	[12]
	3.1.3.1	Chicken intestine	O	8.0	$4.2 \pm 0.6 \times 10^{-6}$	pNPP	HEPES	[147]
	3.1.3.1	Pigeon intestine	O	8.0	$5.9 \pm 0.8 \times 10^{-5}$	pNPP	HEPES	[147]
	3.1.3.1	Calf intestine	O/Ser	8.0	$4.8 \pm 0.9 \times 10^{-6}$	pNPP	HEPES	[147]
	3.1.3.1	Dog intestine	O/Ser	8.0	$1.8 \pm 0.3 \times 10^{-5}$	pNPP	HEPES	[147]
	3.1.3.1	Horse intestine	O/Ser	8.0	$1.2 \pm 0.2 \times 10^{-5}$	pNPP	HEPES	[147]
	3.1.3.1	Rabbit intestine	O/Ser	8.0	$1.4 \pm 0.1 \times 10^{-5}$	pNPP	HEPES	[147]
	3.1.3.1	Sheep intestine	O/Ser	8.0	$7.1 \pm 1.4 \times 10^{-6}$	pNPP	HEPES	[147]
	3.1.3.1	Bovine mucosa	O/Ser	8.0	$8.9 \pm 1.0 \times 10^{-6}$	pNPP	HEPES	[147]
	3.1.3.1	Porcine mucosa	O/Ser	8.0	$1.5 \pm 0.2 \times 10^{-5}$	pNPP	HEPES	[147]
	3.1.3.1	Calf intestine	O/Ser	9.5	$2.1 \pm 0.4 \times 10^{-5,b}$	AttoPhos	DEA	[195]
	3.1.3.1	Calf intestine	O/ser	9.5	$8.6 \pm 1.4 \times 10^{-6}$	AttoPhos	DEA	[195]
	3.1.3.1	Chicken intestine	O	8.0	$1.8 \pm 0.1 \times 10^{-5}$	pNPP	HEPES	[173]
	3.1.3.1	Scylla serrata viscera	O	10	1.1×10^{-3}	pNPP	Sodium carbonate	[193]
Vanadate VO₄³⁻	3.1.3.48	Bovine heart	S/Cys	5.0	$5.4 \pm 0.8 \times 10^{-6}$	pNPP	Sodium acetate	[126]
	3.1.3.48[a]	Bovine liver	S/Cys	5.5	2×10^{-3}	pNPP	Sodium acetate	[180]
	3.1.3.48	Human[c]	S/Cys	7.3	$3.8 \pm 0.2 \times 10^{-7}$	FDP	HEPES	[25]
	3.1.3.48	Human[e]	S/Cys	5.0	3.6×10^{-5}	FDP	Sodium acetate	[196]
	3.1.3.48	Human[f]	S/Cys	5.0	2.4×10^{-5}	pNPP	Sodium acetate	[196]
	3.1.3.48	Human[c]	S/Cys	7.5	$5.6 \pm 0.8 \times 10^{-6}$	pNPP	Tris	[197]
	3.1.3.48	Human[c]	S/Cys	5.5	$4.1 \pm 0.8 \times 10^{-4}$	pNPP	Tris	[197]
	3.1.3.48	Human[g]	DNM	7.5	$9.3 \pm 0.9 \times 10^{-6}$	pNPP	Tris	[197]
	3.1.3.48	Yersinia	S/Cys	5.5	1.1×10^{-6}	pNPP	Acetate	[198]
	3.1.3.48	Yersinia	S/Cys	7.5	1.2×10^{-6}	pNPP	Tris	[198]
	3.1.3.16	λ Phage	DNM	7.8	$7.0 \pm 2.0 \times 10^{-7}$	pNPP	Tris	[182]
	3.1.3.2	Human seminal fluid	N	5.5	7.0×10^{-4}	MUP	Sodium acetate	[185]
	3.1.3.2	Human abdominal epidermis	N/His	5.0	1.9×10^{-6}	pNPP	Sodium 3-3-dimethylglutarate	[184]
	3.1.3.2	Human liver	N/His	5.0	2.0×10^{-7}	pNPP	Sodium acetate	[12]
	3.1.3.2	Human seminal fluid	N	7.1	1.3×10^{-5}	MUP	Imidazole	[185]
	3.1.3.2	Labeo Rohita liver	N	5.5	5×10^{-7}	pNPP	Sodium acetate	[187]
	3.1.3.2	Potato	N/His	7.0	$2.2 \pm 0.2 \times 10^{-7}$	pNPP	2-(N-Morpholino)ethanesulfonic acid	[37]
	3.1.3.2	Potato	N/His	6.0	$2.1 \pm 0.2 \times 10^{-7}$	pNPP	2-(N-Morpholino)ethanesulfonic acid	[37]
	3.1.3.2	Potato	N/His	6.0	$1.3 \pm 0.2 \times 10^{-6}$	pNPP	HEPES	[147]
	3.1.3.2	Wheat germ	N/His	5.0	6.7×10^{-6}	pNPP	Sodium acetate	[12]
	3.1.3.2	Wheat germ	N/His	6.0	$1.6 \pm 0.3 \times 10^{-6}$	pNPP	HEPES	[147]
	3.1.3.2	Porcine uterine fluid[g,h]	DNM	5.5	$4.0 \pm 0.5 \times 10^{-5}$	pNPP	Sodium acetate	[47]
	3.1.3.1	Pigeon intestine	O	8.0	$7.2 \pm 1.0 \times 10^{-6}$	pNPP	HEPES	[147]
	3.1.3.1	Dog intestine	O/Ser	8.0	$2.6 \pm 0.4 \times 10^{-6}$	pNPP	HEPES	[147]
	3.1.3.1	Horse intestine	O/Ser	8.0	$1.1 \pm 0.2 \times 10^{-6}$	pNPP	HEPES	[147]
	3.1.3.1	Rabbit intestine	O/Ser	8.0	$2.7 \pm 0.2 \times 10^{-6}$	pNPP	HEPES	[147]
	3.1.3.1	Sheep intestine	O/Ser	7.5	$8.3 \pm 1.7 \times 10^{-7}$	pNPP	HEPES	[147]
	3.1.3.1	Sheep intestine	O/Ser	8.0	$4.9 \pm 1.0 \times 10^{-7}$	pNPP	HEPES	[147]
	3.1.3.1	Sheep intestine	O/Ser	8.5	$1.5 \pm 0.3 \times 10^{-6}$	pNPP	TAPS	[147]
	3.1.3.1	Sheep intestine	O/Ser	9.0	$4.3 \pm 0.8 \times 10^{-6}$	pNPP	CHES	[147]
	3.1.3.1	Bovine mucosa	O/Ser	8.0	$5.8 \pm 0.7 \times 10^{-7}$	pNPP	HEPES	[147]

3.1.3.1	Porcine mucosa	O/Ser	8.0	$2.6 \pm 0.3 \times 10^{-6}$	pNPP	HEPES	[147]
3.1.3.1	Calf intestine	O/Ser	8.0	$9.7 + 1.9 \times 10^{-7}$	pNPP	HEPES	[147]
3.1.3.1	Calf intestine	O/Ser	8.0	$4.9 \pm 0.4 \times 10^{-7}$	pNPP	HEPPS	[199]
3.1.3.1	Calf intestine	O/Ser	9.5	$2.1 \pm 1.5 \times 10^{-6}$ [b]	AttoPhos	DEA	[195]
3.1.3.1	Calf intestine	O/Ser	9.5	$3.5 \pm 0.4 \times 10^{-6}$	AttoPhos	DEA	[195]
3.1.3.1	Chicken intestine	O/Ser	7.0	$5.7 \pm 1.0 \times 10^{-8}$	pNPP	HEPES	[173]
3.1.3.1	Chicken intestine	O/Ser	8.0	$5.6 \pm 0.8 \times 10^{-7}$	pNPP	HEPES	[147]
3.1.3.1	Chicken intestine	O/Ser	8.0	$2.8 \pm 0.4 \times 10^{-6}$	pNPP	HEPES	[173]
3.1.3.1	Human liver	O/Ser	7.4	6×10^{-7}	pNPP	2-Methyl-2-aminopropan-1-ol, Tes, and Tris	[146]
3.1.3.1	Human liver	O/Ser	9.0	9×10^{-7}	pNPP	2-Methyl-2-aminopropan-1-ol, Tes, and Tris	[146]
3.1.3.1	Human kidney	O/Ser	9.0	6×10^{-7}	pNPP	2-Methyl-2-aminopropan-1-ol, Tes, and Tris	[146]
3.1.3.1	Human small intestine mucosa	O/Ser	9.0	5×10^{-7}	pNPP	2-Methyl-2-aminopropan-1-ol, Tes, and Tris	[146]
3.1.3.1	Rabbit intestine	O/Ser	10.0	1.5×10^{-5}	pNPP	Glycine	[200]
3.1.3.1	Escherichia coli	O/Ser	8.0	$2.3 \pm 0.2 \times 10^{-6}$	pNPP	Tris	[37]
3.1.3.1	Escherichia coli	O/Ser	7.4	$3.5 \pm 0.1 \times 10^{-6}$	pNPP	Tris	[37]
3.1.3.1	Escherichia coli	O/Ser	7.0	$2.2 \pm 0.4 \times 10^{-5}$	pNPP	Tris	[37]
3.1.3.1	Escherichia coli	O/Ser	8.0	2.9×10^{-6}	pNPP	Tris	[145]
3.1.3.1	Escherichia coli	O/Ser	8.0	2.2×10^{-6}	pNPP	Barbital	[145]
3.1.3.1	Escherichia coli	O/Ser	8.0	4×10^{-7}	pNPP	Barbital	[145]
3.1.3.1	Scylla serrate viscera	O	10	1.3×10^{-4}	pNPP	Sodium carbonate	[193]
Chromate CrO$_4^{2-}$ 3.1.3.2	Potato	N/His	6.0	$5.9 \pm 0.5 \times 10^{-7}$	pNPP	2-(N-Morpholino)ethanesulfonic acid	[37]
3.1.3.2	Potato	N/His	7.0	$1.8 \pm 0.2 \times 10^{-6}$	pNPP	2-(N-Morpholino)ethanesulfonic acid	[37]
3.1.3.1	Escherichia coli	O/Ser	7.0	$6.8 \pm 0.7 \times 10^{-4}$	pNPP	Tris	[37]
3.1.3.1	Escherichia coli	O/Ser	7.4	$1.6 \pm 0.2 \times 10^{-3}$	pNPP	Tris	[37]
3.1.3.1	Escherichia coli	O/Ser	8.0	$5.4 \pm 1.7 \times 10^{-3}$	pNPP	Tris	[37]
Molybdate MoO$_4^{2-}$ 3.1.3.48	Bovine heart	S/Cys	5.0	$2.0 \pm 0.7 \times 10^{-5}$	pNPP	Sodium acetate	[126]
3.1.3.48[e]	Bovine liver	S/Cys	5.5	5×10^{-4}	pNPP	Sodium acetate	[180]
3.1.3.48	Human[c]	S/Cys	7.5	$3.7 \pm 0.6 \times 10^{-6}$	pNPP	Tris	[197]
3.1.3.48	Human[d]	DNM	7.5	$1.3 \pm 0.2 \times 10^{-6}$	pNPP	Tris	[197]
3.1.3.16	λ Phage	DNM	7.8	$1.3 \pm 0.3 \times 10^{-3}$	pNPP	Tris	[182]
3.1.3.2	Human abdominal epidermis	N/His	5.0	2.0×10^{-9}	pNPP	Sodium 3-3-dimethylglutarate	[184]
3.1.3.2	Human liver	N/His	5.0	3.6×10^{-8}	pNPP	Sodium acetate	[12]
3.1.3.2	Human seminal fluid	N	5.5	3.3×10^{-4}	MUP	Sodium acetate	[185]
3.1.3.2	Human seminal fluid	N	7.1	8.3×10^{-4}	MUP	Imidazole	[185]
3.1.3.2	Bovine Spleen[g,h]	DNM	6.0	1.9×10^{-6}	pNPP	MES	[186]
3.1.3.2	Labeo rohita liver	N	5.5	1.1×10^{-7}	pNPP	Sodium acetate	[187]
3.1.3.2	Banana	N	5.8	8.0×10^{-8}	PEP	Sodium acetate	[189]
3.1.3.2	Potato	N/His	7.0	$1.1 \pm 0.1 \times 10^{-7}$	pNPP	2-(N-Morpholino)ethanesulfonic acid	[37]

154

Table 4 (Continued)

Inhibitor	EC #	Origin of phosphatase	Active site nucleophile	pH of assay	K_i (M)	Substrate	Assay buffer	Ref.
	3.1.3.2	Potato	N/His	6.0	$4.1 \pm 0.3 \times 10^{-8}$	pNPP	2-(N-Morpholino)ethanesulfonic acid	[37]
	3.1.3.2	Wheat germ	N/His	5.0	5.6×10^{-8}	pNPP	Sodium acetate	[12]
	3.1.3.2	Porcine uterine fluid[a,b]	DNM	5.5	$5 \pm 1 \times 10^{-6}$	pNPP	Sodium acetate	[47]
	3.1.3.1	Escherichia coli	O/Ser	7.0	$4.4 \pm 1.1 \times 10^{-4}$	pNPP	Tris	[37]
	3.1.3.1	Escherichia coli	O/Ser	7.4	$1.0 \pm 0.1 \times 10^{-4}$	pNPP	Tris	[37]
	3.1.3.1	Escherichia coli	O/Ser	8.0	$3.2 \pm 0.3 \times 10^{-4}$	pNPP	Tris	[37]
Tungstate WO$_4^{2-}$	3.1.3.48	Bovine heart	S/Cys	5.0	$5.0 \pm 2.3 \times 10^{-3}$	pNPP	Sodium acetate	[126]
	3.1.3.48[c]	Bovine liver	S/Cys	5.5	3×10^{-1}	pNPP	Sodium acetate	[180]
	3.1.3.48	Human[c]	S/Cys	7.5	$1.8 \pm 0.8 \times 10^{-5}$	pNPP	Tris	[197]
	3.1.3.48	Human[c]	DNM	7.5	$4.5 \pm 0.7 \times 10^{-6}$	pNPP	Tris	[197]
	3.1.3.16	λ Phage	DNM	7.8	$4.2 \pm 1.3 \times 10^{-5}$	pNPP	Tris	[182]
	3.1.3.2	Porcine uterine fluid[a,b]	DNM	5.5	$7.0 \pm 1.3 \times 10^{-7}$	pNPP	Sodium acetate	[47]
	3.1.3.2	Bovine spleen[a,b]	DNM	6.0	1.0×10^{-3}	pNPP	MES	[186]
	3.1.3.2	Human abdominal epidermis	N/His	5.0	1.4×10^{-7}	pNPP	Sodium 3-3-dimethylglutarate	[184]
	3.1.3.2	Human liver	N/His	5.0	1.6×10^{-8}	pNPP	Sodium acetate	[12]
	3.1.3.2	Wheat thylakoid membrane	N	4.6	1.7×10^{-5}	pNPP	Sodium acetate	[201]
	3.1.3.2	Potato	N/His	6.0	$9.2 \pm 0.8 \times 10^{-9}$	pNPP	2-(N-Morpholino)ethanesulfonic acid	[37]
	3.1.3.2	Potato	N/His	7.0	$1.0 \pm 0.9 \times 10^{-8}$	pNPP	2-(N-Morpholino)ethanesulfonic acid	[37]
	3.1.3.2	Wheat germ	N/His	5.0	6.1×10^{-8}	pNPP	Sodium acetate	[12]
	3.1.3.1	Rabbit intestine	O/Ser	10.0	1.7×10^{-5}	pNPP	Glycine	[200]
	3.1.3.1	Rabbit intestine	O/Ser	10.0	1.0×10^{-5}	pNPP	Glycine	[201]
	3.1.3.1	Scylla serrate viscera	O	10	1.5×10^{-3}	pNPP	Sodium carbonate	[193]
	3.1.3.1	Escherichia coli	O/Ser	8.0	$5.9 \pm 0.5 \times 10^{-6}$	pNPP	Tris	[37]
	3.1.3.1	Escherichia coli	O/Ser	7.4	$2.8 \pm 0.1 \times 10^{-6}$	pNPP	Tris	[37]
	3.1.3.1	Escherichia coli	O/Ser	7.0	$6.8 \pm 1.4 \times 10^{-6}$	pNPP	Tris	[37]
Sulfate (SO$_4^{2-}$)	3.1.3.16	λ Phage	DNM	7.8	2.0×10^{-2}	pNPP	Tris	[182]
Sodium Pyrophosphate (P$_2$O$_7$)	3.1.3.2	Human seminal fluid	N	5.5	$>2.5 \times 10^{-2}$	MUP	Sodium acetate	[185]
Vanadate (VO$_4^-$ monomer)	3.1.3.2	Human prostate	N/His	5.5	1.3×10^{-5}	pNPP	MUP	[35]
Vanadate (VO$_4^{2-}$ Dimer)	3.1.3.2	Human prostate	N/His	5.5	7.0×10^{-4}	pNPP	MUP	[35]
Diperoxovanadate	3.1.3.1	Rabbit intestine	O	10	9.1×10^{-6}	pNPP	Glycine	[202]
Vanadyl	3.1.3.48	Human[c]	S/Cys	7.0	1.1×10^{-7}	DiFMUP	MOPS	[203]
VO^{2+}	3.1.3.2	Porcine uterine fluid[a,b]	DNM	5.5	$8.2 \pm 0.8 \times 10^{-5}$	pNPP	Sodium acetate	[47]
	3.1.3.2	Wheat germ	N/His	6.0	$1.5 \pm 0.3 \times 10^{-6}$	pNPP	HEPES	[147]
	3.1.3.2	Potato	N/His	6.0	$6.5 \pm 0.9 \times 10^{-7}$	pNPP	HEPES	[147]
	3.1.3.1	Chicken intestine	O	8.0	$2.2 \pm 0.3 \times 10^{-7}$	pNPP	HEPES	[147]
	3.1.3.1	Pigeon intestine	O	8.0	$8.2 \pm 1.1 \times 10^{-7}$	pNPP	HEPES	[147]
	3.1.3.1	Calf intestine	O/Ser	8.0	$6.4 \pm 1.2 \times 10^{-7}$	pNPP	HEPES	[147]
	3.1.3.1	Dog intestine	O/Ser	8.0	$1.1 \pm 0.2 \times 10^{-6}$	pNPP	HEPES	[147]
	3.1.3.1	Horse intestine	O/Ser	8.0	$1.2 \pm 0.2 \times 10^{-6}$	pNPP	HEPES	[147]

155

	EC	Source	Nucleophile	pH	K_i (substrate)	Buffer	Ref.
	3.1.3.1	Rabbit intestine	O/Ser	8.0	$2.5 \pm 0.2 \times 10^{-6}$ pNPP	HEPES	[147]
	3.1.3.1	Sheep intestine	O/Ser	7.5	$8.3 \pm 2.0 \times 10^{-7}$ pNPP	HEPES	[147]
	3.1.3.1	Sheep intestine	O/Ser	8.0	$1.2 \pm 0.2 \times 10^{-7}$ pNPP	HEPES	[147]
	3.1.3.1	Sheep intestine	O/Ser	8.5	$1.1 \pm 0.2 \times 10^{-6}$ pNPP	TAPS	[147]
	3.1.3.1	Sheep intestine	O/Ser	9.0	$3.5 \pm 0.7 \times 10^{-6}$ pNPP	CHES	[147]
	3.1.3.1	Bovine mucosa	O/Ser	8.0	$2.2 \pm 0.3 \times 10^{-7}$ pNPP	HEPES	[147]
	3.1.3.1	Porcine mucosa	O/Ser	8.0	$2.8 \pm 0.3 \times 10^{-6}$ pNPP	HEPES	[147]
	3.1.3.1	Calf intestine	O/Ser	8.0	$5.5 \pm 0.4 \times 10^{-7}$ pNPP	HEPPS	[199]
	3.1.3.1	Escherichia coli	O/Ser	8.0	1.6×10^{-6} pNPP	Tris	[145]
Phosphomolybdate $MoPO_7^{4-}$	3.1.3.48	Human[c]	S/Cys	7.5	$1.6 \pm 0.2 \times 10^{-7}$ pNPP	Tris	[197]
	3.1.3.48	Human[c]	S/Cys	5.5	$1.4 \pm 0.5 \times 10^{-6}$ pNPP	Tris	[197]
	3.1.3.48	Human[d]	DNM	7.5	$6.0 \pm 1.0 \times 10^{-8}$ pNPP	Tris	[197]
Phosphotungstate $[P(W_3O_{10})_4]^{-3}$	3.1.3.48	Human[c]	S/Cys	7.5	$1.2 \pm 0.2 \times 10^{-6}$ pNPP	Tris	[197]
	3.1.3.48	Human[c]	S/Cys	5.5	$1.0 \pm 0.2 \times 10^{-5}$ pNPP	Tris	[197]
	3.1.3.48	Human[d]	DNM	7.5	$7.9 \pm 0.0 \times 10^{-7}$ pNPP	Tris	[197]
$[C(NH_2)_3]_2[(CH_3)_2AsMo_6O_{15}H]$	3.1.3.2	Leishmania donovani	N	5.5	1.1×10^{-6}	MUP	Sodium acetate	[185]
$(NH_4)_6As_2Mo_{18}O_{62} \cdot xH_2O$	3.1.3.2	Leishmania donovani	N	5.5	6.0×10^{-7}	MUP	Sodium acetate	[185]
$[C(NH_2)_3]_2[(CH_3)_2AsMo_6O_{15}H]$	3.1.3.2	Human seminal fluid	N	5.5	1.6×10^{-6}	MUP	Sodium acetate	[185]
$[(NC_4H_9)_4N]_4Mo_8O_{26}$	3.1.3.2	Human seminal fluid	N	5.5	4.8×10^{-6}	MUP	Sodium acetate	[185]
$(NH_4)_4GeMo_{12}O_{40} \cdot xH_2O$	3.1.3.2	Human seminal fluid	N	5.5	3.9×10^{-6}	MUP	Sodium acetate	[185]
$Na_3PMo_{12}O_{40} \cdot xH_2O$	3.1.3.2	Human seminal fluid	N	5.5	1.5×10^{-6}	MUP	Sodium acetate	[185]
$(NH_4)_6ThMo_{12}O_{42} \cdot 7H_2O$	3.1.3.2	Human seminal fluid	N	5.5	1.0×10^{-5}	MUP	Sodium acetate	[185]
$(NH_4)_6CeMo_{12}O_{42} \cdot 8H_2O$	3.1.3.2	Human seminal fluid	N	5.5	1.0×10^{-5}	MUP	Sodium acetate	[185]
$(NH_4)_6As_2Mo_{18}O_{62} \cdot xH_2O$	3.1.3.2	Human seminal fluid	N	5.5	7.5×10^{-7}	MUP	Sodium acetate	[185]
$[C(NH_2)_3]_2[(CH_3)_2AsMo_6O_{15}H]$	3.1.3.2	Human seminal fluid	N	7.1	1.6×10^{-7}	MUP	Imidazole	[185]

[a] The phosphatase has also been categorized as 3.1.3.2.
[b] Capillary electrophoresis was used to determine K_i values.
[c] Recombinant protein tyrosine phosphatase 1B.
[d] Catalytic domain of protein tyrosine phosphatase-1.
[e] Human low molecular weight phosphotyrosyl phosphatase-A.
[f] Human low molecular weight phosphotyrosyl phosphatase-B.
[g] These enzymes contains a dinuclear metal core which are intricately involved in the reaction mechanism and thus does not fit the traditional mechanism in which an amino acid serves as the active site nucleophile.
[h] Purple acid phosphatase

suggests that expansion of the coordination sphere leads to more potent inhibition.

Phosphate, $PO_4^{3-}(P_i)$, inhibition ranges from 10^{-3} M to 10^{-4} M even when considering alkaline, acid and protein phosphatases as a group and ranging across human, mammalian, plant, bacterial and fungal phosphatases, Table 4. One acid phosphatase, *Labeo rohita* liver, is more strongly inhibited by phosphate with a K_i of 10^{-7} M, and at this point it is not clear why this enzyme would be much more potently inhibited by phosphate [187]. The fact that most of these phosphatases have similar affinity for phosphate is somewhat surprising considering the differences in substrates, substrate specificity, type of phosphatase and origin. Presumably this similarity is a testimony to the similarity of binding of the phosphate in the product binding site and exhibiting product inhibition as suggested previously [68].

To further investigate the interaction of oxometalates with phosphatases we compiled the K_i values for arsenate, vanadate, chromate, molybdate and tungstate for phosphatases, Table 4. Arsenate is a little more effective in inhibiting phosphatases than phosphate and chromate. This is in contrast to the vanadate, molybdate and tungstate anions that are much more potent inhibitors than phosphate. It is has been proposed that these phosphatase inhibitors act as transition state analogs [12]. For vanadate the K_i values range from 10^{-5} to 10^{-7} M when considering alkaline, acid and protein phosphatases from human, mammalian, *E. coli*, plant, and bacterial phosphatases, Table 4. The inhibition by vanadate is both currently used as benchmark information by life scientists and has been used for decades to describe phosphatase acitivity. Vanadate inhibition is generally several of orders more potent than inhibition by phosphate.

Molybdate and tungstate are oxometalates prepared from second row transition metals and as such are a little larger and have different properties than vanadate. The K_i values observed for MoO_4^{2-} and WO_4^{2-} generally range from 10^{-7} to 10^{-9} M. The observed affinities do not follow an obvious pattern for the protein tyrosine phosphatase and apparently the *E. coli* phosphatase continues to have poorer affinities for both molybdate and tungstate than for the other phosphatases. The highest affinities recorded in Table 4 were observed for the human enzymes and the plant acid phosphatases belonging to EC group 3.1.3.2. High affinity was also observed for the EC group 3.1.3.2 enzymes with vanadate, although high affinity with vanadate was also observed for the alkaline phosphatases in group EC 3.1.3.1. The highest affinities have been observed for the molybdate and the tungstate anion exceeding that of vanadate by two orders of magnitude. Both molybdenum and tungsten can form five-coordinate geometries but do so less frequently than vanadium [94]. Although vanadium readily forms octahedrally coordinated complexes, as shown by the analysis in this work, the vanadium bound to the phosphatase remains five-coordinate. In the case of vanadium is it therefore not likely that a higher inhibitory affinity may result from a complex that has a six-coordinate and not five-coordinate vanadium. Several protein complexes in the crystal data-base have been reported with molybdenum [126,130,131] and tungsten [70,72,94,133,149] and a similar analysis can be carried out with these structures. Suffice to say that an exhaustive analysis is beyond the scope of this manuscript but that these X-ray crystal structures exhibit more diverse coordination geometry ranging from tetrahedral to octahedral complexes.

VO^{2+} in the form that exists upon aqueous dissolution of vanadium(IV) salts has also been investigated as inhibitor for phosphatase and the results are summarized in Table 4 [144,147]. It was first examined using the *E. coli* alkaline phosphatase, and found to show an inhibitory affinity similar to that of vanadate [144]. This study was followed up by an extensive survey study of mammalian alkaline phosphatases and a few acid phosphatases [147].

These studies are non-trivial on several counts [147]. First, vanadium(IV) or VO^{2+} readily oxidize to vanadium(V) and vanadate in the pH region where the enzyme is assayed. Studies therefore require extensive purging of solutions to assure that the vanadium(IV) does not oxidize to vanadium(V). Second, the speciation for vanadium(IV) is very complex in the neutral pH range [68]. Specifically, as the pH approaches neutral the VO^{2+} species dimerizes and oligomerizes. This is readily observed by EPR spectroscopy; the eight signal pattern for the VO^{2+} at low pH disappears at neutral pH as expected upon dimerization or oligomerization [85]. Above pH 10–11 a new eight signal pattern emerges which is attributed to the $VO(OH)_3^-$ ion. However, at neutral pH very low levels of species forms and cannot directly be observed by EPR spectroscopy. With the aide of potentiometry and formation constants speciation diagrams have been constructed, and between VO^{2+} and the $VO(OH)_3^-$ in the neutral pH range species such as $(VO(OH))_2^+$ and $VO(OH)^+$ are proposed to exist a low concentration [68,85]. However, should any $VO(OH)_3^-$ form under these conditions, this is also an excellent analog of phosphate, presumably $H_2PO_4^-$ [68]. The inhibition studies of aqueous vanadium(IV) with a range of different mammalian phosphatases demonstrated that vanadium(IV) is inhibitory to these phosphatases. Interesting for some of the alkaline phosphatase sources vanadate was more potent and for others aqueous vanadium(IV) was more potent [144,147]. Because some variation in these alkaline phosphatases would be expected, it is possible that closer analysis of the active site of these enzymes would provide information on the observed selectivity against favoring vanadium(IV) or vanadium(V). However, of all the X-ray structures of vanadium–phosphatases described in this manuscript, only one contains vanadium(IV) so much less information is available on oxidation state IV complexes. Thus, although this result may be due in part to the reactivity of vanadium(IV) at neutral pH in the absence of protecting ligands, the demonstrated inhibition of mammalian alkaline phosphatases by vanadium(IV) suggests that such complexes could possibly form. Indeed, if such protein structures were characterized with vanadium(IV) they would allow comparison with the vanadium(V) structures described in this work.

Finally, we wish to briefly address the fact that other oxometalates than simple vanadate and monomeric oxometalates have been reported to inhibit phosphatases. The most recognized case, decavanadate ($H_nV_{10}O_{28}^{6-n-}$), is a polyoxovanadate that forms in solutions of vanadate between pH 3 and 6.5. This compound, although a large and charged polyoxovanadate [204–206], is found to interact with proteins and cellular components [34,204–208], and has recently also been reported as a phosphatase inhibitor [34]. The mechanism of action of this polyoxovanadate is not well understood and the possibility that a vanadate monomer is abstracted from the decavanadate has not been investigated [197]. However, a series of other polyoxometalates including Keggin, Dawson and other oxometalate shapes have been investigated [197]. As seen from the data in Table 5, some of these anions are very potent and others less so compared to simple vanadate. It appears that the Dawson structures investigated are among the most potent anions, however, some smaller anions are very potent as well. Considering the fact that each of these anions are highly charged and contains many metal ions, the potent inhibition by the Dawson anions for example is less impressive per metal ion. However, the modes of action of these systems are of interest, particularly since a amine-based decavanadate has been reported as a particularly interesting antidiabetic complex [29].

In summary, the affinity of these anions (shown here in the deprotonated form existing at high pH) are in the order of $P_i \approx CrO_4^{2-} < AsO_4^{2-} < VO_4^{3-} \approx VO(OH)_3^- < MoO_4^{2-} < WO_4^{2-}$ although aqueous vanadium(IV) was of the same affinity as vanadate. It appears that P_i similarly inhibits a wide range of phosphatases including alkaline, acid, protein, and bacterial

Table 5
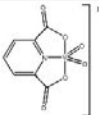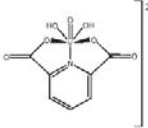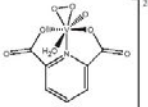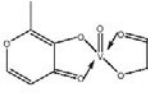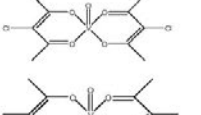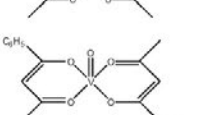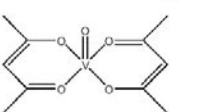The K_i values for vanadium and other metal complexes against different phosphatases.
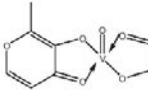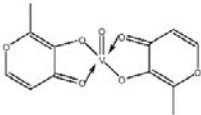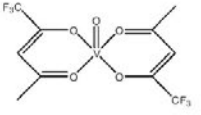
Metal	Structure/formula	Ox	EC #	Origin of phosphatase	Active site nucleophile of enzyme	pH of assay	K_i (M)	Substrate	Assay buffer	Ref.
Vanadium		5	3.1.3.1	Chicken intestine	O/Ser	7.0	$1.9 \pm 0.6 \times 10^{-9}$	pNPP	HEPES	[173]
		4	3.1.3.1	Chicken intestine	O/Ser	7.0	About 6×10^{-6}	pNPP	HEPES	[173]
		5	3.1.3.1	Chicken intestine	O/Ser	8.0	$1.3 \pm 0.1 \times 10^{-5}$	pNPP	HEPES	[173]
		4	3.1.3.48	Human[a]	S/Cys	6.0	7.9×10^{-7}	DiFMUP	Sodium acetate	[210]
		4	3.1.3.48	Human[b]	S/Cys	6.0	9.0×10^{-7}	DiFMUP	Sodium acetate	[210]

158

Table 5 (Continued)

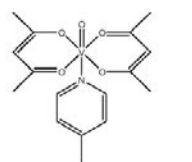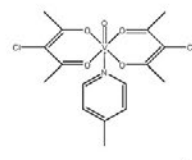| Metal	Structure/formula	Ox	EC #	Origin of phosphatase	Active site nucleophile of enzyme	pH of assay	K_i (M)	Substrate	Assay buffer	Ref.
		4	3.1.3.48	Human[b]	S/Cys	7.0	6.3×10^{-7}	DiFMUP	MOPS	[203]
		4	3.1.3.1	Calf intestine	O/Ser	8.0	$7 \pm 1 \times 10^{-8}$	pNPP	HEPPS	[199]
		4	3.1.3.1	Calf intestine	O/Ser	8.0	$1.5 \pm .1 \times 10^{-7}$	pNPP	HEPPS	[199]
		4	3.1.3.1	Calf intestine	O/Ser	8.0	$3.4 \pm 0.4 \times 10^{-7}$	pNPP	HEPPS	[199]
		4	3.1.3.1	Calf intestine	O/Ser	8.0	$4.0 \pm 0.5 \times 10^{-7}$	pNPP	HEPPS	[199]
		4	3.1.3.1	Calf intestine	O/Ser	8.0	$4.3 \pm 0.4 \times 10^{-7}$	pNPP	HEPPS	[199]

159

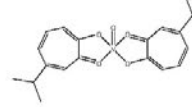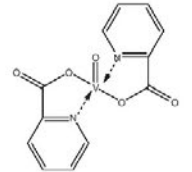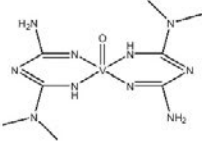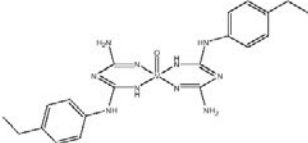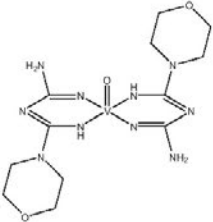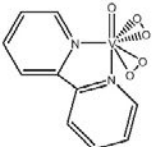|									
	4	3.1.3.1	Calf intestine	O/Ser	8.0	$6.9 \pm 0.4 \times 10$	pNPP	HEPPS	[199]
	4	3.1.3.1	Calf intestine	O/Ser	8.0	$1.0 \pm 0.1 \times 10$	pNPP	HEPPS	[199]
	4	3.1.3.48	Human[b]	S/Cys	7.0	1.5×10^{-7}	DiFMUP	MOPS	[203]
	4	3.1.3.48	Human[b]	S/Cys	7.0	7.0×10^{-7}	DiFMUP	MOPS	[203]

Table 5 (Continued)

Metal	Structure/formula	Ox	EC #	Origin of phosphatase	Active site nucleophile of enzyme	pH of assay	K_i (M)	Substrate	Assay buffer	Ref.
		4	3.1.3.48	Human[b]	S/Cys	7.2	4.2×10^{-8}	pNPP	MOPS	[211]
		4	3.1.3.48	Human[b]	S/Cys	7.2	4.5×10^{-8}	pNPP	MOPS	[211]
		4	3.1.3.48	Human[b]	S/Cys	7.2	5.8×10^{-8}	pNPP	MOPS	[211]
		5	3.1.3.48	Human[b]	S/Cys	7.5	$5.2 \pm 0.9 \times 10^{-6}$	pNPP	Tris	[197]
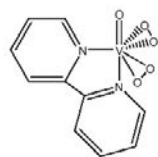
	5	3.1.3.48	Human[c]	S/Cys	7.5	$1.7 \pm 0.3 \times 10$ pNPP	Tris	[197]
	5	3.1.3.1	Rabbit intestine	O/Ser	10	7.1×10^{-5} pNPP	Glycine	[202]
	5	3.1.3.1	Rabbit intestine	O/Ser	10	4.9×10^{-5} pNPP	Glycine	[202]
	5	3.1.3.1	Rabbit intestine	O/Ser	10	5.4×10^{-5} pNPP	Glycine	[202]
	5	3.1.3.1	Rabbit intestine	O/Ser	10	5.9×10^{-5} pNPP	Glycine	[202]
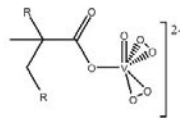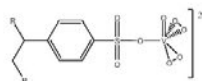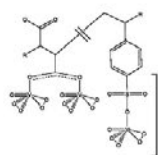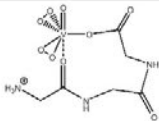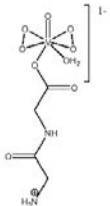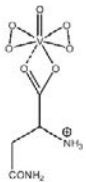
Table 5 (Continued)

Metal	Structure/formula	Ox	EC #	Origin of phosphatase	Active site nucleophile of enzyme	pH of assay	K_i (M)	Substrate	Assay buffer	Ref.
		5	3.1.3.1	Rabbit intestine	O/Ser	10.0	6.0×10^{-6}	pNPP	Glycine	[200]
		5	3.1.3.1	Rabbit intestine	O/Ser	10.0	1.0×10^{-5}	pNPP	Glycine	[200]
		5	3.1.3.1	Rabbit intestine	O/Ser	10.0	1.2×10^{-5}	pNPP	Glycine	[200]
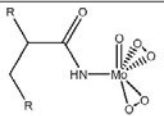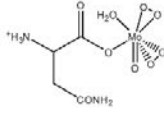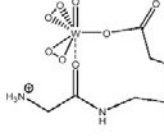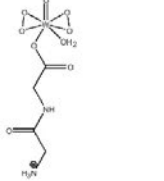
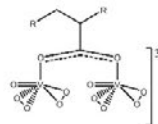|									
		5	3.1.3.1	Rabbit intestine	O/Ser	10.0	1.3×10^{-5}	pNPP	Glycine	[200]
Molybdenum		6	3.1.3.1	Rabbit intestine	O/Ser	10	6.0×10^{-6}	pNPP	Glycine	[202]
		6	3.1.3.1	Rabbit intestine	O/Ser	10	3.1×10^{-5}	pNPP	Glycine	[202]
		6	3.1.3.1	Rabbit intestine	O/Ser	10	1.7×10^{-5}	pNPP	Glycine	[202]

Table 5 (*Continued*)

Metal	Structure/formula	Ox	EC #	Origin of phos-phatase	Active site nucleophile of enzyme	pH of assay	K_i (M)	Substrate	Assay buffer	Ref.
		6	3.1.3.1	Rabbit intestine	O/Ser	10	1.9×10^{-5}	pNPP	Glycine	[202]
		6	3.1.3.1	Rabbit intestine	O/Ser	10	7.5×10^{-6}	pNPP	Glycine	[202]
Tungsten		6	3.1.3.1	Rabbit intestine	O/Ser	10.0	1.2×10^{-5}	pNPP	Glycine	[200]
		6	3.1.3.1	Rabbit intestine	O/Ser	10.0	1.5×10^{-5}	pNPP	Glycine	[200]

Structures are meant to show composition more than actual configuration.

[a] Human low molecular weight protein tyrosine phosphatase.

[b] Recombinant protein tyrosine phosphatase 1B.

[c] Catalytic domain of protein tyrosine phosphatase-1.

phosphatases from varying sources of these enzymes. Vanadate, molybdate, and tungstate are more potent inhibitors and this has previously been attributed to these anions acting as transition state inhibitors [12]. The data show that the variability of inhibition of phosphatases is most obvious when the inhibitor binds as a transition state analog. Collectively it can be concluded that the coordination geometry of four supports product inhibition but that when the coordination number is five or six the transition state of the substrate hydrolysis is the binding si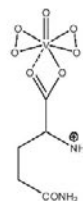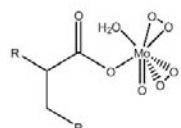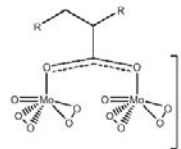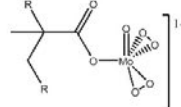te for the inhibitor. As a result, in the case of molybdenum and tungsten their greater inhibition is observed with the oxometalate in the five- or six-coordinate geometry.

5.3. Vanadium complexes

The potent inhibitory effects of the vanadate salts reported in the studies listed in Table 4 created the expectation that vanadium complexes would be potent inhibitors of phosphatase. Despite this expectation, only a few studies are available on inhibitory studies of vanadium complexes in which the inhibition has been characterized to the level of measuring mechanism of inhibition and K_i values. There are numerous studies in which the *relative* inhibitory potency such as EC_{50} values have been measured including work by our groups [91,179,209]. However, in most cases such studies are comparative studies relating the observed inhibition to other compounds in the study. Although a series of compounds may have been investigated in detail, unless the mechanism of inhibition and K_i values were defined they will not be referred to in this section nor summarized in Table 5.

In an early study exploring the inhibition potency of dipicolinato oxovanadium(V) for chicken intestine alkaline phosphatase it was recognized that the vanadium complex decomposes under the conditions of the assay [173]. The K_i determination thus required that the inhibition of free ligand, vanadate, and the complex were measured. With these data and consideration of the speciation of the compound under the assay the determination of the true K_i value for the complex was possible. In this study it was found that the complex K_i (1.9×10^{-6} M) was slightly more potent than vanadate (4.0×10^{-6} M) [173]. Although the complex is found to have an inhibition constant a factor of two smaller than vanadate, these values are within experimental error. The inhibition of two other vanadium compounds with six and seven coordination geometries were also examined, but these were significantly poorer inhibitors than vanadate and the dipicolinato oxovanadium(V) complex [47,173]. The authors concluded based on these observations that the five-coordinate geometry was the near optimal geometry for an enzyme inhibitor in this work [173]. However, at the time the τ value for dipicolinato oxovanadium(V) was not calculated, and it was not recognized that this complex is near the SP [212–214]. The original report did not point out the fact that the complex is not near the TBP geometry that would be adapted in the enzyme active site and although the complex may have the lowest K_i value reported, the value is close to that of vanadate and probably not experimentally distinguishable. Indeed, this system is the first report describing a vanadium complex having the same order of inhibitory potency as vanadate itself. Therefore, assuming that these results are not an artifact, these results support the possibility that the vanadium complex acts by delivering the vanadate to the phosphatase.

However, these studies did document the need for speciation studies when K_i determinations were undertaken, because if the species were not considered/calculated under the conditions of the assay (vide supra Section 2.4), and thus if the complex decomposes, the measured constants will represent a composite of mainly vanadate and vanadium complex; the ligands alone generally have very little effect. In the study of dipicolinato oxovanadium(V) complexes all were micromolar inhibitors of a representative phosphatase

but the five-coordinate complex was the most potent inhibitor [47,173]. All the coordination geometries of the vanadium complexes are inhibitors of similar magnitude, and the inhibition of all the vanadium complexes was within a two orders of magnitude regardless of the ligand. This conclusion still holds when examining all the other complexes in Table 5. The possibility that the dipicolinato dioxovanadium(V) complex simply is a vehicle delivering the vanadate is supported by the fact that all but one of the vanadium–phosphatase complexes reported contains vanadate and not a vanadium coordination complex.

The K_i values were measured for BMOV (also referred to as [VO(malto)$_2$] or bismaltolatooxovanadium(IV)) [203,210], which is closely related to the compound that was carried through for clinical trials for treatment of diabetes [215,216]. These studies were done both on wild-type and recombinant low molecular weight human protein tyrosine phosphatase 1B [210]. As shown in Table 5, the K_i value was very similar to that obtained using vanadate. Speciation studies show that this compound is stable for a limited time [217], and several speciation studies have been reported with this compound showing that it forms adducts under physiological conditions and upon dissolution both cis and trans isomers exist [217–219]. Although speciation was not considered directly in the study measuring the K_i values, other studies have been reported suggesting that under conditions of the enzyme assay at least 50% of the compound is intact. However, the formation of isomers and hydrolysis in solutions makes it more difficult to assign the observed affects to one isomer. Therefore the measured K_i value is an underestimation of the true inhibition of the most potent form in solution.

The potency of a series of peroxovanadium compounds for the rabbit intestine alkaline phosphatase was investigated, Table 5 [197,200,202]. The peroxovanadium compounds have varied stability, with some of them being very stable [23,220–223]. The studies carried out with these compounds yielded K_i values of similar magnitude to those found for the dipicolinato peroxovanadium(V) complex and the chicken intestine alkaline phosphatase [173]; i.e. 10-fold poorer inhibitors than vanadate. It is interesting that one of the peroxovanadium complexes is as effective as vanadate, begging the consideration of the possibility that this peroxovanadium compound may have hydrolyzed. Thus, general studies of stability of these classes of compounds are important, however, in this case the stability of the one specific peroxovanadium compound is in question [200,202]. Corresponding peroxomolybdenum [185,202] complexes were also prepared and tested and found to have similar activity as the peroxovanadium compounds [185,202].

The potency of a series of acetylacetonate vanadium(IV) complexes as inhibitors for calf intestine was also investigated [199]. Vanadium(IV) complexes are often more stable near neutral pH and as such the stability profiles are shifted for the vanadium(IV) complexes compared to vanadium(V) complexes. Although these compounds may be more stable than corresponding vanadium(V) complexes, they too form several species in solution. Several speciation studies have been reported with this class of compounds showing that they form adducts and upon dissolution both cis and trans isomers exist [217,224]. These complexes investigated are found to exhibit K_i values from 0.07×10^{-6} to 1×10^{-6} M, and thus are among the most potent complexes shown in Table 5 [199]. It is interesting that the small subtle changes on the acac-ligand can improve the K_i value for the vanadyl complexes by two orders of magnitude. Indeed, this effect may be attributed to a shift in speciation, because the stability profiles of these compounds are very sensitive to substitution on the acac-moiety. The authors examined the breakdown of their compounds using UV–vis spectroscopy, however, distinction between cis and trans isomers cannot be done using UV–vis spectroscopy [224]. Therefore the increased inhibition observed can be attributed to the mixture of isomers that

forms, and the reported higher potency of the fluorosubstituted acac complex may be due to a shift in isomer stability.

The class of compounds reported to be the most potent inhibitors are those formed by biguanide ligands [211]. Three biguanide-containing complexes are reported all of which have the smallest K_i values in Table 5. Unfortunately, characterization of this class of complexes is limited to the solution studies reported here [211]. Further consideration of these complexes is clearly desirable because they have shown antidiabetic properties [225–228]. These complexes are non-trivial to characterize because they have low solubility and it was difficult to determine their stability in water. Furthermore, the biguanide unit has found previous use as an antidiabetic drug. The ligands metformin [229], and progunil [230,231], are anti-diabetic and anti-malarial drugs, respectively, and are prescribed by physicians for these diseases. Because the ligand compounds have effective biological properties, and are poorly soluble, how much these properties contribute to the observed low inhibition constant is not clear. Although the goal is often to take advantage of the cooperative effects of metal and ligand, working with a ligand that already is effective in treating the disease makes it very difficult in animal studies to deduce the effect of the metal complex. Furthermore, investigations into the vanadium complexes with metformin have led to development of complexes that have insulin enhancing properties, however, they are not dramatically improved over other known vanadium complexes. The biguanide vanadium complexes are the most potent phosphatase inhibitors reported, and have been able to go beyond the other coordination complexes investigated at this level of scrutiny. Thus, continued investigation into this class of compounds would test the possibility that these compounds have properties that can surpass the other complexes investigated to date.

Combined, these studies illustrate several important points. Although many compounds have been tested as inhibitors for phosphatase, most of this information is available in publications reporting a series of compounds and reporting the relative activity of these compounds as inhibitors against different phosphatases using vanadate or phosphate as benchmark values. These studies, report EC_{50} values and not K_i values. Although EC_{50} values are valuable in themselves, they are more difficult to compare to other reports in the literature and such studies also do not determine the mode of action of the inhibition. Therefore, for the comparison here we have only considered the publications in which a more detailed analysis has been undertaken and an inhibition constant, K_i is reported. From the data available for the compounds compiled in Table 5 it is interesting to find that most of the vanadium complexes investigated have inhibitory constants similar to those reported for the vanadate salts. Importantly, these studies show that most vanadium compounds investigated are inhibitory regardless of the coordination number of the compounds. The data also suggest that a range of vanadium compounds are active, and that inhibitory effects are not limited to compounds with the VO_2-unit, 5-coordinate vanadium or peroxovanadium groups.

6. Discussion and future

Vanadate, vanadyl sulfate, and vanadate compounds are well known phosphatase inhibitors and it is common that these inhibitors are used for description of new phosphatase enzymes and enzyme systems [13,23–27,29,232]. In 2004, according to Davies and Hol, only four structures available in the PDB contained vanadium; three structures in which the vanadate was coordinated in a covalent manner to an enzyme and one structure in which the vanadate was coordinate in a non-covalent manner [58]. These four structures have now a decade later grown to 29 structures. The covalently attached vanadate are found in systems in which the vanadate acts as a potent inhibitor and the X-ray structure is reflecting the transition state-like structure of the inhibitor in this protein–vanadate complex. The non-covalently associated vanadate, in contrast, has the vanadium in four-coordinate geometry and the binding is product-like. At this time there are many more examples of vanadium-containing complexes, and the vanadium is not only found as vanadate or five-coordinate complexed vanadate. As described recently [50] and in this review, a few other systems have been characterized in which vanadium is an oligomeric anion or a coordination complex. Namely, divanadate [127], trivanadate [128], and decavanadate [151,233] have all been reported bound with proteins. However, it is important to emphasize that the most common vanadium–phosphatase complexes found in the structural databases, are vanadate–phosphatase complexes. Therefore in most cases, regardless of the structure or the oxidation state the vanadium was in prior to encountering the phosphatase, the product that emerges is a vanadate bound to the phosphatase.

Vanadium as an early transition metal ion is found in the periodic table after chromium and before manganese, but near both molybdenum and tungsten. As a result it has complex speciation chemistry and all oxidation state forms several hydrolysis products under physiological conditions [86,87,219,234]. This is very important, because the oligomerization of vanadate is known to decrease the amount of monomeric vanadate in solution, which is generally the inhibiting form of vanadate. Therefore, the oligomerization reactions change the inhibition profile by vanadate, and as was first discovered with 6-phosphogluconate dehydrogenase and human prostatic acid phosphatase the larger vanadium oligomers (tetramer) and the smaller vanadium dimer rather than vanadate monomer can also inhibit enzymes [78,91]. Recently one bacterial phosphatase was found to structurally demonstrate that the interaction between phosphatases and a higher vanadate oligomer is possible [128] and confirming the earlier report with the human acid phosphatase that vanadate dimer is a more potent inhibitor than vanadate monomer for this enzyme [91]. Decavanadate is a large oxometalate that is significantly different than the smaller readily exchangeable oxovanadates. Although it is large in size, it has been found to interact with proteins, membrane fractions and possibly even lipid interphases. One protein that was found to interact with decavanadate is ribonuclease and perhaps particularly interesting since this enzyme also can interact with other forms of vanadium [205,235–238].

The nature of the inhibition by vanadium salts and coordination complexes is of interest, because if the potency could be mimicked by fine-tuning other systems, very desirable inhibitors could be developed. As stated early on by van Etten [12], it is not clear that the five-coordinate transition state is so desirable because both molybdate and tungstate were more potent inhibitors than vanadate. Although these anions indeed are more potent inhibitors, their anti-diabetic effects in biological systems are less than those observed with vanadate [29,215,216], documenting that phosphatase inhibitory potency is not the only factor important for anti-diabetic properties. Similarly, a study was carried out testing the possibility that the five-coordinate dipicolinatooxovanadium complex was more potent that analogous five-coordinate complexes [173]. Indeed, the observations showed that the five-coordinate complex was a more potent inhibitor than free vanadate anion, the ligand, and two other complexes with six-coordinate vanadium [173]. These findings showed that although the five-coordinate structure was the best, that the other vanadium containing structures were also inhibitors. The question whether the four-coordinate geometry also could be a potent inhibitor was examined in detail by the Tracey group, rationalizing that the inhibitor must be able to expand its coordination sphere in order to covalently bind the inhibitor [232].

We recently investigated the geometry of the X-ray characterized vanadium complexes that inhibit phosphatases [67]. In these previous studies we did not characterize the speciation of the vanadium–phosphatase complexes so that one could truly attribute the inhibition to a particular geometry around the vanadium. With the complex geometries around the vanadium we found that the complexes with five-coordinate geometries display the most potent inhibition. However, many inhibitors for the phosphatases have similar potency as vanadate, possibly reflecting that the complex would hydrolyze under the conditions of the assay. Understanding of the structure allows modeling studies in silico as well as in designing better species for inhibition for experimentation and testing [164,239].

Some proteins undergo major structural changes after binding of allosteric effectors, and therefore the binding of metal containing complexes in the active site has the potential of changing the conformation of the protein. In evaluation of crystallographic structural data one should consider whether the crystal was obtained by co-crystallization with the vanadium-complex or the vanadium-complex was soaked into an existing crystal; soaking experiments favor the structure that has already formed, such that observation of only minor structural changes may be somewhat biased. Although the active site of a protein only represents a very small fraction of the overall protein structure, the existing crystal is likely to influence how the vanadate will bind to the protein and consequently the final structure obtained. Even when beginning with more complicated vanadium complexes, only a few examples of vanadium compounds other than vanadate bound to protein have been found for phosphatases; some structures have been reported among phosphatases as well as other enzymes, though. These complexes document that geometries other than TBP for the vanadium are not uncommon.

The largest group of vanadium–protein complexes in the databases is the hydrolases, including phosphatases [50,51]. However, there are also a large number of structures of proteins containing a vanadium that are the vanadium haloperoxidases [240,241]. Specifically there are two classes of vanadium containing haloperoxidases, proteins that catalyze chlorination reactions, the vanadium chloroperoxidases [241], and proteins that catalyze the bromonation reactions, the vanadium bromoperoxidases [139,142,240,242]. These systems are somewhat related to the topic at hand, because it has been demonstrated that the vanadium haloperoxidases have sequence analogy with low molecular weight acid phosphatases [130,141,243,244]. These proteins contain a vanadium in their active sites, which have been characterized by crystallization. However, the reaction mechanism is very different than that for the phosphatases and many functional mimics have been and continue to be reported [245–247]. Interestingly, when the haloperoxidases do not have a vanadium in their active site (an apoprotein), they can catalyze organic phosphate hydrolysis [141,248,249]. The reaction mechanism for the haloperoxidases has been investigated in detail, and information is available elsewhere on these systems with regard to the protein, the reaction, and applications of the protein [140–142,241,250–252].

Inhibitory studies with different vanadium compounds illustrate several important points. First, many compounds have been tested as inhibitors for phosphatase but most of these studies did not measure K_i value so that comparison among studies are difficult. A few studies with alkaline phosphatases did measure an inhibition constant, K_i and these are summarized in Table 5. From the data shown in Table 5 we find that most vanadium complexes have inhibitory constants similar to those reported for the vanadate salts. Furthermore, the data in Table 5 support that the vanadium compounds are inhibitory regardless of the coordination number of the compounds. The data also suggest that a range of vanadium compounds are potent inhibitors, and that inhibitory effects are not limited to compounds with the VO_2-unit, five-coordinate vanadium or peroxovanadium(V) groups. Of the compounds investigated only one class of compounds show affinities larger than others. However, the biguanide vanadium complexes are a difficult class of compounds to investigate, because their low solubility. For example, the metformin oxovanadium(IV) complex had similar insulin enhancing properties as BMOV but because of the poor solubility of this compound it was difficult to properly investigate the system [225]. Indeed, recent studies with a metformin decavanadate complex have demonstrated unexpected properties including enhanced solubility and anti-diabetic effects [226,227]. The fact is that regardless of what vanadium-containing compound was added to the phosphatase, in all but one vanadium–phosphatase complexes investigated only vanadate remains in the characterized structure. This suggests that when the vanadium–phosphatase complex was formed from vanadium complexes, the ligands' main role is the delivery of the vanadate to the enzyme. Because three vanadium biguanide complexes [178] and several polyoxometalates [178] have demonstrated superior inhibition of phosphatases more studies of these complexes in particular and the delivery of vanadium to the phosphatase and other enzymes in general is desirable.

For a vanadium complex to be chosen to treat a chronic disease such as diabetes its efficacy must be many times greater than the ligand alone due to potential long term metal toxicity issues. Such a requirement is particularly difficult to meet. The study of how these complexes work, however, is likely to yield valuable information for the development of new inhibitors of phosphatases. The requirements for activity are less with respect to acute treatment of a potentially fatal disease such as cancer. Metal-containing drugs have been embraced by physicians for several decades considering the success of platinum-series of drugs [253–255]. Understanding the fundamental nature of the binding in the active site of vanadium–phosphatases complexes can be useful for the development of both metal-containing and organic drugs. In the case of vanadium-based anti-diabetic drugs, the systemic concentration of vanadium was found in some subjects to be too high, so reducing in the overall concentration would be desirable. The development of formulation techniques have been found to improve drug uptake [256].

7. Summary

Vanadate and vanadium compounds are potent inhibitors of phosphatases. The details of the interaction between the vanadium and phosphatases have been characterized in detail for a number of phosphatases that have been found to form protein–vanadium crystals generally with vanadate. Because of the flexibility of vanadium and vanadate to form different coordination environments, several coordination numbers have been observed in these vanadium–protein complexes. The most common form of vanadium–phosphatase complexes has the vanadium in a five-coordinate geometry and covalently attached to the protein. This is the geometry that has been found for 22 of the 29 unique coordination geometries in vanadium–phosphatase complexes examined in this work. In addition, vanadate as a phosphate analog can bind as a product analog in a phosphatase–vanadate complex and one such complex have been reported. Finally, there are a couple of structures with larger oligomeric form of vanadate in the complex.

The most common vanadium–protein complexes have the vanadium in a five-coordinate geometry, which could be either trigonal bipyramidal (TBP) or square pyramidal (SP). Because the difference in the energetics of the TBP and the SP is small, both such geometries in the vanadium–protein complex should be possible. Upon analysis of the active sites' vanadium geometries, we find

that in the overwhelming number of cases, the vanadium geometry is TBP. In the solid state the small molecule structures suggest that the preferred structure from the point of view of the metal complex is SP, and yet the geometry in the protein complexes is TBP. Although the computational optimizations of some of these vanadium–protein complexes have restricted the geometry at the vanadium somewhat and these *are* static X-ray structures, the complexes remain more TBP-like than SP-like. This conclusion stands for all the different classes of phosphatases, regardless of what the active nucleophile is in the active site (N, O, or S). There are several limitations to this analysis of protein structures, but one major one is that nearly all crystals with vanadium are formed by soaking pre-formed apo crystals of the enzyme with vanadium solutions, often very briefly. As noted by Evdokimov et al., "Our experience indicates that soaking, while undoubtedly the quickest route to cocrystals, may not be adequate for proteins with shallow active sites and for large ligands where crystal packing has a high likelihood of generating artifacts [159]." Each of these X-ray structures is also with a vanadium(V) species and only a handful contain a vanadium bound to any ligand other than oxo or a co-factor. The structural information gleaned from these studies, then, may not give as much information about vanadium-containing complexes that are *not* simple oxanions, nor does the static nature of any one complex's structure give a complete picture of the dynamics at an active site.

To follow up this PDB X-ray analysis we surveyed the literature for oxometalates and vanadium-containing complexes that inhibit phosphatases. In the case of oxometalates, it has been recognized for more than 30 years that oxometalates with a coordination number of higher than four are more potent inhibitors [12]. Increased inhibition was correlated with the increased coordination sphere. The increased inhibition was attributed to the anion binding as a transition state analog. This attribution is confirmed by our review of the current literature on this topic. We also reviewed the literature of reported inhibition studies with vanadium-containing complexes. Because of the complicated speciation of vanadium complexes, we chose to only review studies in which either the speciation of the vanadium complexes was investigated or the vanadium complexes were stable. For such studies the proper enzyme kinetic studies could be carried out, and the nature of the inhibition characterized. In most systems we examined the inhibition was competitive with regard to the alkyl phosphate. Only in a few unique cases was the inhibition pattern different than competitive. In all of these systems the vanadium complexes were potent inhibitors.

The analysis carried out in this work exploring the vanadium–phosphatase complexes was done with the anticipation that we would obtain a greater understanding of the factors that lead to the most potent vanadium inhibitor complexes. Our analysis shows that the coordination geometry at the vanadium in the unbound inhibitor complex is not critical, and that several coordination geometries can yield effective inhibitors. As shown by the studies reported with different vanadium compounds, the diverse group of compounds shows activities very similar to that of vanadate and vanadyl sulfate. Because speciation studies were not carried out in detail under the conditions of the enzyme assay in all the studies, and because previous speciation studies reported showed that the compounds were not stable, it would be expected that some of the compounds hydrolyzed before the inhibition assay was conducted. However, even in the studies where the speciation was considered in calculation of the K_i values, the variation in inhibition was still small, and the K_i values of the complexes were near that of vanadate and vanadyl cation. Although many previous authors have suggested that the ligand plays a role and increases the potency dramatically, when comparing the inhibitor potency among the compounds listed in Table 5 the values are of the same

order of magnitude. Thus, we suggest that the potency of inhibitors is not likely to change significantly as the ligand changes. In short, design of new inhibitors based upon vanadium compounds is to be expected to have a similar potency as the salts. Development of new and more potent vanadium-based inhibitors is more likely to be successful if it is a dramatically different compound compared to the structures we have already used, therefore, based on a significantly different base structure or if investigators focus on improving delivery, solubility, and bioavailability.

References

[1] J.R. Knowles, Annu. Rev. Biochem. 49 (1980) 877–919.
[2] R.L. Nelson, P.E. Branton, Mol. Cell. Biol. 4 (1984) 1003–1012.
[3] F.H. Westheimer, Science 235 (1987) 1173–1178.
[4] J.B. Vincent, M.W. Crowder, B.A. Averill, Trends Biochem. Sci. 17 (1992) 105–110.
[5] J. Levering, M.W.J.M. Musters, M. Bekker, D. Bellomo, T. Fiedler, W.M. de Vos, J. Hugenholtz, B. Kreikemeyer, U. Kummer, B. Teusink, FEBS J. 279 (2012) 1274–1290.
[6] W. Vogel, R. Lammers, J.T. Huang, A. Ullrich, Science 259 (1993) 1611–1614.
[7] T. Finkel, J. Cell Biol. 194 (2011) 7–15.
[8] D.L. Nelson, M.M. Cox, Lehninger Principles of Biochemistry, 6th ed., W.H. Freeman and Company, New York, 2013, pp. 433–464.
[9] Z. Cui, S.B. Scruggs, J.E. Gilda, P. Ping, A.V. Gomes, J. Mol. Cell. Cardiol. 71 (2014) 32–42.
[10] A.R. Saltiel, Cell 104 (2001) 517–529.
[11] M. Feldhammer, N. Uetani, D. Miranda-Saavedra, M.L. Tremblay, Crit. Rev. Biochem. Mol. Biol. 48 (2013) 430–445.
[12] R.L. VanEtten, P.P. Waymack, D.M. Rehkop, J. Am. Chem. Soc. 96 (1974) 6782–6785.
[13] M.J. Gresser, A.S. Tracey, P.J. Stankiewicz, in: W. Merlevede, J. DiSalvo (Eds.), Advances in Protein Phosphatases, Leuven University Press, Leuven, Belgium, 1987, pp. 35–57.
[14] J.A. Gordon, Methods Enzymol. 201 (1991) 477–482.
[15] M. Li, W. Ding, B. Baruah, D.C. Crans, R. Wang, J. Inorg. Biochem. 102 (2008) 1846–1853.
[16] S. Sasson, N. Kaiser, M. DanGoor, R. Oron, S. Koren, E. Wertheimer, K. Unluhizarci, E. Cerasi, Diabetologia 40 (1997) 30–39.
[17] A.R. Saltiel, C.R. Kahn, Nature (London) 414 (2001) 799–806.
[18] S. Kaochar, B.P. Tu, Trends Biochem. Sci. 37 (2012) 477–483.
[19] S.G. Clarke, Trends Biochem. Sci. 38 (2013) 243–252.
[20] T. Hunter, Cell 80 (1995) 225–236.
[21] T. Hunter, Cell 100 (2000) 113–127.
[22] J.L. McConnell, B.E. Wadzinski, Mol. Pharmacol. 75 (2009) 1249–1261.
[23] B.I. Posner, R. Faure, J.W. Burgess, A.P. Bevan, D. Lachance, G. Zhang-Sun, I.G. Fantus, J.B. Ng, D.A. Hall, B.S. Lum, J. Biol. Chem. 269 (1994) 4596–4604.
[24] Y. Shechter, J. Li, J. Meyerovitch, D. Gefel, R. Bruck, G. Elberg, D.S. Miller, A. Shisheva, Mol. Cell. Biochem. 153 (1995) 39–47.
[25] G. Huyer, S. Liu, J. Kelly, J. Moffat, P. Payette, B. Kennedy, G. Tsaprailis, M.J. Gresser, C. Ramachandran, J. Biol. Chem. 272 (1997) 843–851.
[26] K.H. Thompson, C. Orvig, in: A. Sigel, H. Sigel (Eds.), Metal Ions in Biological Systems, Marcel Dekker, New York, 2004, pp. 221–252.
[27] P.V. Bharatam, D.S. Patel, L. Adane, A. Mittal, S. Sundriyal, Curr. Pharm. Des. 13 (2007) 3518–3530.
[28] M. Hiromura, A. Nakayama, Y. Adachi, M. Doi, H. Sakurai, J. Biol. Inorg. Chem. 12 (2007) 1275–1287.
[29] A. Zorzano, M. Palacín, L. Marti, S. García-Vicente, J. Inorg. Biochem. 103 (2009) 559–566.
[30] K. Kar, Crit. Rev. Microbiol. 21 (1995) 123–152.
[31] D. Gambino, Coord. Chem. Rev. 255 (2011) 2193–2203.
[32] G.F. Späth, L. Epstein, B. Leader, S.M. Singer, H.A. Avila, S.J. Turco, S.M. Beverley, Proc. Natl. Acad. Sci. U. S. A. 97 (2000) 9258–9263.
[33] R.S. Mendez, B.M. Dorsey, C.C. McLauchlan, M. Beio, T.L. Turner, V.H. Nguyen, A. Su, W. Beynon, J.A. Friesen, M.A. Jones, Int. J. Chem. 6 (2014) 35–49.
[34] T.L. Turner, V.H. Nguyen, C.C. McLauchlan, Z. Dymon, B.M. Dorsey, J.D. Hooker, M.A. Jones, J. Inorg. Biochem. 108 (2012) 96–104.
[35] D.C. Crans, C.M. Simone, A.K. Saha, R.H. Glew, Biochem. Biophys. Res. Commun. 165 (1989) 246–250.
[36] X.-G. Yang, K. Wang, in: W.E.G. Müller, X. Wang, H.C. Schröder (Eds.), Biomedical Inorganic Polymers, Springer, Berlin, Heidelberg, 2013, pp. 1–18.
[37] P.J. Stankiewicz, M.J. Gresser, Biochemistry 27 (1988) 206–212.

[38] P.J. Stankiewicz, A.S. Tracey, D.C. Crans, in: H. Sigel, A. Sigel (Eds.), Metal Ions in Biological Systems, Marcel Dekker, New York, 1995, pp. 287–324.

[39] T.-C. Meng, D.A. Buckley, S. Galic, T. Tiganis, N.K. Tonks, J. Biol. Chem. 279 (2004) 37716–37725.

[40] C.L. Winter, J.S. Lange, M.G. Davis, G.S. Gerwe, T.R. Downs, K.G. Peters, B. Kasibhatla, Exp. Biol. Med. 230 (2005) 207–216.

[41] T.A.S. Brandão, A.C. Hengge, S.J. Johnson, J. Biol. Chem. 285 (2010) 15874–15883.

[42] I.L. Alberts, K. Nadassy, S.J. Wodak, Protein Sci. 7 (1998) 1700–1716.

[43] A.F.A. Peacock, L. Hemmingsen, V.L. Pecoraro, Proc. Natl. Acad. Sci. U. S. A. 105 (2008) 16566–16571.

[44] I. Schomburg, A. Chang, D. Schomburg, Perspect. Sci. 1 (2014) 15–23.

[45] A. Cornish-Bowden, Perspect. Sci. 1 (2014) 74–87.

[46] V.I. Kuznetsov, A.C. Hengge, Biochemistry 52 (2013) 8012–8025.

[47] D.C. Crans, C.M. Simone, R.C. Holz, L. Que, Biochemistry 31 (1992) 11731–11739.

[48] J.E. Coleman, Annu. Rev. Biophys. Biomol. Struct. 21 (1992) 441–483.

[49] D. Gani, J. Wilkie, in: H.A.O. Hill, P.J. Sadler, A.J. Thomson (Eds.), Metal Sites in Proteins and Models, Springer, Berlin, Heidelberg, 1997, pp. 133–175.

[50] S.R. Akabayov, B. Akabayov, Inorg. Chim. Acta 420 (2014) 16–23.

[51] H.M. Berman, J. Westbrook, Z. Feng, G. Gilliland, T.N. Bhat, H. Weissig, I.N. Shindyalov, P.E. Bourne, Nucleic Acids Res. (2000) 235–242.

[52] P.J. O'Brien, D. Herschlag, Biochemistry 41 (2002) 3207–3225.

[53] G. Ramponi, M. Stefani, Biochim. Biophys. Acta – Protein Struct. Mol. Enzymol. 1341 (1997) 137–156.

[54] F. Boehmer, S. Szedlacsek, L. Tabernero, A. Ostman, J. den Hertog, FEBS J. 280 (2013) 413–431.

[55] D. Barford, A.K. Das, M.P. Egloff, Annu. Rev. Biophys. Biomol. Struct. 27 (1998) 133–164.

[56] G. Schenk, N. Mitic, G.R. Hanson, P. Comba, Coord. Chem. Rev. 257 (2013) 473–482.

[57] S.J. Abbott, S.R. Jones, S.A. Weinman, F.M. Bockhoff, F.W. McLafferty, J.R. Knowles, J. Am. Chem. Soc. 101 (1979) 4323–4332.

[58] D.R. Davies, W.G.J. Hol, FEBS Lett. 577 (2004) 315–321.

[59] Enzyme Nomenclature Recommendations of the Nomenclature Committee of the International Union of Biochemistry and Molecular Biology on the Nomenclature and Classification of Enzymes by the Reactions they Catalyse, http://www.chem.qmul.ac.uk/iubmb/enzyme/EC3/ (accessed 16.07.14).

[60] O.O. Coker, S. Warit, K. Rukseree, P. Summpunn, T. Prammananan, P. Palittapongarnpim, BMC Microbiol. 13 (2013).

[61] R.C. Nordlie, J.D. Foster, A.J. Lange, Annu. Rev. Nutr. 19 (1999) 379–406.

[62] J.-D. Rochaix, Biochim. Biophys. Acta Bioenerg. 1807 (2011) 878–886.

[63] A.W. Addison, T.N. Rao, J. Reedijk, J. van Rijn, G.C. Verschoor, J. Chem. Soc. Dalton Trans. (1984) 1349–1356.

[64] S. Alvarez, M. Llunell, J. Chem. Soc. Dalton Trans. (2000) 3288–3303.

[65] S. Alvarez, P. Alemany, D. Casanova, J. Cirera, M. Llunell, D. Avnir, Coord. Chem. Rev. 249 (2005) 1693–1708.

[66] S. Alvarez, B. Menjón, A. Falceto, D. Casanova, P. Alemany, Inorg. Chem. 53 (2014) 12151–12163.

[67] D.C. Crans, M.L. Tarlton, C.C. McLauchlan, Eur. J. Inorg. Chem. (2014) 4450–4468.

[68] D.C. Crans, J.J. Smee, E. Gaidamauskas, L. Yang, Chem. Rev. 104 (2004) 849–902.

[69] D.C. Crans, K.A. Woll, K. Prusinskas, M.D. Johnson, E. Norkus, Inorg. Chem. 52 (2013) 12262–12275.

[70] L. Pettersson, B. Hedman, I. Andersson, N. Ingri, Chem. Scr. 22 (1983) 254–264.

[71] N.D. Chasteen, in: M.J. Clarke, J.B. Goodenough, J.A. Ibers, C.K. Jørgensen, D.M.P. Mingos, J.B. Neilands, G.A. Palmer, D. Reinen, P.J. Sadler, R. Weiss, R.J.P. Williams (Eds.), The Biochemistry of Vanadium, Structure and Bonding, Springer-Verlag, New York, 1983, pp. 105–138.

[72] L. Pettersson, I. Andersson, B. Hedman, Chem. Scr. 25 (1985) 309–317.

[73] D.C. Crans, Comments Inorg. Chem. 16 (1994) 1–33.

[74] D.C. Crans, Comments Inorg. Chem. 16 (1994) 35–76.

[75] Y. Jiang, K. Chakarawet, A.L. Kohout, M. Nava, N. Marino, C.C. Cummins, J. Am. Chem. Soc. 136 (2014) 11894–11897.

[76] E.J. Griffith, J. Am. Chem. Soc. 78 (1956) 3867–3870.

[77] D.C. Crans, C.D. Rithner, L.A. Theisen, J. Am. Chem. Soc. 112 (1990) 2901–2908.

[78] D.C. Crans, E.M. Willging, S.R. Butler, J. Am. Chem. Soc. 112 (1990) 427–432.

[79] I. Andersson, L. Pettersson, J.J. Hastings, O.W. Howarth, J. Chem. Soc. Dalton Trans. (1996) 3357–3361.

[80] M.T. Pope, B.W. Dale, Q. Rev. Chem. Soc. 22 (1968) 527–548.

[81] M.A. Habayeb, J. Hileman, O.E. Can, J. Chem. 58 (1980) 2255–2261.

[82] E. Heath, O.W. Howarth, J. Chem. Soc. Dalton Trans. (1981) 1105–1110.

[83] I. Andersson, S. Angus-Dunne, O. Howarth, L. Pettersson, J. Inorg. Biochem. 80 (2000) 51–58.

[84] H.T. Evans Jr., Inorg. Chem. 5 (1966) 967–977.

[85] N.D. Chasteen, in: L. Berliner, J. Reuben (Eds.), Vanadyl(IV) EPR Spin Probes Inorganic and Biochemical Aspects Biological Magnetic Resonance, Plenum Press, New York, 1981, pp. 53–119.

[86] T. Kiss, T. Jakusch, D. Hollender, A. Dornyei, E.A. Enyedy, J.C. Pessoa, H. Sakurai, A. Sanz-Medel, Coord. Chem. Rev. 252 (2008) 1153–1162.

[87] T. Kiss, A. Odani, Bull. Chem. Soc. Jpn. 80 (2007) 1691–1702.

[88] R. Meier, M. Boddin, S. Mitzenheim, K. Kanamori, in: H. Sigel, A. Sigel (Eds.), Metal Ions in Biological Systems, Marcel Dekker, New York, 1995, pp. 45–88.

[89] P. Buglyo, D.C. Crans, E.M. Nagy, R.L. Lindo, L. Yang, J.J. Smee, W. Jin, L.-H. Chi, M.E. Godzala III, G.R. Willsky, Inorg. Chem. 44 (2005) 5416–5427.

[90] M. Melchior, S.J. Rettig, B.D. Liboiron, K.H. Thompson, V.G. Yuen, J.H. McNeill, C. Orvig, Inorg. Chem. 40 (2001) 4686–4690.

[91] D.C. Crans, R.L. Bunch, L.A. Theisen, J. Am. Chem. Soc. 111 (1989) 7597–7607.

[92] A. Selling, I. Andersson, L. Pettersson, C.M. Schramm, S.L. Downey, J.H. Grate, Inorg. Chem. 33 (1994) 3141–3150.

[93] I.H. Segel, Enzyme Kinetics: Behavior and Analysis of Rapid Equilibrium and Steady State Enzyme Systems, Wiley, New York, 1975.

[94] Z. Lu, D. Dunaway-Mariano, K.N. Allen, Proc. Natl. Acad. Sci. U. S. A. 105 (2008) 5687–5692.

[95] L.L. Madan, B. Gopal, Biochemistry 50 (2011) 10114–10125.

[96] All deposited structures in the Protein Data Bank receive a unique identifying code known as a PDB ID for ease in searching. It is commonly one number followed by a series of three letters/numbers, e.g. 2rar. In this review we have chosen to use lower case letters except for L.

[97] C.J. Ballhausen, H.B. Gray, Inorg. Chem. 1 (1962) 111–122.

[98] J.R. Winkler, H.B. Gray, in: D.M.P. Mingos, P. Day, J.P. Dahl (Eds.), Molecular Electronic Structures of Transition Metal Complexes I, Springer, Berlin, Heidelberg, 2012, pp. 17–28.

[99] F.H. Allen, Acta Crystallogr. B: Struct. Crystallogr. Cryst. Chem. 58 (2002) 380–388.

[100] S. Sheriff, B.R. Beno, W. Zhai, W.A. Kostich, P.A. McDonnell, K. Kish, V. Goldfarb, M. Gao, S.E. Kiefer, J. Yanchunas, Y. Huang, S. Shi, S. Zhu, C. Dzierba, J. Bronson, J.E. Macor, K.K. Appiah, R.S. Westphal, J. O'Connell, S.W. Gerritz, J. Med. Chem. 54 (2011) 6548–6562.

[101] E. Hoppe, C. Limberg, Chem. Eur. J. 13 (2007) 7006–7016.

[102] L. Álvarez, A. Grirrane, R. Moyano, E. Álvarez, A. Pastor, A. Galindo, Polyhedron 29 (2010) 3028–3035.

[103] C.R. Cornman, K.M. Geiser-Bush, J.W. Kampf, Inorg. Chem. 38 (1999) 4303–4308.

[104] J.G. Reynolds, S.C. Sendlinger, A.M. Murray, J.C. Huffman, G. Christou, Angew. Chem. Int. Ed. Engl. 31 (1992) 1253–1255.

[105] D. Homden, C. Redshaw, L. Warford, D.L. Hughes, J.A. Wright, S.H. Dale, M.R.J. Elsegood, Dalton Trans. (2009) 8900–8910.

[106] A. Bilyk, J.W. Dunlop, R.O. Fuller, A.K. Hall, J.M. Harrowfield, M.W. Hosseini, G.A. Koutsantonis, I.W. Murray, B.W. Skelton, R.L. Stamps, A.H. White, Eur. J. Inorg. Chem. (2010) 2106–02126.

[107] G.M. Sheldrick, Acta Crystallogr. A: Found. Crystallogr. 64 (2008) 112–122.

[108] A. Wlodawer, W. Minor, Z. Dauter, M. Jaskolski, FEBS J. 275 (2008) 1–21.

[109] S.W. Wilkins, Acta Crystallogr. A. 69 (2013) 1–4.

[110] Crystallography Matters!, United Nations Educational, Scientific and Cultural Organization, Paris, 2013.

[111] D. Lowe, Chemistry World, Royal Society of Chemistry, Cambridge, 2014 http://www.rsc.org/chemistryworld/2014/07/pipeline-crystal-ball-lies-xray-biomolecules

[112] G.H. Stout, L.H. Jensen, X-ray Structure Determination: A Practical Guide, 2nd ed., John Wiley & Sons, New York, 1989.

[113] G. Rhodes, Crystallography Made Crystal Clear, 3rd ed., Academic Press, New York, 2006.

[114] C. Hammond, The Basics of Crystallography and Diffraction, 3rd ed., International Union of Crystallography, Oxford, 2009.

[115] J.P. Glusker, K.N. Trueblood, Crystal Structure Analysis, Oxford University Press, New York, 2010.

[116] A. Wlodawer, W. Minor, Z. Dauter, M. Jaskolski, FEBS J. 280 (2013) 5705–5736.

[117] R.J. Read, P.D. Adams, W.B. Arendall III, A.T. Brunger, P. Emsley, R.P. Joosten, G.J. Kleywegt, E.B. Krissinel, T. Lütteke, Z. Otwinowski, A. Perrakis, J.S. Richardson, W.H. Sheffler, J.L. Smith, I.J. Tickle, G. Vriend, P.H. Zwart, Structure 19 (2011) 1395–1412.

[118] doi:10.2210/pdb3qcc/pdb (accessed 18.08.14).

[119] J. Kim, D. Rees, Science 257 (1992) 1677–1682.

[120] S.M. Mayer, D.M. Lawson, C.A. Gormal, S.M. Roe, B.E. Smith, J. Mol. Biol. 292 (1999) 871–891.

[121] O. Einsle, F.A. Tezcan, S.L.A. Andrade, B. Schmid, M. Yoshida, J.B. Howard, D.C. Rees, Science 297 (2002) 1696–1700.

[122] T. Spatzal, M. Aksoyoglu, L. Zhang, S.L.A. Andrade, E. Schleicher, S. Weber, D.C. Rees, O. Einsle, Science 334 (2011) 940.

[123] K.M. Lancaster, M. Roemelt, P. Ettenhuber, Y. Hu, M.W. Ribbe, F. Neese, U. Bergmann, S. DeBeer, Science 334 (2011) 974–977.

[124] D. Lukoyanov, V. Pelmenschikov, N. Maeser, M. Laryukhin, T.C. Yang, L. Noodleman, D.R. Dean, D.A. Case, L.C. Seefeldt, B.M. Hoffman, Inorg. Chem. 46 (2007) 11437–11449.

[125] S. Ramaswamy, Science 334 (2011) 914–915.

[126] M. Zhang, M. Zhou, R.L. Van Etten, C.V. Stauffacher, Biochemistry 36 (1997) 15–23.

[127] T.A.S. Brandão, H. Robinson, S.J. Johnson, A.C. Hengge, J. Am. Chem. Soc. 131 (2009) 778–786.

[128] D.J. Rigden, J.E. Littlejohn, K. Henderson, M.J. Jedrzejas, J. Mol. Biol. 325 (2003) 411–420.

[129] C.F. Macrae, I.J. Bruno, J.A. Chisholm, P.R. Edgington, P. McCabe, E. Pidcock, L. Rodriguez-Monge, R. Taylor, J. van de Streek, P.A. Wood, J. Appl. Crystallogr. 41 (2008) 466–470.

[130] K. Ishikawa, Y. Mihara, K. Gondoh, E.-I. Suzuki, Y. Asano, EMBO J. 19 (2000) 2412–2423.

[131] Y. Lindqvist, G. Schneider, P. Vihko, Eur. J. Biochem. 221 (1994) 139–142.

[132] E.B. Fauman, C. Yuvaniyama, H.L. Schubert, J.A. Stuckey, M.A. Saper, J. Biol. Chem. 271 (1996) 18780–18788.

[133] R.D. Makde, S.K. Mahajan, V. Kumar, Biochemistry 46 (2007) 2079–2090.

170

[134] S. Alvarez, personal communication.
[135] M.F.A. Santos, I. Correia, A.R. Oliveira, E. Garribba, J.C. Pessoa, T. Santos-Silva, Eur. J. Inorg. Chem. (2014) 3293–3297.
[136] I. Machado, M. Fernández, I. Becco, B. Garat, R.F. Brissos, N. Zabarska, P. Gamez, F. Marques, I. Correia, J. Costa Pessoa, D. Gambino, Inorg. Chim. Acta 420 (2014) 39–46.
[137] Q.Q. Zheng, D.Q. Jiang, W. Zhang, Q.Q. Zhang, J. Jin, X. Li, H.T. Yang, N. Shaw, W. Zhou, Z. Rao, unpublished work. doi:10.2210/pdb4qih/pdb.
[138] S. Bhattacharyya, R.J. Batchelor, F.W.B. Einstein, A.S. Tracey, Can. J. Chem. 77 (1999) 2088–2094.
[139] A. Messerschmidt, R. Wever, Proc. Natl. Acad. Sci. U. S. A. 93 (1996) 392–396.
[140] M. Weyand, H.J. Hecht, M. Kieß, M.F. Liaud, H. Vilter, D. Schomburg, J. Mol. Biol. 293 (1999) 595–611.
[141] W. Hemrika, R. Renirie, H.L. Dekker, P. Barnett, R. Wever, Proc. Natl. Acad. Sci. U. S. A. 94 (1997) 2145–2149.
[142] M.N. Isupov, A.R. Dalby, A.A. Brindley, Y. Izumi, T. Tanabe, G.N. Murshudov, J.A. Littlechild, J. Mol. Biol. 299 (2000) 1035–1049.
[143] Z. Lu, L. Wang, D. Dunaway-Mariano, K.N. Allen, J. Biol. Chem. 284 (2009) 1224–1233.
[144] K.M. Holtz, B. Stec, E.R. Kantrowitz, J. Biol. Chem. 274 (1999) 8351–8354.
[145] V. Lopez, T. Stevens, R.N. Lindquist, Arch. Biochem. Biophys. 175 (1976) 31–38.
[146] L.E. Seargeant, R.A. Stinson, Biochem. J. 181 (1979) 247–250.
[147] C.M. Simone, Ph.D. thesis, Colorado State University, Fort Collins, CO, 1992.
[148] V. Agarwal, S.A. Borisova, W.W. Metcalf, W.A. van der Donk, S.K. Nair, Chem. Biol. 18 (2011) 1230–1240.
[149] J.Y. Lee, J.E. Kwak, J. Moon, S.H. Eom, E.C. Liong, J.-D. Pedelacq, J. Berendzen, S.W. Suh, Nat. Struct. Mol. Biol. 8 (2001) 789–794.
[150] J.G. Zalatan, T.D. Fenn, A.T. Brunger, D. Herschlag, Biochemistry 45 (2006) 9788–9803.
[151] R.L. Felts, T.J. Reilly, J.J. Tanner, J. Biol. Chem. 281 (2006) 30289–30298.
[152] M.Y. Galperin, M.J. Jedrzejas, Proteins: Struct. Funct. Bioinf. 45 (2001) 318–324.
[153] R.N. Lindquist, J.L. Lynn, G.E. Lienhard, J. Am. Chem. Soc. 95 (1973) 8762–8768.
[154] S. Gonçalves, A.M. Esteves, H. Santos, N. Borges, P.M. Matias, Biochemistry 50 (2011) 9551–9567.
[155] S.-H. Kim, K.L. Constantine, G.J. Duke, V. Goldfarb, J.T. Hunt, S. Johnson, K. Kish, H.E. Klei, P.A. McDonnell, W.J. Metzler, L. Mueller, M.A. Poss, C.R. Fairchild, R.S. Bhide, Bioorg. Med. Chem. Lett. 23 (2013) 4107–4111.
[156] J.N. Andersen, O.H. Mortensen, G.H. Peters, P.G. Drake, L.F. Iversen, O.H. Olsen, P.G. Jansen, H.S. Andersen, N.K. Tonks, N.P.H. Møller, Mol. Cell. Biol. 21 (2001) 7117–7136.
[157] V.I. Kuznetsov, A.C. Hengge, S.J. Johnson, Biochemistry 51 (2012) 9869–9879.
[158] J.M. Denu, D.L. Lohse, J. Vijayalakshmi, M.A. Saper, J.E. Dixon, Proc. Natl. Acad. Sci. U. S. A. 93 (1996) 2493–2498.
[159] A.G. Evdokimov, M. Pokross, R. Walter, M. Mekel, B. Cox, C. Li, R. Bechard, F. Genbauffe, R. Andrews, C. Diven, B. Howard, V. Rastogi, J. Gray, M. Maier, K.G. Peters, Acta Crystallogr. D: Biol. Crystallogr. 62 (2006) 1435–1445.
[160] H. Deng, R. Callender, Z. Huang, Z.-Y. Zhang, Biochemistry 41 (2002) 5865–5872.
[161] M. Zhang, R.L. Van Etten, C.V. Stauffacher, Biochemistry 33 (1994) 11097–11105.
[162] K. Kish, P.A. McDonnell, V. Goldfarb, M. Gao, W.J. Metzler, D.R. Langley, J.W. Bryson, S.E. Kiefer, B. Carpenter, W.A. Kostich, R.S. Westphal, S. Sheriff, Acta Crystallogr. F: Struct. Biol. Cryst. Commun. 67 (2011) 768–774.
[163] National Instibues of Health, Protein Structure Initiative, http://www.nigms.nih.gov/Research/SpecificAreas/PSI/Pages/default.aspx (accessed 29.07.14).
[164] S.C. Almo, J.B. Bonanno, J.M. Sauder, S. Emtage, T.P. DiLorenzo, V. Malashkevich, S.R. Wasserman, S. Swaminathan, S. Eswaramoorthy, R. Agarwal, D. Kumaran, M. Madegowda, S. Ragumani, Y. Patskovsky, J. Alvarado, U.A. Ramagopal, J. Faber-Barata, M.R. Chance, A. Sali, A. Fiser, Z.-y. Zhang, D.S. Lawrence, S.K. Burley, J. Struct. Funct. Genomics 8 (2007) 121–140.
[165] A.K. Pedersen, X.-L. Guo, K.B. Møller, G.H. Peters, H.S. Andersen, J.S. Kastrup, S.B. Mortensen, L.F. Iversen, Z.-Y. Zhang, N.P.H. Møller, Biochem. J. 378 (2004) 421–433.
[166] T.A.S. Brandão, S.J. Johnson, A.C. Hengge, Arch. Biochem. Biophys. 525 (2012) 53–59.
[167] Y.-F. Keng, L. Wu, Z.-Y. Zhang, Eur. J. Biochem. 259 (1999) 809–814.
[168] J. Vijayalakshmi, M.A. Saper, unpublished work. doi:10.2210/pdb2i42/pdb.
[169] Y. Zhang, M. Zhang, Y. Zhang, Biochem. J. 434 (2011) 435–444.
[170] S.C. Yong, P. Roversi, J.E.D. Lillington, O.B. Zeldin, E.F. Garman, S.M. Lea, B.C. Berks, unpublished work. doi:10.2210/pdb3zwu/pdb.
[171] D. Feder, L.W. Guddat, G. Schenk, unpublished work. doi:10.2210/pdb4kkz/pdb.
[172] H.U. Bergmeyer, J.r. Bergmeyer, M. Grassl, Methods of Enzymatic Analysis, 3rd ed., Weinheim, Deerfield Beach, FL, Verlag Chemie, 1983.
[173] D.C. Crans, A.D. Keramidas, C. Drouza, Phosphorus Sulfur Silicon Relat. Elem. 109 (1996) 245–248.
[174] G.M. Rossolini, S. Schippa, M.L. Riccio, F. Berlutti, L.E. Macaskie, M.C. Thaller, Cell. Mol. Life Sci. 54 (1998) 833–850.
[175] N.K. Tonks, C.D. Diltz, E.H. Fischer, J. Biol. Chem. 263 (1988) 6722–6730.
[176] N.K. Tonks, C.D. Diltz, E.H. Fischer, J. Biol. Chem. 263 (1988) 6731–6737.
[177] J. Chernoff, A.R. Schievella, C.A. Jost, R.L. Erikson, B.G. Neel, Proc. Natl. Acad. Sci. U. S. A. 87 (1990) 2735–2739.
[178] L. Lu, X. Gao, M. Zhu, S. Wang, Q. Wu, S. Xing, X. Fu, Z. Liu, M. Guo, Biometals 25 (2012) 599–610.
[179] C.C. McLauchlan, J.D. Hooker, M.A. Jones, Z. Dymon, E.A. Backhus, B.A. Greiner, N.A. Dorner, M.A. Youkhana, L.M. Manus, J. Inorg. Biochem. 104 (2010) 274–281.
[180] G.L. Lawrence, R.L. VanEtten, Arch. Biochem. Biophys. 206 (1981) 122–131.
[181] Y.L. Zhang, Z.Y. Zhang, Anal. Biochem. 261 (1998) 139–148.
[182] N.J. Reiter, D.J. White, F. Rusnak, Biochemistry 41 (2002) 1051–1059.
[183] C. McWhirter, E.A. Lund, E.A. Tanifum, G. Feng, Q.I. Sheikh, A.C. Hengge, N.H. Williams, J. Am. Chem. Soc. 130 (2008) 13673–13682.
[184] P.L. Makinen, J. Invest. Dermatol. 85 (1985) 118–124.
[185] A.K. Saha, D.C. Crans, M.T. Pope, C.M. Simone, R.H. Glew, J. Biol. Chem. 266 (1991) 3511–3517.
[186] J.B. Vincent, M.W. Crowder, B.A. Averill, Biochemistry 30 (1991) 3025–3034.
[187] A. Siddiqua, M. Sherazi, R. Naz, I. Ali, A. Saeed, A.H. Shah, A.R. Khan, M. Ahmad, H.U. Khan, A. Saeed, J. Chem. Soc. Pak. 31 (2009) 801–808.
[188] M.I. Feigen, M.A. Johns, J.H. Postlethwait, R.R. Sederoff, J. Biol. Chem. 255 (1980) 338–343.
[189] W.L. Turner, W.C. Plaxton, Planta 214 (2001) 243–249.
[190] D.C. Crans, C.M. Simone, J.S. Blanchard, J. Am. Chem. Soc. 114 (1992) 4926–4928.
[191] H. Haas, B. Redl, E. Leitner, G. Stoffler, Biochim. Biophys. Acta 1074 (1991) 392–397.
[192] A.H.J. Ullah, B.J. Cummins, Prep. Biochem. 18 (1988) 37–65.
[193] Q.X. Chen, W.Z. Zheng, J.Y. Lin, Z.T. Cai, H.M. Zhou, Biochemistry – Moscow 65 (2000) 1105–1110.
[194] Z.Y. Zhang, Y. Wang, L. Wu, E.B. Fauman, J.A. Stuckey, H.L. Schubert, M.A. Saper, J.E. Dixon, Biochemistry 33 (1994) 15266–15270.
[195] A.R. Whisnant, S.D. Gilman, Anal. Biochem. 307 (2002) 226–234.
[196] M.M. Zhou, J.P. Davis, R.L. VanEtten, Biochemistry 32 (1993) 8479–8486.
[197] Y.S. Heo, J.M. Ryu, S.M. Park, J.H. Park, H.C. Lee, K.Y. Hwang, J. Kim, Exp. Mol. Med. 34 (2002) 211–223.
[198] H. Deng, R. Callender, Z.H. Huang, Z.Y. Zhang, Biochemistry 41 (2002) 5865–5872.
[199] A.J. Ziegler, J. Florian, M.A. Ballicora, A.W. Herlinger, J. Enzyme Inhib. Med. Chem. 24 (2009) 22–28.
[200] D. Kalita, S.P. Das, N.S. Islam, Biol. Trace Elem. Res. 128 (2009) 200–219.
[201] S.P. Das, S.R. Ankireddy, J.J. Boruah, N.S. Islam, RSC Adv. 2 (2012) 7248–7261.
[202] J.J. Boruah, D. Kalita, S.P. Das, S. Paul, N.S. Islam, Inorg. Chem. 50 (2011) 8046–8062.
[203] A.P. Seale, L.A. de Jesus, S.Y. Kim, Y.H. Choi, H.B. Lim, C.S. Hwang, Y.S. Kim, Biotechnol. Lett. 27 (2005) 221–225.
[204] S. Pluskey, M. MahroofTahir, D.C. Crans, D.S. Lawrence, Biochem. J. 321 (1997) 333–339.
[205] J.M. Messmore, R.T. Raines, Arch. Biochem. Biophys. 381 (2000) 25–30.
[206] T. Tiago, M. Aureliano, R.O. Duarte, J.J.G. Moura, Inorg. Chim. Acta 339 (2002) 317–321.
[207] M. Aureliano, D.C. Crans, J. Inorg. Biochem. 103 (2009) 536–546.
[208] M. Aureliano, Inorg. Chim. Acta 420 (2014) 4–7.
[209] C.C. McLauchlan, M.P. Weberski Jr., B.A. Greiner, Inorg. Chim. Acta 362 (2009) 2662–2666.
[210] K.G. Peters, M.G. Davis, B.W. Howard, M. Pokross, V. Rastogi, C. Diven, K.D. Greis, E. Eby-Wilkens, M. Maier, A. Evdokimov, S. Soper, F. Genbauffe, J. Inorg. Biochem. 96 (2003) 321–330.
[211] L.P. Lu, X.L. Gao, M.L. Zhu, S.L. Wang, Q. Wu, S. Xing, X.Q. Fu, Z.W. Liu, M.L. Guo, Biometals 25 (2012) 599–610.
[212] B. Nuber, J. Weiss, K. Wieghardt, Z. Naturforsch. B: Chem. Sci. 33 (1978) 265.
[213] D.C. Crans, M. Mahroof-Tahir, M.D. Johnson, P.C. Wilkins, L. Yang, K. Robbins, A. Johnson, J.A. Alfano, M.E. Godzala III, L.T. Austin, G.R. Willsky, Inorg. Chim. Acta 356 (2003) 365–378.
[214] G.R. Willsky, L.-H. Chi, M. Godzala III, P.J. Kostyniak, J.J. Smee, A.M. Trujillo, J.A. Alfano, W. Ding, Z. Hu, D.C. Crans, Coord. Chem. Rev. 255 (2011) 2258–2269.
[215] K.H. Thompson, C. Orvig, J. Inorg. Biochem. 100 (2006) 1925–1935.
[216] K.H. Thompson, J. Lichter, C. LeBel, M.C. Scaife, J.H. McNeill, C. Orvig, J. Inorg. Biochem. 103 (2009) 554–558.
[217] P. Caravan, L. Gelmini, N. Glover, F.G. Herring, H. Li, J.H. McNeill, S.J. Rettig, I.A. Setyawati, E. Shuter, Y. Sun, A.S. Tracey, V.G. Yuen, C. Orvig, J. Am. Chem. Soc. 117 (1995) 12759–12770.
[218] B.D. Liboiron, K.H. Thompson, G.R. Hanson, E. Lam, N. Aebischer, C. Orvig, J. Am. Chem. Soc. 127 (2005) 5104–5115.
[219] T. Jakusch, D. Hollender, E.A. Enyedy, C.S. Gonzalez, M. Montes-Bayon, A. Sanz-Medel, J.C. Pessoa, I. Tomaz, T. Kiss, Dalton Trans. (2009) 2428.
[220] V. Conte, F. Di Furia, S. Moro, J. Mol. Catal. 94 (1994) 323–333.
[221] A. Butler, M.J. Clague, G.E. Meister, Chem. Rev. 94 (1994) 625–638.
[222] V. Conte, F. Di Furia, S. Moro, J. Mol. Catal. A: Chem. 120 (1997) 93–99.
[223] V. Conte, F. Di Furia, S. Moro, ACS Symp. Ser. 711 (1998) 136–145.
[224] S.S. Amin, K. Cryer, B. Zhang, S.K. Dutta, S.S. Eaton, O.P. Anderson, S.M. Miller, B.A. Reul, S.M. Brichard, D.C. Crans, Inorg. Chem. 39 (2000) 406–416.
[225] L.C.Y. Woo, V.G. Yuen, K.H. Thompson, J.H. McNeill, C. Orvig, J. Inorg. Biochem. 76 (1999) 251–257.
[226] E.G. Vergara, e.S. Lara, A.P. Benítez, A. Mendoza, 15th International Conference on Biological Inorganic Chemistry (ICBIC), Vancouver, Canada, 2011.
[227] A. Chatkon, P.B. Chatterjee, M.A. Sedgwick, K.J. Haller, D.C. Crans, Eur. J. Inorg. Chem. (2013) 1859–1868.
[228] A. Chatkon, A. Barres, N. Samart, S.E. Boyle, K.J. Haller, D.C. Crans, Inorg. Chim. Acta 420 (2014) 85–91.

[229] G.G. Graham, J. Punt, M. Arora, R.O. Day, M.P. Doogue, J.K. Duong, T.J. Fur-long, J.R. Greenfield, L.C. Greenup, C.M. Kirkpatrick, J.E. Ray, P. Timmins, K.M. Williams, Clin. Pharm. 50 (2011) 81–98.
[230] W.R.J. Taylor, N.J. White, Drug Saf. 27 (2004) 25–61.
[231] D.A. Fidock, T.E. Wellems, Proc. Natl. Acad. Sci. U. S. A. 94 (1997) 10931–10936.
[232] F. Nxumalo, N.R. Glover, A.S. Tracey, J. Biol. Inorg. Chem. 3 (1998) 534–542.
[233] D.C. Crans, M. Mahroof-Tahir, O.P. Anderson, M.M. Miller, Inorg. Chem. 33 (1994) 5586–5590.
[234] J. Baes, F. Charles, R.E. Mesmer, The Hydrolysis of Cations, John Wiley & Sons, New York, 1976, pp. 193–210.
[235] A. Wlodawer, M. Miller, L. Sjölin, Proc. Natl. Acad. Sci. U. S. A. 80 (1983) 3628–3631.
[236] B. Borah, C.W. Chen, W. Egan, M. Miller, A. Wlodawer, J.S. Cohen, Biochemistry 24 (1985) 2058–2067.
[237] D. Kostrewa, H.W. Choe, U. Heinemann, W. Saenger, Biochemistry 28 (1989) 7592–7600.
[238] J.E. Ladner, B.D. Wladkowski, L.A. Svensson, L. Sjolin, G.L. Gilliland, Acta Crys-tallogr. D (1997) 290–301.
[239] H.S. Andersen, O.H. Olsen, L.F. Iversen, A.L.P. Sørensen, S.B. Mortensen, M.S. Christensen, S. Branner, T.K. Hansen, J.F. Lau, L. Jeppesen, E.J. Moran, J. Su, F. Bakir, L. Judge, M. Shahbaz, T. Collins, T. Vo, M.J. Newman, W.C. Ripka, N.P.H. Møller, J. Med. Chem. 45 (2002) 4443–4459.
[240] J. Littlechild, E. Garcia Rodriguez, M. Isupov, J. Inorg. Biochem. 103 (2009) 617–621.
[241] A. Messerschmidt, L. Prade, R. Wever, Biol. Chem. 378 (1997) 309–316.
[242] J. Littlechild, E. Garcia-Rodriguez, E. Coupe, A. Watts, M. Isupov, in: K. Kustin, J.C. Pessoa, D.C. Crans (Eds.), Vanadium: The Verastile Metal, 2007, pp. 136–147.
[243] J. Stukey, G.M. Carman, Protein Sci. 6 (1997) 469–472.
[244] A.F. Neuwald, Protein Sci. 6 (1997) 1764–1767.
[245] D. Wischang, O. Brücher, J. Hartung, Coord. Chem. Rev. 255 (2011) 2204–2217.
[246] R. André, F. Natálio, M. Humanes, J. Leppin, K. Heinze, R. Wever, H.C. Schröder, W.E.G. Müller, W. Tremel, Adv. Funct. Mater. 21 (2011) 501–509.
[247] L. Kaysser, P. Bernhardt, S.-J. Nam, S. Loesgen, J.G. Ruby, P. Skewes-Cox, P.R. Jensen, W. Fenical, B.S. Moore, J. Am. Chem. Soc. 134 (2012) 11988–11991.
[248] S. de Macedo-Ribeiro, R. Renirie, R. Wever, A. Messerschmidt, Biochemistry 47 (2008) 929–934.
[249] R. Renirie, W. Hemrika, R. Wever, J. Biol. Chem. 275 (2000) 11650–11657.
[250] J.N. Carter, K.E. Beatty, M.T. Simpson, A. Butler, J. Inorg. Biochem. 91 (2002) 59–69.
[251] N. Tanaka, V. Dumay, Q. Liao, A.J. Lange, R. Wever, Eur. J. Biochem. 269 (2002) 2162–2167.
[252] R. Wever, M.A. van der Horst, Dalton Trans. (2013).
[253] D. Wang, S.J. Lippard, Nat. Rev. Drug Discov. 4 (2005) 307–320.
[254] N. Graf, S.J. Lippard, Adv Drug Deliv. Rev. 64 (2012) 993–1004.
[255] J.J. Wilson, S.J. Lippard, Chem. Rev. 114 (2014) 4470–4495.
[256] R.G. Strickley, in: E.M. John (Ed.), Annu. Rep. Med. Chem., Vol. 43, Academic Press, San Francisco, 2008, pp. 419–451.

172

Appendix X: Multinuclear NMR Studies of Aqueous Vanadium-HEDTA Complexes

This manuscript is published in *Polyhedron* with Xiao (Sherry) Wu as the primary author. For this work, Xiao Wu conducted the experiments, prepared the data, and prepared most of the manuscript. Christopher Rithner assisted in acquiring the NMR data, and Debbie C. Crans was a greatly assisted in guiding this study and preparation of the manuscript. Benjamin J. Peters assisted in guiding Xiao Wu to make sure experimentation and samples were prepared correctly along with fine tuning the manuscript drafts. Benjamin J. Peters would like to give special recognition to Xiao Wu for her determination and love of science.[1]

Reference

(1)   Wu, X.; Peters, B. J.; Rithner, C. D.; Crans, D. C. Multinuclear NMR Studies of Aqueous Vanadium-HEDTA Complexes. *Polyhedron.* **2016,** *114*, 325-332.

Contents lists available at ScienceDirect

Polyhedron
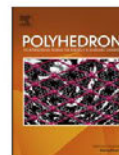
Multinuclear NMR studies of aqueous vanadium–HEDTA complexes

Xiao Wu [a], Benjamin J. Peters [a], Christopher D. Rithner [a], Debbie C. Crans [a,b,*]

[a] Department of Chemistry, Colorado State University, Fort Collins, CO 80523, USA
[b] Department of Cell and Molecular Biology, Colorado State University, Fort Collins, CO 80523, USA

ABSTRACT

N-(2-hydroxyethyl)ethylenediamine-N,N',N'-triacetic acid (HEDTA) is an alternative chelator similar to ethylenediaminetetraacetic acid (EDTA) which is commonly used for metal–ion removal. Because of the introduced asymmetry in the HEDTA ligand, more than one coordination complex can form. The interaction between HEDTA and vanadate has been studied by 1D and 2D, ^{51}V, ^{13}C, and ^{1}H NMR spectroscopies at ambient temperature to determine the complexes formed in solution and to explore the pH dependence on complex formation. Two main complexes form in the reaction between vanadate and HEDTA at a one to one ratio in the pH range between 3 and 11. The first complex, V-HEDTA1, begins to form at pH 6 and decreases as pH increases to pH 10. The second complex, V-HEDTA2, forms above pH 3 and increases with pH until pH 9 where the complex no longer forms. Structurally, V-HEDTA2 is similar to the complex that forms between vanadate and EDTA, whereas the data is consistent with the alkoxy arm of the V-HEDTA2 complex being weakly coordinated. The other complex formed, V-HEDTA1, is structurally different from the vanadate EDTA complex. The formation constants of the V–HEDTA complexes and the β values were calculated for the future use of these constants to predict formation of complexes under biological and environmental studies.

© 2016 Elsevier Ltd. All rights reserved.

1. Introduction

Metal chelation by aminopolycarboxylates [1–4] is important for uses in laboratory settings [5,6], in medicine [7–14], in biological systems [15–20], in technical industrial processes such as mineral dissolution or simply removal of the metal ion [21–23], and for environmental purposes [24–26]. Ethylenediamine-N,N',N'',N'''-tetraacetate (EDTA, Fig. 1a) is the most commonly used general chelator [27–31]. However for specific metal ions, alternative chelators with more beneficial properties, such as ion selectivity and specific binding, have been developed [17,32]. N-(2-hydroxyethyl)ethylenediamine-N,N',N'-triacetic acid, abbreviated HEDTA, is one such alternative chelator (Fig. 1b). HEDTA is a chelator that is found to be particularly effective at abstracting iron [33–35]. Because vanadium can replace iron under some conditions [36] we are interested in investigating the complexes that form between HEDTA and the forms of vanadium present at ambient temperature, in the presence of oxygen, and at varying pH values.

Vanadium in oxidation state V (V(V)) exists in aqueous solution as various oxometalate forms depending on pH [37]. Although the aqueous species that forms at neutral and high pH are anionic (such as $H_2VO_4^-$ and $HV_2O_7^{3-}$) [36,38], the complex species that form of V(V) in aqueous solution coordinates the cationic VO^{3+}, α-cis VO_2^+ or the β-cis VO_2^+ [39–44]. Numerous reports describe vanadium complexes (V(III), V(IV) and V(V)) with EDTA and related ligands both in the solid state and in aqueous solution [39,41,45–48]. Because of the diverse coordination chemistry of vanadium, complexes are found to contain vanadium with both six [40–42,49–51] and seven [31] coordination spheres. In Fig. 2, the reported X-ray structure for the EDTA complex is shown. When the EDTA ligand is modified and two carboxylate ligands are removed from the ethylenediamine unit, the ligand ethylenediamine-N',N''-diacetic acid, EDDA, is tetradentate resulting in the complex shown in Fig. 1c. As a result, this ligand has the potential to form two different complexes with V(V) as shown in Fig. 2. The two different complexes of the EDDA are very different, with the complex with the facial coordination mode resulting in a chemical shift (−490 ppm) significantly further downfield than the complex with the meridional coordination mode (−521 ppm) shown in Fig. 2. Vanadium in oxidation state III often does not contain an oxo group, and a seven coordinate species could form where the
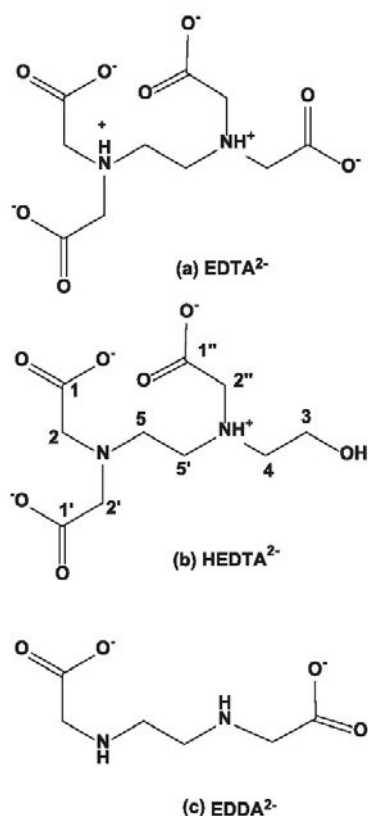
Fig. 1. Common aminopolycarboxylate chelators shown in their dianionic forms are illustrated; (a) ethylenediamine-N,N',N'',N'''-tetraacetate, EDTA; (b) N-(2-hydroxyethyl)-ethylenediamine-N,N',N'-triacetic acid (HEDTA) and its atoms are labeled; (c) ethylenediamine-N',N''-diacetic acid, EDDA.

ligand is coordinated in a heptadentate manner and a water molecule complete the coordination sphere has been reported, (Fig. 2).

Because HEDTA is a derivative of EDTA, the chemistry associated with HEDTA complexes are related to the chemistry of the well-known V-EDTA complexes [39,41]. In the case of the ligand, HEDTA, the perturbation from the EDTA ligand brings asymmetry
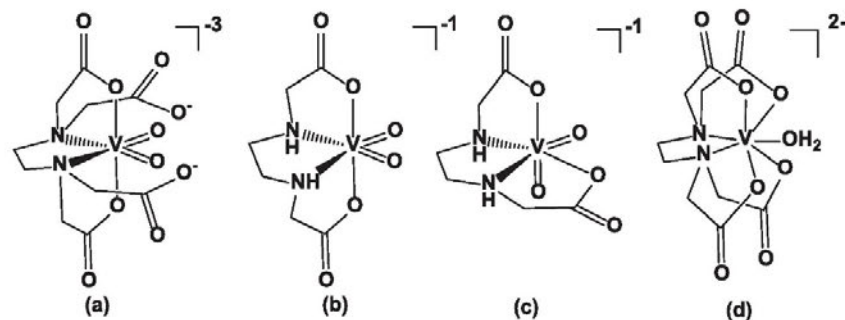
to the ligand and thus more structural possibility for complexation. Indeed, it has previously been reported that two different complexes form between the V-atom and the HEDTA ligand, although a careful structural analysis has not yet been carried out [53]. In the following work we use multinuclear NMR spectroscopy to characterize the complexes that form between HEDTA and V(V) in aqueous solution. ^{13}C and ^{1}H NMR spectroscopic studies allow for characterization of the complexes that form using the chemical shifts of the ligand to define the chelating parts of the ligand [39]. ^{51}V NMR spectroscopy is a sensitive tool for measuring the complexes and the chemical shift differences between the isomers, and can demonstrate that there are some significant structural differences. The ^{51}V NMR spectroscopy is furthermore a very sensitive technique to allow for the calculation of formation constants for the complexes [42,51]. The studies carried out here will characterize the solution structure of the V–HEDTA complexes and provide formation constants that can be used for speciation considerations in applications for the HEDTA ligand.

2. Experimental

2.1. Materials and methods

All chemicals were reagent grade and used without further purification. N-(2-hydroxyethyl)-ethylenediamine-N,N',N'-triacetic acid (HEDTA, ⩾98%) and sodium metavanadate (⩾99.9%) from were purchased from Sigma–Aldrich. Deuterium Oxide (⩾99.9%) was purchased from Cambridge Isotope Laboratories. NaOH (⩾99.2%) and HCl (⩾37.0%, 12.1 M) were purchased from Fisher Scientific. Stock solutions of NaOD (5 M, 1 M, 0.1 M) and DCl (5 M, 1 M, 0.1 M) were prepared by dissolving NaOH and HCl in D_2O and these solutions were stored at ambient temperature. The pD was recorded using an Orion 420 a plus pH meter. The pD equals pH +0.4, where the pH is what is measured by a pH meter (± 0.05) [54].

2.2. Preparation of V–HEDTA compounds

The V–HEDTA solutions for NMR spectroscopy were prepared by mixing sodium metavanadate ($NaVO_3$, 0.183 g, 1.50 mmol) and HEDTA (0.417 g, 1.50 mmol) in a 10 mL volumetric flask for a final concentration of 150 mM. The pD was then adjusted using NaOD and DCl. The sample stability at ambient temperature depended on concentration, pH and storage time. The V–HEDTA solution changed color from yellow to blue consistent with the reduction of the vanadium [55]. Solutions for the spectroscopic studies in this manuscript were prepared fresh unless noted otherwise.

Fig. 2. Crystal structure of VO_2-EDTA in (a) [39,41]; the two V-EDDA complexes [39–41] alpha-cis (b) and beta-cis (c) and of the seven coordinate vanadium in V(III)-EDTA (d) [52].

2.3. 1D NMR spectroscopy

NMR spectra were recorded on a 400 MHz ^{1}H NMR Varian spectrometer operating at 400 MHz for ^{1}H NMR, 100.25 MHz for ^{13}C NMR, and 105 MHz for ^{51}V NMR. The ^{1}H NMR spectra were recorded using a sweep width of about 6410 Hz, a pulse angle of 45°, 8 scans, and a relaxation delay of 1.0 s. DSS (sodium 3-(trimethylsilyl)-1-propanesulfonate) was used as an external reference [41,56].

The ^{13}C NMR spectra were recorded using a sweep width of about 25 kHz, a pulse angle of 45°, 1000 scans and a relaxation delay of 1.0 s. The ^{13}C NMR spectra were referenced to external DSS [41,56].

The ^{51}V spectra were recorded using a sweep width of about 43.103 kHz, a pulse angle of 90° and 4096 scans. The ^{51}V NMR spectra were referenced to external [VO$_2$DEA]$^-$ at −488 ppm [42]. Using the known total vanadium concentrations and the mole fraction of each species, the concentration of the V–HEDTA complexes and other oxovanadate species were calculated. The reported data represent the average values from three different samples [40]. The pD of each sample was tested before and after NMR experiments.

2.4. 2D NMR spectroscopy

The homonuclear ^{51}V 2D-EXSY was done at 105 MHz using a Varian NMR spectrometer. The sample contained 150 mM vanadate and 150 mM HEDTA at a pD of 8.58. The spectra recorded consisted of 200 t_1 increments, 256 scans per t_1 increment, 1000 complex points, and a receiver gain of 32 dB. Each scan had a relaxation time of 15 ms, mixing time of 2 ms, and acquisition time of 25 ms. The spectral width was 40.322 KHz. These conditions are similar to those reported previously [57]. The heteronuclear ^{1}H–^{13}C HMQC was run using a Varian Spectrometer. The samples studied consisted of 150 mM vanadate and 150 mM HEDTA at a pD values of 5.6, 7.0, and 9.7. The spectra for each sample consisted of 96 t_1 increments, 8 scans per increment, and a receiver gain of 28 dB. Each scan had a relaxation delay of 1.0 s.

3. Results and discussion

3.1. Multinuclear NMR studies of V-HEDTA1 complex at alkaline pD

Vanadate and HEDTA solutions each were clear after preparation. When mixing these aqueous solutions together above pH 8, the solution turned yellow indicative of V–HEDTA formation. Because decavanadate is yellow/orange, it was necessary to rule out the possibility that the yellow color was due to decavanadate. This possibility was rejected because the ^{51}V NMR spectra of the yellow solutions at alkaline pH did not show the presence of the three signals for decavanadate in the chemical shift range −516 to −424 ppm (V_a = −516 ppm, V_b = −502 ppm and V_C = −424 ppm [58]), (Fig. 3). We concluded that the yellow color was due to the yellow V-HEDTA1 complex. Upon aging, the color of the 150 mM V–HEDTA complex remained yellow at pH above 8 after storage for more than a week. The stability of the solutions decrease with decreasing pH and increase with decreasing concentrations as indicated by blue color formation. At pH 7.7 the solutions remains yellow for 4 days at 150 mM, and at 15 mM (at 1.5 mM the color is very faint). At pH 10 and 2 the solutions are slightly less stable than at pH 7.7 (the color remains yellow for 3–4 days at 150 mM and at 15 mM). At pH 5 the solution remains yellow for 4 days at 150 mM and at 15 mM as found at pH 7.7. The blue color is indicative of the presence of reduced vanadium [55].
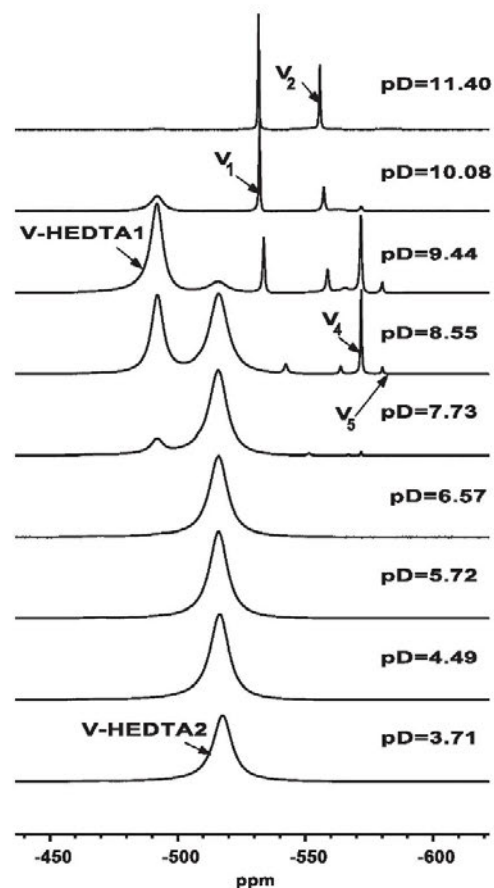
Fig. 3. ^{51}V NMR spectra of 150 mM vanadate and 150 mM HEDTA at varying pD values. The two main vanadate–HEDTA complexes are marked as V-HEDTA1 and V-HEDTA2, and the vanadate oxoanions as monomer V_1, dimer V_2, tetramer V_4, and pentamer V_5.

As seen in Fig. 3, two V–HEDTA complexes form; the V-HEDTA1 exist above pD 8 and the V-HEDTA2 complex exist from pD 3–9. Speciation studies carried out by NMR spectroscopy were done in deuterium oxide and thus the pH is actually the pD and will be described as such in this manuscript. The ^{51}V NMR spectra show that a V-HEDTA1 peak at −492 ppm and V-HEDTA2 at −516 ppm and these peaks did not change with varying pD values although the V-HEDTA1 was previously reported at −497 ppm, presumable reflecting the variation in conditions [41]. There is a difference in the line broadening between the two signals and the t_1 values were measured and found to be 0.6 mS for V-HEDTA1, 0.4 mS for V-HEDTA2 and 8 mS for the vanadate tetramer. The linebroadening of the V-HEDTA1 (590 Hz) is broader than the V-HEDTA2 (850 Hz) and the linebroadening for the tetramer (150 Hz) is slightly higher that those reported previously [57]. Because the t_1 (assumed to approximate T_2 when the vanadium is in the extreme narrowing limit) is inversely proportional to the linewidth and the lifetime of V-HEDTA1 is longer than the V-HEDTA2 and the ratio near π we conclude that the signals are not exchange broadened and the complexes are stable on the NMR timescale.

177

The HEDTA ligand contains three carboxylate groups, one hydroxyl group and two amine functionalities allowing for it to be able to form complexes with vanadium chelating in a 4, 5, 6, or 7 coordinate manner according to previous studies with a range of metal ions [39,52,59–61]. Combination of V(V) with HEDTA in aqueous solution at pD 7 presumably involves combination of the monomeric vanadate, HVO_4^{2-} and the trianionic form of HEDTA, shown in Fig. 3 (1). This complex is likely to contain a VO_2^+ unit, and one possible structure has previously been suggested (1) [41] and a second structure is shown (2). The β-cis motif has been characterized by X-ray for another polydentate amino-carboxylate ligand complex, the β-cis V-EDDA complex, and thus the geometry shown in structure (2) was considered.[40] We do not show the less likely isomer when the alkoxy group is bound trans to the oxo ligand because the trans effect of the oxo group would not stabilize a strong bond as those generally observed with coordinated alkoxy ligands [62]. The isomer shown for structure (2) will have the carboxylate group in the trans position and the alkoxy group bound in the equatorial plane (see Fig. 4).

To investigate the connectivity, ^{13}C NMR spectra were recorded in deuterium oxide. As shown in Fig. 3 at pD 10.14, V-HEDTA1 is the major V–HEDTA complex so the resonances observed can be attributed to free ligand (42.7% of total HEDTA) and V-HEDTA1 (57.3% of total HEDTA). The two partial ^{13}C NMR spectra are shown in Fig. 5a and b. The free ligand peaks are labeled as L_x on the spectra leaving total 8 signals belonging to the complex free ligand and 10 additional signals belonging to the complex V-HEDTA1. Chelation to the vanadium increases the chemical shift of the free ligand as reported previously for a number of vanadium complexes and referred to as the CIS (Coordination Induced Shift, CIS = $\delta_{bond} - \delta_{free}$) [41]. This is indicative of a strong bond to the vanadium. Three different carboxylate signals are shown, two of which are around 180 ppm in the partial spectrum shown in Fig. 5a and indicate that they represent free carboxylates. One carboxylate is coordinated to the vanadium at a chemical shift around 185 ppm, Fig. 5a. This leaves 7 signals to be observed for the rest of the complex, and these are all shown in the ^{13}C NMR spectrum in Fig. 5b. The alkoxide methylene group in the arm bound to the vanadium is readily identified at 75 ppm. The carboxylate arm bound to the vanadium is readily identified at 67 ppm, and the two free carboxylate arms and the CH_2 in the alkoxide arms are at 63, 63 and 55 ppm, respectively.

However, the ^{51}V NMR chemical shift is -492 ppm. This is very high for an EDTA-type complex that is found at –521 ppm. The

complexes that generally appear in the region of −490 ppm are $[VO_2DEA]^-$ and $[VO_2TEA]^-$ complexes that do not contain carboxylate coordination to the V-atom as well as complex $[VO_2bicine]^-$, although in the later case the five coordinate geometry is not firmly established [51]. A complex formed with N-(hydroxyethyl)-glycine was observed at −506 ppm suggesting that the hydroxyl group coordination will increase the chemical shift. Furthermore, studies of the $[VO_2EDDA]^-$ complexes showed that the meridional coordination of the α-cis complex gave a ^{51}V NMR chemical shift of −515 ppm and the facial coordination of the EDDA ligand in the β-cis complex resulted in a chemical shift of −505 ppm [39,40]. Thus, the coordination of the alkoxy group and in a facial β-cis manner could result in a chemical shift for the complex at higher resonance lending support to assignment of the −490 ppm V-HEDTA1 complex as structure (2). However, chemical shifts near −490 ppm have been reported for V(V) complexes with coordination of hydroxyl groups in ligands such as EDDE and EDTE and thus assuming that the complexes are six coordinate presumable a structure analogous to (1) will be observed at this chemical shift [41]. This conclusion is also supported by the smaller linewidth of the peak at −492 ppm compared to the complexes at −521 ppm indicating that the V-HEDTA1 has a more symmetric structure than the V-HEDTA2. Additional ^1H NMR spectra and HMQC spectra are shown in the supplemental materials confirming this assignment (Figs. S1–S4). We recorded solution IR spectra (Fig. S4) and these show the broadening of the V=O stretch supporting the interpretation that the structure of the V-HEDTA1 complex varies from the V-EDTA-type complex possible induced by the coordination of an alkoxy group or by a different coordination environment.

3.2. Multinuclear NMR studies of V-HEDTA2 complex at acidic pD

As the pH decreases, the amount of V-HEDTA1 decreases and instead a second complex V-HEDTA2 forms as shown in Fig. 3. In a solution of pH 7.74, 127 mM V-HEDTA2 formed, 18.9 mM V-HEDTA1 formed, and there was 3.42 mM of free ligand and vanadate. The second complex was investigated in a solution containing 150 mM HEDTA and 150 mM vanadate at pD values less than 7 where the solution exclusively contained the HEDTA2 complex. Combination of V(V) with HEDTA in aqueous solution at pD 7 presumably involves combination of $H_2VO_4^-$ and the dianionic form of HEDTA for form possible structures shown in Fig. 6. This complex is likely to contain a VO_2^+ unit, two possible structures have previously been referred to in the literature (3) [41] and (4) [63], and a third structure is shown (Fig. 6) (5–6).

In order to characterize the free carboxylate groups ^{13}C NMR spectra were recorded of the solution at pD 7.74 and the partial spectra are shown in Fig. 7. In Fig. 7a, the ^{13}C NMR signals of the carboxylic acid region show that two of the carboxylates are bound to the vanadium (signal between 180 and 184.5 ppm) and one is free. From the spectra of the additional part of the molecule (Fig. 7b), 7 signals were identified. The CH_2–OH arm and the CH_2–N signal next to it were found to be very broad. In addition, the CIS values were significantly less (6.5 ppm and 4.5 ppm) than observed for the V-HEDTA1 complex. These observations indicate that although some interaction may exist, this bond was not as strong as the bond formed in complex V-HEDTA1. We interpreted these two very broad signals, C_3 and C_4, to be due to a rapidly exchanging hydroxyl group on the timescale of the NMR experiments. The signals for the C_2 and $C_{2'}$ groups are shifted downfield (3.5 ppm and 3.1 ppm) and consistent with chelated sidearms. The $C_{2'}$ peak shifted the least and is assigned to a free arm. Based on analysis of the CIS values for the ^{13}C signals, we conclude that the structures similar to that reported previously [41], structure (3), but that the association of the free hydroxyl arm with
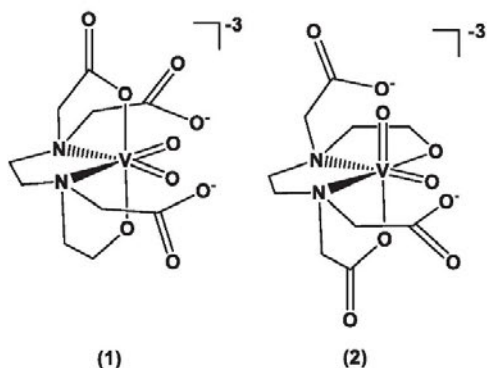

Fig. 4. Two possible structures for V-HEDTA1 are shown. Both structures involve chelation of the vanadium by two N-atoms, one carboxylate, an alkoxy group and two oxo group. The two unbound carboxylate groups are either α-cis (1) [41] or β-cis (2) to one another.
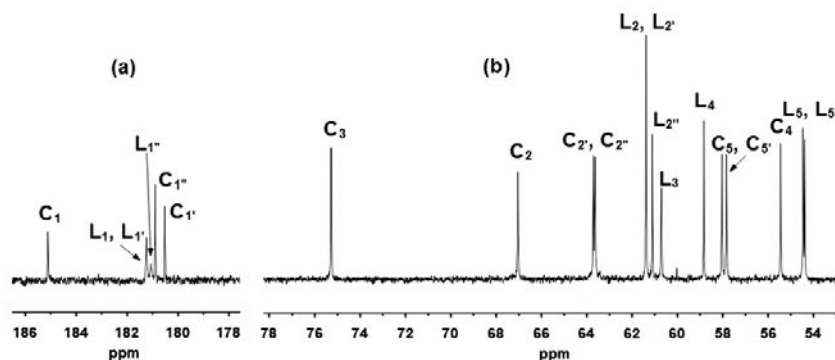
Fig. 5. Partial ^{13}C NMR spectra of a solution 150 mM vanadate and 150 mM HEDTA forming V–HEDTA, oxovanadates and free HEDTA at pD 10.14. The HEDTA carbon skeleton is labeled according to the numbering system shown in Fig. 1 using C_x for the complex and L_x for free ligand.
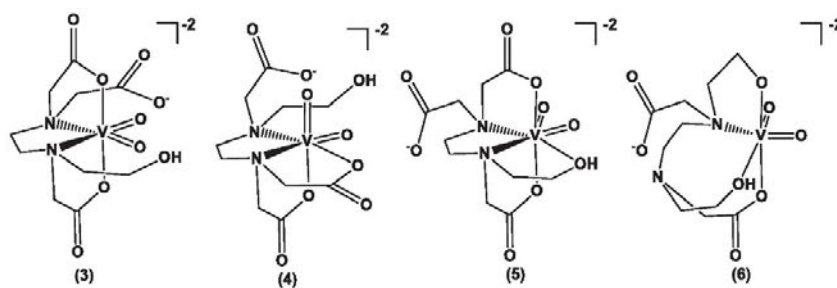
Fig. 6. Four potential structures for the V–HEDTA2 complex and a fourth structure contains a broken V–N bond. Structure (**3**) was suggested by Crans et al. [41] and (**4**) was considered by Sivák et al. [63]. Structure (**5**) and (**6**) were introduced here.
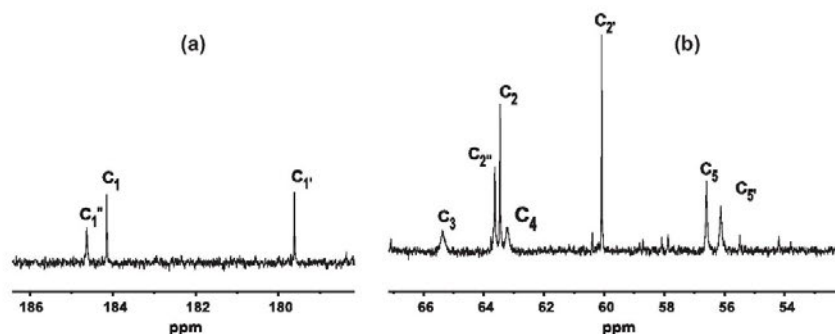
Fig. 7. Partial ^{13}C NMR of V–HEDTA solutions (150 mM HEDTA, 150 mM vanadate at pD 7.74). The C_x is labeled on HEDTA carbon skeleton as shown in Fig. 1.

the vanadium may render this complex seven coordinate (structure (**5**)) because the alkoxide group is loosely bound to the V-atom. Although seven coordinate complexes exist such a V(III)-EDTA complex (Fig. 2) and a protonated V(III)–HEDTA complex [31,52,59] the seven coordinate complexes will require significant distortion, as shown in structure (**5**). Alternatively, one can envision the signal broadening of the ligand being due to breaking and reformation of a V–N bond as shown in structure (**6**) (Fig. 6). This would be consistent with the fact that the V–N bonds are weak to start with because they are trans to the oxo groups.

Furthermore, the C-atoms coordinated to the N-groups are also broadened. This is evidence consistent with bond cleavage on the timescale of the experiment. Structure (**6**) illustrate the bond breaking of the N-hydroxyethyl group, which by the ^{13}C NMR is associated the least with the V-atom, however, the other V–N-bond could also be similarly broken (structure (**6′**) – not shown). All three interpretations (structures (**5**), (**6**) and (**6′**)) document the flexibility in the V-HEDTA2 complex under these conditions.

The structure represented in (**4**) is an intriguing structure, but not one that is consistent with the CIS shifted and broadened signal

for the alkoxy arm. The ^{51}V NMR chemical shift for the V-HEDTA2 is -521 ppm, which is identical to the value for the V–EDTA complex and very near the signals for the two V-EDDA complexes (-505 and -515 ppm). To better describe the association between the hydroxyl arm and the vanadium, structure (5) and (6) both are better representative for the V-HEDTA2 complex. However, considering that the former studies were done at much higher ionic strength than these studies, minor differences are to be expected. It is possible that the differences in spectral parameters are at least in part due to differences in the ionic strength and other conditions of the study [41]. We therefore recorded the HMBC spectrum (see Supplemental material Fig. S5). Specifically the protons in position 2″ are identified by their coupling to the protons in position 4. The chemical shift of the proton on C2″ and the ^{13}C chemical shift of this acetyl arm is complexed to the vanadium indicative of structure (3) or (6) but not structure (4). This allowed us to conclude that the observed spectrum is either that of structure (3) or (6) shown in Fig. 3.

3.3. Conversion among V-HEDTA1 and V-HEDTA2 complexes

Because the two V–HEDTA complexes have such different chemical shifts, some significant structural differences may exist and may be evident in the rate of complex formation and ligand exchange. A series of vanadium complexes have previously been characterized in detail with regard to structure and ligand interchange using ^{51}V NMR spectroscopy [51,57]. We similarly used EXSY spectroscopy to investigate whether conversion among the V–HEDTA complexes and oxovanadates were observable and whether the V-HEDTA1 and V-HEDTA2 exchange was sufficiently fast to be observed in this time regime.

Specifically a sample at pD 8.6 containing 150 mM HEDTA and 150 mM vanadate was subjected to an EXSY experiment and the result is shown in Fig. 8. The spectrum was recorded using an overall acquisition time of 15 ms with a mixing time of 2 ms. The diagonal of the spectrum shows all signals although the lower intensity of the V–HEDTA complexes is consistent with the faster relaxing complexes compared to the vanadate oligomers. Off-diagonal

signals between the oligomers are observed as reported previously [57]. However, no exchange is observed between the oxovanadate and either of the V–HEDTA complexes or between the complexes themselves. This experiment confirms that these complexes form on a longer time-scale than vanadate oligomerization reaction and other reactions.

The diagonal of the 2D EXSY spectrum shows a much smaller peak for V-HEDTA2 than shown in Fig. 3. This difference arose because of the parameters by which the EXSY spectrum was recorded. The V-HEDTA2 complex has a shorter relaxation time than the V-HEDTA1 and the added recording time decreases the signal for this species because some of the signal will already have partially relaxed by the time the spectrum will be recorded. This spectrum thus support the t_1 measurements documenting the faster relaxation time of V-HEDTA2 and the fact that these complexes are not exchange broadened.

3.4. Formation and Stability Constants for V-HEDTA1 and V-HEDTA2 complexes

The concentrations of various vanadate species are sensitive to pD, and consequently the reaction of vanadium and HEDTA is very sensitive to the pD. From the integration of the ^{51}V NMR spectra shown in Fig. 3, it was possible to calculate the V–HEDTA complex and the vanadium oligomers concentrations listed in Table 1. The formation of the complexes as a function of pD and the ratio of [V–HEDTA]/[V_1] calculated are listed in Table 1 as well. Because the concentration of V_1 is increasing, the change in the ratio is a combination of complex concentration and [V_1]. The [V–HEDTA1]/[V_1] ratio confirms that this is a complex that is more stable at the higher pD, because the ratio increases until pD 9.44 at which point it decreases. The decrease in the ratio is tied to the dramatic increase in [V_1]. In contrast, the [V–HEDTA2]/[V_1] ratio continues to decrease as the pH and the [V_1] concentration increase. With this information we can examine the reaction and estimate the equilibrium constant (K_{eq}) and the β under low ionic strength conditions.
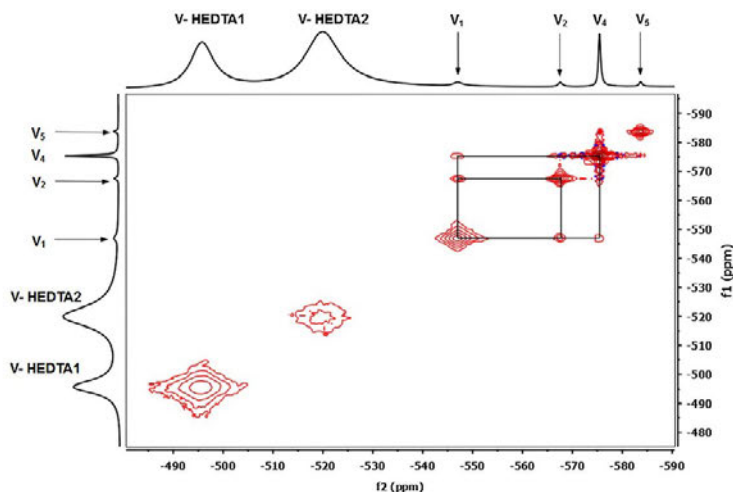
Fig. 8. 2D ^{15}V EXSY NMR spectroscopy were recorded at pD 8.55 of a solution containing 150 mM HEDTA and 150 mM sodium vanadate. The standard Agilent-NMR NOESY pulse sequence that uses States-TPPI encoding in t_1 was used to obtain pure phase spectra after a mixing time of 1.5 ms. A spectral window of 40 kHz was acquired in both the direct and indirect dimensions. Two hundred transients were acquired with an acquisition time in t_2 of 2 ms for each of the 200 complex t_1 increments. The total recycle time for each transient was about 40 ms. The data was apodized with a Gaussian function and zero-filled in both dimensions prior to Fourier transformation. The final digital resolution was 20 Hz/pt in both F2 and F1.

180

Table 1
Reaction between 150 mM HEDTA and 150 mM Vanadate in 100% D_2O.[a]

pD	[V-HEDTA1]	[V-HEDTA2]	[V-HEDTA$_{tot}$]	[V_1]	[V-HEDTA1]/[V_1]	[V-HEDTA2]/[V_1]	[V-HEDTA$_{tot}$]/[V_1]
6.97	5.57	143	150	0.290	19.2	493	512
7.59	14.1	134	148	0.515	27.3	261	288
8.06	26.7	119	146	0.905	29.5	131	161
8.55	86.1	55.0	141	1.63	52.8	34.0	86.6
9.44	98.9	21.5	120	8.48	11.7	2.50	14.2
10.1	77.5	3.35	80.9	38.6	2.01	0.087	2.10

[a] All concentrations are represented in mM.

The reaction forming V-HEDTA1 takes place in the pH range where HVO_4^{2-} formed (pH near and above 8) and $HEDTA^{2-}$ (between pH values 5.5 and 9.7) are major components. The equilibrium reactions thus can be described as shown in (1) or calculated in terms of the β using H_2VO_4 equivalents shown in (2). Where the $VO_2(HEDTA)^{3-}$ complex is described as the (1,1,0) species. The equilibrium constant and the $\beta(1,1,0)$ can be calculated and the average values are shown in (3) and (4) as pH independent values.

$$H_2HEDTA^{2-} + H_2VO_4 \rightleftharpoons VO_2(HEDTA)^{3-} + 2H_2O \quad (1)$$

$$rH_2HEDTA^{2-} + sH_2VO_4 + tH^+ \rightleftharpoons (H_2HEDTA^{2-})_r(H_2VO_4)_s(H^+)_t \quad (2)$$
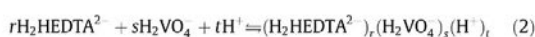
$$K_{eq,V-HEDTA1} = [VO_2(HEDTA)^{3-}]/[H_2VO_4^-][(H_2HEDTA)^{2-}] \quad (3)$$

$$\beta(r,s,t) = ((H_2HEDTA^{2-})_r(H_2VO_4)_s(H^+)_t) / [H_2HEDTA^{2-}]^r[H_2VO_4^-]^s[H^-]^t \quad (4)$$

and when

$$\beta(r,s,t) = \beta(1,1,0)$$
$$= ((H_2HEDTA^{2-})(H_2VO_4^-))/[H_2HEDTA^{2-}][H_2VO_4^-] \quad (5)$$

The reaction forming V-HEDTA2 takes place in the pH range before $H_2VO_4^-$ deprotonates (pD below 8) and $HEDTA^{2-}$ exists (below and near pH 5.5). This reaction is described in Eq. (6) and calculated in terms of the β using $H_2VO_4^-$ equivalents shown in (6) where the $VO_2(HEDTA)^{2-}$ complex is the (1,1,1) species. QUOTE $VO_2(HEDTA)^{2-}$ complex is the (r,s,t) species with (1,1,1). The equilibrium constant and the $\beta(1,1,1)$ QUOTE $\beta(1,1,1)$ are shown in Eqs. (8) and (9).

$$H_2HEDTA^{2-} + H_2VO_4^- \rightleftharpoons VO_2(HHEDTA)^{2-} + OH^- + H_2O \quad (6)$$

$$H_2HEDTA^{2-} + H_2VO_4^- + H^+ \rightleftharpoons (H_2HEDTA^{2-})(H_2VO_4^-)(H^+) \quad (7)$$

$$K_{eq,V-HEDTA2} = [VO_2(HHEDTA)^{2-}][OH^-]/[H_2VO_4^-][(H_2HEDTA)^{2-}] \quad (8)$$

$$\beta(1,1,1) = ((H_2HEDTA^{2-})(H_2VO_4^-(H^+))/[H_2HEDTA^{2-}][H_2VO_4^-][H^+] \quad (9)$$

The pK_a values for HEDTA and vanadate were previously determined under a range of conditions from 0.1 M KCl to 2.0 M [LiClO$_4$] [64]. The data shown in Table 1 was obtained in the absence of salts to mimic the environmental conditions with less salt. We chose to use the reported pK_a values for HEDTA reported by Chaberek [64] under ironic strength 0.1 conditions and the pK_a values for vanadate reported by Heath [37] in a solution of 2.0 mol dm^{-3} [LiClO$_4$] because their conditions were also at low ionic strength. Using the Henderson–Hasselbalch equation the concentrations of [H$_2$VO$_4^-$] or [HVO$_4^{2-}$] and [HEDTA^{2-}] or [HEDTA^{3-}] were calculated. The constants are listed in Table 2.

Table 2
The β constants and equilibrium constants calculated in this work.[a]

	log β	$-\log K_{eq}$
V-HEDTA1 ($\beta(1,1,0)$)	5	2
V-HEDTA2 ($\beta(1,1,1)$)	13	0.5

[a] The pK_a values for HEDTA 2.64, 5.33, and 9.73 was reported by Chaberek in 0.1 ionic strength using KCl [64]. The pK_a values for [H$_2$VO$_4^-$] and [HVO$_4^{2-}$] in 2.0 mol dm^{-3} [LiClO$_4$] were 7.1, and 12 as reported by Heath [37].

Corresponding value for the log β reported for the V-EDTA complexe is 18 documenting that both these V–HEDTA complexes are not as strong as the V-EDTA complex [65].

4. Conclusion

The HEDTA chelator is an alternative chelating agent replacing the less specific EDTA chelator for environmental and biological applications. In this work, we characterized two major complexes that formed with regard to structure and stability in aqueous solution. The vanadium atom forms a complex in which the HEDTA ligand coordinates in a tetradentate manner at high pH. The complex that forms at neutral pH has five functionalities associated with the vanadium and thus the HEDTA is pentacoordinate. The complexes begin to form at pH 3 and extend above pH 9 and thus combined encompass a significant part of the physiological pH range. However, the stability pattern for the two complexes are different and thus proper speciation considerations of this chelator should take into account the two complexes separately.

Appendix A. Supplementary data

Supplementary data associated with this article can be found, in the online version, at http://dx.doi.org/10.1016/j.poly.2016.01.001.

References

[1] D.K. Garner, S.B. Fitch, L.H. McAlexander, L.M. Bezold, A.M. Arif, L.M. Berreau, J. Am. Chem. Soc. 124 (2002) 9970.
[2] E. Szajna, P. Dobrowolski, A.L. Fuller, A.M. Arif, L.M. Berreau, Inorg. Chem. 43 (2004) 3988.
[3] T. Moriuchi, M. Yamaguchi, K. Kikushima, T. Hirao, Tetrahedron Lett. 48 (2007) 2667.
[4] M. Mahroof-Tahir, A.D. Keramidas, R.B. Goldfarb, O.P. Anderson, M.M. Miller, D. C. Crans, Inorg. Chem. 36 (1997) 1657.
[5] C. Drouza, M. Vlasiou, A.D. Keramidas, Dalton Trans. 42 (2013) (1840) 11831.
[6] M. Vlasiou, C. Drouza, T.A. Kabanos, A.D. Keramidas, J. Inorg. Biochem. 147 (2015) 39.
[7] V. Prachayasittikul, S. Prachayasittikul, S. Ruchirawat, V. Prachayasittikul, Drug Des. Dev. Ther. 7 (2013) 1157.

[8] H. Faneca, V.A. Figueiredo, I. Tomaz, G. Gonçalves, F. Avecilla, M.C. Pedroso de Lima, C.F.G.C. Geraldes, J.C. Pessoa, M.M.C.A. Castro, J. Inorg. Biochem. 103 (2009) 601.
[9] D.C. Crans, J. Org. Chem. 80 (2015) 11899.
[10] K.H. Thompson, J. Lichter, C. LeBel, M.C. Scaife, J.H. McNeill, C. Orvig, J. Inorg. Biochem. 103 (2009) 554.
[11] J.C. Pessoa, S. Etcheverry, D. Gambino, Coord. Chem. Rev. 301–302 (2015) 24.
[12] A. Zorzano, M. Palacín, L. Marti, S. García-Vicente, J. Inorg. Biochem. 103 (2009) 559.
[13] D. Rehder, G. Santoni, G.M. Licini, C. Schulzke, B. Meier, Coord. Chem. Rev. 237 (2003) 53.
[14] C. McLauchlan, J. Hooker, M. Jones, Z. Dymon, E. Backhus, B. Greiner, N. Dorner, M. Youkhana, L. Manus, J. Inorg. Biochem. 104 (2010) 274.
[15] J. Porath, J.A.N. Carlsson, I. Olsson, G. Belfrage, Nature 258 (1975) 598.
[16] J. Carrasco-Castilla, A.J. Hernández-Álvarez, C. Jiménez-Martínez, C. Jacinto-Hernández, M. Alaiz, J. Girón-Calle, J. Vioque, G. Dávila-Ortiz, Food Chem. 135 (2012) 1789.
[17] P.F. Bell, R.L. Chaney, J.S. Angle, Plant Soil 130 (1991) 51.
[18] T. Kiss, A. Odani, Bull. Chem. Soc. Jpn. 80 (2007) 1691.
[19] C.C. Mclauchlan, B.J. Peters, G.R. Willsky, D.C. Crans, Coord. Chem. Rev. 301–302 (2015) 163.
[20] T. Jakusch, J. Costa Pessoa, T. Kiss, Coord. Chem. Rev. 255 (2011) 2218–2226.
[21] E. Repo, J.K. Warchoł, A. Bhatnagar, M. Sillanpää, J. Colloid Interf. Sci. 358 (2011) 261.
[22] A. Naeem, P. Westerhoff, S. Mustafa, Water Res. 41 (2007) 1596.
[23] J.D. Ostergen, G.E. Brown, G.A. Parks, T.N. Tingle, Environ. Sci. Technol. 33 (1999) 1627.
[24] G. Chauhan, K.K. Pant, K.D.P. Nigam, Ind. Eng. Chem. Res. 52 (2013) 16724.
[25] F.G. Kari, W. Giger, Environ. Sci. Technol. 29 (1995) 2814.
[26] H. Xue, L. Sigg, F.G. Kari, Environ. Sci. Technol. 29 (1995) 59.
[27] T. Mizuta, J. Wang, K. Miyoshi, Inorg. Chim. Acta 230 (1995) 119.
[28] T. Mizuta, T. Yamamoto, K. Miyoshi, Y. Kushi, Inorg. Chim. Acta 175 (1990) 121.
[29] T. Mizuta, T. Yoshida, K. Miyoshi, Inorg. Chim. Acta 165 (1989) 65.
[30] H. Okazaki, K. Tomioka, H. Yoneda, Inorg. Chim. Acta 74 (1983) 169.
[31] K. Miyoshi, J. Wang, T. Mizuta, Inorg. Chim. Acta 228 (1995) 165.
[32] J.M. Wilson, R.F. Carbonaro, Environ. Chem. 8 (2011) 295.
[33] A.C.H. Durham, Cell Calcium 4 (1983) 33.
[34] P. Glentworth, B. Wiseall, C.L. Wright, A.J. Mahmood, J. Inorg. Nucl. Chem. 30 (1968) 967.
[35] P. Almendros, D. Gonzalez, J.M. Alvarez, Plant Soil 368 (2013) 251.
[36] D.C. Crans, J.J. Smee, E. Gaidamauskas, L. Yang, Chem. Rev. 104 (2004) 849.
[37] E. Heath, O.W. Howarth, J. Chem. Soc., Dalton Trans. (1981) 1105.
[38] D.C. Crans, K.A. Woll, K. Prusinskas, M.D. Johnson, E. Norkus, Inorg. Chem. 52 (2013) 12262.
[39] L.W. Amos, D.T. Sawyer, Inorg. Chem. 11 (1972) 2692.
[40] D.C. Crans, A.D. Keramidas, M. Mahroof-Tahir, O.P. Anderson, M.M. Miller, Inorg. Chem. 35 (1996) 3599.
[41] D.C. Crans, P.K. Shin, J. Am. Chem. Soc. 116 (1994) 1305.
[42] D.C. Crans, P.K. Shin, Inorg. Chem. 27 (1988) 1797.
[43] I. Correia, J. Costa Pessoa, M.T. Duarte, R.T. Henriques, M.F.M. Piedade, L.F. Veiros, T. Jakusch, T. Kiss, Á. Dörnyei, M. Castro, Chem. A Eur. J. 10 (2004) 2301–2317.
[44] M.R. Maurya, A.A. Khan, A. Azam, S. Ranjan, N. Mondal, A. Kumar, F. Avecilla, J. C. Pessoa, Dalton Trans. 39 (2010) 1345.
[45] J.-F. Jen, M.-H. Wu, T.C. Yang, Anal. Chim. Acta 339 (1997) 251.
[46] J.-F. Jen, S.-M. Yang, Anal. Chim. Acta 289 (1994) 97.
[47] M.A.M. Ameer, Mat. wiss. Werkstofftech. 34 (2003) 583.
[48] E. Alberico, G. Micera, D. Sanna, A. Dessì, Polyhedron 13 (1994) 1763.
[49] D. Crans, A. Keramidas, S. Amin, O. Anderson, S. Miller, J. Chem. Soc., Dalton Trans. (1997) 2799.
[50] J.C. Robles, Y. Matsuzaka, S. Inomata, M. Shimoi, W. Mori, H. Ogino, Inorg. Chem. 32 (1993) 13.
[51] D.C. Crans, P.M. Ehde, P.K. Shin, L. Pettersson, J. Am. Chem. Soc. 113 (1991) 3728.
[52] M. Shimoi, Y. Saito, H. Ogino, Chem. Lett. 18 (1989) 1675.
[53] Z. Chen, G. Owens, R. Naidu, Anal. Chim. Acta 585 (2007) 32.
[54] P.K. Glasoe, F.A. Long, J. Phys. Chem. 64 (1960) 188.
[55] H.N. Shankar, T. Ramasarma, Mol. Cell. Biochem. 129 (1993) 9.
[56] D.S. Wishart, C.G. Bigam, J. Yao, F. Abildgaard, H.J. Dyson, E. Oldfield, J.L. Markley, B.D. Sykes, J. Biomol. NMR 6 (1995) 135.
[57] D.C. Crans, C.D. Rithner, L.A. Theisen, J. Am. Chem. Soc. 112 (1990) 2901.
[58] S. Ramos, R.O. Duarte, J.J. Moura, M. Aureliano, Dalton Trans. (2009) 7985.
[59] M. Shimoi, Y. Saito, H. Ogino, Bull. Chem. Soc. Jpn. 64 (1991) 2629.
[60] K. Kanamori, K. Ino, K.I. Okamoto, Acta Crystallogr., Sect. C 53 (1997) 672.
[61] J.J. Smee, J.A. Epps, G. Teissedre, M. Maes, N. Harding, L. Yang, B. Baruah, S.M. Miller, O.P. Anderson, G.R. Willsky, Inorg. Chem. 46 (2007) 9827.
[62] G. Zampella, J.Y. Kravitz, C.E. Webster, P. Fantucci, M.B. Hall, H.A. Carlson, V.L. Pecoraro, L. De Gioia, Inorg. Chem. 43 (2004) 4127–4136.
[63] M. Sivák, M. Maďarová, J. Tatiersky, J. Marek, Eur. J. Inorg. Chem. 2003 (2003) 2075–2081.
[64] S. Chaberek, A.E. Martell, J. Am. Chem. Soc. 77 (1955) 1477.
[65] A. Ringbom, S. Sitonen, B. Skrifvars, Acta Chem. Scand. 11 (1957) 551.

Appendix XI: Does Anion-Cation Organization in Na⁺-Containing X-Ray Crystal Structures Relate to Solution Interactions in Inhomogeneous Nanoscale Environments: Sodium-Decavanadate in Solid State Materials, Minerals, and Microemulsions

This manuscript is published in *Coordination Chemistry Reviews* with Debbie C. Crans as the primary author. For this work, Craig C. Mclauchlan acquired most of the data and preparation of the crystallography sections, Xiao Wu assisted in the preparation of a couple tables within the manuscript, and Debbie C. Crans brought all the ideas together and wrote the reverse micelle section. Benjamin J. Peters prepared figures 8, 11, 16, and 17. Benjamin Peters also assisted with preparation of the reverse micelle section, finding and understanding the computational studies, and fine tuning the manuscript.[1]

Reference

(1)   Crans, D. C.; Peters, B. J.; Wu, X.; McLauchlan, C. C. Does Anion-Cation Organization in Na$^+$-Containing X-Ray Crystal Structures Relate to Solution Interactions in Inhomogeneous Nanoscale Environments: Sodium-Decavanadate in Solid State Materials, Minerals, and Microemulsions. *Coord. Chem. Rev.* **2017,** *344*, 115-130.

Review

Does anion-cation organization in Na⁺-containing X-ray crystal structures relate to solution interactions in inhomogeneous nanoscale environments: Sodium-decavanadate in solid state materials, minerals, and microemulsions

CrossMark

Debbie C. Crans [a,b,*], Benjamin J. Peters [a], Xiao Wu [a,c], Craig C. McLauchlan [c,*]

[a] Department of Chemistry, Colorado State University, Fort Collins, CO 80523, United States
[b] Cell and Molecular Biology Program, Colorado State University, Fort Collins, CO 80523, United States
[c] Department of Chemistry, Illinois State University, Campus Box 4160, Normal, IL 61790-4160, United States

ABSTRACT

Bonding is commonly examined in the solid state and determined by placement of atoms and molecules. Bonding in solution is equally important but much less accessible because these systems are more fluid and thus difficult to characterize the exact bonding motifs. This paper gleans information from the bonding in solid-state structures including more complex mineral systems with varying microenvironments to the bonding within inhomogeneous solutions at the nanoscale. The analysis for the solid state uses structurally well-described anion systems combined with a range of cations and their association in the solid state of both synthetic and naturally-occurring materials, minerals. Detailed solid-state structural information is available on the >180 decavanadate structures reported, however, because the structures will be compared with aqueous nanodroplets of dissolved decavanadate captured within reverse micelles, the abundant Na⁺ cations stabilizing the reverse micellar interface formed with anionic surfactant focuses the current comparison to Na⁺-containing materials. As a result the structures observed for the Na⁺-containing decavanadate materials led to identification of the Na⁺-containing subclusters and the information is used to provide information on the decavanadate in nanosized water droplets found when a decavanadate anion associating with an Na⁺ interface in a bis-2-ethylhexyl-sulfosuccinate (AOT) reverse micelles.

© 2017 Elsevier B.V. All rights reserved.

Contents

* Corresponding authors at: Department of Chemistry, Colorado State University, Fort Collins, CO 80523, United States (D.C. Crans).
  E-mail address: debbie.crans@colostate.edu (D.C. Crans).

1. Introduction and background

With the expansion of materials science, many materials with complex and elaborate combinations in their compositions are being discovered and produced. The increased components and complexities of these materials point to the increasing importance of microenvironments within complex structures and accompanying wide ranges of various types of bonding. The description of the materials and their bonding pattern is therefore becoming more and more important to understanding the systems detailed properties [1]. The concepts of bonding for materials are deeply nested in many areas of science and include not only chemistry, but also minerology and nanoscience [2–7]. Here we will focus on materials in which the microenvironments are critical for the properties of the system. For example, many decavanadate- ($V_{10}O_{28}^{6-}$, abbreviated V_{10}) types of minerals contain microenvironments with different types of structures, and within the material not only ionic or covalent bonds exist, but also a mixture of the two types of bonding [5,8–20]. Because the interactions between the V_{10} anion and its environment are important to the structures that form, specific interactions with cations are critical. In many studies, Na^+ is a counter ion for V_{10} and the surfactant used to form microemulsions and thus we are interested in investigating further the types of arrangements that Na^+ will form with the V_{10} anion. We will then proceed to demonstrate that the placement of V_{10} within various microenvironments in the solid state actually has similarities to the properties of V_{10} in the reverse micellar microenvironment of a nanodroplet.

The properties and bonding of V_{10}, a complex anion and a member of a family of polyoxometalates, will first be briefly reviewed. The structure of V_{10} reported initially by Evans [21] shows that the compound consists of ten vanadium-centered octahedra with oxygen atoms at each corner of the octahedra [21–25]. The ten octahedra are connected in a way that the structure is based on six octahedral units combined in a plane, and two octahedra above and two below the plane, see Fig. 1. Although alternative structures exist and are found in, for example decatungstate [26,27], the core structure of V_{10} has been demonstrated for about 180 different structures based on searches of the Cambridge Crystal Structure Database (CSD) [28] and International Crystal Structure Database (ICSD) [29]. A series of structural motifs/units between the V_{10} cores in local microenvironments have been reported and these will be described in detail below [1]. The specific bonding in the V_{10} structures varies and includes bonding a) between neighboring oxometalate cores and cations, b) through oxometalate cores and H-bonding, or, alternatively, c) both ionic bonding with cations and with different types of H-bonding to water [1]. By analysis of the solid-state structures we were able to identify structural patterns that can be used to describe the aqueous ionic bonding observed in nanodroplets of the oxometalate and the counter ions.

In nanoscience, the concept and understanding of microenvironments is critical for tuning the structures and the properties
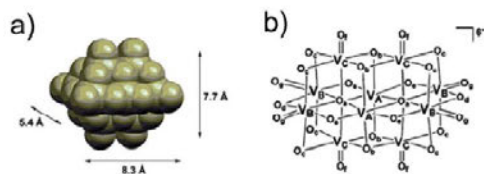
of the systems at hand [30]. Per definition a microenvironment is small and the environment does not extend but instead is adjacent to or incorporated in other environments. The specific structures that form upon combining a surfactant or a lipid with water and oil depend on the amounts of water, oil and surfactant/lipid. Various structures may spontaneously form including micelles, reverse micelles or liposomes [31–42]. The microenvironment existing in a water droplet within reverse micelles is surrounded by the surfactant, specifically for our interests bis-2-ethylhexyl-sulfosuccinate (AOT), and an organic solvent such as isooctane (2,2,4 trimethylpentane), cyclohexane, or benzene. The size of the reverse micelle (RM) is generally proportional with the ratio of $[H_2O]/[AOT]$ within the organic solvent and referred to as the w_o. In the case of the AOT reverse micelles in isooctane or cyclohexane the water droplets radius range from 2 to 15 nm [43,44]. The system is a dynamic system with the shape changing and water penetrating the interface. In AOT/RM systems much work has been done exploring the properties of the water pool, and characterization of this water compared to bulk water have shown that at small (2–4 nm-sized water droplets) much of the water present is associated with the interface [35,45,46].

In this work, we are examining a Na^+-AOT reverse micellar water pool, Na^+-containing V_{10} structures, in which one can approach the possibility of correlating structure in the solid state with the solution state found in the nanosized water droplet [47,48]. *We propose that in the small RMs the water may be structurally viewed and organized similarly to the clusters observed in the microenvironments in the solid-state, Na^+-containing V_{10}-structures and minerals. To investigate this hypotheses we compare Na^+-containing V_{10} within the microenvironments of solid state crystals and minerals with that of the nanosized-water droplet formed in a reverse micelle.*

2. Speciation

Oxometalate molecules are very sensitive to their environment so that a change in pH, ionic strength or concentration can cause a change in the composition and thus the structure [49–52]. Because of this sensitivity of these anionic species to their environments, both in the solid state and solution state detailed characterization are needed to fully appreciate the properties of the anion/material. The structural characterization of the complex anion, V_{10}, in the solid state provides data on the fundamental V_{10}-unit of the systems and has generally been the focus of many structural characterization of V_{10}-structures [1,12,21,22,24,52–69]. However, exploration of the detailed interactions between the V_{10} and the counter ions [1,24,66,68] are particularly important because they allow for categorization of these systems [1], and the interaction of V_{10} with counter ions and the H-bonding in the supramolecular network. After a brief definition of the concepts of speciation, we will describe the complex anions that form in solution from vanadate, VO_4^{3-}, the naturally occurring structures found in the mineralogy literature, and finally the speciation distribution that has been observed in solution in nanoclusters.

2.1. Speciation, concepts and nomenclature

The definition of species as described by IUPAC describes the composition and its distribution between the different chemical compositions (species) within a defined system [23,70–77]. Speciation analysis is the process generally carried out in aqueous solutions where molecules of the same atoms but different composition are considered different species [74,76,78,79].

$$pH^+ + qM + rL \rightleftharpoons [(H^+)_p(M)_q(L)_r] \qquad (1)$$

Fig. 1. Illustration of the structure of V_{10}, a) octahedral and b) $V_{10}O_{28}^{6-}$ [21–25]. Image modified with permission from Ref. [25].
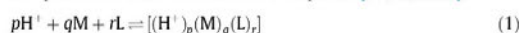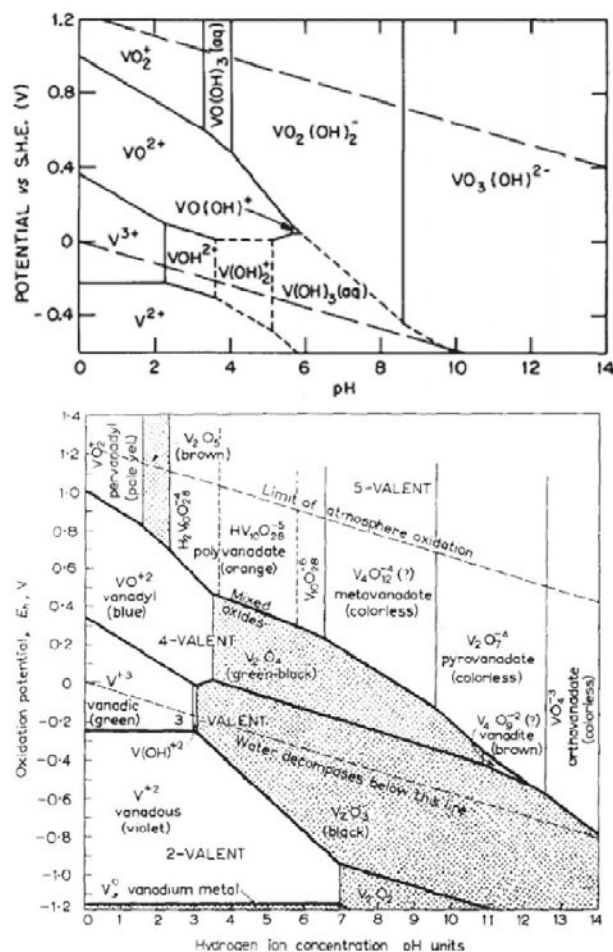
Fig. 2. a) Pourbaix diagram of vanadium as pH changes and b) a speciation program identifying the conditions for V$_{10}$ minerals. Reproduced with permission from a) Ref. [70] (copyright John Wiley and Sons) and b) Ref. [78].

$$(p \ q \ r) = \frac{[(H^+)_p(M)_q(L)_r]}{(H^+)^p(M)^q(L)^r} \qquad (2)$$

As shown in Eq. (1), varying amounts of three components, a proton (H$^+$), a metal ion (M) and a ligand coordinated to the M (L) will lead to a complex. In Eq. (2) the calculation of the formation constant for the species (p.q.r) is shown. Therefore, complexes that form, i.e. $[(H^+)_p(M)_q(L)_r]$ and $[(H^+)_{p'}(M)_q(L)_{r'}]$ are different species when (p,q,r) is different from (p',q',r'). The values for the constants p, q, and r for a complex are determined by a titration followed by the iterative calculation of the constants of the one species in the presence of others describing the entire system using computations in an iterative process [70,76,77,80–82].

The potentiometric studies are most effective when a large pH range is examined. Speciation studies result in a series of constants that describe the system and allow for the prediction of species

distribution diagrams showing the different vanadium species that exist at varying pH values and redox potentials. Examples of these are shown in Fig. 2 at two different vanadium concentrations. In Fig. 2a the overall concentration of vanadium is very low, M, resulting in a speciation diagram where the complexes (p,q,r) simplifies to (p,1,0) where p is the number of H$^+$ (the component of the system changing). It well known that the simple change in pH leads to various vanadium species [23,71,75,77,78,83]. However, the Pourbaix diagram shown in Fig. 2b reported by the mineralogists early on show distinction for speciation and formation of the higher oligomeric oxovanadates. Specifically, Fig. 2b show the conditions where orange V$_{10}$ forms and that the different protonated states of V$_{10}$ exist as well as the tetranuclear oxovanadates, Fig. 2b. It is important to recognize that at mM V-concentration oligomeric forms of vanadate are observed (*vide infra*, Section 2.4) [3,78].

2.2. Solid state bonding and structural organization of V_{10}

Bonding in the solid state is defined based on the placement of molecules in space [2,4,6,7]. Therefore as described by Shannon and Brown the interest of the scientific community has been focused on systems with bonding atoms in close proximity in space to form molecules [84–87]. Many of these types of systems have previously been described in detail and we refer the reader elsewhere for further discussion on the topic [85–88]. In the solid state V_{10} and Na^+ structures contain bonding that can be covalent, ionic or a combination thereof. However, in solution, these interactions are compounded by the ionic interactions in solution which are fluid where the ions are not fixed in space, although some time of organization may exist.

Specifically, the bond valence sums (BVS) technique is useful for describing the bonding geometry of metal ions in which the orbitals give several options for coordination geometry [84–87]. In such cases the number of electrons and the orbitals that are filled define the predicted geometries. These concepts have eloquently been described by Roald Hoffman and involve back-calculating the bonding to the central metal ion in the properly assigned coordination geometry [2,4,7].

Although there is a potential for a huge number of different oxometalate structures, certain repeat units and building blocks have been found to form, with the key units for oxovanadates being 1, 2, 4, 5, and 10 metal atoms for the smaller oxovanadates, although structures with 3 V-atoms have also been reported [71,76,89]. Focusing on the structure of V_{10}, the early X-ray structure solidified the base structure [8,21,22] illustrated in Fig. 1. The 10 V-atoms are combined to form a structure which now has been identified to form in at least 180 other X-ray structures. However, more recently, V_{10} was found to form isolated units and substructures as described as depending on the protonation state of the V_{10}. Duarte and co-workers examined the known V_{10} structures in 2003 and categorized the 59 known structures at the time [1]. That is, when the V_{10} is protonated the potential for H-bonding is greater, the H_xV_{10} can interact with each other in addition to interacting directly with water molecules, counter ions or both, a phenomenon long-recognized in the mineralogical community [5,9,90–92].

The polymeric oxovanadates or polyoxovanadates belong to classes of compounds characterized as materials forming a wealth of different clusters in which the V-atoms are surrounded by O-atoms in an octahedral arrangement [49–51,72]. The structural variety is further complicated by the fact that many clusters form with mixed M content and are then referred to as oxometalates and polyoxometalates (POMs). The potential exists for unlimited number of species ranging from mononuclear or dinuclear species to medium sizes of clusters with V_{10}, Keggin and Dawson structures and up to the giant molecules such as the polyoxomolybdates containing hundreds of M-ions [49–51].

An interesting case of the bonding relates to the protonation of V_{10} in the solid state. Although protonation of a heteroatom generally lengthens a bond, such changes are not always easily identified in the solid state, because the additional factors relating to the coordination geometry, molecular geometry, orbital overlap, and interactions in the crystal. However, factors such as stability of the compound, and the kinetics of exchange processes may also effect the bond lengths resulting in lengths that do not always reflect the increase anticipated by protonation. Because of the low electron density of a H-atom, it is not always possible to identify the location of protons without extensive spectroscopic studies. Evidence by ^{17}O NMR spectroscopy supports protonation of a triply bridging $_3$-O-atom in the V_{10} molecule in aqueous solution [93], whereas ^{51}V NMR spectroscopy data suggest protonation of the doubly bridged $_2$-O-atom [94]. A combination of X-ray and bond valence sum analysis support protonation of the terminal oxo group on some occasions as well [22].

Size and charge on cations are related to the number of water molecules and the hydration of the V_{10} anion in the solid state. This is discussed independently in the chemical literature [1,63,95,96], and mineralogical literature [5,9,90–92] by many groups [24,68,97]. Importantly mixed metal compounds, or amine-based cations in combination with metal ions gives many options to optimize the structures available. The potential for H-bonding further enriches the opportunities for formation of desirable solid state structures, and in Fig. 3a and b two different types of dimeric units created by different mode of H-bonding [1].

Classification described by Ferreira da Silva et al. [1] systematically describes the many possible interaction of V_{10} cores based on the three distinct faces of the cluster core and the protonation state. The reader is referred to that review for full details, but briefly the V_{10} core may be found in structures as discrete monomers (M), dimers (D), or extended structures that extend in 1-dimension (1-D), 2-dimensional (2-D), and 3-dimension (3-D) chains. Within the 2-D classification, Ferreira da Silva et al. further classified the V_{10} cores into sub-types based on interaction of the V_{10} core with just water (type a), just (counter)-cations (type c), or both water and cations (type b) [1]. With a more extensive survey of structures, here we extend those sub-types to the M, D, 1-D, and 3-D designations as well.

At this time a large number of different protonated systems exist and the formation of two different H-bonded V_{10} dimers has been highlighted with the V_{10} being doubly protonated (H_2V_{10}). They used Nakamura and Ozeki's formulation [98] of the two dimer arrangements (through H-bonding) as a) horizontal and b) vertical, Fig. 3. Structural arrangements suggest the formation of dimeric units within the material, and thus the potential for
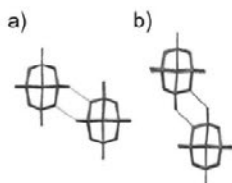

Fig. 3. Two different types of dimeric units created by different modes of H-bonding within the V_{10} structure: a) horizontal, b) vertical. Modified with permission from Ref. [1].
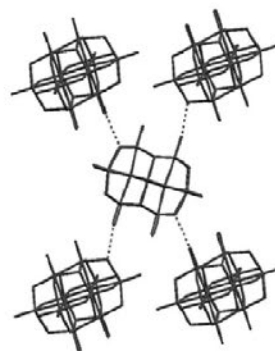

Fig. 4. H-bonded H_3V_{10} in a 1D/2D network. Reproduced with permission from Ref. [1].

Table 1
Minerals containing decavanadate ($V_{10}O_{28}^{6-}$) of the Pascoite Family.

		Reference
A. {$V_{10}O_{28}$}$^{6-}$ Decavanadates		
Huemulite	$Na_4Mg(V_{10}O_{28})\cdot24(H_2O)$	[14]
Hughesite	$Na_3Al(V_{10}O_{28})\cdot22(H_2O)$	[16]
Hummerite	$K_2Mg_2(V_{10}O_{28})\cdot16H_2O$	[9]
Kokinosite	$Na_2Ca_2(V_{10}O_{28})\cdot24H_2O$	[20]
Lasalite	$Na_2Mg_2(V_{10}O_{28})\cdot20H_2O$	[12]
Magnesiopascoite	$MgCa_2(V_{10}O_{28})\cdot16H_2O$	[11]
Pascoite	$Ca_3(V_{10}O_{28})\cdot17H_2O$	[8,10]
Postite	$MgAl_2(V_{10}O_{28})(OH)_2\cdot27H_2O$	[17]
Schindlerite	$Na_2(H_3O)_4(V_{10}O_{28})\cdot10H_2O$	[19]
Wernerbaurite	$Ca_2(H_3O)_2(V_{10}O_{28})\cdot16H_2O$	[19]
B. {$H_xV_{10}O_{28}$}$^{(6-x)-}$ Protonated Decavanadates		
Gunterite	$Na_4(H_2V_{10}O_{28})\cdot22H_2O$	[15]
Rakovanite	$Na_3(H_3V_{10}O_{28})\cdot15H_2O$	[13]
C. Mixed-Valence [($V_x^{4+}V_{10-x}^{5+})O_{28}$]$^{(6+x)-}$ Vanadylvanadate		
Nashite	$Na_3Ca_2[(V^{4+}V_9^{5+})O_{28}]\cdot24H_2O$	[18]

formation of extended structures when these units are combined through interactions with water or cations. Indeed, examples of such structures have been reported with 1-D and 2-D extended networks and the former is shown in the rubidium salt of $H_4V_{10}^{2-}$, Fig. 4 [1].

The potential for forming additional classes of materials was readily demonstrated by examining structures of triprotonated (H_3V_{10}) and tetraprotonated V_{10} (H_4V_{10}) and their extended networks. Diversifying the structures was demonstrated by the selection of the needed counter ion for charge balance and the interplay between the H-bonding with the protonated V_{10}, water and counter ion.

2.3. Speciation in solid state – Mineralogy

For more than 100 years geologists and mineralogists have worked on characterizing the solid state of minerals, including vanadium-containing minerals. A wide range of minerals contain vanadium [3] and as a result there is an extensive literature that describes the detailed structure of these minerals. Minerals containing V_{10} were first reported over 50 years ago by Evans [21,53,78,99], and others more recently [8,100], see Table 1 [13,15,17,19]. Increasing number of rocks are reported to be

associated with biomineralization processes [101,102] but the number of reports of new types of structures that contain the V_{10}-anion have not yet been associated with such processes. Were any clusters associated with such processes, it might provide clues on the formation mechanism of some V_{10} minerals.

The V_{10} minerals listed in Table 1 constitute examples that the solid-state V_{10} anions in geological deposits contain pockets of microenvironments. These minerals contains changing microenvironments depending on temperature, pH, and oxidation milieu as shown in the Pourbaix diagram for a V-Ca system Fig. 5a and b. These solid state structures demonstrate that in some sense "speciation" is observed in the V_{10}-containing minerals. These naturally occurring microenvironments may facilitate the formation of one mineral species over another, despite being located geographically in the same proximity. Fig. 5a shows the effect that local conditions such as pH and temperature can have on major species in vanadium mineral formation. Not surprisingly, the Pourbaix diagrams shown previously in Fig. 2 are also available for minerals, Fig. 5b. The geochemistry of these minerals is very interesting as it likely involved reduction over time of pre-existing minerals [103].

Examination of the microenvironments in mineralogy offers an insight to the chemistry of V_{10} in such microenvironments with examination of the Pascoite family of minerals, Table 1 [20], so naturally-occurring V_{10} species will reside in the mineral where they were originally formed. The V_{10} species remain there until water reaches the rock, and assists the dissolution of the V_{10}. The properties of the synthetic materials created in the laboratory show some analogy with the naturally-occurring V_{10}-containing minerals.

Both simple and complex minerals have the same coordination environments for metal centers and local ions, typically, but how they are stacked together determines the composition [5,6,9,90–92]. The same remains true for V_{10}-containing structures. Extended structures and interactions of decavanadate with water, cations, and V_{10} itself has been investigated [1,65,98]. These arrangements in 3-dimensions have implications in mineralogy and chemistry, but there are also extensions to possible crystal engineering [104]. The ability to predict what structures will be (most) stable in the solid state is valuable to each of those fields, and efforts have been made on that front with V_{10} species as well.

Bond valence sums (BVS) have long been used in solid structures to examine and predict stable structures in geology [5,6,9,85–88,90–92]. Hawthorne used the ability of BVS to predict stable
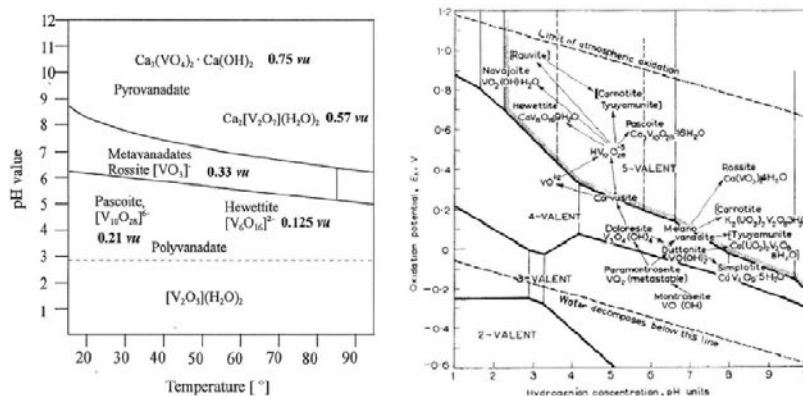

Fig. 5. Left: Effect of temperature and pH on stable vanadate mineral formation. Right: Effect of oxidation potential and pH on stable vanadate mineral formation. Ref. [78] Reproduced with permission from Refs. [5,78], respectively.
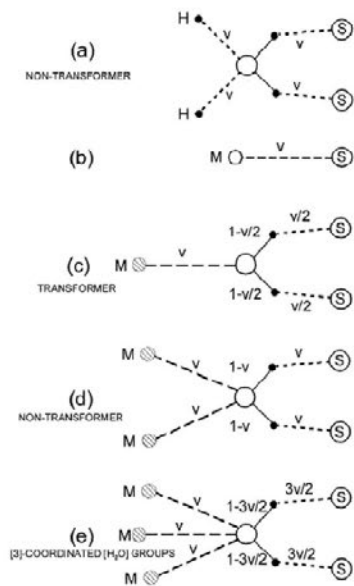
Fig. 6. The coordination geometries of metal ions (depicted by M) to water molecules (depicted by a circle) and then to the mineral (depicted by S). The water is coordinating directly to the mineral; a) direct coordination between the metal ion and coordinating water; b) one metal ion is coordinated to the water molecule that is H-bonding through two sites to the mineral; c) two metal ions are coordination to a water molecule that is H-bonded to the mineral through two sites; d) two metal ions are coordinated to a water molecule that is H-bonded to the mineral through two sites; e) three metal ions are coordinated to a water molecule that is H-bonded to the mineral through two sites. Adapted with permission from Ref. [6].

geological structures and highlighted the role of water in the process [90,91]. Fig. 6 demonstrates how water can coordinate to metal ions in hypothetical geometric arrangements and thus how water directly or indirectly impacts the cation-anion interactions. Specifically, in Fig. 6a the water is coordinating directly to the metal, in Fig. 6b there is direct coordination between the metal ion and coordinating water, in Fig. 6c one metal ion is coordinated to the water molecules that is H-bonding though two sites to the metal. In Fig. 6d and e two or three metal ions are coordinated to a water molecule that is H-bonded to the mineral through two

sites. As a result water molecule(s) are likely to modulate the charge on the metal cation and anion both depending on the details in the relationship between the cation and anion, and effectively lowering the valence charge felt by a given cation on a given anion (Fig. 6c and e). In contrast such effects are not observed in bonding arrangement shown in Fig. 6a and d. The water, then, may act as a mediator between the cation and anion with or without lowering the valence charge felt. Hawthorne was able to predict whether structures would be stable, effectively using Pauling's principles of electroneutrality, and by predicting how many water molecules would be necessary to allow a stable structure of certain cations and anions [6].

The nature of the bonding between V_{10} and a range of cations was explored using the approach by Hughes and the many V_{10} structures reported previously [10]. A plot of the number of waters per cation vs anions per bond originating ("emanating") from cation (to normalize the data) was generated for a series of known V_{10} species, including natural minerals and is shown in Fig. 7a. The correlation is high and may even be higher because the exact location of the protons on some of the structures may change after reevaluation using the modern techniques currently available. As noted by Hughes, this type of correlation only works for a given system and connectivity [10]. If one considers the V_{10} core, there are 22 bond valence acceptor oxygen atoms emanating from outside the core that can engage in such interactions with cations [10]. Regardless, the calculations still employ 28 as the number of "anions" in these calculations to normalize the results on the x axis. For the data shown, we have retained the 28 anion convention. For cations, this system neglects the two vanadium atoms in the V_{10} core (referred to as the "structural unit" of Hawthorne [90]) and only focuses on the cations outside of the central anion (the "interstitial" portion of the system [90]). The calculations work best for simple cations that can actually interact directly with water. However, the calculations do not hold well for ammine/ammonium-containing cations, which are incapable of directly interacting with water in the same coordination geometry (data not shown). We refer the reader to [10] for further details. The number of cations per anion in the formula unit is however, easily measured, and the number of bonds emanating from a cation is fairly consistent for a given cation. Therefore, this analysis can be used to estimate the bonding arrangement for unknown structures or simply counted for known structures. The correlation allows one to predict the number of water molecules that need to be present for a given number of cations of a given valence (or charge). As shown in Fig. 7a the majority of structures have less than 6 H_2O molecules for each anion, although some of the newer materials reported seem to deviate significantly from this graph.
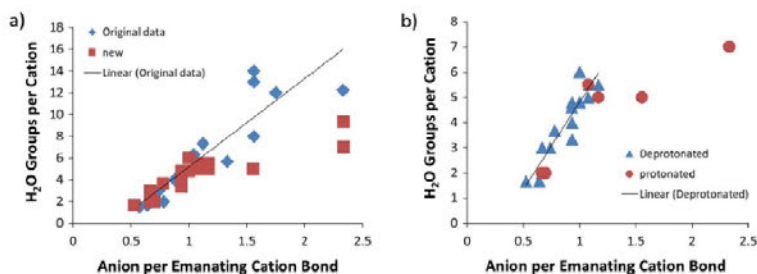

Fig. 7. The number of waters is plotted per cation in a structure vs. number of anions per bond emanating from cation a) reported by Ref. [10] with Hughes' original data (◆) along with inclusion of newer mineral structures (■); b) the same plot selecting only sodium-containing structures for both deprotonated V_{10} (▲) and protonated V_{10} species (●).

It is clear from Fig. 7b that the majority of the sodium-containing species correlate well. There are only few protonated species, but the deviation among these are on an average greater than the deprotonated species, showing in most cases a distinct and clear difference in the protonated species. The largest outliers are the naturally occurring minerals schindlerite ($Na_2[H_3O]_4[V_{10}O_{28}]\cdot10H_2O$) and rakovanite ($Na_3[H_3V_{10}O_{28}]\cdot15H_2O$). Interestingly, the authors describing these minerals suggested that the protons are on the surrounding water or V_{10} core, respectively.

2.4. Speciation in aqueous solution

Ionic bonding is generally found in solid-state structures of oxometalates, but as the material is dissolved in bulk solution the cation dissociates in solution and is separated from the anion [73,105]. Solution studies can be done to investigate the nature of the species in solution [51,106,107]. Depending on the techniques used the studies will be exploring coordination geometry and potential ligand coordination examining how many species are in solution, and their structure [73,96,105]. The possibility that the compound is the same that it was in the solid state can be determined [80,108]. The similarity in structure between solution and solid state is often assumed by chemists even though there is more flexibility for bonding in the solution state. However, in the case of vanadium compounds in solution the rates of conversion are often fast and thus the compounds will change upon dissolution [82,109]. That is, several species will form in solution and the species in solution are not simply the forms that have been observed in the solid state. Regardless of the compounds being investigated, any such characterization must address the specific speciation.

Vanadate readily dissolves to form the colorless oxovanadates that exchange with each other forming the mononuclear, dinuclear, tetranuclear and pentanuclear species [35,77]. However, these species stand in sharp contrast to the yellow V_{10} structure that forms at pH between 2 and 6.5 as the thermodynamically most favorable species as long as the concentration is high [35]. Although not often appreciated by life scientists when working with vanadate solutions, the speciation is critical and understanding of pH and temperature on these equilibria are sometimes not conducive to the standard method of preparing a vanadate solution, for instance, an enzymology assay [110]. As shown in Fig. 8 the color change is very dramatic and indicative of the change in the V-geometry and the spectroscopic properties of the V-atom. The formation constants that describe these reactions are pH dependent, but at very low concentrations the presence of V_{10} becomes less favorable, and it is no longer observable at sub-micromolar concentrations in bulk aqueous solutions [23,70,71,111,112].

Fig. 9. The ^{51}V NMR spectrum of the V_{10} anion. Three signals, V_A, V_B and V_C, represent the different types of signals present that exist in the anion. Two of these signals report on changes in pH.
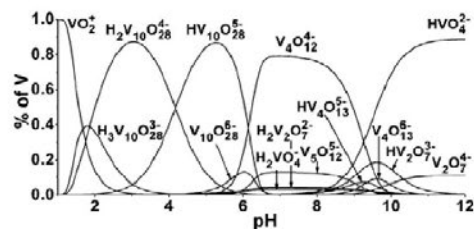
Fig. 10. Aqueous solution species distribution of V(V) as a function of pH at 0.200 M. Reproduced with the permission of the American Chemical Society from Ref. [36].

The V_{10} can also be spectroscopically monitored using ^{51}V NMR spectroscopy [35,47], which is extremely sensitive to chemical environment, including protonation state [113–115]. In Fig. 9 the spectrum for V_{10} is shown. Three different signals are observed: the V_A, the non-oxovanadium in the center of the V_{10}, and the V_B and V_C vanadium atoms are the surface V—O atoms [47,48,116]. The charge on V_{10} can be from 3– to 6– at acidic pH values. The latter equilibria are expressed in Eq. (3)–(5) in aqueous solutions [23,71,83,112].

$$HV_{10}O_{28}^{5-} \rightleftharpoons V_{10}O_{28}^{6-} + H^+ \qquad pKa = 5\,5 - 6\,0 \qquad (3)$$

$$H_2V_{10}O_{28}^{4-} \rightleftharpoons HV_{10}O_{28}^{5-} + H^+ \qquad pKa = 3\,1 - 3\,7 \qquad (4)$$

$$H_3V_{10}O_{28}^{3-} \rightleftharpoons H_2V_{10}O_{28}^{4-} + H^+ \qquad pKa \approx 2 \qquad (5)$$
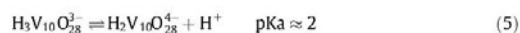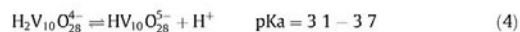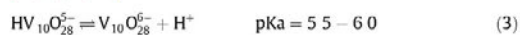
In summary, perhaps more so than in other systems readers may know, the stability of V_{10} in solution depends on the specific species and the conditions of the solution. That is the specific pH, the concentration of the species, the ionic strength and other physical parameters all define the system. In Fig. 10 we illustrate
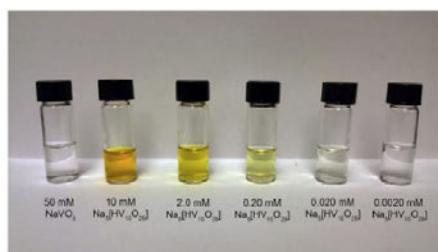

Fig. 8. Solutions of V(V). Starting from the left is colorless sodium vanadate (pH 8.2) going to varying concentrations of sodium V_{10} (pH 5.0).
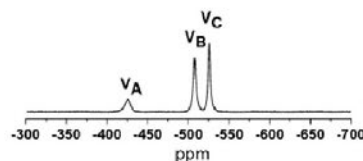

Fig. 11. General representation of a (a) liposome, (b) micelle, and a (c) reverse micelle.

191

a speciation diagram, and it is readily seen that several protonated forms of V_{10} are observed, but that at low pH only the VO^{2+} is predicted to form, and at high pH the labile vanadates are predicted to form.

3. Aqueous nanoenvironments created in microemulsions and reverse micelles

Chemistry at the nanoscale often is not like the chemistry found in bulk. The reactions and the solvent may be the same but the confinement modify the chemistry leading to important differences [31–42]. Systems in which confined chemistry offer advantages can take place are gaining increased interest, because the scientific community is recognizing that possibilities for unique and specific reactivities exist. A range of colloidal systems with membrane-like interfaces have been described with properties depending on the specific nature of the surfactant, water, and the hydrophobic solvent. Fig. 11 depicts a few of the possible structures that may form including liposomes (Fig. 11a), micelles (Fig. 11b), and reverse micelles (Fig. 11c) [31–42].

Reverse micelles are self-assembled nanosized structures in which a nanosized water pool exists (Fig 11c) [43,44]. Reverse micelles (RMs) generally form in the region of low water content and high concentrations of surfactant and organic solvent (see section 4.3 and 4.4). In systems such as AOT reverse micelles in organic solvents, much work has been done exploring the nature of the water pool, characterization of this water, numerous applications of reverse micelles to enhance chemical and enzyme reactivity, and for use in many model studies [35,45,46].

Characterization of the systems has been done using multiple methods and extensive work by a range of different approaches focuses on the system as well as on the reactivity of a p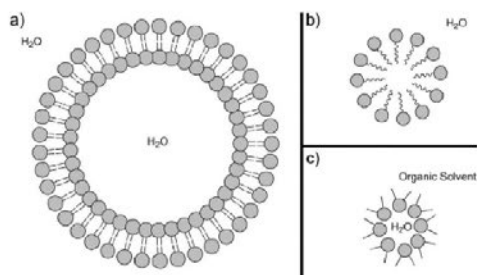articular material when added to these colloidal systems. A wide range of properties are found depending on the nature of the system. For example, in the case of AOT isooctane reverse micelles the system becomes a convenient tool that can be used by even a non-expert. Even so, for studies using these dynamic nanosized water droplets some characterization is critical in order to be able to analyze the forthcoming result properly [47,48]. Measure of the size of this water pool should routinely be done and can conveniently be obtained using dynamic light scattering for RMs. Some examples of such data also including studies with V_{10} are summarized in Table 2 [48,96]. The data listed in Table 2 include the hydrodynamic radius (r_h), water pool radius (r_w), aggregation number (number of AOT molecules per reverse micelle, $_{agg}$), the H_2O per reverse micelle, and similar values in the presence of V_{10} within the reverse micelles where appropriate. The calculated amount of water per reverse micelle was estimated by dividing the volume of the water pool by the volume of a water molecule. The number

of V_{10} molecules per reverse micelle was calculated here from the data given by Sanchez-Lombardo [96].

In water droplets with diameters of 2–4 nm the water molecules are associated with the interface causing a reduction in the fluidity of the water molecules [117]. Many studies have been done characterizing the nature of the water pool. Generally two different types of water molecules are described, the bulk and the interfacial layer [117]. The interfacial layer is referred to as the Stern layer [117]. This layer is 2–3 waters thick and adjacent to the interface [48,96]. Although it is generally recognized that the Na^+ will associate with the interface, accurate calculations of the amounts of H_2O molecules in the water-layer should also include consideration of the Na^+ ions in the interface. However, the dynamic nature of these systems and the movement of the cations makes such considerations less trivial, and thus was not included in the numbers shown in Table 2.

4. Exploring structural organization of systems involving sodium (Na^+)

The bonding between the V_{10} anion and its environment is important to the specific structures that form. Because here we are considering the nanosized water droplets within AOT-oil-water types of systems and Na^+ is the counter ion of AOT [31–42], we are particularly interested in the interactions of Na^+ with V_{10}. Undoubtedly the Na^+ ion is intricately involved in the interaction with the water droplet interface with the surfactant, and we are likely to benefit from further characterizing the types of arrangements that Na^+ will form with the V_{10} anion in various types of microenvironments. In the following section we will explore the solid-state interactions of Na^+ with V_{10}, and the interactions of Na^+ within the nanodroplets in reverse micellar microemulsions.

4.1. V_{10} X-ray structures containing Na^+

To understand the interactions of Na^+ with V_{10} in the solid state, we examined the previously reported Na^+-containing structures from the over 180 known V_{10} crystal structures. The solid-state X-ray structures of the previous sodium-(Na^+-)containing V_{10} are listed in Table 3. The reported structures include V_{10} structures both with and without direct bonding to other V_{10} anions as previously categorized by da Silva [1]. Beyond $V_{10}\cdots V_{10}$ interactions (illustrated here through hydrogen bonding in Figs. 3 and 4), there are also other more ionic interactions, namely interactions of the V_{10} anion directly with water, directly with the cation, or directly with both water and the cation. Protonation states are as indicated in the published works where available, but it is established that assignment of protonation in the solid-state is difficult and relies

Table 2

AOT/isooctane reverse micellar (RM) parameters for w_o systems ranging from 4 to 30. The measurements were done with ^1H NMR spectroscopy and dynamic light scattering (DLS) with and without V_{10} present.

w_o	r_h (nm)	r_w (nm)	$_{agg}$	Calculated amounts of H_2O per RM (V/V)	r_h (nm)	r_h (nm) V_{10}	r_h (nm) monomolybdenum nonavanadate	V_{10} per RM
4	2.5	1.0	35	140				
6	2.8	1.4	50	380	3.1	3.6	3.8	0.2
8	3.2	1.6	72	570	3.4	3.7	4.5	0.3
10	3.4	1.9	98	960		4.4		0.3
12	3.7	2.2	129	1500	3.8	4.6	4.9	0.5
16	4.2	2.9	215	3400				
20	4.4	3.5	302	6000	5.0	5.0	5.0	1.1
25	5.2	4.3	447	11,000				
30	6.2	5.1	613	19,000				
Ref.	[43]	[43]	[43]		[96]	[96]	[96]	

Table 3

A list of properties of sodium ion (Na^+) containing V_{10} structures including formula, protonation state represented by number of protons, database where structure is deposited, code,[a] specific Na^+ arrangement, classification (M, D, 1-D, 2-D(a,b,c))[b,c] and the literature sources.

Formula	H_xV_{10}	Database[a]	Code/PDF #	Na arrange	Classification[b]	Ref
$[Na_2(H_2O)_8]_2H_2[V_{10}O_{28}]\cdot4H_2O$	2	ICSD	01-080-8939	$(Na_2O_{w8}O_{c2})$	M, 2-D zigzag, b	[120]
$Na_6(H_2O)_{21}[V_{10}O_{28}]\cdot4H_2O$	0	ICSD	01-076-4274	$(Na_2O_{w8})_x$; $Na(O_w)_4(O_c)_2$	3-D	[62]
$Na_{5.22}Li_{0.78}[V_{10}O_{28}]\cdot20H_2O$	0	ICSD	01-073-3695	$Na_3O_{14} = Na(O_w)_6$, and $Na(O_w)_4(O_c)_2$	M, 2-D, b	[121]
$\{[Na(H_2O)_4]_6[V_{10}O_{28}]\cdot2H_2O\}_n$	0	X	X	$Na_2(O_w)_8(O_c)_2$	M, 2-D, b	[64]
$Na_2[V_4^{IV}V_2^{V}\{(OCH_2)_3CCH_2CH_3\}_4]$	0	CCSD	SUJNAM	$Na(O_c)_3$	M, 3-D, c	[122]
$CuNa_4V_{10}O_{28}\cdot23H_2O$	0	ICSD	01-072-3605	Infinite Chains of $[Na(O_w)^c(\ -O_w)_2Cu(O_w)_2(\ -O_w)_2$ $Na(O_w)_2(\ -O_{w2})Na(O_w)_2(\ -O_{w2})]_\infty$ and $NaO_{w5}O_c$	M, 3-D, b	[57]
$K_4Na[HV_{10}O_{28}]\cdot10H_2O$	1	ICSD	01-072-3864	Mostly K: NaO_6	M, 1-D	[60]
$(C_6H_{13}N_4)_2Na_2[H_2V_{10}O_{28}]\cdot8H_2O$	2	CCSD	COFGOT	Na2 between clusters and water	M, 2-D, a	[123]
$(H_3NCH_2CH_2NH_3)_2\ [Na_2(H_2O)_{10}]$ $[V_{10}O_{28}]$	0	CCSD	MAJKUE	$[Na_2(O_w)_{10}]^{2+}$	M, 3-D, b	[61]
$K_4Na_2[V_{10}O_{28}]\cdot10H_2O$	0	ICSD	01-073-3662	$[Na_2(O_w)_{10}]^{2+}$	M, 3-D, b	[119]
$K_4Na_2[V_{10}O_{28}]\cdot10H_2O$	0	ICSD	01-072-3633	Extended chains of cations with water. Mostly K	M, 3-D, b	[58]
$Na_3[V_{10}O_{28}]$ $(C_4N_3OH_5)_3(C_4N_3OH_6)_3\cdot10H_2O$	0	X	X	$Na(O_c)(O_w)_5(O_{cyt})$	M, 3-D, b	[63]
$Na_4(Me_4N)_2[V_{10}O_{28}]\cdot20\ H_2O$	0	CCSD	PIQSUD	3 unique $NaO_{w5}O_c$	M, 3-D, b	[124]
$(NH_4)_4Na_2[V_{10}O_{28}]\cdot10H_2O$	0	ICSD	01-070-4736	$[Na_2(O_w)_{10}]^{2+}$	M, 3-D, b	[55,125]
$Na_4Ni[V_{10}O_{28}]\cdot23H_2O$	0	X	X	Infinite Chains of $[Na(O_w)_2(\ -O_w)_2Na(O_w)_2(O_c)_2(\ -O_w)_2$ $Na(O_w)_2]_\infty$	M, 3-D, b	[126]
$[Ni(H_2O)_6]_2[Na(H_2O)_2]_2[V_{10}O_{28}]\cdot$ $4H_2O$	0	X	X	$\{[Na(H_2O)_3][Ni(H_2O)_6][Na(H_2O)_3]\}^{4+}$	M, 1-D, b	[56]
Minerals						
$MgNa_4(V_{10}O_{28})\cdot24(H_2O)$	0	X	X	$Na_2(OH_2)_{14}$ in zigzag chain (to inf); MgO_{w6}	M, 3-D, b	[14]
$AlNa_3(V_{10}O_{28})\cdot22(H_2O)$	0	ICSD	01-080-6038; 00-063-0350	$Na_3(OH_2)_{12}O_2$ trimer	M, X-D, a	[16]
$Mg_2Na_2(V_{10}O_{28})\cdot20H_2O$	0	ICSD	01-077-8157	$[Na_2O_4(OH_2)_6]$	M, X-D, b	[12]
$Na_2(H_3O)_4(V_{10}O_{28})\cdot10H_2O$	4	X	X	$[Na_2(H_2O)_{10}]$ dimer that is linked to four hydronium ions by hydrogen bonding	M, 2-D, a	[19]
$Na_4(H_2V_{10}O_{28})\cdot22H_2O$	2	X	X	$NaO_2(H_2O)_2$; $Na(O_w)_5O_c$	M, X-D, b	[15]
$Na_3(H_3V_{10}O_{28})\cdot15H_2O$	3	ICSD	01-080-3923	$NaO_{c4}O_{w2}$; $Na_2(O_w)10$	M, X-D, b	[13,127]
$Na_6[V_{10}O_{28}]\cdot18\ H_2O$	0	ICSD	01-071-1907	$Na_6(H_2O)_9$ stitching together	M	[54]
$Mg_2Na_2[V_{10}O_{28}]\cdot20H_2O$	0	ICSD	01-073-9313	Na bridging V_{10} unit with 3 waters.	M, 3-D, b	[59]
$MgNa_4[V_{10}O_{28}]\cdot23H_2O$	0	X	X	Chains: $NaO_{w4}O_{c2}$; NaO_{w6} with Mg	M, 2-D, b	[128]
$Rb_3[Na(H_2O)_8][HV_{10}O_{28}]\cdot4H_2O$	1	X	X	$Na(O_w)_6$, $RbO_{c5}O_{w4}$	1-D zigzag, b	[129]
$Ca_2Na_2[V_{10}O_{28}]\cdot24H_2O$	0	X	X	$[Na_2(O_w)_{10}]^{2+}$; corner-share to CaO_{w8}	M, 3-D, a	[20]
$Ca_2Na_3[(V^{4+}V_9^{5+})_{10}O_{28}]\cdot24H_2O$	0	X	X	$[Na_3Ca_2(OH_2)_{22}\cdot2H_2O]^{7+}$	M, 3-D, b	[18]
$[Na_6(H_2O)_{20}][V_{10}O_{28}]\cdot4H_2O$	0	ICSD	01-079-1787	$[Na_3(H_2O)_{10}]^{3+}$	3-D	[62]
$K_2Na_4[V_{10}O_{28}]\cdot18H_2O$	0	X	X	4 clusters of 4 NaO_{w6} KO_3	M, 3-D, b	[130]
$[Na_3(H_2O)_9]_{2n}[V_{10}O_{28}]_n$	0	X	X		Polymer	[131]
$[(C_6H_{13}N_4)_2[Na(H_2O)_8]_2]$ $[H_2V_{10}O_{28}]\cdot6H_2O$	2	CCSD	VOPLUJ	$Na(O_w)_6$	M, 2-D, a	[131]
$(HN(CH_2CH_2)_3NH)_2(Na(H_2O)_2)_2$ $(HV_{10}O_{28})\cdot2H_2O$	1	CCSD	WEZREZ	$Na(O_w)_2(O_c)_4$	M, 3-D, b	[132]
$(C_2H_{10}N_2)_5Na_2[V_{10}O_{28}]_2\cdot10\ H_2O$	0	CCSD	XISGUB	Na in space. Likely H-bond to O_w and O_c	M, 3-D, b	[133]
$Cs_4[V_{10}O_{28}]\cdot10H_2O$	0	X	X	$[Na_2(O_w)_{10}]^{2+}$, Cs^+ to cluster	M, 3-D, b	[134]
$(C_7H_{16}NO_3)_2[Na_4(H_2O)_{16}[V_{10}O_{28}]\cdot$ MeOH	0	CCSD	MOSKIQ	$Na_4(H_2O)_{16}(O_c)_2$ chain/tetramer	M, 3-D, b	[69]
$(C_4H_{10}N)_4Na_4[H_6Mo_6NiO_{24}]$ $[V_{10}O_{28}]\cdot18H_2O$	0	CCSD	PIDDUD	$Na(O_w)_4(O_M)(O_c)$; $Na(O_w)_2(OM)_2(Omorph)$	M, 3-D (1-D), b	[135]
$(C_4H_{10}N)_6Na_2[H_6Mo_6NiO_{24}]$ $[H_2V_{10}O_{28}]\cdot10H_2O$	2	CCSD	PIDFAL	$[Na(H_2O)_2(O_cO^m)_2(\ -O_w)_2$	M, 2-D, b	[135]

[a] Databases ICSD: Inorganic Crystal Structure Database, Ref. [29]; CSD: Cambridge Crystal Structure Database, Ref. [28]; X, not located.

[b] After Refs. [1,98].

[c] The structural classification codes listed are as follows: M for monomer, D for dimer, 1-D for 1-dimensional chains in the structure, 2-D for 2-dimentional and 3-D for three dimensional materials in the specific structure (a,b,c) in Table 3.

on a combination of spectroscopy and X-ray crystallography [13,118].

Many of the solution speciation studies of V_{10} mentioned above (Sections 2.2 and 2.4) were conducted at fairly high concentration and although those studies predict protonated species in acidic solution, not very many protonated V_{10} structures have been isolated in the solid state; mostly the isolated species are completely deprotonated. The data in Tables 1 and 3 highlight that most V_{10} species consist of a V_{10} unit that is 6– and all V(V). Nearly every

example has isolated monomeric V_{10} species, not V_{10} connected directly through hydrogen bonding, and the structures are modulated by water. Most of the Na^+-containing species exist with water as well [1,95]; the Na^+ ion binds directly to the anions in some cases, but is often present in an octahedral NaO_6 environment with oxygen atom donation from water, or the V_{10} anions, or both. Those interactions are indicated in Table 3 will be highlighted but it should also be noted that the sodium ions organize in several typical patterns as well, namely they tend to cluster in edge-shared
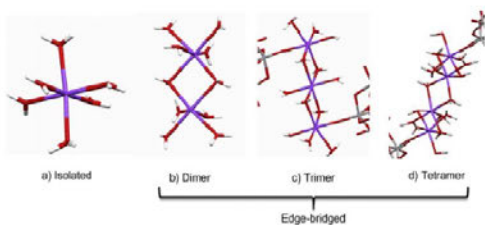
Fig. 12. Four different types of supportive Na$^+$-based structures in V$_{10}$ X-ray structures. a) the isolated and aquated octahedral Na$^+$ as Na(O$_w$)$_6$; b) a dinuclear Na$_2^{2+}$-hydrated cluster, [Na(O$_w$)$_4$($_2$-O$_w$)$_2$]$_2^{2+}$; c) a trinuclear Na$_3^{3+}$ bridge between two different V$_{10}$ clusters, {[Na(O$_w$)$_3$(O$_c$)($_2$-O$_w$)$_2$]$_2$Na(O$_w$)$_r$}$^{3+}$; d) a tetranuclear arrangement showing extensive organization within the microenvironment of the clusters, {[Na(O$_c$)(O$_w$)$_3$($_2$-O$_w$)$_2$ Na(O$_w$)$_2$($_2$-O$_w$)$_2$]$_2^{4+}$. O$_w$, O from water, O$_c$, O from the cluster.

NaO$_6$ octahedra with water. Such an arrangement serves to moderate the charge as discussed earlier (Section 2.2) and by Hawthorne [5,6,90–92].

In Fig. 12 we illustrate the bonding related to the Na$^+$ for four sub-clusters found in V$_{10}$ X-ray structures. These clusters represent general patterns we found while compiling the data in Table 3. Specifically, the system should be characterized as an interaction described as indirect and through water (isolated and dinuclear) or direct (trinuclear and tetranuclear clusters) association between cation and anion [1,95]. Perhaps surprisingly, the protonation dramatically changed the types of sub-structures that the Na$^+$ and V$_{10}$ engaged in. Because we are interested in exploring structural patterns that could potentially provide information on the systems relating to those found in nanosized water droplets, we have focused on the structures in which the V$_{10}$ or H$_x$V$_{10}$ structure is isolated in the overall framework of the material. Although not recognized initially, this did result in a focus on fully deprotonated V$_{10}$ anions because many protonated forms of V$_{10}$ form dimeric and other structures as described above in Figs. 3 and 4. These arrangements can be used to categorize the different structures and as discussed below can serve to help understand the differences in the V$_{10}$ anions found in the nanodroplets.

An important note to the reader is needed regarding our generation of Table 3 (and tables like it in the future) because it contains V$_{10}$ structures with sodium cations characterized by X-ray analysis as well as the sodium-containing V$_{10}$ minerals characterized by X-ray analysis. Information was obtained from both the chemistry literature [1,95] and mineralogy literature [5,6,9,90–92]. The two communities publish on similar topics and together extending knowledge in the field. However, because of the two parallel areas it became nontrivial to compile a fully comprehensive list of V$_{10}$ structures containing sodium. For example, both areas used their own structural database, with limited crossover and cross-depositing. Specifically, a search for V$_{10}$ structure affords 179 V$_{10}$ structures in the CSD. However, this list excludes all the V$_{10}$ structures that do not contain C and there are many of those particularly in the mineral literature. Even IUCr journals with their extensive checks miss previously-published structures from the other database. An example of such a compound that was published separately in each database is K$_4$Na$_2$[V$_{10}$O$_{28}$]·10H$_2$O [58,119]. In practice this means that a list of structures that began as ten structures to be included in Table 3 became 38 with other searches of the ICSD [29] and then identifying references within those references, some of which were in the older literature and not in the databases (and non-trivial to access/examine).

The structures that are compiled in Table 3 include a number of very different types of structures. The unprotonated V$_{10}$ structure
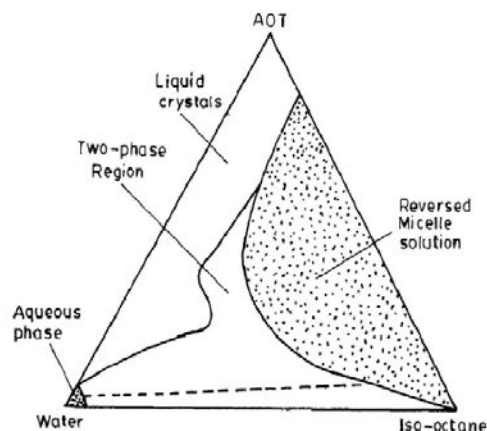

Fig. 13. The phase diagram for Na$^+$-AOT. The sections of the diagram are labeled with the various phases. More details are found in the Refs. [44,141]. Reproduced with permission from Ref. [141].

(with a charge of minus 6 species) is by far the most common class of structures. The protonation of the structures in solid-state increased structural diversity dramatically and several new minerals of this class has recently been identified, see Table 1 [13,15]. A relationship between size and charge on cation was found relating to the number of waters of hydration in solid-state with the size of the crystal. This association provided a direct relationship sensitive to compound microenvironments and a topic of interest to this work and an example of a topic that has not been given attention in the literature previously.

4.2. Na$^+$ in reverse micelles – experimental data

Na$^+$-AOT is the most common surfactant used for preparation of reverse micelles. AOT is the abbreviation for bis(2-ethylhexyl)sulfo succinate and Na$^+$ is the most common cation. AOT contains three chiral centers, but is available with mixed stereochemistry. Bulk solution is generally the medium of choice, and certainly is the system that we know the most about. However, with increasing challenges to materials that we are making and multifunctional properties, it is becoming more and more desirable that molecules are more multifaceted with more complex properties. As a result, colloidal systems and soft materials are becoming more important because they can solubilize non-traditional molecules for many applications.

The nanosized water droplets prepared from Na$^+$-AOT can range in properties depending on size, surfactant and organic solvent. Application of microemulsions has become a new media for a variety of purposes [31,32,35,43,44,46,136–140] and there are several popular surfactants to choose from (CTAB, DSS, Triton) and much work has been done characterizing them both experimentally and computationally [33,141–150]. In Fig. 13 we show a ternary phase diagram that describes some of the different types of phases that form in such a colloidal system from isooctane, AOT, and water [141]. Some of the defined structures that can form in these systems include emulsions, liquid crystals and other phases.

Here we describe the Na$^+$-AOT reverse micelles, because we have experimentally examined the chemistry of V$_{10}$ in nanosized droplets prepared from Na$^+$-AOT and isooctane or cyclohexane [37,47,48,96,151–153]. In addition, there are a number of computational studies done on Na$^+$-AOT using both Gaussian, molecular

dynamic, and alternate computational methods [33,139,142–150]. Although work has also been done with other related systems [153–159], this review will focus on considerations that can be made with this system. The V_{10} anions may be stable in the reverse micelles because of the interaction with the Na$^+$ atoms that aggregate at the reverse micellar interface presumably as a consequence of solvation. Although computational studies may seem far from the crystal structures containing Na$^+$ for the V_{10}, we hope that the following considerations allow the reader to see how the fields are merging and that the solid-state experimental data can also be used for comparison of the computational methods.

4.3. Na$^+$ in reverse micelles – computational data

Many theoretical and computational methods [33,142–150] were used focusing on different aspects of the colloidal systems including reverse micelles and their interactions with metal ions. These studies include examining the effects of different counter ions as well as adding more salt to the system. Chen and coworkers calculated concentration profiles using a simulation box enclosing 20 surfactants molecules with additives such as NaCl, CaCl$_2$ and Na$_2$SO$_4$ using all atoms molecular mechanics [142]. The concentration profiles, radial distribution functions and mean squared displacement of the systems are calculated. The ratio of the area of per AOT molecule is 3.69:3.70:3.61:3.68 for 4 different systems in the simulation box (no additive: 20 molecules of NaCl: 20 molecules of CaCl$_2$: 20 molecules of Na$_2$SO$_4$). Only small differences were observed in the volumes for the head groups of the AOT molecules and the AOT alkyl chains were readily dissolved well into the isooctane phase. Experimental data have shown that the presence of salts affects the microemulsion structures differently at low and high water concentration [147]. Increased salt concentration at low water content suppresses oligomerization of the microemulsions. However, at higher water content it reduces the microemulsion (reverse micellar) size. These results underline the fact that the structures and dynamics are dependent not only on the electrostatic repulsion between AOT headgroups but also hydration effects by salts [147].

Using molecular dynamic calculations, Ladanyi and Levinger investigated the mobility of the metal ions in the water pool of metal ion-AOT reverse micelles [145,146]. They examined the AOT structures form from Na$^+$, K$^+$ and Cs$^+$ AOT surfactants. The cation was very important to the nature of the structures that formed, and three different types of interface mobilities were observed for the water layer at the interface [145]. In contrast, the mobility of the water molecules in the core water pool changed only slightly as the cation changed. The authors suggest that the differences in interfacial mobility are strongly correlated with structural features, such as the ion-water coordination and the extent such coordination disrupts the water hydrogen network [145]. Similar conclusions were reached by Chowdhary and Ladanyi using molecular dynamic simulations focusing on single-molecule relaxation of water within the RM [143]. They also found that the mobility, particularly at the interface, is reduced significantly. They also observed that the ion-dipole interactions with the sodium counter ions slow down the relaxation of the water molecules at the interface, which further demonstrated a large difference between the interface layer and the bulk.

Pal and coworkers [33] used Monto Carlo and molecular dynamics simulations to examine the distribution of alkali cations and concluded that the larger cations favor the interface. They arrived at this conclusion based on considerations of enthalpic contributions, that these enthalpic contributions reflects with the solvation energies of the cations in water and they conclude that solvation control the ion-exchange process. For example, they found that the hydration number of the first water shell for Li$^+$ in

the water core (radius 14.1 Å) was similar to that observed at infinite dilution in bulk water [33]. This suggests that some of the results using this method will be similar to those observed in solution and represent inherent properties of the system.

Computational studies done with these reverse micelles [149] describe this region as solid-like and with up to 80–90% sodium right at the interface near the charged sulfonate group [145,146]. These studies have also demonstrated that the size of the cation can affect the system dramatically. The size of the cation can affect the stability of the reverse micelles which can be experimentally verified by observing large differences in the sizes and the shapes that each cation-AOT forms. The larger cations will also replace sodium at the interface when both are present showing that despite the alterations in shape and size of the reverse micelles, larger cations are more stable at the interface rather than in the bulk water pool [33,47,147]. This was attributed to the solvation energy differences between a large cation and Na$^+$. In Fig. 14 we show the simulated structure generated from Me-AOT systems for small parts of the interfaces including Li$^+$, Na$^+$, K$^+$ and Cs$^+$ counter ions, and distinct differences are observed in the location and the dynamics of these counter ions [145,146,149]. Specifically, the larger cations allow for much less flexibility in the system than the smaller cations but still will replace Na$^+$ at the interface. However, nonetheless, the adjacent Stern layer is fairly rigid as anticipated.

Although these systems are not at the stage of showing the molecular structure that is observed in the crystal structures, they do underline several points. First, the water pools in the reverse micelles structures show rigidity. Second, there is likely to be some interaction within the water molecules, and although these may not be represented as of yet by the computational studies, they are undoubtedly there. The differences in conformations observed are likely to reflect some of the differences in the properties of these entities, and embracing the types of considerations shown here in which we add a counter ion to link the association with the Na$^+$ ions, some deeper understanding of this system can be made.

4.4. V$_{10}$ in reverse micelles

V$_{10}$ was placed in AOT reverse micelles and studies were conducted investigating how the ^{51}V NMR chemical shifts changed upon addition to the water droplet. The experiments were done by adding either vanadate (V$_1$, VO$_4^{3-}$) or V$_{10}$ to the water droplets in the microemulsion resulting in suspensions containing reverse micelles in a range of different sizes with V$_{10}$. These studies showed that V$_{10}$ resided in the middle of the waterpool [35,47].

The pH is critical for the formation of V$_{10}$ anions, and how the chemical shifts of V$_{10}$ changed as a function of pH in aqueous solution and solutions added to reverse micelles [47,48,116]. The charge on V$_{10}$ will be from 3 to 6 depending on pH as described above in Eq. (3)(5). Studies in reverse micelles loaded with V$_{10}$ molecules show a V$_{10}$ anion in the 6− deprotonated state regardless of the pH of the solution added to the reverse micelle. As shown in Fig. 10 the ^{51}V NMR spectrum of a V$_{10}$ solution at pH 3.1 was placed in the nanosized water droplets, however, the resulting spectra shown in Fig. 15 illustrate that the signals for the V$_{10}$ changed. Despite the initial pH of the water solution the chemical shifts of V$_{10}$ in the reverse micelles demonstrate that the pH around the V$_{10}$ is approaching neutral in reverse micellar water pools.

In Fig. 16 we show a cartoon illustrating this system in which both Na$^+$ and V$_{10}$ are present. We added the V$_{10}$ anion in the reverse micelle at different sizes and at different pH values. Interestingly, the V$_{10}$ has been found to reside near the center of the reverse micelle. Furthermore, the H$^+$ that may have accompanied
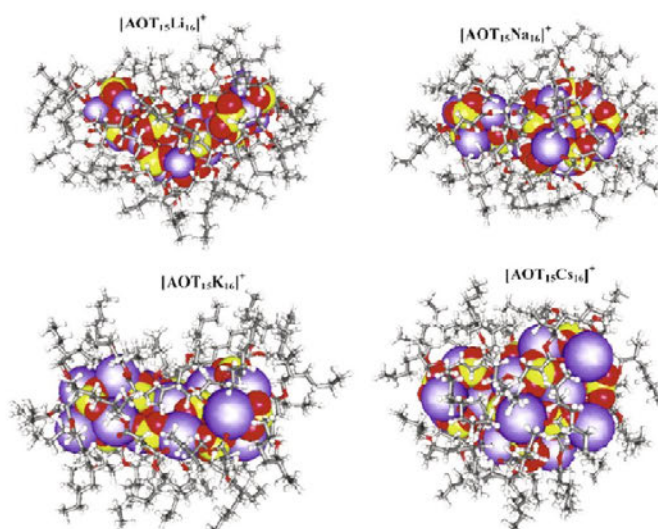
Fig. 14. These representations are results of simulations probing the conformation of the Metal Ion-AOT systems. Adapted with permission from the American Chemical Society from Ref. [149].
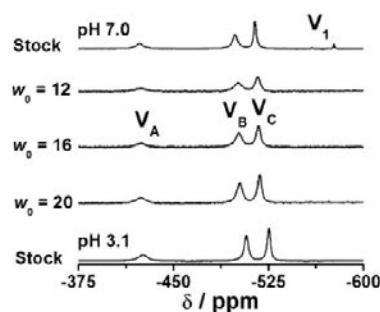

Fig. 15. The ^{51}V NMR spectra shown are 10 mM V_{10} samples in D_2O at pH 7.0, 3.1, and reverse micelles of varying sizes with an internal V_{10} concentration of 10 mM at pH 3.1. Reproduced with permission from the American Chemical Society from Ref. [47].

this anion are found to go to the interface and Na^+ ions will take their place. That is V_{10} generally deprotonates to form the protonation state with either 6^- or one proton associated with the anion. This phenomenon has been observed in many different systems [47], and as a result it appears that there must be a gradient in the water droplet, because the pH at the interface is more acidic than at the V_{10} anion at the center of the reverse micelle. Despite such detailed information and suggested organization of the layers next to the interface, attempts have not yet been made to associate the types of order observed in crystal structure with that found in the solutions of these reverse micelles.

The smallest reverse micelle large enough to contain V_{10} is a w_o 5–6 [48]. The dimensions of smaller reverse micelles simply cannot fit the large anion (for dimensions see Fig. 1). Only 2–3 water molecules fit at the interface, and, as a result a V_{10} anion that is solvated [96]. In nanoscale water droplets the V_{10} persist regardless of the

potential statistical distribution of the V-atoms in the water droplet (see below). The seemingly lower likelihood that 10 V-atoms would remain in one reverse micelle and others would be empty is experimentally favored over the alternative where a distribution with the average number of V-atoms goes below 10.

For a w_o 6 reverse micellar system, a calculation assuming volumes of water molecule and reverse micelle water pool predicts about 380 water molecules without V_{10} inside and ~50 AOT, meaning ~50 Na^+ ions [43]. The V_{10} necessarily displaces some water from the RM to afford the conclusion that there exists only 2–3 layers of water molecules. The V_{10} also necessarily brings 3 (or even 6) Na^+ ions to balance charge in the system. So many ions in the Stern layer, then, would likely lead to the formation of extended chains of corner-sharing or edge-bridging NaO_6 octahedra. The facts presented here support a *hypothesis that the V_{10} anions may continue to exist in the reverse micelles favored by the interaction with the Na^+ atoms at the reverse micellar interface* presumably as a consequence of solvation. This suggest that the X-ray structures that are most likely to describe the structures in the water pools are those in which deprotonated V_{10} is found as discrete units within the structures. Several structures are shown in Table 3 containing Na^+ or alternatively both Na^+ and water, where both are binding to the V_{10} anion. We described a number of such structures in the solid-state section including clusters with infinite chains such as those represented by $Na_6[V_{10}O_{28}] \cdot xH_2O$ [54,62].

5. Summary and implications of the work

Cation-anion interactions remain central to chemistry and the materials that forms through chemical reactions. Historically these interactions are precisely characterized in the solid state, and structural variation due to cation-anion, H-bonding and other attractive and repulsive forces. However, much of chemistry takes place in solution and in this state the characterization often is more complex and less straightforward, so many chemists do not even
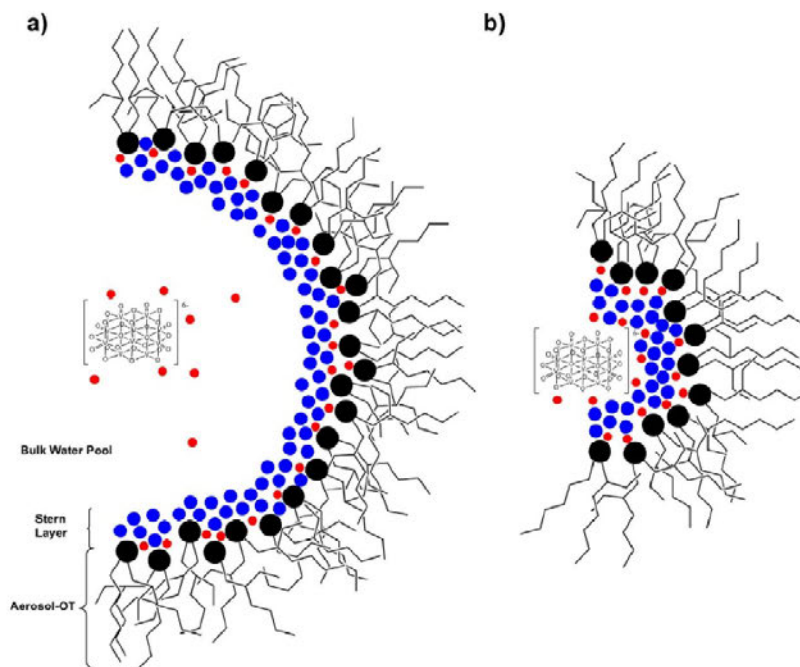
Fig. 16. A cartoon illustrating the location of the Na_ ions in the Stern layer (aqueous layer) in a w_o 12 (a) and w_o 5 (b) Na⁺-AOT reverse micelle as well as the V_{10} anion with sodium counter ions. The drawing captures the predictions reported by a number of computational studies suggesting 80–90% of the Na⁺ ions are as are the interface, and shows the placement of V_{10} within both sizes of reverse micelles For details see Refs. [131,132]. Red = Na⁺, blue = H_2O at the Stern layer, black = charged sulfonate head group.

consider characterization in media other than the solid state as structural characterization. Furthermore, areas such as mineralogy often work on similar systems, but research is reported in a different manner and deposited in different databases (see Table 3 and references therein), thus hindering progress by cross-fertilization of the natural overlap that exist. In the preceding review, we have taken an inorganic system, the V_{10} anion, in solid state material characterized by X-ray crystallography [1,12,21,22,24,52–66,68,69] and examined the anion-cation interactions. Because we were particularly interested in bridging the solid-liquid types of states, we collected the information available on V_{10} in nanosized droplets to investigate if the solid-state information could be used to describe the order of the system in the liquid state.

First, we characterized the V_{10} anion and its properties in solution. Vanadates can form other species so the pH range where only V_{10} forms is very limited. However, at the pH range where V_{10} is thermodynamically most stable, solutions can be investigated and the effects of different cations interacting with the V_{10} can be studied. In order to investigate such effects we have successfully in the past used nanosized water droplets formed using a microemulsion system. Several ternary surfactant-organic solvent-water model systems have been studied in detail, and particularly the AOT-isooctane (or cyclohexane)-water system has been found to be effective in characterizing the factors important to facilitate stability [96]. As described the V_{10} has several protonation states, but placement in the nanosized droplet result in one pH and formation of a mixture of V_{10} in the protonated 5– and deprotonated 6– species [96]. It was indeed surprising that regardless of the pH of the aqueous solution, placement of the

mM concentrations of anion into the reverse micelle resulted in a solution near pH 5.5–6.5. Spectroscopic studies combined with a simple computational analysis were done showing that the anion was located in the middle of the nanosized waterpool [47]. Considering that the V_{10} is highly negatively charged and the interface of the reverse micelle is negatively charged as well, these findings are all in line with the scientific expectations.

Investigating the known and characterized X-ray structures of Na⁺-containing V_{10} structures, information was gained on the specific interactions of Na⁺ with V_{10}. We found that distinct patterns emerged and that these patterns were very specific optimizing interactions between the anion and cation. Indeed, we found that some of these interactions could be purely ionic whereas other examples of some of these systems involved bonds with some covalent nature. Monomeric, dimeric, trimeric and tetrameric edge-sharing octahedral clusters were observed within the X-ray structures forming a microenvironment for the Na⁺ ions. Importantly, the Na⁺ was found to be six-coordinate in an octahedral geometry in all structures investigated. This was true for both the X-ray structures of synthetic compounds (Table 3), as well as the naturally occurring minerals containing V_{10}. The number of structurally-characterized protonated V_{10} materials was much smaller, and these systems were found to be more complex with the V_{10}-anion forming a microenvironment with H-bonding V_{10} anions (see Tables 1 and 3). These types of microenvironments were previously described in detail by documenting the variety of structures that could form. Combining the information regarding the V_{10}-microenvironments with that of the Na⁺-microenvironments leads to the development of patterns that
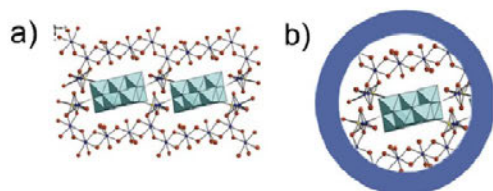
197

Fig. 17. The illustration of how the X-ray structures of Na$^+$-V$_{10}$ could potentially be used to describe the solution nanosystems forming in microemulsions. a) The Na$^+$-V$_{10}$ complex and b) the depiction of a Na$^+$-V$_{10}$ complex captured within a surfactant-bound nanosphere. The structure of a) is reproduced with the permission of the International Union of Crystallography from Ref. [121].

could be anticipated in these structures, and indeed, this is observed for some of the materials investigated.

Characterization of solution materials is more complex, but undoubtedly order exists in solutions as well. The phenomena of structural order in solutions has recently been described for polyoxometalate systems in solution and this organization has been referred to as soft oxometalates (SOMs) by some [160–162]. Indeed, studies with reverse micelles containing V$_{10}$ in nanosized water droplets have provided confirmation that order is observed in systems with V$_{10}$ in reverse micelles. This has been observed for NaAOT/isooctane systems containing V$_{10}$ [25,37,47,68] as well as for V$_{10}$ in Igepal/isooctane systems [153]. However, solutions are also characterized using a range of computational studies. These studies range from Gaussian studies to molecular dynamic studies. Although these calculations are generally based on very different premises than those of X-ray structures, they do demonstrate that the cations are located in some cases near the surfactant head group, and that the Na$^+$ ion is penetrating the interface. These are important facts, because this documents that the structures observed by X-ray crystallography may be useful to model the structures observed in solution. Although there were many different structures representing the Na$^+$-V$_{10}$ type of interactions, some described the structural order that we observe in the reverse micelle. Fig. 17a shows a known structure of a material with the V$_{10}$ anion in a lattice of water-surrounded-Na$^+$ cations [16]. This structure allows one to easily picture how the limited water molecules in the presence of Na$^+$ cations could both be surrounded by the surfactant in a RM as illustrated in Fig. 17b. The structure illustrated in Fig. 17b is part of a X-ray structure and counterions provide the charge balance. Similarly, such charge balance can be anticipated in reverse micelles because of the counterions associated with the interface. We and others have shown that there is a layer of H$_2$O adjacent to the surfactant interface, and that some of the more elaborate structures of Na$^+$-V$_{10}$ complexes [16,62,69,121] are beginning to demonstrate structures involving water associated with the V$_{10}$ anion. At this point we can confirm that *in the small RMs the water can be structurally viewed and its organization be considered similarly to suitable microenvironments in the solid-state of Na$^+$-containing V$_{10}$-structures and minerals. Our working hypothesis providing the goal to write this review can be confirmed. The compilations of Na$^+$-containing V$_{10}$ X-ray structures have provided a structural framework upon which future investigations can be developed and comparison of the microenvironments of solid-state crystals and minerals with that of the nanosized-water droplet can be successful.*

Currently, there is some information on structural details at the interface of the AOT (or other) surfactant(s) and the aqueous phase in RMs [163–167]. However, the simple strategy suggested here using the solid-state systems to guide the structural and computational investigations demonstrate how powerful the structural

information that the X-ray structures provides to us, and suggests that this type of approach and structural data should be used in the future. Indeed, this manuscript documented that some of the data needed to complete the literature on this system were found in the mineralogy literature (see Tables 1 and 3). Furthermore, the potential role of water should be considered since water can interact directly with anions and cations both provided additional stability and structural diversity. The combined examples of Na$^+$-containing V$_{10}$ structures in this manuscript document that structures found in the mineralogy literature are highly relevant and contain microdomains that strongly highlights examples of interesting binding, suggesting that one should work across the disciplines when investigating these systems.

References

[1] J.L.F. da Silva, M.F.M. da Piedade, M.T. Duarte, Inorg. Chim. Acta 356 (2003) 222–242.
[2] R. Hoffmann, Acc. Chem. Res. 4 (1971) 1–9.
[3] H.T. Evans Jr., J.S. White Jr., Mineral. Rec. 18 (1987) 333–340.
[4] R. Hoffmann, Rev. Mod. Phys. 60 (1988) 601–628.
[5] M. Schindler, F.C. Hawthorne, W.H. Baur, Can. Mineral. 38 (2000) 1443–1456.
[6] M. Schindler, F.C. Hawthorne, Can. Mineral. 39 (2001) 1225–1242.
[7] M. Rahm, R. Hoffmann, J. Am. Chem. Soc. 138 (2016) 3731–3744.
[8] A.G. Swallow, F.R. Ahmed, W.H. Barnes, Acta Crystallogr. 21 (1966) 397–405.
[9] J.M. Hughes, M. Schindler, J. Rakovan, F.E. Cureton, Can. Mineral. 40 (2002) 1429–1435.
[10] J.M. Hughes, M. Schindler, C.A. Francis, Can. Mineral. 43 (2005) 1379–1386.
[11] A.R. Kampf, I.M. Steele, Can. Mineral. 46 (2008) 679–686.
[12] J.M. Hughes, W.S. Wise, M.E. Gunter, J.P. Morton, J. Rakovan, Can. Mineral. 46 (2008) 1365–1372.
[13] A.R. Kampf, J.M. Hughes, J. Marty, M.E. Gunter, B. Nash, Can. Mineral. 49 (2011) 595–604.
[14] F. Colombo, R. Baggio, A.R. Kampf, Can. Mineral. 49 (2011) 849–864.
[15] A.R. Kampf, J.M. Hughes, J. Marty, B. Nash, Can. Mineral. 49 (2011) 1243–1251.
[16] J. Rakovan, G.R. Schmidt, M.E. Gunter, B. Nash, J. Marty, A.R. Kampf, W.S. Wise, Can. Mineral. 49 (2011) 1253–1265.
[17] A.R. Kampf, J.M. Hughes, J. Marty, B. Nash, Can. Mineral. 50 (2012) 45–53.
[18] A.R. Kampf, J.M. Hughes, J. Marty, F.H. Brown, Can. Mineral. 51 (2013) 27–38.
[19] A.R. Kampf, J.M. Hughes, J. Marty, B. Nash, Can. Mineral. 51 (2013) 297–312.
[20] A.R. Kampf, J.M. Hughes, B. Nash, J. Marty, Can. Mineral. 52 (2014) 15–25.
[21] H.T. Evans Jr., Inorg. Chem. 5 (1966) 967–977.
[22] H.T. Evans, M.T. Pope, Inorg. Chem. 23 (1984) 501–504.
[23] L. Pettersson, I. Andersson, B. Hedman, Chem. Scr. 25 (1985) 309–317.
[24] D.C. Crans, M. Mahroof-Tahir, O.P. Anderson, M.M. Miller, Inorg. Chem. 33 (1994) 5586–5590.
[25] N. Samart, J. Saeger, K.J. Haller, M. Aureliano, D.C. Crans, J. Mol. Eng. Mater. 2 (2014) 1440007, 1440001–1440021.
[26] N.V. Kuratieva, S.P. Khranenko, S.A. Gromilov, J. Struct. Chem. 55 (2014) 285–289.
[27] O.Y. Poimanova, S.V. Radio, K.Y. Bilousova, D.V. Khaustov, V.N. Baumer, G.M. Rozantsev, J. Coord. Chem. 68 (2015) 4170–4183.
[28] C.R. Groom, I.J. Bruno, M.P. Lightfoot, S.C. Ward, Acta Crystallogr., Sect. B: Struct. Sci. Cryst. Eng. Mater. 72 (2016) 171–179.
[29] in, FIZ Karlsruhe, Karlsruhe, Germany, 2007.
[30] D.L. Long, E. Burkholder, L. Cronin, Chem. Soc. Rev. 36 (2007) 105–121.
[31] P.L. Luisi, M. Giomini, M.P. Pileni, B.H. Robinson, Biochim. Biophys. Acta 947 (1988) 209–246.
[32] J.J. Silber, A. Biasutti, E. Abuin, E. Lissi, Adv. Colloid Interface Sci. 82 (1999) 189–252.
[33] S. Pal, G. Vishal, K.S. Gandhi, K.G. Ayappa, Langmuir 21 (2005) 767–778.
[34] A.S. Narang, D. Delmarre, D. Gao, Int. J. Pharm. 345 (2007) 9–25.
[35] D.C. Crans, N.E. Levinger, Acc. Chem. Res. 45 (2012) 1637–1645.
[36] I.J. Waters, Y. Shahzad, J.C. Mitchell, Curr. Pharm. Anal. 8 (2012) 272–277.
[37] A. Chatkon, P.B. Chatterjee, M.A. Sedgwick, K.J. Haller, D.C. Crans, Eur. J. Inorg. Chem. (2013) 1859–1868.
[38] P.S.W. Yeung, G. Eskici, P.H. Axelsen, Biochim. Biophys. Acta, Biomembr. 1828 (2013) 2314–2318.
[39] Y. Zhao, H.K. Cho, L. Widanapathirana, S.Y. Zhang, Acc. Chem. Res. 46 (2013) 2763–2772.
[40] S.H. Mohd-Setapar, S.N. Mohamad-Aziz, C.S. Chuong, M.A.C. Yunus, M.A.A. Zaini, M.J. Kamaruddin, Chem. Eng. Commun. 201 (2014) 1664–1685.

[41] Y.H. Huang, S.P.C. Cole, T.G. Cai, Y. Cai, Oncol. Lett. 12 (2016) 11–15.
[42] D. Arora, S. Jaglan, Trends Food Sci. Technol. 54 (2016) 114–126.
[43] A. Maitra, J. Phys. Chem. 88 (1984) 5122–5125.
[44] T. De, A. Maitra, Adv. Colloid Interface Sci. 59 (1995) 95–193.
[45] M.D. Fayer, Physiology 26 (2011) 381–392.
[46] M.D. Fayer, Acc. Chem. Res. 45 (2012) 3–14.
[47] B. Baruah, J.M. Roden, M. Sedgwick, N.M. Correa, D.C. Crans, N.E. Levinger, J. Am. Chem. Soc. 128 (2006) 12758–12765.
[48] B. Baruah, L.A. Swafford, D.C. Crans, N.E. Levinger, J. Phys. Chem. B 112 (2008) 10158–10164.
[49] M.T. Pope, B.W. Dale, Quart. Rev. Chem. Soc. 22 (1968) 527–548.
[50] M.T. Pope, Isopolyanions and heteropolyanions, in: G. Wilkinson Sir, R.D. Gillard, J.A. McCleverty (Eds.), Comprehensive Coordination Chemistry. The Synthesis, Reactions, Properties, & Applications of Coordination Compounds, Pergamon Press, New York, 1987, pp. 1023–1058.
[51] M.T. Pope, A. Müller, Angew. Chem. Int. Ed. Engl. 30 (1991) 34–48.
[52] M. Aureliano, D.C. Crans, J. Inorg. Biochem. 103 (2009) 536–546.
[53] H.T. Evans Jr., A.G. Swallow, W.H. Barnes, J. Am. Chem. Soc. 86 (1964) 4209–4210.
[54] A. Durif, M.T. Averbuch-Pouchot, J.C. Guitel, Acta Crystallogr., Sect. B 36 (1980) 680–682.
[55] D. Fratzky, M. Schneider, S. Rabe, M. Meisel, Acta Crystallogr., Sect. C 56 (2000) 740–741.
[56] T. Higami, M. Hashimoto, S. Okeya, Acta Crystallogr., Sect. C 58 (2002) i144–i146.
[57] A. Iida, T. Ozeki, Acta Crystallogr., Sect. C 59 (2003) i41–i44.
[58] U. Lee, H.-C. Joo, Acta Crystallogr., Sect. E 59 (2003) i122–i124.
[59] A. Iida, T. Ozeki, Acta Crystallogr., Sect. C 60 (2004) i43–i46.
[60] U. Lee, H.-C. Joo, Acta Crystallogr., Sect. E 60 (2004) i22–i24.
[61] G.-B. Li, S.-H. Yang, M. Xiong, J.-H. Lin, Acta Crystallogr., Sect. C 60 (2004) m612–m614.
[62] H.-X. Guo, Z.-L. Yao, Acta Crystallogr., Sect. C 63 (2007) i51–i53.
[63] N. Bošnjaković-Pavlović, A. Spasojević-de Biré, I. Tomaz, N. Bouhmaida, F. Avecilla, U.B. Mioč, J.C. Pessoa, N.E. Ghermani, Inorg. Chem. 48 (2009) 9742–9753.
[64] J. Nilsson, E. Nordlander, U. Behrens, D. Rehder, Acta Crystallogr., Sect. E 66 (2010) i30–i31.
[65] N. Bošnjaković-Pavlović, J. Prévost, A. Spasojević-de Biré, Cryst. Growth Des. 11 (2011) 3778–3789.
[66] E.G. Vergara, E.S. Lara, A.P. Benítez, A. Mendoza, in: 15th International Conference on Biological Inorganic Chemistry (ICBIC), Vancouver, Canada, 2011.
[67] T.L. Turner, V.H. Nguyen, C.C. McLauchlan, Z. Dymon, B.M. Dorsey, J.D. Hooker, M.A. Jones, J. Inorg. Biochem. 108 (2012) 96–104.
[68] A. Chatkon, A. Barres, N. Samart, S.E. Boyle, K.J. Haller, D.C. Crans, Inorg. Chim. Acta 420 (2014) 85–91.
[69] A. Galani, V. Tsitsias, D. Stellas, V. Psycharis, C.P. Raptopoulou, A. Karaliota, J. Inorg. Biochem. 142 (2015) 109–117.
[70] J. Baes, F. Charles, R.E. Mesmer, The First Transition Series. Vanadium, in: The Hydrolysis of Cations, John Wiley & Sons, New York, 1976, pp. 193–210.
[71] L. Pettersson, B. Hedman, I. Andersson, N. Ingri, Chem. Scrip. 22 (1983) 254–264.
[72] J.T. Rhule, C.L. Hill, D.A. Judd, R.F. Schinazi, Chem. Rev. 98 (1998) 327–358.
[73] I.A. Weinstock, J. Cowan, E.M.G. Barbuzzi, H. Zeng, C.L. Hill, J. Am. Chem. Soc. 121 (1999) 4608–4617.
[74] D.M. Templeton, F. Ariese, R. Cornelis, L.G. Danielsson, H. Muntau, H.P. Van Leeuwen, R. Lobinski, Pure Appl. Chem. 72 (2000) 1453–1470.
[75] T. Kiss, A. Odani, Bull. Chem. Soc. Jpn. 80 (2007) 1691–1702.
[76] D.C. Crans, K.A. Woll, K. Prusinskas, M.D. Johnson, E. Norkus, Inorg. Chem. 52 (2013) 12262–12275.
[77] D. Rehder, J. Inorg. Biochem. 147 (2015) 25–31.
[78] H.T. Evans Jr., R.M. Garrels, Geochim. Cosmochim. Acta 15 (1958) 131–149.
[79] K.A. Doucette, K.N. Hassell, D.C. Crans, J. Inorg. Biochem. (2016).
[80] D.C. Crans, P.M. Ehde, P.K. Shin, L. Pettersson, J. Am. Chem. Soc. 113 (1991) 3728–3736.
[81] K. Elvingson, D.C. Crans, L. Pettersson, J. Am. Chem. Soc. 119 (1997) 7005–7012.
[82] K. Elvingson, A.D. Keramidas, D.C. Crans, L. Pettersson, Inorg. Chem. 37 (1998) 6153–6160.
[83] G.R. Willsky, K. Halvorsen, M.E. Godzala III, L.-H. Chi, M.J. Most, P. Kaszynski, D.C. Crans, A.B. Goldfine, P.J. Kostyniak, Metallomics 5 (2013) 1491–1502.
[84] R.D. Shannon, Acta Crystallogr., Sect. A 32 (1976) 751–767.
[85] I.D. Brown, Chem. Soc. Rev. 3 (1978) 359–376.
[86] I.D. Brown, Structure and Bonding in Crystals, Academic Press, New York, 1981.
[87] I.D. Brown, J. Appl. Crystallogr. 29 (1996) 479–480.
[88] R.D. Shannon, R.X. Fischer, Am. Mineral. 101 (2016) 2288–2300.
[89] D.C. Crans, J. Smee, E. Gaidamauskas, L. Yang, Chem. Rev. 104 (2004) 849–902.
[90] F. Hawthorne, Acta Crystallogr., Sect. A 39 (1983) 724–736.
[91] F.C. Hawthorne, Z. Kristallogr. 201 (1992) 183–206.
[92] M. Schindler, F.C. Hawthorne, W.H. Baur, Chem. Mater. 12 (2000) 1248–1259.
[93] W.G. Klemperer, W. Shum, J. Am. Chem. Soc. 99 (1977) 3544–3545.
[94] O.W. Howarth, M. Jarrold, J. Chem. Soc., Dalton Trans. (1978) 503–506.
[95] I. Correia, F. Avecilla, S. Marcao, J.C. Pessoa, Inorg. Chim. Acta 357 (2004) 4476–4487.
[96] I. Sanchez-Lombardo, B. Baruah, S. Alvarez, K.R. Werst, N.A. Segaline, N.E. Levinger, D.C. Crans, New J. Chem. 40 (2016) 962–975.
[97] V.A. Grigoriev, C.L. Hill, I.A. Weinstock, J. Am. Chem. Soc. 122 (2000) 3544–3545.
[98] S. Nakamura, T. Ozeki, J. Chem. Soc., Dalton Trans. (2001) 472–480.
[99] H.T. Evans, M.E. Mrose, U.S Geological Survey, 1955, pp. 861–875.
[100] C.E. Gordillo, E. Linares, R.O. Toubes, H. Winchell, Am. Mineral. 51 (1966) 1.
[101] L.A. Estroff, Chem. Rev. 108 (2008) 4329–4331.
[102] K.N. Olafson, R. Li, B.G. Alamani, J.D. Rimer, Chem. Mater. 28 (2016) 8453–8465.
[103] R.B. Wanty, M.B. Goldhaber, Geochim. Cosmochim. Acta 56 (1992) 1471–1483.
[104] D. Braga, F. Grepioni, G.R. Desiraju, Chem. Rev. 98 (1998) 1375–1406.
[105] W.A. Neiwert, J.J. Cowan, K.I. Hardcastle, C.L. Hill, I.A. Weinstock, Inorg. Chem. 41 (2002) 6950–6952.
[106] S.E. O'Donnell, M.T. Pope, J. Chem. Soc., Dalton Trans. (1976) 2290–2297.
[107] Y.V. Geletii, C.L. Hill, A.J. Bailey, K.I. Hardcastle, R.H. Atalla, I.A. Weinstock, Inorg. Chem. 44 (2005) 8955–8966.
[108] D.C. Crans, H. Chen, O.P. Anderson, M.M. Miller, J. Am. Chem. Soc. 115 (1993) 6769–6776.
[109] D.C. Crans, C.D. Rithner, L.A. Theisen, J. Am. Chem. Soc. 112 (1990) 2901–2908.
[110] J.A. Gordon, Methods Enzymol. 201 (1991) 477–482.
[111] D.C. Crans, R.L. Bunch, L.A. Theisen, J. Am. Chem. Soc. 111 (1989) 7597–7607.
[112] D.C. Crans, J.J. Smee, E. Gaidamauskas, L. Yang, Chem. Rev. 104 (2004) 849–902.
[113] D. Rehder, H.C. Bechthold, A. Kececi, H. Schmidt, M. Siewing, Z. Naturforsch., B: Chem. Sci. 37 (1982) 631–645.
[114] O.W. Howarth, Prog. NMR Spectrosc. 22 (1990) 453–483.
[115] D. Rehder, T. Polenova, M. Buhl, Vanadium-51 NMR, in: G.A. Webb (Ed.) Annual Reports on NMR Spectroscopy, Vol. 62, 2007, pp. 49–114.
[116] D.C. Crans, B. Baruah, N.E. Levinger, Biomed. Pharmacother. 60 (2006) 174–181.
[117] A.M. Dokter, S. Woutersen, H.J. Bakker, J. Chem. Phys. 126 (2007).
[118] V.W. Day, W.G. Klemperer, D.J. Maltbie, J. Am. Chem. Soc. 109 (1987) 2991–3002.
[119] P.M. Matias, J.C. Pessoa, M.T. Duarte, C. Madeira, Acta Crystallogr., Sect. C 56 (2000) e75–e76.
[120] G.Z. Kaziev, A.V. Oreshkina, S. Holguin Quinones, A.F. Stepnvoa, V.E. Zavodnik, A. de Ita, D.A. Alekseev, Koord. Khim. 36 (2010) 899–902.
[121] R. Ksiksi, M. Graia, T. Jouini, Acta Crystallogr., Sect. E 61 (2005) i177–i179.
[122] M.I. Khan, Q. Chen, D.P. Goshorn, J. Zubieta, Inorg. Chem. 32 (1993) 672–680.
[123] M.-C. Shao, Z.-Y. Zhang, C.-A. Bai, L. Zhang, Y.-Q. Tang, Acta Crystallogr., Sect. A 40 (1984) C222.
[124] P.Y. Zavalij, T. Chirayil, M.S. Whittingham, Z. Kristallogr., New Cryst. Struct. (1997) 321.
[125] I. Cavaco, J.C. Pessoa, S.M. Luz, M.T. Duarte, P.M. Matias, R.T. Henriques, R.D. Gillard, Polyhedron 14 (1995) 429–439.
[126] Z.-G. Sun, L.-S. Long, Y.-P. Ren, R.-B. Huang, L.-S. Zheng, S.W. Ng, Acta Crystallogr., Sect. E 58 (2002) i34–i36.
[127] T. Duraisamy, A. Ramanan, J.J. Vittal, Cryst. Eng. 3 (2000) 237–250.
[128] H.N. Miras, R.G. Raptis, N. Lalioti, M.P. Sigalas, P. Baran, T.A. Kabanos, Chem. Eur. J. 11 (2005) 2295–2306.
[129] O.V. Yakubovich, I.M. Steele, E.V. Yakovleva, O.V. Dimitrova, Acta Crystallogr., Sect. C 71 (2015) 465–473.
[130] U. Lee, Acta Crystallogr., Sect. E 62 (2006) i176–i178.
[131] S. Yerra, B.K. Tripuramallu, S.K. Das, Polyhedron 81 (2014) 147–153.
[132] I. Khan, S. Ayesh, E. Yohannes, R.J. Doedens, Front. Biosci. 8 (2003) i177–i183.
[133] M.I. Khan, S. Tabussum, C. Zheng, Synth. React. Inorg. Met.-Org. Chem. 30 (2000) 1773–1790.
[134] O.E. Piro, E.L. Varetti, S.A. Brandán, A.B. Altabef, J. Chem. Crystallogr. 33 (2003) 57–63.
[135] Y. Yang, L. Xu, F. Li, X. Qu, Inorg. Chem. Commun. 33 (2013) 142–146.
[136] B.K. Paul, S.P. Moulik, J. Dispersion Sci. Technol. 18 (1997) 301–367.
[137] S.P. Moulik, B.K. Paul, Adv. Colloid Interface Sci. 78 (1998) 99–195.
[138] J. Eastoe, M.J. Hollamby, L. Hudson, Adv. Colloid Interface Sci. 128 (2006) 5–15.
[139] G.V. Mudzhikova, E.N. Brodskaya, Colloid J. 74 (2012) 269–279.
[140] O.F. Silva, M.A. Fernandez, J.J. Silber, R.H. de Rossi, N.M. Correa, ChemPhysChem 13 (2012) 124–130.
[141] B. Tamamushi, N. Watanabe, Colloid Polym. Sci. 258 (1980) 174–178.
[142] Y.J. Chen, G.Y. Xu, S.L. Yuan, H.Y. Sun, Colloids Surf. A 273 (2006) 174–178.
[143] J. Chowdhary, B.M. Ladanyi, J. Phys. Chem. A 115 (2011) 6306–6316.
[144] M.L. Guan, D.K. Ma, S.W. Hu, Y.J. Chen, S.M. Huang, Inorg. Chem. 50 (2011) 800–805.
[145] M.R. Harpham, B.M. Ladanyi, N.E. Levinger, J. Phys. Chem. B 109 (2005) 16891–16900.
[146] M.R. Harpham, B.M. Ladanyi, N.E. Levinger, K.W. Herwig, J. Chem. Phys. 121 (2004) 7855–7868.
[147] R. Kawai-Hirai, M. Hirai, J. Appl. Crystallogr. 40 (2007) S274–S278.
[148] G. Longhi, S.L. Fornili, V.T. Liveri, Phys. Chem. Chem. Phys. 17 (2015) 16512–16518.
[149] G. Longhi, S.L. Fornili, V.T. Liveri, S. Abbate, D. Rebeccani, L. Ceraulo, F. Gangemi, Phys. Chem. Chem. Phys. 12 (2010) 4694–4703.
[150] E. Negro, R. Latsuzbaia, A.H. de Vries, G.J.M. Koper, Soft Matter 10 (2014) 8685–8697.

[151] D.C. Crans, C.D. Rithner, B. Baruah, B.L. Gourley, N.E. Levinger, J. Am. Chem. Soc. 128 (2006) 4437–4445.

[152] D.C. Crans, B. Baruah, A. Ross, N.E. Levinger, Coord. Chem. Rev. 253 (2009) 2178–2185.

[153] M.A. Sedgwick, D.C. Crans, N.E. Levinger, Langmuir 25 (2009) 5496–5503.

[154] J. Stover, C.D. Rithner, R.A. Inafuku, D.C. Crans, N.E. Levinger, Langmuir 21 (2005) 6250–6258.

[155] D.E. Warschawski, A.A. Arnold, M. Beaugrand, A. Gravel, E. Chartrand, I. Marcotte, BBA Biomembranes 1808 (2011) 1957–1974.

[156] N.M. Correa, J.J. Silber, R.E. Riter, N.E. Levinger, Chem. Rev. 112 (2012) 4569–4602.

[157] A.G. Sostarecz, E. Gaidamauskas, S. Distin, S.J. Bonetti, N.E. Levinger, D.C. Crans, Chem. Eur. J. 20 (2014) 5149–5159.

[158] S.V. Perez, A.F. Olea, M.P. Garate, Curr. Top. Med. Chem. 14 (2014) 774–780.

[159] P. Guilbaud, T. Zemb, Curr. Opin. Colloid Interface Sci. 20 (2015) 71–77.

[160] P. Thomas, C.Y. Pei, B. Roy, S. Ghosh, S. Das, A. Banerjee, T. Ben, S.L. Qiu, S. Roy, J. Mater. Chem. A 3 (2015) 1431–1441.

[161] S. Das, S. Biswas, T. Balaraju, S. Barman, R. Pochamoni, S. Roy, J. Mater. Chem. A 4 (2016) 8875–8887.

[162] S. Das, S. Roy, RSC Adv. 6 (2016) 37583–37590.

[163] S.S. Quintana, R.D. Falcone, J.J. Silber, N.M. Correa, ChemPhysChem 13 (2012) 115–123.

[164] E. Odella, R.D. Falcone, J.J. Silber, N.M. Correa, Phys. Chem. Chem. Phys. 16 (2014) 15457–15468.

[165] M.A. Luna, N.M. Correa, J.J. Silber, R.D. Falcone, F. Moyano, J. Phys. Org. Chem. 29 (2016) 580–585.

[166] A.K. Shaw, S.K. Pal, J. Phys. Chem. B 111 (2007) 4189–4199.

[167] G. Kaur, L. Chiappisi, S. Prevost, R. Schweins, M. Gradzielski, S.K. Mehta, Langmuir 28 (2012) 10640–10652.

200

Appendix XII: A Synthetic Isoprenoid Lipoquinone, Menaquinone-2, Adopts a Folded Conformation in Solution and at a Model Membrane Interface

Reference

(1)   Koehn, J. T.; Magallanes, E. S.; Peters, B. J.; Beuning, C. N.; Haase, A. A.; Zhu, M. J.; Rithner, C. D.; Crick, D. C.; Crans, D. C. A Synthetic Isoprenoid Lipoquinone, Menaquinone-2, Adopts a Folded Conformation in Solution and at a Model Membrane Interface. *J. Org. Chem.* **2018,** *83* (1), 275-288.

A Synthetic Isoprenoid Lipoquinone, Menaquinone-2, Adopts a Folded Conformation in Solution and at a Model Membrane Interface

Jordan T. Koehn,[†] Estela S. Magallanes,[†] Benjamin J. Peters,[†] Cheryle N. Beuning,[†] Allison A. Haase,[†] Michelle J. Zhu,[†] Christopher D. Rithner,[†] Dean C. Crick,[‡,§] and Debbie C. Crans*[,†,‡]

[†]Chemistry Department, [‡]Cell and Molecular Biology Program, and [§]Microbiology, Immunology, and Pathology Department, Colorado State University, Fort Collins, Colorado 80523, United States

S Supporting Information

ABSTRACT: Menaquinones (naphthoquinones, MK) are isoprenoids that play key roles in the respiratory electron transport system of some prokaryotes by shuttling electrons between membrane-bound protein complexes acting as electron acceptors and donors. Menaquinone-2 (MK-2), a truncated MK, was synthesized, and the studies presented herein characterize the conformational and chemical properties of the hydrophobic MK-2 molecule. Using 2D NMR spectroscopy, we established for the first time that MK-2 has a folded conformation defined by the isoprenoid side-chain folding back over the napthoquinone in a U-shape, which depends on the specific environmental conditions found in different solvents. We used molecular mechanics to illustrate conformations found by the NMR experiments. The measured redox potentials of MK-2 differed in three organic solvents, where MK-2 was most easily reduced in DMSO, which may suggest a combination of solvent effect (presumably in part because of differences in dielectric constants) and/or conformational differences of MK-2 in different organic solvents. Furthermore, MK-2 was found to associate with the interface of model membranes represented by Langmuir phospholipid monolayers and Aerosol-OT (AOT) reverse micelles. MK-2 adopts a slightly different U-shaped conformation within reverse micelles compared to within solution, which is in sharp contrast to the extended conformations illustrated in literature for MKs.
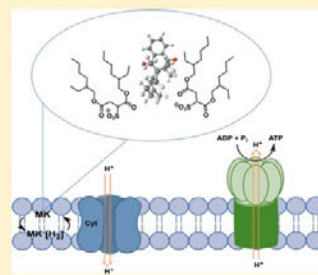
■ INTRODUCTION

Isoprenoids are among the most numerous and diverse compounds found in nature.[1−3] It was reported that 55,000 of these naturally occurring compounds had been identified by 2007;[3] an estimate that increased to 70,000 in 2015.[1] Classes of isoprenoids include lipoquinones, sterols, carotenoids, prenylated proteins, dolichols, monoterpenes, and sesquiterpenes. These compounds are involved in diverse functions such as electron transport, hormone function, membrane structure and fluidity, vision, photoprotection, insect reproduction, fragrance, and defense. The solution structures of many of these compounds, such as the sterols, are well studied. However, the conformations of long linear polymers of isoprene units such as those found in the side-chains of lipoquinones involved in bacterial and eukaryotic electron transport systems (ETS) have not been characterized.[4−7] Lipoquinones are small hydrophobic molecules that shuttle electrons between the membrane-bound protein complexes acting as electron acceptors and donors in the respiratory ETS. Two major structural groups of lipoquinones are recognized: ubiquinones (or benzoquinones, UBQ) typically found in eukaryotes and Gram-negative prokaryotes and menaquinones (or naphthoquinones, MK) typically found in Gram-positive prokaryotes, including many pathogens such as *Mycobacterium tuberculosis*. The roles and applications of

lipoquinone derivatives are currently being explored where a range of different approaches are used for combatting human diseases.[8−20] This manuscript aims to characterize the conformation of a synthetic truncated MK analog within organic solutions and within a model membrane interface as well as document the redox potential of these systems accompanying the conformational studies.

Here, we use an abbreviation system where MK with two isoprene units is MK-2 and with nine isoprene units is MK-9, Figure 1. Naturally occurring lipoquinones are characterized by the presence of an isoprenyl side-chain of varying length from 1 to 14 isoprene units[21,22] depending on the species of origin; a characteristic long used to assist taxonomic efforts. Textbooks often represent UBQ and MK as "Q" or "MQ" in illustrations of the ETS, and in primary literature they are generally shown in an extended conformation, Figure 1.[7,23,24] The extended conformation of these molecules seems highly unlikely in light of the one-step cyclization of squalene epoxide, an isoprenoid compound containing six isoprene units, to form the protosterol cation, which contains the basic steroidal ring system with eight chiral centers.[25,26] Woodward reported the cyclization of this
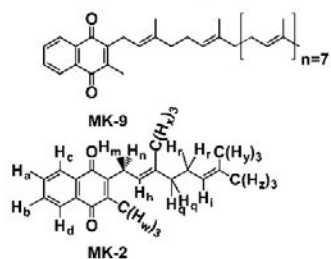
275

Figure 1. Structure of menaquinone-9 (MK-9), a representative MK found in *Mycobacterium tuberculosis* (top) and MK-2, a simplified MK analog (bottom), is also shown. Protons are labeled on MK-2 for spectral interpretation.

polyisoprenoid squalene epoxide forming only one stereoisomer out of the possible 256 (2^8) in 1953.[25,26] The stereospecificity of this reaction requires preorganization of the epoxide before protonation, and such a conformer is not the extended conformation commonly depicted in the literature.

Small angle X-ray diffraction experiments with the isoprenoid dolichol, an alcohol with 18−20 isoprene units, indicated that the molecule adopted a helical structure in organic solvent.[27] The conformation of the isoprenoid moiety in MK derivatives is likely important to its function as an electron-transfer agent and other biological roles. Although nothing is known about the conformation of MK derivatives, limited conformational analysis is available on different classes of compounds including alkanes, alkenes, and fatty acids with much simpler structures.[28−42] The all-*trans* conformations of alkanes are generally considered the most stable, and therefore, it is expected that the most prevalent conformation of an alkane is the fully extended alkyl chain.[28] A few studies have been reported with simple alkanes and a range of other, more complex compounds with large alkane-components such as in polyenes and fatty acids.[29,30] The U-shape in fatty acids was described when bound to a fatty acid binding protein (FABP), where the alkyl chain region of two fatty acids, palmitic and oleic acids, folds over in the shape of a U.[39,40] In 2008, X-ray crystal structure analysis, as well as NMR spectroscopy, also supported the U-shaped conformation of amphiphilic alkyl chains bound to a synthetic receptor where the folded C_8, C_{10}, and C_{12} conformations have anticlinal as well as *gauche* arrangements.[39,40] Based on these few examples, we hypothesized that MKs will adopt folded conformations depending on specific environmental conditions.

In this manuscript, we describe the synthesis and characterization of a truncated MK derivative with two isoprene units. MK-2 (Figure 1) can be characterized in detail and serves as a

representative MK reference compound as it is the simplest MK containing a napthoquinone and repeating isoprenyl side-chain allowing comparison to more complex MK-derivatives found in various microorganisms.[6,43,44] First, the conformation of MK-2 was investigated in organic solvents (polar and hydrophobic). Next, because we are ultimately interested in the function of these derivatives, we measured the electrochemical potential of MK-2 in the organic solvents where the conformations were determined. Finally, the location and conformation of MK-2 in simple membrane model systems was examined. Combined, our results show that MK-2 folds into a U-shaped conformation in solution contrary to common perception and that a folded, slightly different U-shaped conformation also exists in the presence of a simple model lipid membrane interface.

■ RESULTS AND DISCUSSION

Synthesis of MK-2. MK-2 was synthesized using a procedure in literature (Scheme 1).[45,46] First, menadione **1** was reduced to the corresponding menadiol **2** using aqueous sodium dithionite. Geraniol **3** was coupled to menadiol **2** using the Lewis acid catalyst, boron trifluoride. This preparation produced a yield of 20% overall, which is lower than the reported MK-2 preparation with the deuterated analog in literature.[45] The lower yield appears to be due to extensive alkylation at the C2 position instead of the desired C3 position; however, this side product is readily separated using column chromatography. Highly pure material yields a yellow solid upon crystallization at −20 °C and retains this state when warmed to room temperature, while material with impurities does not crystallize and remains a red oil.

1D ^{1}H NMR Spectroscopic Studies of MK-2 in Different Solvents. MK-2 was first characterized using 1D ^{1}H NMR spectroscopy. Figure 2 shows ^{1}H NMR spectra of MK-2 in isooctane (2,2,4-trimethylpentane), d_5-pyridine, d_6-benzene, d_3-acetonitrile, d_6-DMSO, and D_2O. The observed chemical shifts of MK-2 vary dramatically in the different solvents shown. Hydrophobic solvent environments including aliphatic (iso-octane) and aromatic (d_5-pyridine and d_6-benzene) as well as hydrophilic (d_3-acetonitrile, d_6-DMSO, and H_2O/D_2O) solvent environments generate very different spectroscopic signatures. For example, the pairs of aromatic protons, H_a/H_b and H_c/H_d, are significantly different in the two different classes of solvents. This observed variation in chemical shift could be attributed to conformational changes of MK-2 in the various solvent environments investigated, alterations of the electronic state due to interaction with the solvent, or most likely, a combination of both. Focusing on the ^{1}H NMR spectra of MK-2 in the three hydrophilic solvents, d_3-acetonitrile, d_6-DMSO, and D_2O, some differences and similarities are observed (Figure 2). The MK-2 spectrum in D_2O required significantly more scans to produce a reasonable spectrum because of the poor solubility in D_2O. The

Scheme 1. Synthetic Route To Prepare MK-2 4 from Menadiol 2 and Geraniol 3 using Lewis Acid Catalyst Conditions[45,46]
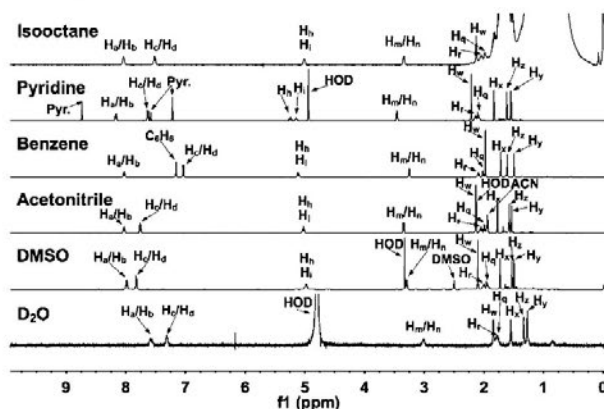
204
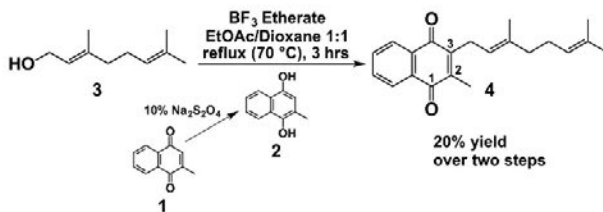
Figure 2. 1D ^{1}H NMR (400 MHz) spectra of MK-2 in hydrophilic (d_6-DMSO, d_3-acetonitrile, and D$_2$O) and hydrophobic [isooctane (2,2,4-trimethylpentane), d_5-pyridine, and d_6-benzene] solvents. Proton peak text labeling corresponds to MK-2 structure in Figure 1.

proton chemical shifts generally are observed further upfield in D$_2$O, presumably indicative of more aggregation in this solvent. The alkene H$_h$ and H$_i$ proton signals are not observed in the D$_2$O spectrum because of overlap with the HOD peak. However, the HOD signal in the d_6-DMSO spectrum is observed at 3.3 ppm, which allows for observation of the alkene protons, H$_h$ and H$_i$, at 4.9 ppm. The spectrum of MK-2 in d_6-DMSO is very similar to that in d_3-acetonitrile, and both also have some similarities to the MK-2 spectrum in D$_2$O. The aromatic protons, H$_a$/H$_b$, shifted about 0.2 ppm from the H$_c$/H$_d$ signals in both solvents. This suggests that these protons remain in similar chemical environments in these two solvent environments. Combined, these three spectra provide a representation of the properties of the MK-2 in a hydrophilic solvent environment.

Next, the aromatic and alkene protons were examined in the hydrophobic solvents, isooctane, d_5-pyridine, and d_6-benzene (Figure 2). Here, protons H$_a$, H$_b$, H$_c$, H$_d$, H$_h$, and H$_i$ are observed and readily identified. The signals from alkene protons, H$_h$ and H$_i$, are both further downfield compared to the signals in hydrophilic solvents, and most interestingly, the two alkene protons become nonchemical shift equivalent in d_5-pyridine. This contrasts with the aliphatic protons in the spectrum in d_6-benzene, which are like those in d_6-DMSO except for H$_q$, H$_r$, H$_w$, and H$_z$. The changes in the chemical shifts are most distinctive in the aromatic and alkene protons, suggesting that there are some major differences in their respective environments. Together, these differences strongly indicate that MK-2 is sensitive to the solvent environment. However, information from 2D NMR experiments is needed to elucidate if this change in chemical shift is due to conformational variations and/or solvent effect.

^{1}H–^{1}H 2D NOESY and ^{1}H–^{1}H 2D ROESY NMR Spectroscopic Studies of MK-2 in d_6-DMSO and d_5-Pyridine. Differences between the conformations observed in d_6-DMSO vs d_5-pyridine are likely manifested by the conformation minimizing the unfavorable interactions with the solvent environment and maximizing favorable intramolecular interactions with the isoprenyl side-chain. To investigate the conformation of MK-2 in organic solvents, we utilized two different but complementary 2D NMR methods, ^{1}H–^{1}H 2D NOESY and ^{1}H–^{1}H 2D ROESY. Figure 3 shows the ^{1}H–^{1}H 2D NOESY and ROESY NMR spectra of MK-2 in d_6-DMSO and

portions of the spectrum in d_5-pyridine. Figure 3A shows the complete ^{1}H–^{1}H 2D NOESY spectrum of MK-2 in d_6-DMSO and Figure 3B–C shows zoomed in regions of interest in the NOESY and ROESY spectra collected in d_6-DMSO, respectively (see Figures S3–S4 for full spectra). Figure 3D–F shows zoomed in regions of interest in the NOESY and ROESY spectra collected in d_5-pyridine, respectively (see Figures S6–S7 for full spectra). Figure 3B,D illustrates that MK-2 alkene protons, H$_h$ and H$_i$, are in similar environments in d_5-pyridine and d_6-DMSO due to the observance of similar NOE cross peaks. In both solvents, Figure 3B,D shows NOE cross peaks illustrating that H$_h$ and H$_i$ interact with H$_n$/H$_m$, H$_q$, H$_r$, and H$_z$. Figure 3B,D shows NOE cross peaks demonstrating proton H$_w$ interacts with protons H$_h$/H$_i$ and H$_m$/H$_n$ in both d_6-DMSO and d_5-pyridine. Figure 3C,E shows partial ^{1}H–^{1}H 2D ROESY NMR spectra where the focus is on proton H$_w$ in d_6-DMSO and d_5-pyridine (see Figures S4 and S7 for full spectra and Figure S9 for NOE/ROE correlation traces (slices)). Figure 3B–C shows partial spectra for MK-2 in d_6-DMSO, where NOE and ROE cross peaks indicate the H$_w$ proton interacts with H$_q$, H$_r$, H$_x$, and H$_y$. However, the lack of ROE cross peaks in Figure 3E shows H$_w$ does not interact with H$_y$ or H$_z$ in d_5-pyridine (observed cross peaks between H$_w$ and H$_y$ or H$_z$ in d_5-pyridine are likely due to TOCSY exchange). The observation of cross peaks shows that there are similar interactions between the aromatic and alkene protons in the two solvents; however, there is a twist around the C–C bond leading to closer proximity of the H$_w$ with the H$_q$, H$_r$, H$_x$, and H$_y$ protons in d_6-DMSO. The NOE and ROE cross peaks in the d_6-DMSO spectrum in Figure 3 clearly support a folded, U-shaped conformation for MK-2 in d_6-DMSO. However, evidence of a folded conformation for MK-2 is not as definitive in d_5-pyridine due to the lack of NOE and ROE cross peaks between H$_w$ and H$_y$ or H$_z$. If MK-2 did adopt a U-shaped conformation in d_5-pyridine, it would have a conformation as shown in Figure 4B, where the distance between H$_w$ and H$_y$/H$_z$ is beyond observation in the ^{1}H–^{1}H 2D NOESY and ROESY NMR experiment. This conformation for MK-2 in d_5-pyridine is based on other NOE/ROE cross peaks observed (i.e., H$_w$ to H$_h$, H$_w$ to H$_q$ or H$_r$, H$_w$ to H$_x$). Figure 3F illustrates π–π stacking between pyridine and part of the napthoquinone ring, which could possibly explain the lack of interaction between H$_w$ and H$_y$ or H$_z$.
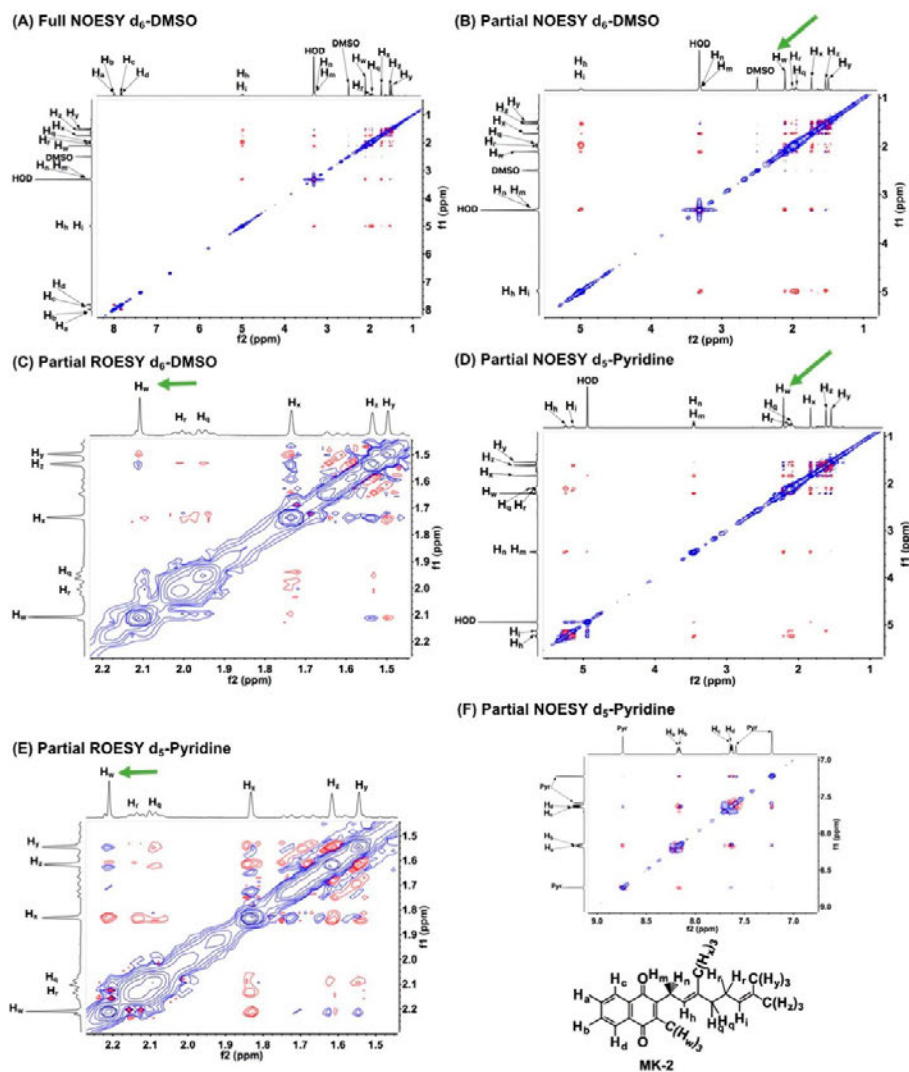
205

Figure 3. ^{1}H−^{1}H 2D NOESY and ^{1}H−^{1}H 2D ROESY NMR (400 MHz) spectra of 20 mM MK-2 in d_6-DMSO and d_5-pyridine at 26 °C. (A) Full ^{1}H−^{1}H 2D NOESY NMR spectrum of MK-2 in d_6-DMSO. (B) Partial ^{1}H−^{1}H 2D NOESY NMR spectrum of MK-2 in d_6-DMSO. (C) Partial ^{1}H−^{1}H 2D ROESY NMR spectrum of MK-2 in d_6-DMSO. (D) Partial ^{1}H−^{1}H 2D NOESY NMR spectrum of MK-2 in d_5-pyridine. (E) Partial ^{1}H−^{1}H 2D ROESY NMR spectrum of MK-2 in d_5-pyridine. (F) Partial ^{1}H−^{1}H 2D ROESY NMR spectrum of MK-2 in d_5-pyridine illustrating stacking interactions. Blue intensity contours represent negative NOE's or ROE's, and red intensity contours represent positive NOE's or ROE's. A standard NOESY pulse sequence was used consisting of 200−256 transients with 16 scans in the f1 domain using a 500 ms mixing time and a 1.5 s relaxation delay. A standard ROESYAD pulse sequence was used consisting of 200 or 256 transients with 16 scans in the f1 domain using a 400 ms mixing time and a 2.0 s relaxation delay. The structure of MK-2 is shown with a proton labeling scheme key. Green arrows indicate proton H_w, where the observed cross peaks differed the most between the two solvents studied.

Illustrating MK-2 Conformations using Molecular Mechanics. MK-2 has a short repeating isoprenyl chain (C_{10}) but contains enough carbons to produce numerous degrees of rotational freedom; therefore, even the truncated version of MK, MK-2, can assume many different conformations. Using molecular mechanics calculations, we explored the energy surface and visualized specific conformations defined by the ^{1}H−^{1}H 2D NOESY and ROESY NMR experiments of MK-2 in
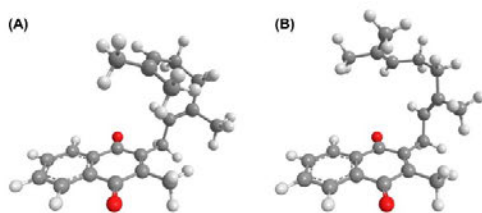
Figure 4. MK-2 conformations generated using MMFF94 calculations to illustrate the conformations elucidated by the 2D NMR studies. (A) Illustrates the MK-2 conformation in d_6-DMSO determined from ^{1}H−^{1}H 2D NOESY and ROESY NMR spectral data cross peak interactions (66.8 kcal/mol, and internuclear distance H_w−H_y: 2.6 Å). (B) Illustrates a potential U-shaped MK-2 conformation in d_5-pyridine consistent with the ^{1}H−^{1}H 2D NOESY and ROESY NMR spectral data cross peak interactions (66.7 kcal/mol, and internuclear distance H_w−H_y: 6.1 Å). See Supporting Information for a table of selected proton to proton distances for conformations A and B.

d_6-DMSO and d_5-pyridine. Specific conformations were generated based on distances imposed by the NMR data and then energy optimized to produce realistic bond lengths and angles for these conformations. Finally, an energy was calculated to ensure that the conformation was at a reasonable energy. Longer calculations generally lead to rotations around bonds and conformations not exactly as those suggested from the NMR data (see below and Supporting Information). The intent with the molecular mechanics calculations was to illustrate conformations corresponding to the ^{1}H−^{1}H 2D NOESY and ROESY NMR spectral data in d_6-DMSO and d_5-pyridine constrained by all cross peak interactions observed as well as to provide visual aids (Figure 4). One of the low-energy conformations generated for MK-2 has a conformation (Figure 4A, 66.8 kcal/mol, H_w−H_y: 2.6 Å) consistent with the 2D NOESY and ROESY spectral parameters observed in d_6-DMSO. Figure 4B illustrates a potential conformation of MK-2 that is consistent with the 2D NOESY and ROESY spectral parameters observed in d_5-pyridine (66.7 kcal/mol, H_w−H_y: 6.1 Å). See Table S1 for selected proton to proton distances for conformations seen in Figure 4A−B consistent with the 2D NOESY and ROESY NMR spectral parameters. The MK-2 conformation determined in d_6-DMSO adopts a folded, U-shaped conformation.

Fewer NOE and ROE cross peaks were observed in d_5-pyridine that would indicate a folded conformation, and although this does not preclude a folded conformation, it does suggest that the H_w−H_y internuclear distance is longer and outside the observable range using the ^{1}H−^{1}H 2D NOESY and ROESY NMR experiment. We based this folded conformation off other NOE and ROE cross peaks observed, which were suggestive of folding (see Figure 3 and related discussion). However, a U-shaped conformation has been observed by NMR analysis in another aromatic solvent, d_6-benzene, for n-dodecane.[34] The U-shaped conformations shown in Figure 4 are representative of many possible stable conformations MK-2 could adopt. For comparison, Figure S12C shows another favorable conformation for MK-2 that has a characteristic U-shape. The energy of the conformation C shown in Figure S12C was the lowest energy we found. This conformation was obtained by subjecting an extended MK-2 conformation to 10,000 iterations followed by an energy minimization, illustrating that nonextended conformations are readily reached and energetically favorable.

Combined, the stability of the U-shaped conformations shown by these simple calculations is in line with work reported that showed ^{1}H NMR spectra of n-pentane and n-hexane measured in polar and spherical solvents such as DMSO favor *gauche* conformations as well as the reported U-shaped conformations of alkyl chains bound to synthetic receptors.[39,40,47] The folded conformations for MK-2 demonstrated herein from experiments align with reported computationally determined conformations for MK analogs.[48] However, it is contrary to the general expectation that the all-*trans* conformations of alkanes or alkyl components are the most stable.[7,23,24,28]

In addition to the U-shaped conformations seen in conformations A and B in Figure 4, a series of alternative conformations of MK-2 (Figure S12D−E) were also generated from the structures most often depicted by representations in the literature and then were energy optimized. Conformations D−H in Figure S12 were generated to compare these conformations energetically to the two U-shaped conformations shown in Figure 4A−B. The energies of conformations D−H in Figure S12 were all higher (~11 to ~23 kcal/mol) than the conformations found in d_6-DMSO, d_5-pyridine, and conformation C (Figure S12). Additional analysis of conformations and a table of selected internuclear distances of MK-2 conformations from Figure 4 and Figure S12 are given in Table S1.

Selected simple alkanes and a few other, more complex compounds with long alkyl-segments such as in polyenes and fatty acids report that the extended and folded forms are comparable in energy to the all-*trans* form.[29,30] The "pentane effect" for longer chains destabilizes the *gauche* conformations because of unfavorable g$^+$g$^−$ arrangements, which increases the energy by ~0.55 kcal/mol with each kink in the chain.[29,30] In contrast, *gauche* arrangements are often energetically favored because of entropic contributions.[31,32] This is in part due to the spatial requirements that all molecules exert and can be justified using limited sphere considerations.[33] *Gauche* arrangements tend to favor folded conformations where the degree of folding of n-alkanes (C_5−C_{32}) in solution depends on the strength of the dispersion force of the solvent[35] and the degree of folding increases with increasing chain length of the solute.[34,36] Other molecules that contain alkyl chains such as fatty acids and polyethylene derivatives have also been reported as either extended chains or in folded conformations depending on physical and environmental conditions.[31,32,37,38] Conformational analysis of long chain allylic polyunsaturated fatty acid chains using Hartree−Fock calculations showed that conformational differences between the all-*trans* and helical folded structures are only a few kcal/mol.[37] Ultimately, there are a few but strongly convincing examples[30,39−42] that folded and/or U-shaped conformations are likely to become much more important than have been recognized previously. The studies presented herein represent a new class of compounds that adopt a U-shaped conformation, illustrating that these folded conformations are likely to be important and may impact the biological function of these lipoquinone systems. It is very important to recognize the molecular plasticity, which allows the alkyl chain to assume shapes depending on the complementary structures or influences of the immediately surrounding environment.

Electrochemistry of MK-2 in Different Solvents. Our interest in these systems relates to the fact that the redox potential of MK is important in shuttling electrons between protein complexes. Although the focus of this manuscript has been on the conformations of these compounds, we are particularly interested in redox properties because we are aiming

to investigate the function of these systems as well. For MKs to carry out this process, MKs must associate with the trans-membrane proteins involved in the electron-transfer processes.[49] The electron-transfer processes all take place within or near the membrane interface with two one electron reduction processes sequentially forming the radical anion (semiquinone) and then the dianion.[50−52] Even though there has been many reports in literature on the redox potentials of MK derivatives, the origin of these changes is not well understood.[50−52] These processes are particularly poorly understood when the quinones are present in a hydrophobic molecule that is entirely or partly located in the membrane of a biological system. Although, it is premature to correlate conformation with redox potential, we are seeking systematic information where redox potentials and conformations are known (i.e., within different organic solvents) and the electrochemical data on this system becomes an important frame of reference because the conformational analysis has been carried out. We hypothesized that the redox potential of MK-2 will vary based on organic solvent environment.

Although this hypothesis would be anticipated to be confirmed, it is important to measure how and if the magnitude of the redox potential changes as the solvent environment changes because the function of MK-2 is tied to the redox potentials. Initially, redox studies were planned to be carried out in DMSO, acetonitrile, and benzene; however, because of low solubility of all of the electrolytes examined in benzene, benzene was replaced with pyridine as a representative aromatic solvent.[53] The electrolyte tetrabutylammonium perchlorate (TBAP) was chosen because 1D ^{1}H NMR studies showed that the addition of TBAP to MK-2 solutions (solvents: d_6-DMSO, d_5-pyridine, d_3-acetonitrile) did not affect the observed chemical shifts of the MK-2 protons, and thus no evidence for artifacts due to ion pairing would be observed (see Supporting Information for further description of the electrochemical analysis, and see Figure S13 for MK-2/TBAP NMR studies).

MK-2's first electrochemical potential is the one electron reduction of the quinone to semiquinone ($Q/Q^{\bullet-}$), and the second is the one electron reduction of the semiquinone to the dianion ($Q^{\bullet-}/Q^{2-}$), Scheme S1.[50−52] The cyclic voltammo-gram's (CVs) of MK-2 and an internal standard of ferrocene (Fc^+/Fc) in three organic solvents are shown in Figure 5. The $Q/Q^{\bullet-}$ $E_{1/2}$ vs Fc^+/Fc for MK-2 in DMSO, CH$_3$CN, and pyridine were measured to be −1.155 (±0.001) V, −1.230 (±0.003) V, and −1.331 (±0.001) V, respectively. As shown in Figure 5, we included the Fc^+/Fc reference in the data presented. These results are consistent with $Q/Q^{\bullet-}$ $E_{1/2}$ vs Fc^+/Fc values given for 1,4-naphthoquinone.[50,54] The values determined experimentally for $Q^{\bullet-}/Q^{2-}$ $E_{1/2}$ vs Fc^+/Fc for MK-2 in DMSO, CH$_3$CN, and pyridine were measured to be −1.863 (±0.008) V, −1.902 (±0.012) V, and −2.075 (±0.003) V, respectively (Table S2). In Figure 6, the half-wave potentials are plotted showing the trend that both redox processes are more readily reduced in DMSO than CH$_3$CN or pyridine similar to the trend observed in literature for 1,4-napthoquinone potentials.[54]

In summary, during the first electrochemical process producing the semiquinone, MK-2 has the most positive potential in DMSO and the most negative potential in pyridine, showing MK-2 is slightly more reducible in DMSO than pyridine or CH$_3$CN. The observation of differing redox potentials between organic solvents supports the second hypothesis that the redox potential of MK-2 is influenced by the specific organic solvent, where a contributing factor to the observed changes is due to the differences between the dielectric constant of each
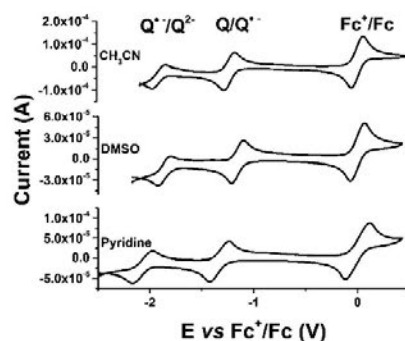

Figure 5. Three representative CVs of 2 mM MK-2 in CH$_3$CN, DMSO, and pyridine. The potentials are referenced to the Fc^+/Fc couple (2 mM) determined in each solvent. From left to right, redox processes are $Q^{\bullet-}/Q^{2-}$, $Q/Q^{\bullet-}$, and Fc^+/Fc. Each sample has 0.1 M TBAP and was degassed with argon gas for 10 min at ambient room temperature before spectra were recorded. Current sweeps are in the anodic direction from −2 V to 1 V and back to −2 V. A 100 mV scan rate was used.
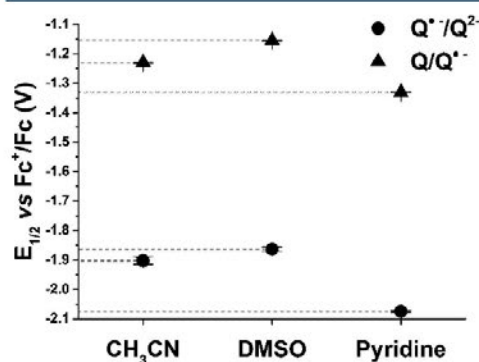

Figure 6. Measured $E_{1/2}$ (vs Fc^+/Fc in V) of MK-2 $Q/Q^{\bullet-}$ and $Q^{\bullet-}/Q^{2-}$ redox processes vs solvent. Added lines show the distinction between each solvent for each redox process. Each solvent was run in triplicate with error bars shown. Student's t test indicated the half wave potentials of each redox process are significantly different in each solvent ($p < 0.01$ for $Q^{\bullet-}/Q^{2-}$ CH$_3$CN-DMSO and $p < 0.0001$ for all other comparisons). See Supporting Information for details.

solvent. The different organic solvents influence the observed redox potential of MK-2, and from the 2D NMR studies on the conformation of MK-2, slight differences in conformation were observed, which may suggest that a combination of solvent effect and conformational differences of MK-2 may affect the redox potential.

Interaction of Langmuir Phospholipid Monolayers with MK-2. The physiologically relevant environment for MKs is in association with membranes; therefore, we also studied the interaction of MK-2 with a more direct model membrane interface, a phospholipid monolayer. Several membrane models exist including Langmuir phospholipid monolayers, liposomes, micelles, and reverse micelles (RM) (Figure 7).[55−61] Each model system has advantages and disadvantages, and we have chosen to investigate the
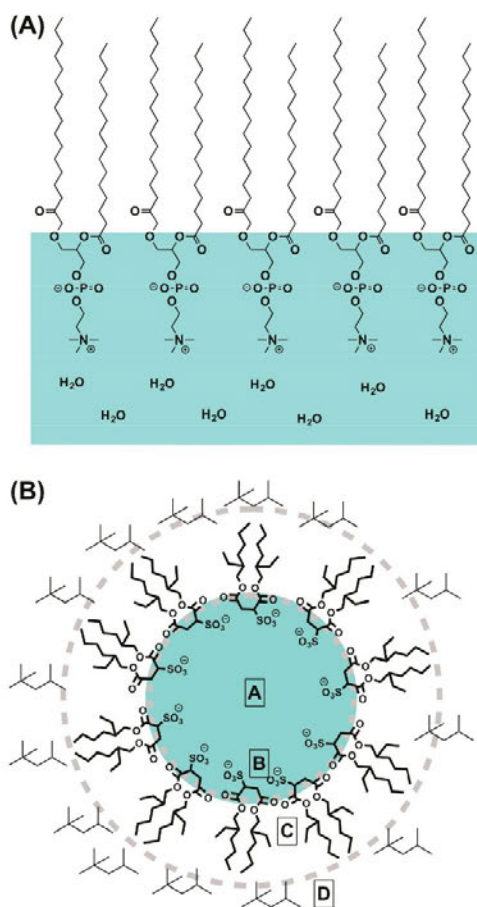
Figure 7. Schematic diagram of (A) a Langmuir phospholipid monolayer and (B) a RM present in a microemulsion. Labeling for the RM is as follows: the water pool (A), the Stern layer (B), the surfactant tails (C), and the organic solvent, isooctane (D).

phospholipid monolayer because of MKs direct association with a membrane and the RM system because RMs allow for the determination of molecular placement and conformation of MK-2 within the interface.[55−61]

First, we describe our studies with Langmuir phospholipid monolayers[60,61] consisting of phospholipids to gain insight into the interactions between two classes of phospholipids (dipalmitoylphosphatidylcholine (DPPC) or dipalmitoylphosphatidylethanolamine (DPPE)) and MK derivatives. These studies will demonstrate how the phospholipid packing is affected by the presence of MK derivatives as it interacts with the phospholipid interface (Figure 7A).[60,62−65] Due to the low solubility of MK-2 in aqueous environments, the Langmuir phospholipid monolayer studies involve experimental protocols used for other materials with low solubility in water, such as UBQ.[66,67] Figure 8 shows the change in surface pressure as a

function of area per molecule of DPPC or DPPE in the presence of various amounts of MK-2. The resulting compression moduli as functions of surface pressure are shown in Figure S14.

The compression isotherm of DPPC shows a transition at ~8 mN/m and both DPPC and DPPE collapse at ~55 mN/m similar to findings reported in literature.[68] The compression isotherm of the 1:1 mixture of DPPC and MK-2 shows a disappearance of the gas to liquid phase transition at 8 mN/m, suggesting there is a condensing effect of MK-2 with DPPC at a high area per molecule/low surface pressure. Moving to DPPE, the 1:1 mixture of MK-2 with DPPE reduces the collapse pressure of the film to 50 mN/m, showing destabilization of the DPPE film. The pure MK-2 films had limited stability shown by a maximum surface pressure of ~20 mN/m. This result suggests MK-2 forms a less stable film than the phospholipids.[66−68] To understand the interactions of MK-2 with DPPE and DPPC further, the compression moduli were calculated using equation 4 (see Supporting Information), where the compression modulus is the measure of the compressibility of the film.

Our results are interpreted as MK-2 having a condensing effect on DPPC phospholipid films at high area per molecule/low pressure and destabilization of DPPE phospholipid films. The resulting mixed films (DPPC/MK-2 or DPPE/MK-2) were also consistent with reported UBQ, suggesting similar trends where UBQ was shown to be compressed out of the phospholipid interface.[66,67,69] In summary, MK-2 has a condensing effect on DPPC phospholipid films, a destabilization of DPPE phospholipid films, and is most likely compressed out of the phospholipid film similar to UBQ.[66,67,69] Unfortunately, these studies do not directly show whether a folded or extended conformation of MK-2 exists. A folded conformation occupies a larger volume than the extended conformation, which would affect packing within the phospholipid interface. Our studies do demonstrate that MK-2 interacts with the phospholipid model membrane interfaces of DPPC and DPPE even above physiologically relevant pressures. It is possible that the observation of the destabilization of the DPPE phospholipid films (not observed for DPPC) by the presence of the MK may suggest a folded MK-2 conformation that does not fit in the organization of the DPPE film (possibly related to packing of the phospholipid).

1D ¹H NMR Spectroscopic Studies of MK-2 in RMs. Our ultimate objective was to characterize the molecular details of MK-2's association with membrane-like interfaces. This characterization includes determining the location and conformation of MK-2; therefore, the RM model system was investigated (Figure 7B).[60,62−65,70] In the RM, a ternary microemulsion system forms when a surfactant is dissolved in an organic solvent and the addition of water creates nanosized water droplets encased in surfactant.[56,63,65,70−72] This dynamic, yet simple, model can provide molecular detail on location and conformation of MK at an interface using NMR spectroscopy, whereas the use of phospholipids such as DPPC can have overlapping proton signals with key MK proton signals making interpreting conformational information very complex.[70,73−76] RM systems provide information regarding the location, conformation, and physical interactions of MK with lipid films and potentially membranes, which allowed us to examine our third hypothesis that the membrane interface influences the conformation of the MK derivative.

To explore the location of MK-2 at a lipid/water interface further, studies were conducted using a simple microemulsion interfacial system, which allows for identification of molecular placement. Figure 9 shows a stack plot of 1D ¹H NMR spectra for
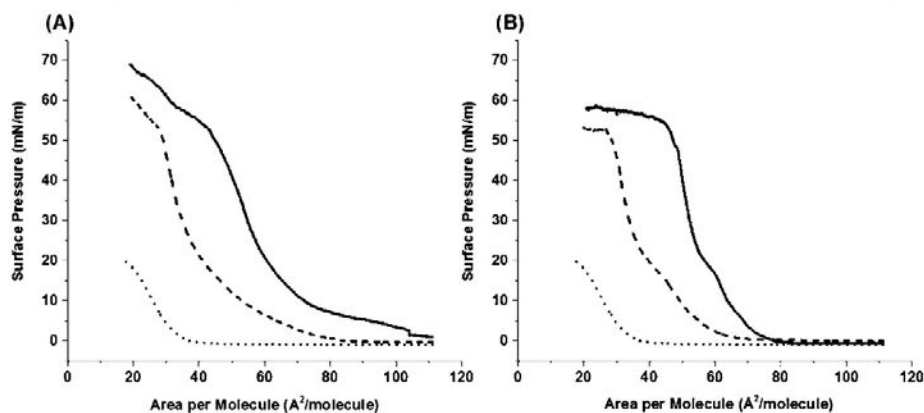
Figure 8. Compression isotherms of MK-2 films (dotted lines), DPPC or DPPE phospholipid films (solid lines), or a 50:50 mixture of MK-2 and phospholipid (dashed line). On the left (A) are the resulting compression isotherms of MK-2 and DPPC, while on the right (B) are the resulting compression isotherms of MK-2 and DPPE.
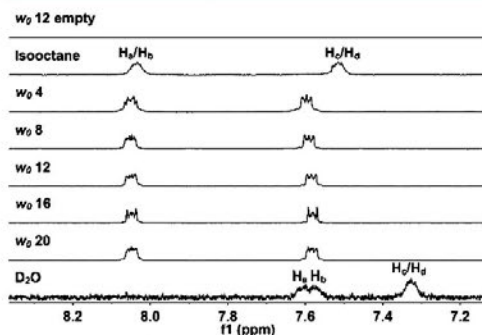

Figure 9. 1D ^{1}H NMR (400 MHz) spectra of MK-2's aromatic protons, H_a, H_b, H_c, and H_d in D_2O, isooctane, and different sized RMs. Proton peak text labeling corresponds to MK-2 proton labeling scheme key found in Figure 3. H_a, H_b, H_c, and H_d protons undergo a chemical shift upon inclusion inside RMs.

the aromatic protons (H_a/H_b and H_c/H_d) of MK-2 in solutions of D_2O, isooctane, or isooctane solutions of MK-2 containing RMs (D_2O/AOT/isooctane microemulsions) of various sizes (w_0: 4, 8, 12, 16, and 20, where $w_0 = [D_2O]/[AOT]$) and for comparison with an empty AOT/isooctane RM. The aromatic MK-2 protons in the AOT/isooctane RMs are similar to the signals observed in isooctane but very different from the signals observed in D_2O. The distance between H_a/H_b and H_c/H_d is 0.52 ppm in isooctane, 0.47 ppm in the RM, and 0.27 ppm in D_2O. This suggests that the environment of the MK-2 protons in the AOT/isooctane RMs is more like an environment in isooctane than D_2O, where MK-2 is no longer in isooctane but associating with the AOT molecules. The signals from the H_c/H_d protons in the AOT/isooctane RMs do change slightly as the RM size increase or decreases. This observation is also consistent with MK-2 penetrating and residing in the interface.

To verify that the RMs formed in the samples used and that the properties of the samples are consistent with previous studies,[61,63,70,77,78] dynamic light scattering (DLS) experiments

were carried out. These studies confirmed the formation of RMs, and that the RM did not change significantly upon the addition of MK-2. This was carried out by measuring the sizes in the presence and absence of MK-2 and confirming that the size was as those reported previously (data not shown).[63] Overall, these results are consistent with MK-2 penetrating the RM model membrane interface; however, 2D studies are described below to get more information regarding the placement and conformation of MK-2 within the RM system.

^{1}H−^{1}H 2D NOESY and ROESY NMR Spectroscopic Studies of MK-2 in a RM Model Membrane System. To provide further evidence regarding the location, orientation, and conformation of MK-2 within RMs, we obtained the ^{1}H−^{1}H 2D NOESY NMR spectrum and the ^{1}H−^{1}H 2D ROESY NMR spectrum of MK-2 in a w_0 12 RM, Figures 10 and 11. Figure 10 shows a partial ^{1}H−^{1}H 2D NOESY and ROESY NMR spectra indicating both AOT and MK-2 protons, whereas Figure 11 focused in on selected proton interactions specifically in the NOESY spectrum (see Figures S10−S11 for full spectra). Figure 11A shows cross peaks between the aromatic H_a/H_b and H_c/H_d and parts of the AOT CH_2 and CH_3 tail groups (i.e., H8′ and H10′ protons, see Figure 12 for AOT proton labeling key). Figure 11B shows cross peaks between alkene protons, H_i and H_h, with HOD and AOT's H1, H1′, H3, and H3′ protons and only evidence of a weak interaction between MK-2 and isooctane. These interactions are consistent with placement of MK-2 between the AOT tails, as shown using a depth perception drawing in Figure 12.

Regarding the conformation of MK-2 associated with the RM−water interface, the NOE and ROE cross peaks in Figure 10 show interactions between H_w and H_x/H_y and between H_w and the alkene protons, H_h/H_i, which is consistent with a folded, U-shaped conformation. In the proposed conformation, the C2−C6 atom to atom distance in MK-2's isoprenyl side-chain was found to be 3.6 Å, which is consistent with a U-shape (g^+g^-) conformation, Figure 13) for MK-2 placed at the RM interface (see Supporting Information for further discussion and internuclear distances of different MK-2 conformations). An illustration of an MK-2 conformation consistent with these observations is shown in Figure 13. This U-shaped conformation
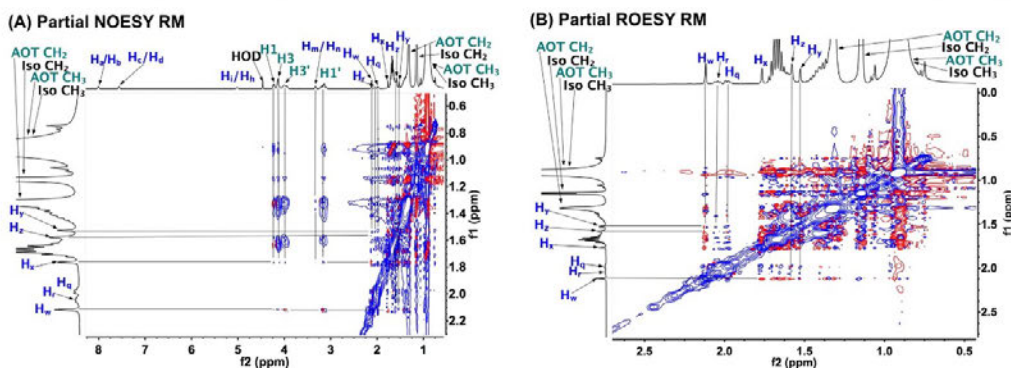
Figure 10. Partial $^1H-^1H$ 2D NOESY and ROESY NMR (400 MHz) spectra of MK-2 inside w_0 12 RM at 26 °C. (A) Partial $^1H-^1H$ 2D NOESY NMR spectrum in a w_0 12 RM. (B) Partial $^1H-^1H$ 2D ROESY NMR spectrum in a w_0 12 RM. Blue to blue proton text labeling shows MK-2 to MK-2 interactions, teal to teal proton text labeling shows AOT to AOT interactions, and blue to teal proton text labeling shows MK-2 to AOT interactions. Blue intensity contours represent negative NOE's or ROE's and red intensity contours represent positive NOE's or ROE's. A standard NOESY pulse sequence was used consisting of 256 transients with 16 scans in the f1 domain using a 200 ms mixing time and a 1.5 s relaxation delay. A standard ROESYAD pulse sequence was used consisting of 256 transients with 16 scans in the f1 domain using a 200 ms mixing time and a 2.0 s relaxation delay. See Figure 3 for MK-2 proton labeling scheme key and Figure 12 for AOT proton labeling scheme key.

Figure 11. Partial $^1H-^1H$ 2D NOESY NMR (400 MHz) spectra of MK-2 inside a w_0 12 RM at 26 °C illustrating interactions of MK-2 with the AOT surfactant tails. (A) Interactions between MK-2's aromatic protons and AOT. (B) Interactions between MK-2 alkene protons and AOT. The blue to blue proton text labeling shows MK-2 to MK-2 interactions, teal to teal proton text labeling shows AOT to AOT interactions, and blue to teal proton text labeling shows MK-2 to AOT interactions. Blue intensity contours represent negative NOE's, and red intensity contours represent positive NOE's. A standard NOESY pulse sequence was used consisting of 256 transients with 16 scans in the f1 domain using a 200 ms mixing time and a 1.5 s relaxation delay. See Figure 3 for MK-2 proton labeling scheme key and Figure 12 for AOT proton labeling scheme key.
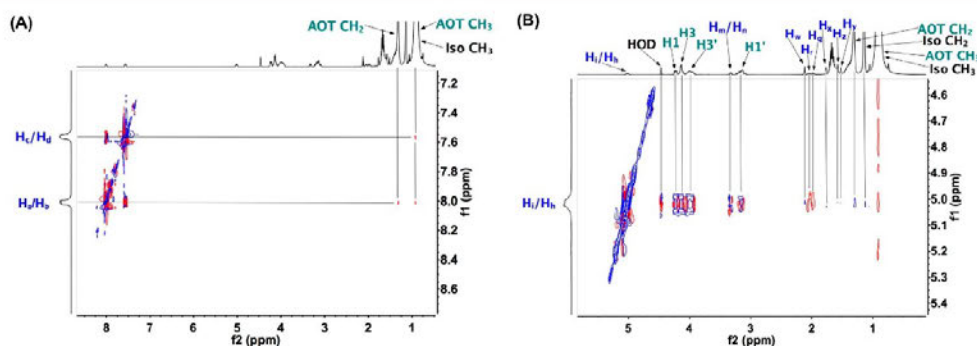
observed when MK-2 is associated within the RMs changed slightly from that observed in d_6-DMSO regarding where the double bond overlaps with the napthoquinone moiety. The overlap of the alkene and napthoquinone functionalities in the conformation associated with the interface is best illustrated by the top view in Figure 13B. Importantly, the U-shape fold remains, but slight rotation around the C–C bond facilitates the conformational changes in the U-shape.

Implications of Folded Conformations for MK Derivatives. Natural MKs contain a naphthoquinone and an isoprenyl side-chain with some variable number of repeating isoprene units, where MKs support the electron-transfer reactions in a range of systems.[6,43] MK-2 was synthesized allowing for detailed characterization of the molecule. The results presented herein for MK-2 suggests that other important MK derivatives in biology will adopt folded conformations as well and demonstrates the

need to prepare and study such derivatives both experimentally and computationally.

The extended conformations of long chain biological molecules such as fatty acids and polyenes are generally shown in the literature if the structure is presented.[7,23,24] However, a few studies of isoprene conformers and 1,3 acyclic dienes show the extended *trans* alkane conformations compare in energy with folded or helical conformations.[79,80] Although the folded conformations in those studies may be slightly higher in energy than unfolded conformations, the difference is surprisingly small. The C–C single bond lengths reported for stearic acid decreases under high pressure.[42] These bond shrinkages cause conformational and shape changes in stearic acid favoring folded conformations.[42] Previous studies using high-temperature UV-absorption spectroscopy, molecular orbital calculations, and gas-phase electron diffraction found that isoprene and chloroprene
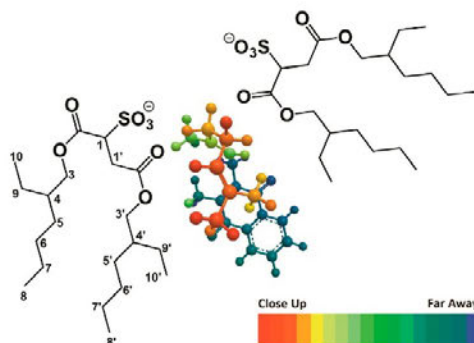
211

Figure 12. Illustration of MK-2's proposed folded, U-shaped conformation and placement in the RM interface. This arrangement is consistent with ^{1}H–^{1}H 2D NOESY and ROESY NMR spectral data obtained in a w_0 12 RM; however, MK-2 likely tumbles freely within the interface but maintains interactions with the region of AOT shown in the illustration. Color depth fading legend shows dark red as closer in distance and dark blue as farther in distance from the reader. AOT proton labeling scheme key is shown.
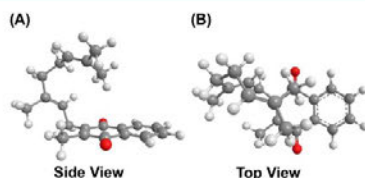

Figure 13. MK-2 conformation at an interface visualized using MMFF94 calculations. Molecular mechanics simulations generating the 3D conformation of MK-2 in a RM that is consistent with ^{1}H–^{1}H 2D NOESY and ROESY NMR spectral data. (A) Side view of energy minimized conformation (63.5 kcal/mol, and internuclear distance H_w–H_z: 4.0 Å) showing MK-2's isoprene side-chain adopting a hook-like shape also known as a folded, U-shaped conformation. (B) Top view of energy minimized conformation showing the terminal isoprene methyl groups overlapping the carbonyl groups on the napthoquinone.

conformations did, in fact, favor folded conformations.[81,82] Although these conditions are nonphysiological, they do demonstrate that changes in a physical parameter can affect the preferred conformation. Previous work has been carried out with fatty acids where the experimental studies showed that the conformations of the alkane portion of the fatty acids can and do change similar to conformations of MK-2 as shown in this work.[37] Our studies confirm the first hypothesis that MKs have different conformations depending on specific environmental conditions, which was achieved by first synthesizing MK-2 and then demonstrating that a U-shaped, folded conformation was adopted in d_6-DMSO, which was different from the conformation in d_5-pyridine.

Conformations can affect reactivity, and as in this case, the electron-transfer reactions facilitated by MK. MK forms complexes with several enzymes during the electron-transfer processes, and although kinetic characterizations of these systems have been reported,[83–85] less is known structurally. The redox potentials of MK-2 depicted in Figure 6 illustrate the trend where the most positive potential is in DMSO and the most

negative potential is in pyridine, which agrees with literature reports on menadione.[50,54] These results have identified that the redox potential of MK-2 changes as a function of solvent, and the origin of this change (presumably in part due to a change in dielectric constant between solvents) and whether these observed solvent effects can be associated with changes in conformation should be investigated in the future using both suitable high-level computational methods as well as electrochemistry. Indeed, the change in redox potential is likely to be important, and since there is no conjugation between the isoprenyl side-chain and napthoquinone, these effects are very interesting and may reflect that the energy required for the reduction is determined by the energy difference of the HOMO–LUMO gap in the two different conformations.[86] Orbital analysis of the HOMO–LUMO gap could potentially be informative and describe the origin of the observed varied biological effects of a series of N-alkyl MK derivatives that have been reported.[87,88] For example, replacement of a CH_2 group with a N atom modifies the parent system, creating a class of compounds with a nitrogen bound directly to the "naphthoquinone group." These molecules have dramatically different biological properties than the parent MK derivatives,[87,88] and it is possible that these activities could be related to the change in fundamental physical and chemical properties that occurs with N-alkyl isoprenoid substitution of the naphthoquinone ring. Combined, these results confirm the second hypothesis that the redox potential of MK-2 is influenced by organic solvent environment (in part due to dielectric constant of solvent), which is likely important for understanding the mechanistic details in MK metabolism.

The third hypothesis involves determining if the association of MK with the membrane interface influences the conformation of the MK derivative. We investigated the interaction of MK-2 with a phospholipid Langmuir monolayer, which is a simple 2D model of a single leaflet of a cell membrane.[59,89,90] The fact that MK-2 interacts with the phospholipid monolayer is consistent with the expected MK affinity for the hydrophobic phospholipids that make up the cell membrane. Langmuir monolayer studies support interaction of MK-2 with the phospholipid monolayer interface; however, the lipoquinone is likely compressed out of the interfacial portion of the phospholipid monolayer into the more hydrophobic alkyl tail groups on the top of the monolayer as the pressure increases. Unfortunately, Langmuir phospholipid monolayer studies could not determine the conformation of MK-2; however, the RM surfactant interface complements studies with the phospholipid monolayer interface. The question of folding was further investigated by combining ^{1}H NMR spectroscopic studies of MK-2 in organic solution and in a simple model membrane system, RMs. The conformation of MK-2 was characterized in organic solvents and was found to differ slightly from the conformation when it was associated with the surfactant interface within RMs. It is to be expected that MK-2 would have an affinity for the interface because of its hydrophobicity, which agrees with results observed in the RM system. The RM interface is known to be penetrated by water molecules and thus less packed than a biological membrane and, therefore, has a lower interface pressure meaning MK-2 is unlikely to be compressed out once inside.[63,70,91] The ^{1}H NMR spectroscopic studies in RMs allowed us to observe the association of MK-2 with the interface molecules as well as with itself in its folded state. The ^{1}H–^{1}H 2D NOESY and ROESY NMR spectral data indicate that the U-shaped conformation of MK-2 (Figure 13) remained intact while

212

associating with the RM model membrane interface; however, the overlap between the alkene and the napthoquinone varies with the specific environment. The small changes in the U-shaped conformation document the environmental influence on the conformational folding of MK-2. These results are very important because they document the possibility that MK derivatives in the cell membrane environment may be folded, and if so, such folds will impact the interaction with proteins in the ETS and affect reactivity and function.

Naturally occurring lipoquinones are characterized by the presence of an isoprenyl side-chain of varying length depending on the species of origin. MK-2's isoprenyl side-chain is shorter than most lipoquinones involved in electron transport; therefore, it may not fully mimic the interactions generated by MK derivatives with longer isoprene chains with the membrane or the enzyme systems. However, these results show that the folding of MK-2 is very important and may suggest that MK derivatives with the longer isoprenyl side-chains may adopt folded conformations as well. Understanding how MK-2 and other MK derivatives fold in a hydrophobic environment is critical to gauge how these molecules will behave within a biological membrane associated with the ETS.

Investigation of the conformation of a particular MK derivative's location and conformation will also allow for a more realistic interpretation of data obtained with the novel fluorogenic probe, a vitamin K analog, reported to fluoresce after reduction to the quinol.[92] Studies with this new probe may help provide information on the role that vitamin K plays in key redox processes. Accurate information obtained from the use of this probe would provide better quality data regarding photosynthesis and cellular respiration, and future consideration of MK derivatives location and conformation will be important for proper interpretation of the results obtained from the use of this probe.[92]

■ CONCLUSIONS

Conformations exhibited by alkanes and alkenes are essential for explaining trends in reactivity and manifestation of physical properties, but little is understood regarding biological systems with hydrophobic small components containing alkyl segments. The studies presented in this manuscript describe the chemical and biochemical properties of MK, which is an essential component of the ETS in many Gram-positive bacteria, including pathogens such as *Mycobacterium tuberculosis*, *Mycobacterium leprae*, and *Staphylococcus aureus*, to name a few. We report for the first time in this class of molecules that MK-2 adopts a folded, U-shaped conformation in organic solution. The specific nature of the conformation varied within different organic solvents and thus confirmed our first hypothesis that MK-2 conformations are very sensitive to their environment. These findings contrast with the simple, extended conformation represented in textbooks and the literature that is shown for MK derivatives as well as the more common "Q", belonging to the UBQ family of lipoquinones.

The change in the observed redox potentials of MK-2 with different organic solvents confirmed our second hypothesis. This is important for future studies probing the function of the substrate and potential correlation between conformation and redox potential of MK derivatives, and although most of the studies in this manuscript are of a structural nature, it is important to recognize that the function is likely related to the conformation of the MK-derivative. The discovery that MK-2 adopts a folded conformation may suggest that other MK

derivatives will have similar conformations, which ultimately will impact all the biological systems in which MKs have a role such as within the ETS in specific Gram-positive bacterial pathogens. The result of a stable U-shape conformation in solution and within an interface is important as little information is available on essential hydrophobic biological components.

Although the NMR spectral data illustrated using molecular mechanics allowed for the conclusion that MK-2's conformation is environment dependent, it was important to investigate if this U-shaped conformation remained at a membrane-like interface. We used two membrane model systems to investigate this question. The more physiologically relevant DPPC/DPPE phospholipid monolayers confirmed that MK-2 interacted with the phospholipid interface similar to UBQs; however, the conformation of MK-2 remained unspecified. Complementary studies using the AOT-RM model membrane system allowed determination of the molecular location of MK-2 as penetrating the water–surfactant interface as well as the conformation of MK-2 within the RM interface. We found that the folded, U-shaped conformations observed in organic solution remained upon association with the AOT-RM interface, but the U-shaped conformation differed slightly indicating the interface's environmental influence on conformation. Together, these results support the interpretation that the MKs conformation remains folded in a U-shape even in contact with a model membrane interface, which agrees with our third hypothesis.

More broadly, the results of this study will also enhance our understanding of folded conformations for chemically and biologically important hydrophobic small molecules in solutions and confined hydrophobic environments. The shape and, thus, the conformation of these molecules are relevant for molecular recognition motifs and the processing of these molecules within the membrane. This manuscript represents the first attempt to characterize the conformation as well as the chemical and biochemical properties manifested by the conformation of any electron transferring lipoquinone derivative. Although many studies have been carried out with these systems kinetically, the conformation and how this impacts the biological chemistry has not yet been addressed.

■ EXPERIMENTAL SECTION

Preparation of (E)-2-(3,7-Dimethylocta-2,6-dien-1-yl)-3-methylnaphthalene-1,4-dione (4). To a 500 mL round-bottom Schlenk flask were added a stir bar, diethyl ether (100 mL), and menadione (5.00 g, 29.0 mmol). Then, 10% aq. $Na_2S_2O_4$ (100 mL, 57.4 mmol) was added, and the solution immediately turned dark red. After 30 min of stirring at ambient temperature, the solution was clear yellow. The aqueous layer was separated and extracted with diethyl ether (3×, 100 mL). The combined organic extracts were washed with sat. $NaHCO_3$ (100 mL), followed by DDI H_2O (100 mL), and last with brine (100 mL). The combined organic extracts were dried with anhydrous Na_2SO_4 and then concentrated under reduced pressure at room temperature. The crude powder was triturated with pentane (50 mL), vacuum filtered, and washed with pentane (100 mL) to yield 4.25 g as a pale purple solid. Menadiol formation is indicative by ^1H NMR ($CDCl_3$) by the presence of a peak at 6.64 ppm and is consistent with literature.[93]

To a 100 mL round-bottom Schlenk flask was added ethyl acetate (16 mL) and 1,4-dioxane (16 mL), which was purged/evacuated with argon repeatedly. Then, crude menadiol (2.50 g, 4:1 menadiol:menadione by NMR integration, 11.5 mmol) was added, followed by geraniol (1.92 g, 12.5 mmol), and then dropwise addition of fresh BF_3 etherate (0.8 mL). The solution was allowed to reflux at 70–72 °C for 3 h under argon. The dark orange colored reaction mixture was quenched with ice-H_2O (100 mL) and then extracted with diethyl ether (3×, 100 mL). The yellow

organic extracts were washed with sat. NaHCO$_3$ (100 mL), washed with DDI H$_2$O (100 mL), washed with brine (100 mL), dried with anhydrous Na$_2$SO$_4$, and then concentrated under reduced pressure at room temperature to yield 3.71 g of crude red oil. The crude oil was purified by flash column chromatography (1000 mL of 230–400 mesh SiO$_2$, 70 mm column, 20:1 pentane/ethyl acetate). The yellow oil obtained was dried under reduced pressure (~125 mTorr) overnight to yield 0.713 g (2.31 mmol, 20.1% yield) as a yellow solid. The scale of this reaction was ~14 times larger than the previously reported synthesis.[45] ^{1}H NMR (400 MHz, d_6-DMSO) δ: 7.96–8.01 (m, 2H), 7.80–7.84 (m, 2H), 4.96–5.00 (m,2H), 3.30 (d, 2H, J = 4 Hz), 2.10 (s, 3H), 1.92–2.04 (m, 4H), 1.73 (s, 3H), 1.53 (s, 3H), 1.49 (s, 3H). ^{13}C NMR (100 MHz, d_6-DMSO) δ: 184.7, 183.6, 145.3, 142.9, 136.4, 133.9, 131.5, 130.7, 125.9, 125.8, 123.9, 119.4, 26.0, 25.4, 25.4, 17.5, 16.1, 12.4. LRMS (ESI 70 eV, EtOAc) m/z: [(M + H)$^+$] Calcd for C$_{21}$H$_{25}$O$_2$ 309.2; found 309.2. HRMS (ESI, OTOF) m/z: [(M + H)$^+$] Calcd for C$_{21}$H$_{25}$O$_2$ 309.1849; found 309.1851.

Mass Spectrometry. Low-resolution mass spectrometry (LRMS) experiments were conducted by electron spray ionization mass spectrometry (ESI) on an Agilent technologies 6130 Quadrupole LCMS. High-resolution mass spectrometry (HRMS) experiments were carried out using an Agilent 6220 TOF LC/MS ("OTOF") interfaced to an Agilent 1200 HPLC with electrospray (ESI) mode.

NMR Spectroscopic Studies. 1D and 2D ^{1}H studies were carried out both in organic solvents and more complex media (see below for RM studies). ^{1}H and ^{13}C spectra were recorded using a Varian Model MR400 or Model Inova400 operating at 400 and 100 MHz, respectively. Chemical shift values (δ) are reported in ppm and referenced against the internal solvent peaks in ^{1}H NMR (d_6-DMSO, δ at 2.50 ppm; CDCl$_3$, δ at 7.26 ppm; d_5-pyridine, δ at 8.74 ppm; d_3-acetonitrile, δ at 1.94 ppm; D$_2$O, δ at 4.79 ppm) and in ^{13}C NMR (d_6-DMSO, δ at 39.52 ppm). All NMR spectra were recorded at either 22 or 26 °C.

Solution 1D ^{1}H NMR Spectroscopic Studies. Samples were prepared by dissolving ~5 mg of MK-2 in either 0.5 mL of isooctane, d_5-pyridine, C$_6$D$_6$, d_3-acetonitrile, d_6-DMSO, or D$_2$O. The MK-2 sample in D$_2$O was vortexed for ~1 h to dissolve maximum amount of MK-2. The NMR spectrum was collected by running 32 scans and was locked onto the deuterated solvent except for isooctane, which was ran unlocked using CDCl$_3$ as a spectral window reference.

Sample Preparation for Solution ^{1}H–^{1}H 2D NOESY and ROESY NMR Spectroscopic Studies. To prepare the samples in d_6-DMSO and d_5-pyridine, 0.0031 g of MK-2 was dissolved in 0.5 mL of solvent to yield a 20 mM solution of MK-2. The NMR tubes containing the MK-2 solution were purged with argon prior to data collection.

^{1}H–^{1}H 2D NOESY and ROESY NMR Spectroscopy in Organic Solution. 2D NMR spectroscopic studies in organic solution were carried out on a Varian model MR400 400 MHz magnet at 26 °C. A standard NOESY pulse sequence was used consisting of either 200 or 256 transients with 16 scans in the f1 domain using a 500 ms mixing time, 45° pulse angle, and a 1.5 s relaxation delay. A standard ROESYAD pulse sequence was used consisting of either 200 or 256 transients with 16 scans in the f1 domain using a 400 ms mixing time, 45° pulse angle, and a 2.0 s relaxation delay. The NMR was locked onto either d_6-DMSO or d_5-pyridine and referenced to the internal solvent peak. The resulting spectrum was processed using MestReNova NMR software version 10.0.1.

Molecular Mechanics Calculations. To obtain visual aids of MK-2 conformations, Merck molecular force field 94 (MMFF94) molecular mechanics gas-phase simulations were conducted using ChemBio3D Ultra 12.0 at 25 °C. Starting conformations were obtained from ChemDraw structures or by rotating desired bonds and then either had simulations run or simply an energy minimized to achieve the desired conformation. Conformations A–B in Figure 4 were generated and then energy minimized with a root-mean-square (RMS) gradient of 0.1 and up to 50 iterations to obtain conformations that agreed with our interpretation of the cross peak observations in the ^{1}H–^{1}H 2D NOESY and ROESY NMR spectral data. One simulation was run for 10,000 iterations and then energy minimized using an MMFF94 energy minimization calculation using 500 iterations with a RMS gradient of 0.001 to achieve conformation C in Figure S12C. Conformations D–H

in Figure S12 were generated by rotating bonds to achieve the desired conformation followed by an energy minimization using 20–50 iterations and an RMS gradient of 0.1. A table of structural parameters such as selected distances between hydrogen atoms within the conformations and energies calculated for the 3D conformations can be found in the Supporting Information section.

Electrochemistry Methods. All electrochemistry was performed on a CHI 750D potentiostat. For the cyclic voltammetry (CV), a classical three electrode system was used with scan rate of 100 mV/s at 22 °C. The working electrode was a glassy carbon electrode (BASi MF2012, 3 mm), and the counter electrode was a platinum wire electrode (BASi MW1032). The Ag$^+$/Ag reference electrode (BASi MW1085) was constructed by inserting a Ag wire into a freshly prepared solution of organic solvent (CH$_3$CN, DMSO, or pyridine) with 0.1 M TBAP and 0.01 M AgNO$_3$. Detailed experimental, instrumentation, and analysis are available in the Supporting Information.

Langmuir Monolayer Compression Isotherms. The subphase for each experiment consisted of approximately 50 mL of a 20 mM sodium phosphate buffer (pH 7.4). The phospholipid solution was prepared by dissolving powdered phospholipid into a chloroform:methanol (9:1, v:v) solution to produce 1 mM phospholipid stock solution. The film applied to the subphase consisted of 20 μL of phospholipid stock solution or a 50:50 mole fraction mixture of MK-2 with either DPPC or DPPE. The resulting film was equilibrated for 15 min and then compressed using a Teflon ribbon at a rate of 10 mm/min (2.4 Å^2/chain). The surface pressure was measured using the Wilhemy plate method where a wire probe was used as the plate on a Kibron μTrough XS.[94] The reported compression isotherms are reported as an average of three trials (constructed by averaging the three isotherms in excel). See Supporting Information for compression modulus data and interpretation.

Sample Preparation for RM NMR Spectroscopic Studies. A 0.50 M AOT stock solution was made by dissolving AOT (5.56 g, 12.5 mmol) in isooctane (25.0 mL). RMs were prepared by mixing the 0.50 M AOT stock solution with D$_2$O (pH 7.0) and then vortexed until clear. MK-2 RMs were made in a similar manner except an 11.2 mM MK-2 stock solution was prepared by directly dissolving MK-2 in the 0.50 M AOT/isooctane solution. Then, the MK-2-AOT-isooctane stock solution along with D$_2$O (pH 7) were used to make RMs.

1D ^{1}H NMR Spectroscopic Studies of AOT/Isooctane RMs That Contain MK-2. 1D ^{1}H NMR spectroscopic experiments were carried out using a Varian Inova 400 MHz instrument using routine parameters (pulse angle: 45°, relaxation delay of 1 s) at 22 °C. The RM spectra were internally referenced using the isooctane methyl peak set to 0.904 ppm.[95] Data analysis and spectrum workup were done using the NMR software, MestReNova version 10.0.1.

Sample Preparation for ^{1}H–^{1}H 2D NOESY and ROESY NMR Spectroscopic Studies (RMs). To prepare the AOT/isooctane stock solution, 0.22 g AOT (0.50 mmol) was dissolved into isooctane (1.0 mL) for a final 0.50 M AOT stock solution. Then 0.035 g (1.10 mmol) of MK-2 was dissolved into the 0.50 M AOT stock solution for a final concentration of 110 mM MK-2. Then, 892.6 μL of MK-2 AOT/isooctane stock solution was mixed with 107.3 μL of D$_2$O (pH = 7) and then vortexed until clear. This final mixture results in a w_0 12 RM microemulsion with an overall concentration of MK-2 being 100 mM (~29 molecules per RM).

^{1}H–^{1}H 2D NOESY and ROESY NMR Spectroscopic Studies in AOT/Isooctane w_0 12 RM. 2D NMR samples were ran using similar conditions used previously[61] using a Varian model MR400 400 MHz magnet at 26 °C. A standard NOESY pulse sequence was used consisting of 256 transients with 16 scans in the f1 direction using a 200 ms mixing time, 45° pulse angle, and a relaxation delay of 1.5 s. A standard ROESYAD pulse sequence was used consiting of 256 transients with 16 scans in the f1 direction using a 200 ms mixing time, 45° pulse angle, and a relaxation delay of 2.0 s. The NMR was locked onto 10% D$_2$O, and the spectrum was referenced to the isooctane methyl peak at 0.904 ppm as previously reported.[95] The resulting spectrum was processed using MestReNova NMR software version 10.0.1. The 3D structure illustration within a RM was drawn using

214

ChemBioD Ultra 12.0 and ChemBio3D Ultra 12.0 based on spectral parameters described under results.

ASSOCIATED CONTENT

Supporting Information

The Supporting Information is available free of charge on the ACS Publications website at DOI: 10.1021/acs.joc.7b02649.

General experimental information; 1D and 2D NMR spectroscopic and structural data of MK-2, MK-2 conformational analysis, and relevant internuclear distances; electrochemistry experimental and data/discussion; ^{1}H NMR of MK-2 with TBAP; Langmuir monolayer compression modulus of MK-2 and interpretation (PDF)

AUTHOR INFORMATION

Corresponding Author

*E-mail: Debbie.Crans@colostate.edu

ORCID

Jordan T. Koehn: 0000-0003-3008-6303
Debbie C. Crans: 0000-0001-7792-3450

Notes

The authors declare no competing financial interest.

ACKNOWLEDGMENTS

REFERENCES

(1) Beller, H. R.; Soon Lee, T.; Katz, L. Nat. Prod. Rep. 2015, 32, 1508.

(2) Frank, A.; Groll, M. Chem. Rev. 2017, 117, 5675.

(3) Thulasiram, H. V.; Erickson, H. K.; Poulter, C. D. Science 2007, 316, 73.

(4) da Costa, M. S.; Albuquerque, L.; Nobre, M. F.; Wait, R. In Methods in Microbiology: Taxonomy of Prokaryotes; Rainey, F., Oren, A., Eds.; Elsevier Academic Press Inc: San Diego, CA, 2011; Vol. 38, p 197.

(5) Kroppenstedt, R. M.; Mannheim, W. Int. J. Syst. Bacteriol. 1989, 39, 304.

(6) Collins, M. D.; Jones, D. Microbiol. Rev. 1981, 45, 316.

(7) Meganathan, R. Vitam. Horm. 2001, 61, 173.

(8) Caluwe, R.; Pyfferoen, L.; De Boeck, K.; De Vriese, A. S. Clin. Kidney J. 2016, 9, 273.

(9) Bergdoll, L.; ten Brink, F.; Nitschke, W.; Picot, D.; Baymann, F. Biochim. Biophys. Acta, Bioenerg. 2016, 1857, 1569.

(10) Epand, R. M.; Walker, C.; Epand, R. F.; Magarvey, N. A. Biochim. Biophys. Acta, Biomembr. 2016, 1858, 980.

(11) Villaume, M. T.; Sella, E.; Saul, G.; Borzilleri, R. M.; Fargnoli, J.; Johnston, K. A.; Zhang, H.; Fereshteh, M. P.; Murali Dhar, T. G.; Baren, P. S. ACS Cent. Sci. 2016, 2, 27.

(12) Choi, S. R.; Larson, M. A.; Hinrichs, S. H.; Bartling, A. M.; Frandsen, J.; Narayanasamy, P. Future Med. Chem. 2016, 8, 11.

(13) Matarlo, J. S.; Lu, Y.; Daryaee, F.; Daryaee, T.; Ruzsicska, B.; Walker, S. G.; Tonge, P. J. ACS Infect. Dis. 2016, 2, 329.

(14) Szamosvari, D.; Bottcher, T. Angew. Chem., Int. Ed. 2017, 56, 7271.

(15) Vilcheze, C.; Hartman, T.; Weinrick, B.; Jain, P.; Weisbrod, T. R.; Leung, L. W.; Freundlich, J. S.; Jacobs, W. R. Proc. Natl. Acad. Sci. U. S. A. 2017, 114, 4495.

(16) Upadhyay, A.; Fontes, F. L.; Gonzalez-Juarrero, M.; McNeil, M. R.; Crans, D. C.; Jackson, M.; Crick, D. C. ACS Cent. Sci. 2015, 1, 292.

(17) Vos, M.; Esposito, G.; Edirisinghe, J. N.; Vilain, S.; Haddad, D. M.; Slabbaert, J. R.; Van Meensel, S.; Schaap, O.; De Strooper, B.; Meganathan, R.; Morais, V. A.; Verstreken, P. Science 2012, 336, 1306.

(18) Nakagawa, K.; Hirota, Y.; Sawada, N.; Yuge, N.; Watanabe, M.; Uchino, Y.; Okuda, N.; Shimomura, Y.; Suhara, Y.; Okano, T. Nature 2010, 468, 117.

(19) Hiratsuka, T.; Furihata, K.; Ishikawa, J.; Yamashita, H.; Itoh, N.; Seto, H.; Dairi, T. Science 2008, 321, 1670.

(20) Newman, D. K.; Kolter, R. Nature 2000, 405, 94.

(21) Collins, M. D.; Shah, H. N.; Minnikin, D. E. J. Appl. Bacteriol. 1980, 48, 277.

(22) Thomson, R. H. Naturally Occurring Quinones; Chapman & Hall: London, 1971.

(23) Cooper, G. M.; Hausman, R. E. The Cell: A Molecular Approach, 5th ed.; Sinauer Associates, Inc.: Sunderland, MA, 2009.

(24) Nelson, D. L.; Cox, M. M. Lehninger Principles of Biochemistry, 5th ed.; W. H. Freeman and Company: New York, 2008.

(25) Woodward, R. B.; Bloch, K. J. Am. Chem. Soc. 1953, 75, 2023.

(26) Hess, B. A., Jr.; Smentek, L. Angew. Chem., Int. Ed. 2013, 52, 11029.

(27) Murgolo, N. J.; Patel, A.; Stivala, S. S.; Wong, T. K. Biochemistry 1989, 28, 253.

(28) Lowry, T. H.; Richardson, K. S. Mechanism and Theory in Organic Chemistry, 3rd ed.; Harper & Row Publishers: New York, 1987.

(29) Klauda, J. B.; Brooks, B. R.; et al. J. Phys. Chem. B 2005, 109, 5300.

(30) Choudhury, R.; Barman, A.; Prabhakar, R.; Ramamurthy, V. J. Phys. Chem. B 2013, 117, 398.

(31) Chum, S. P.; Knight, G. W.; Ruiz, J. M.; Phillips, P. J. Macromolecules 1994, 27, 656.

(32) Robertson, M. B.; Klein, P. G.; Ward, I. M.; Packer, K. J. Polymer 2001, 42, 1261.

(33) Cao, M.; Monson, P. A. J. Phys. Chem. B 2009, 113, 13866.

(34) Nikki, K.; Inakura, H.; Wu-Le; Suzuki, N.; Endo, T. J. Chem. Soc., Perkin Trans. 2 2001, 2370.

(35) Nikki, K.; Nakagawa, N. Org. Magn. Reson. 1983, 21, 552.

(36) Nikki, K. Magn. Reson. Chem. 1990, 28, 385.

(37) Law, J. M. S.; Setiadi, D. H.; Chass, G. A.; Csizmadia, I. G.; Viskolcz, B. J. Phys. Chem. A 2005, 109, 520.

(38) Kanicky, J. R.; Shah, D. O. J. Colloid Interface Sci. 2002, 256, 201.

(39) Ko, Y. H.; Kim, Y.; Kim, H.; Kim, K. Chem. - Asian J. 2011, 6, 652.

(40) Ko, Y. H.; Kim, H.; Kim, Y.; Kim, K. Angew. Chem., Int. Ed. 2008, 47, 4106.

(41) Schramm, M. P.; Rebek, J., Jr. Chem. - Eur. J. 2006, 12, 5924.

(42) de Sousa, F. F.; Freire, P. T. C.; Saraiva, G. D.; Lima, J. A.; Alcantara, P.; Melo, F. E. A.; Mendes, J. Vib. Spectrosc. 2010, 54, 118.

(43) Collins, M. D.; Kroppenstedt, R. M. FEMS Microbiol. Lett. 1987, 44, 215.

(44) Bentley, R. Pure Appl. Chem. 1975, 41, 47.

(45) Suhara, Y.; Wada, A.; Tachibana, Y.; Watanabe, M.; Nakamura, K.; Nakagawa, K.; Okano, T. Bioorg. Med. Chem. 2010, 18, 3116.

(46) Payne, R. J.; Daines, A. M.; Clark, B. M.; Abell, A. D. Bioorg. Med. Chem. 2004, 12, 5785.

(47) Tynkkynen, T.; Hassinen, T.; Tiainen, M.; Soininen, P.; Laatikainen, R. Magn. Reson. Chem. 2012, 50, 598.

(48) Ishihara, M.; Sakagami, H. Anticancer Res. 2007, 27, 4059.

(49) Lancaster, C. R. D.; Haas, A. H.; Madej, M. G.; Mileni, M. Biochim. Biophys. Acta, Bioenerg. 2006, 1757, 988.

(50) Prince, R. C.; Leslie Dutton, P.; Malcolm Bruce, J. FEBS Lett. 1983, 160, 273.

(51) Guin, P. S.; Das, S.; Mandal, P. C. Int. J. Electrochem. 2011, 2011, 816202.

(52) Dryhurst, G.; Kadish, K. M.; Scheller, F.; Renneberg, R. Biological Eletrochemistry; Academic Press: New York, 1982.

(53) Luder, W. F.; Kraus, P. B.; Kraus, C. A.; Fuoss, R. M. J. Am. Chem. Soc. 1936, 58, 255.

(54) Jaworski, J. S.; Leniewska, E.; Kalinowski, M. K. J. Electroanal. Chem. Interfacial Electrochem. 1979, 105, 329.

(55) Baruah, B.; Roden, J. M.; Sedgwick, M.; Correa, N. M.; Crans, D. C.; Levinger, N. E. J. Am. Chem. Soc. 2006, 128, 12758.

(56) Odella, E.; Falcone, R. D.; Silber, J. J.; Correa, N. M. ChemPhysChem 2016, 17, 2407.

(57) Diaz-Fernandez, Y.; Foti, F.; Mangano, C.; Pallavicini, P.; Patroni, S.; Perez-Gramatges, A.; Rodriguez-Calvo, S. *Chem. - Eur. J.* **2006**, *12*, 921.

(58) Pallavicini, P.; Diaz-Fernandez, Y.; Pasotti, L. *Coord. Chem. Rev.* **2009**, *253*, 2226.

(59) Stefaniu, C.; Brezesinski, G.; Mohwald, H. *Adv. Colloid Interface Sci.* **2014**, *208*, 197.

(60) Sostarecz, A. G.; Gaidamauskas, E.; Distin, S.; Bonetti, S. J.; Levinger, N. E.; Crans, D. C. *Chem. - Eur. J.* **2014**, *20*, 5149.

(61) Peters, B. J.; Groninger, A. S.; Fontes, F. L.; Crick, D. C.; Crans, D. C. *Langmuir* **2016**, *32*, 9451.

(62) Riter, R. E.; Kimmel, J. R.; Undiks, E. P.; Levinger, N. E. *J. Phys. Chem. B* **1997**, *101*, 8292.

(63) Maitra, A. *J. Phys. Chem.* **1984**, *88*, 5122.

(64) Durantini, A. M.; Falcone, R. D.; Silber, J. J.; Correa, N. M. *ChemPhysChem* **2016**, *17*, 1678.

(65) Lepori, C. M. O.; Correa, N. M.; Silber, J. J.; Falcone, R. D. *Soft Matter* **2016**, *12*, 830.

(66) Hoyo, J.; Torrent-Burgues, J.; Guas, E. *J. Colloid Interface Sci.* **2012**, *384*, 189.

(67) Quinn, P. J.; Esfahani, M. A. *Biochem. J.* **1980**, *185*, 715.

(68) Patterson, M.; Vogel, H. J.; Prenner, E. J. *Biochim. Biophys. Acta, Biomembr.* **2016**, *1858*, 403.

(69) Roche, Y.; Peretti, P.; Bernard, S. *J. Therm. Anal. Calorim.* **2007**, *89*, 867.

(70) De, T. K.; Maitra, A. *Adv. Colloid Interface Sci.* **1995**, *59*, 95.

(71) Sedgwick, M. A.; Trujillo, A. M.; Hendricks, N.; Levinger, N. E.; Crans, D. C. *Langmuir* **2011**, *27*, 948.

(72) Zan, G. T.; Wu, Q. S. *Adv. Mater.* **2016**, *28*, 2099.

(73) Kuchler, A.; Yoshimoto, M.; Luginbuhl, S.; Mavelli, F.; Walde, P. *Nat. Nanotechnol.* **2016**, *11*, 409.

(74) Dharaiya, N.; Bahadur, P. *Colloids Surf., A* **2012**, *410*, 81.

(75) Dumas, C.; Meledandri, C. J. *Langmuir* **2015**, *31*, 7193.

(76) Kaur, G.; Chiappisi, L.; Prevost, S.; Schweins, R.; Gradzielski, M.; Mehta, S. K. *Langmuir* **2012**, *28*, 10640.

(77) Sanchez-Lombardo, I.; Baruah, B.; Alvarez, S.; Werst, K. R.; Segaline, N. A.; Levinger, N. E.; Crans, D. C. *New J. Chem.* **2016**, *40*, 962.

(78) Crans, D. C.; Levinger, N. E. *Acc. Chem. Res.* **2012**, *45*, 1637.

(79) Bock, C. W.; Panchenko, Y. N.; Krasnoshchiokov, S. V.; Aroca, R. *J. Mol. Struct.* **1987**, *160*, 337.

(80) Squillacote, M. E.; Semple, T. C.; Mui, P. W. *J. Am. Chem. Soc.* **1985**, *107*, 6842.

(81) Mui, P. W.; Grunwald, E. *J. Phys. Chem.* **1984**, *88*, 6340.

(82) Gundersen, G.; Thomassen, H. G.; et al. *J. Mol. Struct.* **1991**, *243*, 385.

(83) Fujimoto, N.; Kosaka, T.; Yamada, M. *Menaquinone as Well as Ubiquinone as a Crucial Component in the Escherichia coli Respiratory Chain*; InTech: Rijeka, Croatia, 2012.

(84) Lai, C.-T.; Li, H.-J.; Yu, W.; Shah, S.; Bommineni, G. R.; Perrone, V.; Garcia-Diaz, M.; Tonge, P. J.; Simmerling, C. *Biochemistry* **2015**, *54*, 4683.

(85) Yano, T.; Rahimian, M.; Aneja, K. K.; Schechter, N. M.; Rubin, H.; Scott, C. P. *Biochemistry* **2014**, *53*, 1179.

(86) Peover, M. E. *J. Chem. Soc.* **1962**, 4540.

(87) Chadar, D.; Camilles, M.; Patil, R.; Khan, A.; Weyhermuller, T.; Salunke-Gawali, S. *J. Mol. Struct.* **2015**, *1086*, 179.

(88) Kathawate, L.; Joshi, P. V.; Dash, T. K.; Pal, S.; Nikalje, M.; Weyhermuller, T.; Puranik, V. G.; Konkimalla, V. B.; Salunke-Gawali, S. *J. Mol. Struct.* **2014**, *1075*, 397.

(89) McQuaw, C. M.; Sostarecz, A. G.; Zheng, L.; Ewing, A. G.; Winograd, N. *Langmuir* **2005**, *21*, 807.

(90) Demel, R. A.; Geurts Van Kessel, W. S. M.; Zwaal, R. F. A.; Roelofsen, B.; Van Deenen, L. M. *Biochim. Biophys. Acta, Biomembr.* **1975**, *406*, 97.

(91) Choi, Y.; Attwood, S. J.; Hoopes, M. I.; Drolle, E.; Karttunen, M.; Leonenko, Z. *Soft Matter* **2014**, *10*, 206.

(92) Belzile, M.-N.; Godin, R.; Durantini, A.; Cosa, G. *J. Am. Chem. Soc.* **2016**, *138*, 16388.

(93) Dobrinescu, C.; Iorgulescu, E. E.; Mihailciuc, C.; Macovei, D.; Wuttke, S.; Kemnitz, E.; Parvulescu, V. I.; Coman, S. M. *Adv. Synth. Catal.* **2012**, *354*, 1301.

(94) Girard-Egrot, A.; Blum, L. J. Langmuir-Blodgett Technique for Synthesis of Biomimetic Lipid Membranes. In *Nanobiotechnology of Biomimetic Membranes*; Ferrari, M., Martin, D. K., Eds.; Springer: New York, 2007; p 23.

(95) Samart, N.; Beuning, C. N.; Haller, K. J.; Rithner, C. D.; Crans, D. C. *Langmuir* **2014**, *30*, 8697.

216

List of Abbreviations

4, 4-dimethyl-4-silapentane-1-sulfonic acid……………………………………………………………………………DSS

Aerosol-OT………AOT

Benzamide……BA

Benzhydrazide………BHZ

Benzoate………B^-

Benzoic Acid……HB

Black Lipid Membrane……………………………………………………………………………………………………BLM

Brewster Angle Microscopy…………………………………………………………………………………………BAM

Dipalmitoylphosphatidylcholine…………………………………………………………………………………DPPC

Dipalmitoylphosphatidylethanolamine………………………………………………………………………DPPE

Double Deionized………………………………………………………………………………………………………DDI

Dynamic Light Scattering…………………………………………………………………………………………DLS

Infrared……IR

Isoniazid……INH

Isonicotinamide……iNIC

Lysophosphatidylcholine……………………………………………………………………………………………LPC

Menaquinone……MK

Menaquinone-9………MK-9

Minimum Inhibitory Concentration…………………………………………………………………………MIC

Mycobacterium tuberculosis………………………………………………………………………………………*Mtb*

Nicotinamide……NIC